ELECTROMAGNETIC WAVE MODELS FOR POLARIMETRIC REMOTE SENSING OF GEOPHYSICAL MEDIA

by

SON V. NGHIEM

B.S., Texas A & M University
December 1985

S.M., Massachusetts Institute of Technology
May 1988

E.E., Massachusetts Institute of Technology
February 1991

Submitted to the Department of Electrical Engineering and Computer Science
in Partial Fulfillment of the Requirements for the Degree of

DOCTOR OF PHILOSOPHY

at the

MASSACHUSETTS INSTITUTE OF TECHNOLOGY

May 1991

Signature of Author _____
Department of Electrical Engineering and Computer Science
May, 1991

Certified by _____
Jin Au Kong
Thesis Supervisor

Accepted by _____
Arthur C. Smith
Chairman, Departmental Committee on Graduate Students

ELECTROMAGNETIC WAVE MODELS FOR POLARIMETRIC REMOTE SENSING OF GEOPHYSICAL MEDIA

by

Son V. Nghiem

Submitted to the Department of Electrical Engineering and Computer Science
on May 2, 1991 in partial fulfillment of the requirements for the
Degree of Doctor of Philosophy

ABSTRACT

Fully polarimetric data convey additional information regarding the remotely sensed media and thereby provide more accurate identification and classification of terrain types in sensor imagery. For applications in polarimetric remote sensing, electromagnetic wave models describing wave propagation and scattering mechanisms are presented, experimental data and theoretical results are compared, and corresponding polarization signatures are discussed.

Geophysical media usually contain inhomogeneities in a random manner and often stratified into multiple layers. For such media, polarimetric multi-layer anisotropic random medium models are developed. The models are started with simple scatterers of uniform size, spheroidal shape, and two-phase mixing; then, the complexity is increased for multi-species media with multi-phase and distributions of scatterer orientations, sizes, and shapes which are varied under dynamic environmental conditions. Scattering effects of the random media are described by three-dimensional correlation functions with variances and correlation lengths corresponding to the fluctuation strengths and the physical geometry of the inhomogeneities, respectively. With proper consideration of singularities in the dyadic Green's function, the strong fluctuation theory is used to calculate effective permittivities which account for the modification of wave speed and attenuation in the presence of the scatterers. The distorted Born approximation is then applied to obtain correlations of the scattered fields. In the derivation of the scattered fields, phase information is preserved and multiple wave interaction between the inhomogeneities and the layer boundaries are incorporated in the dyadic Green's function for layered media. From the correlations of the scattered fields, covariance matrices, Mueller matrices, and polarization signatures are calculated in terms of scattering coefficients to characterize polarimetric scattering properties of the geophysical media.

The models are used to obtain theoretical results for experimental data comparisons at microwave frequencies. For vegetation, data from a soybean canopy are compared not only as a function of incident angle but also over an extended period of time since multi-temporal data are available. Polarization signatures corresponding to various growth stages of the soybean show temporal variations which reveals the effect of the soil surface and the change in biophysical parameters. For sea ice, theoretical and experimental backscattering results are matched over the available range of incident angles. Polarization signatures for sea ice of different types with and without snow cover are calculated. Special features observed in the signatures pertaining to the different ice types are related to the polarimetric scattering coefficients and explained physically. Thermal variations of sea ice characteristics and structures are also considered.

Thesis Supervisor: Jin Au Kong
Title: Professor of Electrical Engineering

Acknowledgments

I would like to express my sincerest thank to Professor Jin A. Kong for his teaching fundamental concepts in electromagnetics with the most systematic way, for his guidance in all academic matters, for his expert supervision in research, and for his constructive criticism and his enthusiastic support. I always learn from his subtle sophistication and his great simplicity.

I am very grateful to Dr. Robert T. Shin for his reading and suggestions in the thesis, for many interesting technical discussions, and for his enthusiastic and valuable times he gave me. Thank you very much, Dr. Shin.

To Professor Frederic R. Morgenthaler, my deep gratitude for his cordial teaching, advice, and suggestions in many aspects all along my graduate years including reading this thesis.

I sincerely thank Dr. Thuy Le Toan for her insightful discussions and the collaboration in vegetation research. Many Thanks to Drs. Charles A. Luther, Anthony J. Gow, and Donald K. Perovich for the sea ice experiments, to Dr. Kevin O'Neill for the soil experiments, and to Drs. Serpil Ayasli and Jack Fleischman for the forest experiment.

I would like to thank all the group members for providing the exciting technical discussions, interesting seminars, and friendly environment. They are Dr. Sami Ali, Dr. Alain Priou, Dr. Ismo Lindell, Dr. Arthur Jordan, Dr. Min Lee, Dr. Tsuneki Yamasaki, Dr. Soon Poh, Dr. Ari Sihvola, Dr. Maurice Borgeaud, Dr. Eric Yang, Dr. Check-Fu Lee, Dr. Jean-Fu Kiang, Dr. Freeman Lin, Dr. Michael Tsuk, Dr. Ann Tulintseff, Dr. Brian Yang, Dr. Diane Gaylor, Dr. David Sheen, Zhuzhen Li, Wen-Ke

Wang, Gizheng Gu, Albert Swartz, Harold Lim, Kevin Li, Cheung-Wei Lam, Greg Zancewicz, Robert Atkins, David Arnold, Ike Chang, Steve Rogers, Richard Kim, Karen Adler, Keith Groves, Jake Xia, Ali Tassoudji, Murat Veysoglu, Chih Hsu, John Oates, Li-Fang Wang, Yoshihisa Hara, Gregory Huang, William Au, Sue Syu, Ping Chiang, Margery Brother, Ming-Yu Wei Lin, Kit-Wah Lai, Sara Larson, and Barbara Roman. To the computer managers Dr. Eric Yang, Dr. Michael Tsuk, and Hsiu-Chi Han, I very much appreciate your maintaining and making the computers most convenient to the users. To my amigo Herng-Aung Yueh together with Florence and Richard and my other amigo Hsiu-Chi Han together with Lydia, many thanks for your helps and I always cherish our wonderful times. I thank Tue Nguyen, Tien Nguyen, Thuy Duong, Viet Anh, and Vu Phan for their warmth friendship.

I am deeply grateful to the Moyers who welcomed my family with all their hearts and provided us with crucial helps during our beginning days in the United States. You are the symbol of kindness.

For all their love, understanding, and support, I thank my brothers, sisters, nephews, and nieces: Huong Nghiem and Hung Tran and John Meo, Duong Nghiem and Kim Trieu, Giang Nghiem and Quang Dam and Dat, Ngo Lieu and Hy Ma and Phuong and Thanh and Thu and Oanh, Hau Lieu and Hien Le and Viet and Lieu, Ho Lieu and Quyen Ton, Quyen Lieu and Loan Dinh and Linh and My, Chuong Huynh and Tuyet Nguyen and Bi and Nga and Nam, Khanh Lieu and Dong Phan, and Hue Tran and Nhieu Tran.

Specially, I thank my parents, Minh V. Nghiem and Bui T. Dang, and my parents in-law, Khon Lieu and Tran Tran. How could I ever repay their unbounded love everlasting throughout time and prevailing over hardship. To my parents, I dedicate this work.

To my beloved wife, Anh Lieu, I wish to acknowledge her understanding, encouragement, and her typing the thesis. I also dedicate this work to her.

To my parents

To my wife

Table of Contents

List of Figures

Figures in Chapter 1

Figures in Chapter 2

Figures in Chapter 3

Figures in Chapter 4

Figures in Chapter 5

Figures in Chapter 6

Figure in Appendix B

List of Tables

Tables in Chapter 3

Tables in Chapter 5

Chapter 1
Introduction

1.1 Description of the Thesis

In this thesis, electromagnetic wave models derived from Maxwell's equations for applications in polarimetric remote sensing of geophysical media are presented. The models will be layered, anisotropic, and fully polarimetric as compared to many existing models which are for conventional remote sensing. Moreover, the models will cover media started with simple scatterers of uniform size, spheroidal shape, and two-phase mixing; then, the complexity is increased for multi-species media with multi-phase and distributions of scatterer orientations, sizes, and shapes which are varied under dynamic environmental conditions.

First considered is a review on the analytic wave, modified radiative transfer, and traditional radiative transfer theories. Polarimetric descriptions such as scattering matrix, covariance matrix, Mueller matrix, Stokes vector, polarization signature, and polarimetric scattering coefficients are then discussed. Theoretical models are developed in the subsequent chapters increasingly in physical complexity along with experimental result comparisons, interpretations, and simulations for various media including snow, sea ice, and vegetation at microwave frequencies. From the models, effective permittivities of the media are calculated with the extended strong fluctuation theory and polarimetric scattering coefficients are derived under the distorted Born approximation. The last chapter will summarize the thesis.

1.2 Review of Theoretical Models

With the advances of sensor technology especially the airborne and space borne SAR with multi-frequency and multi-polarization capability, remote sensing of geophysical media has drawn considerable efforts on experimental campaigns and theoretical models. In the modeling of the media, theoretical models are developed based on different fundamental principles, assumptions, and approximations resulting in various domains of validity for certain physical processes which require a variety of model input parameters. It is the purpose of this section to review the theoretical models. Considerations will be given to the model realism, commonalities, and incompatibilities. The realism herein signifies the incorporation of the dominant physical processes, the applicability of the models to the commonly encountered geophysical characteristics, and the realizability of input parameters either observable or inferable from measured data. The commonalities and incompatibilities are thereby the intercomparison of models in terms of the model realism as specified. These tasks necessitate a systematical review methodology.

a. Review Methodology

Theoretical models for remote sensing of geophysical media are reviewed systematically as illustrated in the chart of Figure 1.2.1. Formulated from Maxwell's equations, the theoretical models can be classified into the analytic Wave Theory (WT) and the Modified Radiative Transfer (MRT) theory which is a more rigorous version of the traditional Radiative Transfer (RT) theory. The WT and MRT are therefore closely related and both can account for the coherent effect of wave propagation in different directions. Though similar in form to the MRT, the RT is based on the energy transport equation which deals directly with the wave intensity.

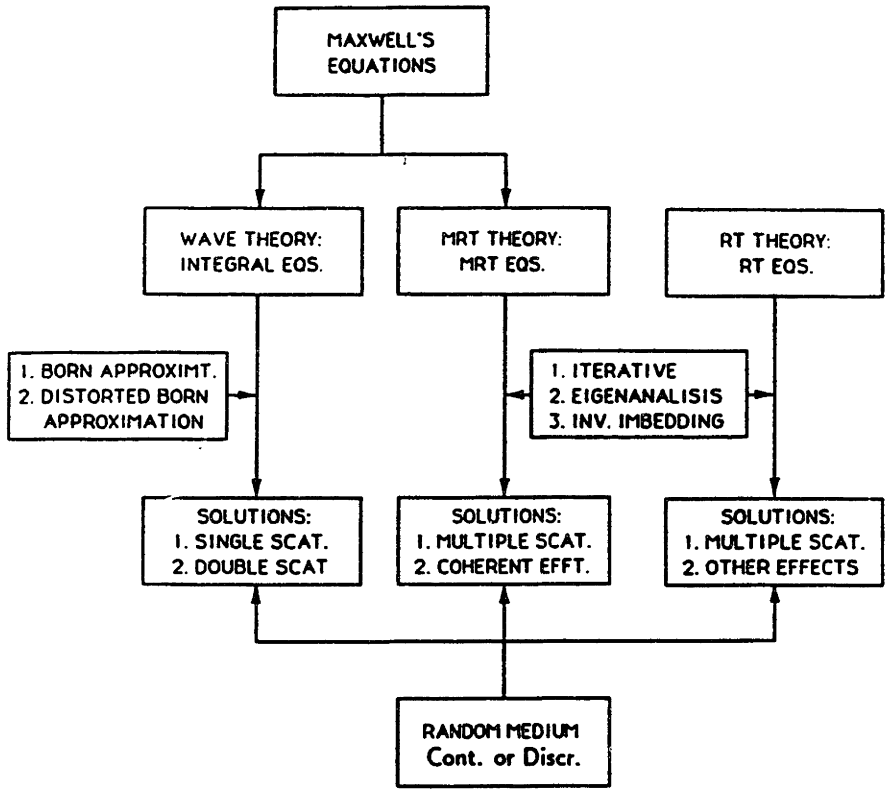

Figure 1.2.1 Review chart for theoretical models

For each theory, there are several methods under various approximations for obtaining solutions utilizing the concept of continuous or discrete random medium. In WT, wave equations are transformed into integral equations and often solved with the Born, the distorted Born, or the renormalization method. The MRT and RT equations have been solved with the method of iteration, discrete ordinate eigenanalysis, or invariant imbedding. Consequently, the solutions are restricted in the corresponding regions of validity and requiring different forms of input parameters. From the assumptions, the approximations, and the solution methods, the obtained results can be seen as to account for which physical processes applicable in which physical conditions and structures. The commonalities and incompatibilities of the models can thus be recognized. By following this methodology, the theoretical models for remote sensing will be reviewed in the categories of the analytic wave, the modified radiative transfer, and the traditional radiative transfer theories.

b. Analytic Wave Theory

In the analytic wave theory, wave equations are derived directly from Maxwell's equations. To obtain analytical solutions, approximations are necessary. Among those are the Rytov and the Born approximations. In the Rytov approach, the field in a medium with randomly embedded inhomogeneities is expressed in terms of a complex phase in the exponent of an exponential function to describe the distortion of the phase front and the attenuation of the wave due to scattering. The resulting equation governing the complex phase is a nonlinear wave equation which can be linearized by applying the Rytov approximation and the solution can then be obtained. In the Born method, the field is written in form of an integral equation exactly derivable from the wave equation with the use of dyadic Green's functions. The solution is obtained by truncating an iterative series expression of the integral equation. While both approximations require weak fluctuations on the inhomogeneous permittivity of the random medium, the Rytov approximation can have a larger range of validity in the fluctuation strength. The Born approximation, however, is a simpler and can be applied more generally without a priori knowledge of the field [1].

With the Born approximation, the medium has been modeled with an isotropic two-layer [2], isotropic multi-layer [3], anisotropic two-layer [4], or isotropic-anisotropic three-layer configuration [5] to calculate the conventional scattering coefficients. The number of layers is herein defined as equal to the number of interfaces; thus, an n-layer configuration contains $n+1$ different regions. In polarimetric remote sensing, Mueller and covariance matrices which characterize fully polarimetric scattering properties of the media are calculated for an isotropic two-layer [6] or an anisotropic two-layer configuration [7]. Physically, the first order Born approximation corresponds to the single scattering process and the second order corresponds the double scattering and so on. In isotropic random media containing spherical scatterers, the depolarization giving rise to the cross polarization return is due to the second and

higher order term (multiple scattering) [6,8]. Stronger depolarization effect can come from the first-order term (single scattering) in anisotropic random media [4,7] and non-spherical scatterers [58]. As discussed, the Born approximation is limited to weak fluctuations in sparse and tenuous media.

For denser or less tenuous media, improvements on the Born approximation are necessary. The distorted Born approximation has been applied in the modeling of random media [9-12]. This approximation takes into account the dissipation and scattering losses and also the modification of wave speed due to the embedded scatterers; therefore, multiple scattering has been considered to some extent. Physically, the first order distorted Born approximation describes the single scattering process of the mean field and can also be interpreted as the first-order multiple scattering process. Another method for the improvement is the renormalization technique which has been carried out to the first order [13], second order [14], and higher order for a half-space isotropic random medium [15]. For a two-layer anisotropic medium, the renormalization has been applied to derive the Dyson equation for the mean field and the Bethe-Salpeter equation for the scattered field which are respectively solved under the nonlinear and the ladder approximations [16].

For media with strong permittivity fluctuations, the strong fluctuation theory is used in conjunction with the distorted Born approximation. In the strong fluctuation theory [17], the Dyson equation is derived with the renormalization method and solved with the bilocal approximation. In the bilocal approximated Dyson equation, the observation and the source points in the random medium can coincide with each other to give rise to the singularity in the dyadic Green's function. The singularity needs be taken into account properly by decomposing the Green's function into a principal value part and a singular part corresponding to the source exclusion volume. The singular part of the Green's function is determined by the elimination of secular term and depends on the shape of the exclusion volume. By using the strong

fluctuation theory, effective permittivities and variances of the random medium are obtained for isotropic and anisotropic random media [17,18]. Scattering coefficients are then calculated under the distorted Born approximation with the effective permittivities for the mean dyadic Green's function. In conventional remote sensing, the method has been applied to an isotropic half-space of snow [19], an anisotropic half space [20], an isotropic-anisotropic three-layer configuration [21], and an isotropic two-layer configuration with second-order distorted Born approximation [22]. In remote sensing of vegetation, the strong fluctuation theory is thus applicable to both sparse or dense canopy. For sea ice, embedded brine inclusions are usually small compared to a wavelength in microwave frequency range and have a permittivity distinctively higher than that of the background ice; the strong fluctuation theory is suitable in this case.

To characterize the random media mentioned in the above methods, either the continuous or the discrete random medium can be used. For the continuous model, the medium has been described by three-dimensional correlation functions with variances and correlation lengths corresponding to the fluctuation strengths and the physical geometries of the scatterers, respectively. The inputs to the continuous model are the variances, the correlation lengths, the background mean permittivities, the thicknesses of the layers, and the directions of wave incidence and scattering. If the strong fluctuation theory is used, the inputs are correlation lengths, the constituent permittivities and fractional volumes in the random medium, the layer thicknesses, and the incident and scattering directions. The continuous model has been used in [2-10,13-18,20,21]. In the discrete model, the inhomogeneities are considered as discrete scatterers embedded in a background medium and the inputs are the permittivities, the fractional volumes, the shapes, the sizes, the orientation distributions of the scatterers, the permittivity of the background, the layer thickness, and the incident and scattering directions [11,12]. The continuous and discrete models can be

seen as related in the sense that the correlation functions can be derived for a given set of discrete scatterers with specified size and shape distributions [25] or can be obtained from digitized images of the discrete scatterers in the random medium [24,26]. Further approximations have been made in the derivations of effective permittivities or the mean field such as the low-frequency [11,12,17] or the Foldy approximation [11,12], respectively. The low-frequency approximation requires the size of the scatterers to be small compared to the wavelength and the Foldy approximation requires weak permittivity fluctuations. These approximations can be relaxed at the expense of mathematical complication.

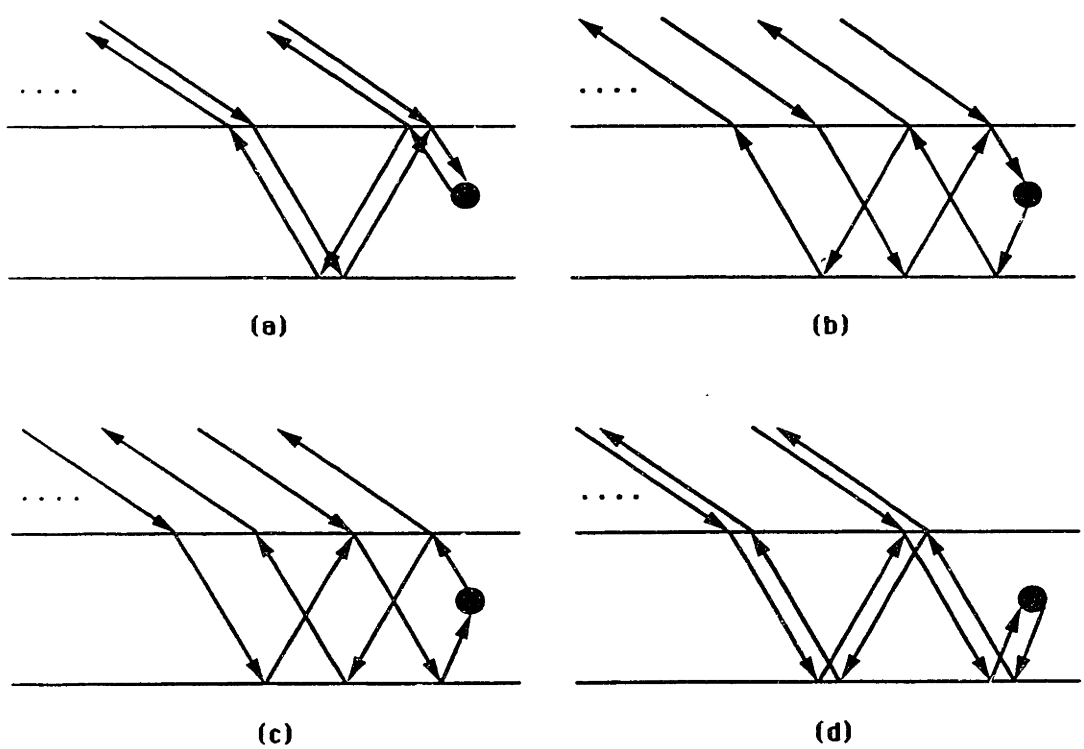

Figure 1.2.2 Interaction processes between boundaries and scatterer

An important advantage of the analytic wave theory is the preservation of phase information. Derived from wave equations of layered media with the use of dyadic Green's functions which are available in [3,27-29], WT solutions contain all

multiple interactions due to the boundaries at the layer interfaces; therefore, all coherent effects for wave propagation in different directions such as constructive and destructive interferences are included. The interactions due to the interface boundaries are illustrated in Figure 1.2.2 where the dots represent the continuing multiple reflection and transmission processes at the boundaries. As observed from the figure, the scattered field is composed of four interaction processes in the isotropic media; consequently, the first-order covariance of the scattered field has 16 terms. For an anisotropic medium, each of the waves either going up or down can be ordinary or extraordinary waves resulting in 16 terms for the fields and 256 terms in the first-order covariance [7]. For vegetation canopy such as rice field with an underlying water layer, the upper-boundary is negligible. Nevertheless, if the attenuation in the canopy is not too high, then the water-boundary effect due to the terms of the types (b-d) in Figure 1.2.2 are significant and the interference effects are important. For a dry-snow layer, the medium is not too lossy at microwave frequencies and the boundary effect are essential.

c. Modified Radiative Transfer Theory

In an effort to reformulate the phenomenological radiative transfer theory which is based on the energy transport equation [30-32], Maxwell's equations are used to derive the RT equation. From an examination of the relationship between the RT theory and Maxwell's equations in random media [33], it is found that the RT equation can be obtained from Maxwell's equations under certain conditions: the fields are either statistically quasi-homogeneous or highly directional as in a laser beam, the scattering effect is weak and the permittivity fluctuations are small and nearly statistically stationary. The weak fluctuation condition allows the ignorance of the fluctuation part of the Green's function in the covariance integral of scattered field; this approximation is equivalent to the ladder approximation for the Bethe-Salpeter equation [34].

When there exist interface boundaries, the mean field can propagate in different directions due to the transmission and reflection at the boundaries. Because of the treatment fundamentally with intensity in RT theory, the RT equation does not account for the coherent effect. In this case, the MRT theory is necessary to provide additional terms which accommodate the coherent effect due to wave propagation in different directions. In this theory, the scattered intensity are seen to be given rise to by both the mean intensity and the scattered intensity itself. Thus, the coherent and the multiple scattering effects are accounted for. In the two-layer case with a random medium having one-dimensional laminar structure [35] or a half-space random medium with three-dimensional correlation function [36], the MRT equations are derived with the Dyson equation for the mean fields and the Bethe-Salpeter equation for the scattered fields. The two-variable expansion technique is used to solve for the mean Green's function from the Dyson equation under the nonlinear approximation. The ladder approximation is then applied to the Bethe-Salpeter equation to obtained the MRT equations. The coherent effect is shown to be more significant for random medium with weaker fluctuation strength [35]. Thus, unless the layered medium is very highly scattering, the coherent effect is important since it comes from the mean field which is the zeroth-order solution.

In a two-layer isotropic case, the method used in [35,36] is applied to obtain the MRT equations [37]. The first-order MRT results for the copolarized backscattering coefficients σ_{hh} and σ_{vv} are compared to the results in WT with the first-order Born approximation. The comparison shows that the results from the two different methods have the same solution structure but the attenuation in the Born approximation accounts only for dissipation while the attenuation in the MRT method has an additional term due to the scattering loss [37]. Consequently, the Born results for the backscattering coefficients are higher than those of MRT. Physically, this is due to fact that the additional scattering loss has a shielding effect on the scatterer. In

the very low scattering limit, the Born and MRT approaches, however, give the same results. When the variance of the permittivity fluctuations is increased, the shielding effect due to scattering becomes more important and the two results deviate.

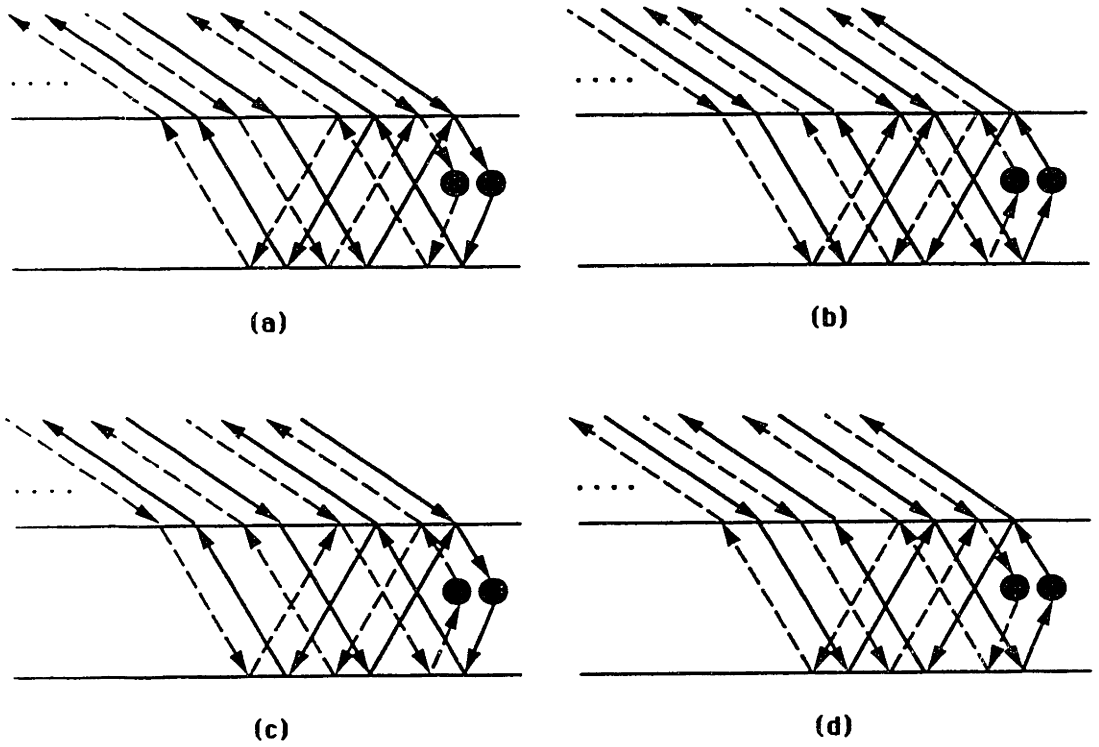

Figure 1.2.3 RT includes only (a) and (b) while MRT include all interactions

Recently, MRT equations are obtained for incoherent electromagnetic field intensities of ordinary and extraordinary waves in a two-layer anisotropic random medium [38]. The MRT results in [38] include the incoherent-field multiple scattering terms which are neglected in the first-order renormalization method. Similar to the WT, the MRT can account for the coherent effect. In the backscattering direction, the MRT equations include terms responsible for the phenomenon of backscattering enhancement which has been observed in laboratory controlled experiments [39]. Examples of these terms due to the coherent effect of constructive interferences are shown in Figure 1.2.3 [38] where the dashed arrows represent the complex conju-

gates of the continuous-arrow term. As reviewed in this section, the MRT equations obtained by using the Dyson equation under the nonlinear approximation and the Bethe-Salpeter equation under the ladder approximation can account for the multiple scattering and the coherent effect. In [33-37], correlation functions are used to characterize the random media and the models thus require the same physical input parameters as discussed in the last section. Further discussions on solution methods of the MRT equations are considered in the next section for RT equations since the two equation forms are similar.

d. Radiative Transfer Theory

The traditional radiative transfer theory is phenomenologically based on the energy transport equation [30-32]. In this theory, the propagation and scattering of the electromagnetic field intensity are described in terms of the Stokes vector governed by the energy transport equations. Constituents of the RT equations are an extinction matrix, a phase matrix, and an emission vector. The extinction matrix characterizes the attenuation due to both absorption and scattering losses. The phase matrix describes the coupling of electromagnetic intensities from other directions into the direction under consideration. The emission vector depicts the source due to thermal emission which can be neglected in the active remote sensing since the emission source is usually small compared to the radar transmitted and scattered signals. Furthermore, the inhomogeneity of temperature, scattering, or absorption profiles and the effects of rough interfaces can be included in the RT equations. Both the continuous and the discrete random medium concepts can be used in the derivations of the constituents in the RT equations [30-32,40].

The RT equations are integro-differential equations whose solutions can be obtained with different methods [30-32,40]. In the iterative method, the scattering is considered as a small perturbation. The solutions to the RT equations are then written as a perturbation series. Each order in the series can be calculated by iteration

of the previous order by using the scattering parameter as the iterative parameter; therefore, the iterative method is applicable only to random media with weak scattering effects. In the discrete ordinate-eigenanalysis method, the RT integro-differential equations are solved numerically by discretizing the propagation directions into a finite number of directions to transform the integro-differential equations into a system of ordinary differential equations with constant coefficients which can be solved by eigenanalysis; this method is applicable for media with homogeneous profiles. For random media with inhomogeneous profiles of temperature, scattering, or absorption, the method of invariant imbedding is used. In this method, the RT equations with the boundary values are converted into first-order ordinary differential equations with initial values. The initial value problem is started at zero slab thickness and then stepped forward in layer thickness. To incorporate the volume and rough surface scatterings in the RT theory [32,40-45], the rough interfaces are considered by modifying the boundary conditions of the RT equations and the matrix-doubling method has been developed to account for both scattering mechanisms.

Concerning only with the intensities of electromagnetic waves, the RT theory can phenomenologically account for more complexity in the random media. Random media with isotropic scatterers with specified particles size distributions have been treated with Mie scattering [46]. For nonuniform absorption, scattering, and temperature profiles, the method of invariant imbedding has been applied to media with laminar and three-dimensional random fluctuations [47]. The problem of multilayer media has also been considered for two-layer configuration with Mie [48] and Rayleigh [49] scattering and for three-layer configuration with continuous random medium [50]. For nonspherical scatterers, the T-matrix method is used to calculate the scattering function of each individual particle and a rotation matrix is used to relate the T-matrix to the principal frame for given probability density function of the Eulerian angles which describe the orientation of the particles [51]. RT theory has

been applied to cylindrical structure [52], vertically oriented spheroidal particles [53], randomly oriented circular discs [54], randomly positioned and oriented ellipsoids [55], and elliptic shape [56]. For dense and nontenuous media with small spherical particles, dense medium radiative wave equations are obtained from the Dyson equation under the quasicrystalline approximation with coherent potential and the Bethe-Salpeter equation under the ladder approximation of correlated scatterers [57]. With more complexity, the RT theory thus requires more input parameters such as the shape, size, and orientation of the scatterers together with their distributions and also the parameters for surface roughness.

In comparison to the RT theory, the MRT equations has the form of RT equations; thus, the RT solution methods such as the iterative and the eigenanalysis techniques are applicable to obtain MRT solutions. As discussed, the RT theory can account for more medium complexity, such as surface roughness, compared to the WT and MRT theories. For surface roughness, incoherent sum of the volume and surface scatterings are applied [3,5]. This incoherent sum does not accommodate the multiple-scattering interaction between the rough surface and the volume inhomogeneities as taken into account in the RT theory. However, the RT theory cannot account for the coherent effect as in the WT and MRT theories. This is due to intensity basis of the RT theory. Examples of terms that are included in the MRT but not in RT theory are shown on Figure 1.2.3. Thus, the RT theory is applicable in cases where the coherent effects are negligible; for instance, a layer of vegetation that is dense and lossy so that the effect of the lower boundary is not important.

e. Summary

Theoretical models have been reviewed in this section. The RT theory can account for more complicated properties of the media but ignores the phase information which is important to polarimetric remote sensing with monostatic radar. The MRT can account for both the phase and the multiple scattering but involves with more

mathematical complexity which limits the applicability to simple media. The WT can account for the coherent effect and all the multiple interaction between medium interface and scatterer, the multiple scattering to some extent, and rather complex medium characteristics. In this thesis, the WT is chosen to develop theoretical models for applications in polarimetric remote sensing of geophysical media whose polarimetric scattering properties can be described with many methods discussed in the next section.

1.3 Polarimetric Descriptions

To describe electromagnetic polarization properties, various methods have been devised. In 1852, Sir George Stokes [59] introduced four quantities, known as the Stokes parameters, to characterize a beam of partially polarized light. The Stokes parameters were later (1888) modified by Lord Rayleigh [60] in his treatment of "Interference of Polarized Light". As a geometrical representation, Poincaré [61] denoted polarization states with points on a sphere called the Poincaré sphere. In 1948, Mueller [62] considered the Stokes parameters as components of a vector which, due to "the effect of an optical instrument," could be transformed into another vector by a real 4×4 matrix. Expressed in two orthogonal polarimetric components, the incident and the scattered fields are related by the Jones matrix [63] or the complex scattering matrix [64,65]. To characterize the polarimetric scattering properties of random media, the covariance matrix is defined by the product of the polarimetric feature vector and its transposed complex conjugate [66]. Various forms of the Mueller matrix, or Stokes matrix, and other polarimetric descriptions [67-79] have been used. In the following subsections, the polarimetric descriptions used in this thesis are considered.

a. Scattering Matrix

Let an incident electric field $(\overline{E}_i)$ propagate in the direction of incident wave vector

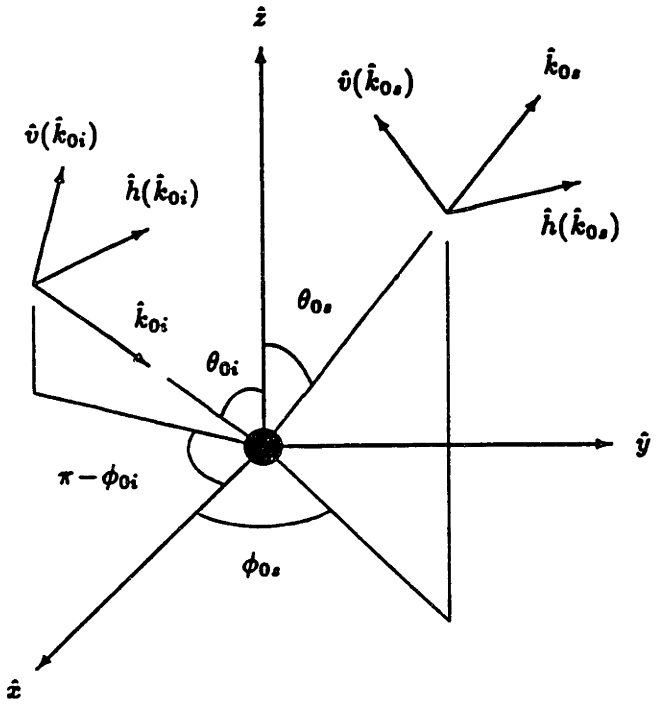

Figure 1.3.1 Coordinate systems

$\overline{k}_{0i}$ and illuminate the scatterer giving rise to the scattered field $(\overline{E}_s)$ propagating in the direction of scattered wave vector $\overline{k}_{0s}$ as shown in Figure 1.3.1. Associated with the incident field, Cartesian coordinate system $(\hat{h}(k_{0zi}), \hat{v}(k_{0zi}), \hat{k}_{0i})$, connoted as the incident basis, is defined with respect to vertical direction $\hat{z}$ of the global Cartesian coordinate system $(\hat{x}, \hat{y}, \hat{z})$ as follows

$$\hat{h}(k_{0zi}) = \frac{\hat{z} \times \overline{k}_{0i}}{\left|\hat{z} \times \overline{k}_{0i}\right|}, \quad \hat{v}(k_{0zi}) = \frac{\overline{k}_{0i} \times \hat{h}(k_{0zi})}{\left|\overline{k}_{0i} \times \hat{h}(k_{0zi})\right|} \tag{1a}$$

$$\hat{k}_{0i} = \overline{k}_{0i}/\left|\overline{k}_{0i}\right| \quad \text{with} \quad \overline{k}_{0i} = k_{xi}\hat{x} + k_{yi}\hat{y} + k_{0zi}\hat{z} \tag{1b}$$

Similarly, scattered basis $(\hat{h}(k_{0zs}), \hat{v}(k_{0zs}), \hat{k}_{0s})$ is determined by

$$\hat{h}(k_{0zs}) = \frac{\hat{z} \times \overline{k}_{0s}}{\left|\hat{z} \times \overline{k}_{0s}\right|}, \quad \hat{v}(k_{0zs}) = \frac{\overline{k}_{0s} \times \hat{h}(k_{0zs})}{\left|\overline{k}_{0s} \times \hat{h}(k_{0zs})\right|} \tag{1c}$$

$$\hat{k}_{0s} = \overline{k}_{0s}/\left|\overline{k}_{0s}\right| \quad \text{with} \quad \overline{k}_{0s} = k_{xs}\hat{x} + k_{ys}\hat{y} + k_{0zs}\hat{z} \tag{1d}$$

In (1), the incident and the scattered wave vectors can be expressed in terms of the angles in Figure 1.3.1 such that $\theta_{0s} = \theta_{0i}$ and $\phi_{0s} = \phi_{0i} + \pi$ in the backscattering direction.

Expressed in the incident basis, E_{hi} and E_{vi} are the components of $\overline{E}_i$ in directions $\hat{h}(k_{0zi})$ and $\hat{v}(k_{0zi})$, respectively. For scattered field $\overline{E}_s$, the components in the scattered basis are E_{hs} along $\hat{h}(k_{0zs})$ and E_{vs} along $\hat{v}(\hat{k}_{0zs})$. This coordinate connotation will be convenient for the subsequent derivation of the scattered field. The incident and scattered fields are then related by scattering matrix $\overline{\overline{F}}$ defined by

$$\begin{bmatrix} E_{hs} \\ E_{vs} \end{bmatrix} = \frac{e^{ikr}}{r} \overline{\overline{F}} \cdot \begin{bmatrix} E_{hi} \\ E_{vi} \end{bmatrix} = \frac{e^{ikr}}{r} \begin{bmatrix} f_{hh} & f_{hv} \\ f_{vh} & f_{vv} \end{bmatrix} \cdot \begin{bmatrix} E_{hi} \\ E_{vi} \end{bmatrix} \tag{2}$$

where factor e^{ikr}/r is the spherical wave transformation and scattering matrix element $f_{\mu\nu}$ is for scattered polarization μ and incident polarization ν with μ and ν being h or v.

In the backscattering direction, relation $f_{hv} = f_{vh}$ holds for reciprocal media when $\overline{E}_s$ is delineated in the incident basis. Note that the transformation of backscattered field $\overline{E}_s$ from the scattered basis to the incident basis results in the sign changes of f_{hh} and f_{hv}. Hereafter, only backscattering is considered.

b. Covariance Matrix

The polarimetric backscattering information pertaining to a remotely sensed geophysical terrain can be conveyed in form of polarimetric feature vector $\overline{X}$ defined with illuminated area A and the scattering matrix elements in the expression

$$\overline{X} = \lim_{\substack{r\to\infty \\ A\to\infty}} \sqrt{\frac{4\pi r^2}{A}} \frac{e^{ikr}}{r} \begin{bmatrix} f_{hh} \\ f_{hv} \\ f_{vv} \end{bmatrix} \tag{3}$$

As an ensemble average of the product between polarimetric feature vector $\overline{X}$ and its transposed complex conjugate $\overline{X}^{\dagger}$, covariance matrix $\overline{\overline{C}}$ characterizes the

fully polarimetric scattering properties of the geophysical media; explicitly,

$$\overline{\overline{C}} = \left\langle \overline{X} \cdot \overline{X}^{\dagger} \right\rangle = \lim_{A \to \infty} \frac{4\pi}{A} \left\langle \begin{bmatrix} f_{hh} f_{hh}^* & f_{hh} f_{hv}^* & f_{hh} f_{vv}^* \\ f_{hv} f_{hh}^* & f_{hv} f_{hv}^* & f_{hv} f_{vv}^* \\ f_{vv} f_{hh}^* & f_{vv} f_{hv}^* & f_{vv} f_{vv}^* \end{bmatrix} \right\rangle \tag{4}$$

where the asterisk denotes the complex conjugate and the angular brackets are for the ensemble average. It is obvious from (4) that the covariance matrix is hermitian.

In the above definitions of the polarimetric feature vector and the covariance matrix, reciprocity relation $f_{hv} = f_{vh}$ has been implied for the reciprocal media under consideration. Consequently, no loss of information results from dismissing f_{vh}. It should be noted that the reciprocity relation elicits the implementation of the scattered-to-incident basis transformation.

c. Mueller Matrix

The scattering effects of geophysical terrain can also be described by the Mueller matrix which relates the Stokes vectors of the incident and the scattered fields. For the incident field, the Stokes vector is

$$\overline{I}_i = \begin{bmatrix} I_i \\ Q_i \\ U_i \\ V_i \end{bmatrix} = \begin{bmatrix} I_{hi} + I_{vi} \\ I_{hi} - I_{vi} \\ U_i \\ V_i \end{bmatrix} \tag{5}$$

where the components of $\overline{I}_i$ are defined based on the linear polarimetric components of $\overline{E}_i$ and the free-space intrinsic impedance η in the following equations

$$I_{hi} = \frac{1}{\eta} E_{hi} E_{hi}^* , \qquad I_{vi} = \frac{1}{\eta} E_{vi} E_{vi}^* \tag{6a}$$

$$U_i = \frac{2}{\eta} \mathrm{Re}\left(E_{vi} E_{hi}^*\right) , \quad V_i = \frac{2}{\eta} \mathrm{Im}\left(E_{vi} E_{hi}^*\right) \tag{6b}$$

For the field backscattered from reciprocal media, the Stokes vector has the form

$$\bar{I}_s = \begin{bmatrix} I_s \\ Q_s \\ U_s \\ V_s \end{bmatrix} = \begin{bmatrix} I_{hs} + I_{vs} \\ I_{hs} - I_{vs} \\ U_s \\ V_s \end{bmatrix} \tag{7}$$

whose components are defined with the ensemble averages of the scattered field components as

$$I_{hs} = \frac{1}{\eta} \lim_{\substack{r\to\infty \\ A\to\infty}} \frac{4\pi r^2}{A} \left\langle E_{hs} E_{hs}^* \right\rangle \tag{8a}$$

$$I_{vs} = \frac{1}{\eta} \lim_{\substack{r\to\infty \\ A\to\infty}} \frac{4\pi r^2}{A} \left\langle E_{vs} E_{vs}^* \right\rangle \tag{8b}$$

$$U_s = \frac{2}{\eta} \lim_{\substack{r\to\infty \\ A\to\infty}} \frac{4\pi r^2}{A} \mathrm{Re} \left\langle E_{vs} E_{hs}^* \right\rangle \tag{8c}$$

$$V_s = \frac{2}{\eta} \lim_{\substack{r\to\infty \\ A\to\infty}} \frac{4\pi r^2}{A} \mathrm{Im} \left\langle E_{vs} E_{hs}^* \right\rangle \tag{8d}$$

Relating the incident to the scattered Stokes vectors, Mueller matrix $\overline{\overline{M}}$ depicts the backscattering effect by

$$\bar{I}_s = \overline{\overline{M}} \cdot \bar{I}_i = \begin{bmatrix} M_{11} & M_{12} & M_{13} & M_{14} \\ M_{21} & M_{22} & M_{23} & M_{24} \\ M_{31} & M_{32} & M_{33} & M_{34} \\ M_{41} & M_{42} & M_{43} & M_{44} \end{bmatrix} \cdot \begin{bmatrix} I_i \\ Q_i \\ U_i \\ V_i \end{bmatrix} \tag{9}$$

In the incident basis, the Mueller matrix is a 4×4 matrix composed of 16 elements which are derived from equations (2,5-9) and written in terms of the scattering matrix elements as

$$M_{11} = \lim_{A\to\infty} \frac{4\pi}{A} \frac{1}{2} \left\langle f_{hh} f_{hh}^* + 2 f_{hv} f_{hv}^* + f_{vv} f_{vv}^* \right\rangle \tag{10a}$$

$$M_{12} = \lim_{A\to\infty} \frac{4\pi}{A} \frac{1}{2} \left\langle f_{hh} f_{hh}^* - f_{vv} f_{vv}^* \right\rangle = M_{21} \tag{10b}$$

$$M_{13} = \lim_{A\to\infty} \frac{4\pi}{A} \mathrm{Re} \left\langle f_{hh} f_{hv}^* + f_{hv} f_{vv}^* \right\rangle = M_{31} \tag{10c}$$

$$M_{14} = \lim_{A\to\infty} \frac{4\pi}{A} \mathrm{Im} \left\langle f_{hh} f_{hv}^* + f_{hv} f_{vv}^* \right\rangle = -M_{41} \tag{10d}$$

$$M_{22} = \lim_{A\to\infty} \frac{4\pi}{A} \frac{1}{2} \left\langle f_{hh} f_{hh}^* - 2 f_{hv} f_{hv}^* + f_{vv} f_{vv}^* \right\rangle \tag{10e}$$

$$M_{23} = \lim_{A\to\infty} \frac{4\pi}{A}\mathrm{Re}\left\langle f_{hh} f_{hv}^* - f_{hv} f_{vv}^* \right\rangle = \quad M_{32} \tag{10f}$$

$$M_{24} = \lim_{A\to\infty} \frac{4\pi}{A}\mathrm{Im}\left\langle f_{hh} f_{hv}^* - f_{hv} f_{vv}^* \right\rangle = -M_{42} \tag{10g}$$

$$M_{33} = \lim_{A\to\infty} \frac{4\pi}{A}\mathrm{Re}\left\langle f_{hh} f_{vv}^* + f_{hv} f_{hv}^* \right\rangle \tag{10h}$$

$$M_{34} = \lim_{A\to\infty} \frac{4\pi}{A}\mathrm{Im}\left\langle f_{hh} f_{vv}^* \right\rangle = -M_{43} \tag{10i}$$

$$M_{44} = \lim_{A\to\infty} \frac{4\pi}{A}\mathrm{Re}\left\langle f_{hh} f_{vv}^* - f_{hv} f_{hv}^* \right\rangle \tag{10j}$$

For given transmit and receive antenna polarizations, the received power is proportional to a scattering coefficient defined in terms of the Mueller matrix as [70,77,80]

$$\sigma(\alpha_r, \beta_r; \alpha_i, \beta_i) = \frac{\bar{I}_r^{\mathrm{T}} \cdot \overline{\overline{T}} \cdot \overline{\overline{M}} \cdot \bar{I}_i}{2 I_r I_i} \tag{11}$$

where T denotes the transpose and Mueller matrix $\overline{\overline{M}}$ is symmetrized by diagonal matrix $\overline{\overline{T}}$ whose diagonal elements are $T_{11} = T_{22} = T_{33} = -T_{44} = 1$. Stokes vector $\bar{I}_m$ in (11) depends on orientation angle α_m and ellipticity angle β_m (Figure 1.3.2) as follows

$$\bar{I}_m = \begin{bmatrix} I_m \\ Q_m \\ U_m \\ V_m \end{bmatrix} = I_m \begin{bmatrix} 1 \\ \cos 2\alpha_m \cos 2\beta_m \\ \sin 2\alpha_m \cos 2\beta_m \\ \sin 2\beta_m \end{bmatrix} \tag{12}$$

with antenna operating mode $m = i$ for transmitting (incident) and $m = r$ for receiving. The orientation angles vary from 0° to 180° with 0° corresponding to $\hat{h}$ and 90° to $\hat{v}$ direction. The ellipticity angles range from −45° to 45° with 0° corresponding to linear, positive values to right-hand, and negative values to left-hand waves. The polarization states can be described geometrically by the Poincaré sphere with the upper hemisphere for right-hand polarizations and the lower for left-hand [81]. If the same antenna is used for both transmitting and receiving, the transmit and receive polarizations are identical and the corresponding scattering cross section is called the copolarized signature [80].

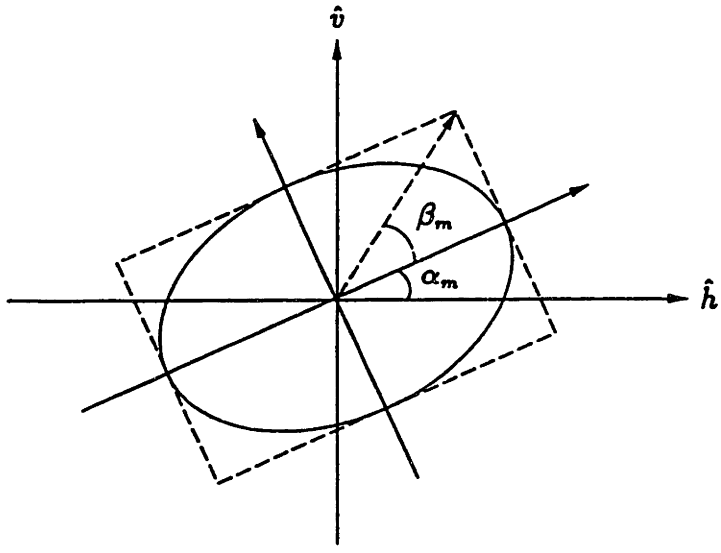

a Polarization ellipse

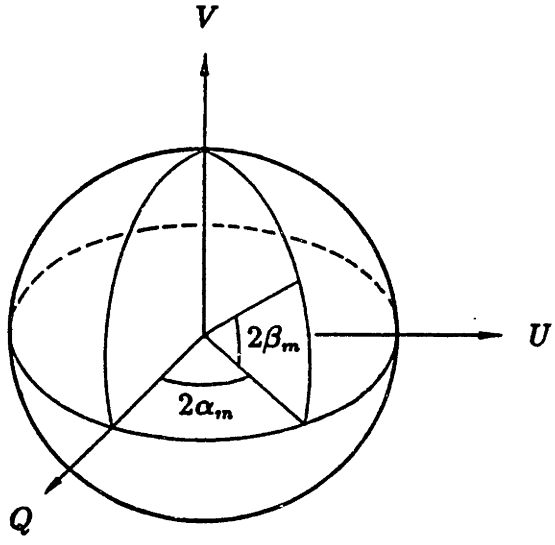

b Poincaré sphere

Figure 1.3.2 Geometrical representations of polarizations.

d. Scattering Coefficients

For polarimetric backscattering, the scattering coefficients are defined by [7]

$$\sigma_{\mu\tau\nu\kappa} = \lim_{\substack{r\to\infty \\ A\to\infty}} \frac{4\pi r^2}{A} \frac{\left\langle E_{\mu s}\, E^*_{\nu s} \right\rangle}{E_{\tau i}\, E^*_{\kappa i}} \tag{13}$$

where subscripts μ, ν, τ, and κ can be h or v. The components of the scattered field in (13) are obtained by measuring the h and the v returns while the incident field is transmitted exclusively with h or v polarization. From (2), this measurement procedure can be described mathematically by the following equations relating the scattered to the incident field components

$$E_{\mu s} = \frac{e^{ikr}}{r}\left(f_{\mu\tau}E_{\tau i} + f_{\mu\kappa}E_{\kappa i}\right)\Big|_{E_{\kappa i}=0} = \frac{e^{ikr}}{r} f_{\mu\tau}E_{\tau i} \tag{14a}$$

$$E_{\nu s} = \frac{e^{ikr}}{r}\left(f_{\nu\tau}E_{\tau i} + f_{\nu\kappa}E_{\kappa i}\right)\Big|_{E_{\tau i}=0} = \frac{e^{ikr}}{r} f_{\nu\kappa}E_{\kappa i} \tag{14b}$$

Substituting (14) in (13) renders polarimetric backscattering coefficient $\sigma_{\mu\nu\tau\kappa}$ in terms of scattering matrix components

$$\sigma_{\mu\tau\nu\kappa} = \lim_{A\to\infty} \frac{4\pi}{A}\left\langle f_{\mu\tau} f^*_{\nu\kappa}\right\rangle \tag{15}$$

By means of (15), the covariance matrix can be expressed with the backscattering coefficients as

$$\overline{\overline{C}} = \begin{bmatrix} \sigma_{hhhh} & \sigma_{hhhv} & \sigma_{hhvv} \\ \sigma^*_{hhhv} & \sigma_{hvhv} & \sigma_{hvvv} \\ \sigma^*_{hhvv} & \sigma^*_{hvvv} & \sigma_{vvvv} \end{bmatrix} \tag{16}$$

in which diagonal element σ_{hhhh}, σ_{hvhv}, and σ_{vvvv} are conventional backscattering coefficient σ_{hh}, σ_{hv}, and σ_{vv}, respectively. Normalized to $\sigma = \sigma_{hhhh}$, the covariance matrix can be formed as

$$\overline{\overline{C}} = \sigma \begin{bmatrix} 1 & \beta\sqrt{e} & \rho\sqrt{\gamma} \\ \beta^*\sqrt{e} & e & \xi\sqrt{\gamma e} \\ \rho^*\sqrt{\gamma} & \xi^*\sqrt{\gamma e} & \gamma \end{bmatrix} \tag{17}$$

where intensity ratio γ and e and correlation coefficient ρ, β, and ξ are

$$\gamma = \frac{\sigma_{vvvv}}{\sigma}, \quad e = \frac{\sigma_{hvhv}}{\sigma} \tag{18a}$$

$$\rho = \frac{\sigma_{hhvv}}{\sigma\sqrt{\gamma}}, \quad \beta = \frac{\sigma_{hhhv}}{\sigma\sqrt{e}}, \quad \xi = \frac{\sigma_{hvvv}}{\sigma\sqrt{\gamma e}} \tag{18b}$$

In terms of the polarimetric backscattering coefficients, the Mueller matrix elements can also be written as

$$M_{11} = \frac{1}{2}(\sigma_{hhhh} + 2\sigma_{hvhv} + \sigma_{vvvv}) \tag{19a}$$

$$M_{12} = \frac{1}{2}(\sigma_{hhhh} - \sigma_{vvvv}) = M_{21} \tag{19b}$$

$$M_{13} = \mathrm{Re}(\sigma_{hhhv} + \sigma_{hvvv}) = M_{31} \tag{19c}$$

$$M_{14} = \mathrm{Im}(\sigma_{hhhv} + \sigma_{hvvv}) = -M_{41} \tag{19d}$$

$$M_{22} = \frac{1}{2}(\sigma_{hhhh} - 2\sigma_{hvhv} + \sigma_{vvvv}) \tag{19e}$$

$$M_{23} = \mathrm{Re}(\sigma_{hhhv} - \sigma_{hvvv}) = M_{32} \tag{19f}$$

$$M_{24} = \mathrm{Im}(\sigma_{hhhv} - \sigma_{hvvv}) = -M_{42} \tag{19g}$$

$$M_{33} = \mathrm{Re}(\sigma_{hhvv}) + \sigma_{hvhv} \tag{19h}$$

$$M_{34} = \mathrm{Im}(\sigma_{hhvv}) = -M_{43} \tag{19i}$$

$$M_{44} = \mathrm{Re}(\sigma_{hhvv}) - \sigma_{hvhv} \tag{19j}$$

The use of the reciprocity relation for the media under consideration has been implied in the expressions for the covariance and the Mueller matrices. As seen from (16) and (19), both matrices are fully expressible with the complete set of polarimetric backscattering coefficients containing 9 independent parameters and therefore convey the same information regarding the terrain scattering properties. In the subsequent chapters, the polarimetric backscattering coefficients will be derived with the scattered field in the scattered basis for reciprocal geophysical media with a layer configuration. Then, the scattered-to-incident basis transformation is applied to calculate the covariance and the Mueller matrices.

Chapter 2
Layer Model with Spheroidal Scatterers

2.1 Introduction

Presented in this chapter is a three-layer isotropic-anisotropic random medium model which can account for fully polarimetric backscattering from geophysical media under the effects of precipitation such as sea ice under snow or vegetation under fog. The model configuration in Figure 2.2.1 has four different regions separated by three interfaces. The covering layer is modeled as an isotropic random medium. The middle layer is described as an anisotropic random medium due to the preferred alignment of nonspherical scatterers. The underlying layer is considered as a homogeneous half space. The scattering effects of the random media are characterized by three-dimensional correlation functions of spheroidal form with variances and correlation lengths corresponding to the fluctuation strengths and the physical geometries of the scatterers, respectively. The strong fluctuation theory is used to calculate the effective permittivities and the distorted Born approximation is then applied to obtain the complete set of polarimetric backscattering coefficients.

2.2 Configuration and Formulation

The scattering configuration is depicted in Figure 2.2.1. Region 0 is air with real permittivity ϵ_0. Region 1 is a scattering medium with isotropic scatterers randomly

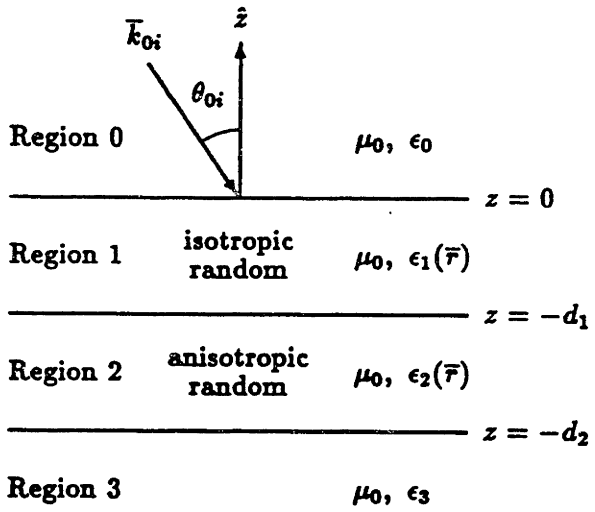

Figure 2.2.1 Scattering configuration

embedded such as snow or fog whose electrical property can be characterized by inhomogeneous permittivity $\epsilon_1(\overline{r})$. Region 2 contains nonspherical scatterers constituting an anisotropic random medium such as sea ice or vegetation which has spatially dependent permittivity $\epsilon_2(\overline{r})$. Region 3 is the underlying half space with homogeneous permittivity ϵ_3. The three regions are assumed to have identical permeability μ. The infinite planar interfaces at location $z = -d_1$ and $z = -d_2$ in Cartesian coordinate system $(\hat{x}, \hat{y}, \hat{z})$ are shown in Figure 2.2.1. Due to the preferred alignment of the nonspherical scatterers, the medium in region 2 is considered as effectively uniaxial with optic axis z' tilted off the z-axis by angle ψ in the yz-plane as illustrated in Figure 2.2.2.

In the phasor notation defined with $e^{-i\omega t}$ [81], time-harmonic total field $\overline{E}_0(\overline{r}), \overline{E}_1(\overline{r})$, and $\overline{E}_2(\overline{r})$, respectively in region 0, 1, and 2, satisfy the following wave equations

$$\nabla \times \nabla \times \overline{E}_0(\overline{r}) - k_0^2 \overline{E}_0(\overline{r}) = 0 \tag{1}$$

$$\nabla \times \nabla \times \overline{E}_1(\overline{r}) - k_0^2 \frac{\epsilon_1(\overline{r})}{\epsilon_0} \overline{E}_1(\overline{r}) = 0 \tag{2}$$

$$\nabla \times \nabla \times \overline{E}_2(\overline{r}) - k_0^2 \frac{\epsilon_2(\overline{r})}{\epsilon_0} \overline{E}_2(\overline{r}) = 0 \tag{3}$$

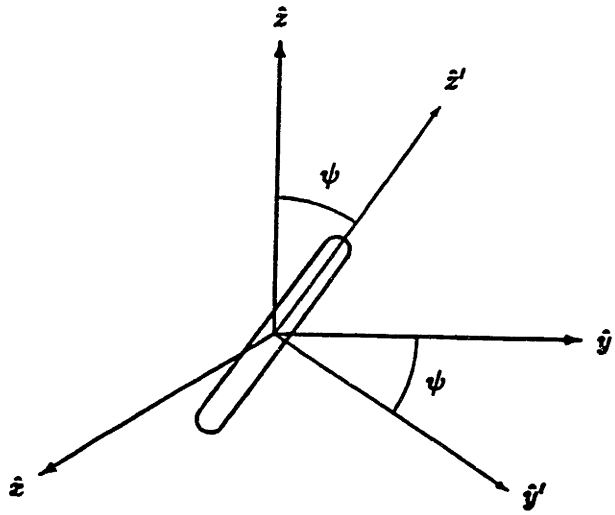

Figure 2.2.2 Geometry of scatterer in region 2

where the free-space wavenumber is $k_0 = \omega\sqrt{\mu\epsilon_0}$ and ω is the angular frequency. In the remote sensing of geophysical media, strong permittivity fluctuations are often encountered. The strong fluctuation theory [17] is therefore necessitated in the calculations of the random-medium effective permittivities. Deterministic permittivity $\overline{\overline{\epsilon}}_{g1} = \epsilon_{g1}\overline{\overline{I}}$, where $\overline{\overline{I}}$ is the unit dyadic, and $\overline{\overline{\epsilon}}_{g2}$ are introduced in both sides of (2) and (3), respectively, and the following vectors for $m = 1$ and $m = 2$

$$k_0^2\overline{\overline{Q}}_m(\overline{r}) \cdot \overline{E}_m(\overline{r}) = k_0^2\left[\frac{\epsilon_m(\overline{r})\overline{\overline{I}} - \overline{\overline{\epsilon}}_{gm}}{\epsilon_0}\right] \cdot \overline{E}_m(\overline{r}) \tag{4}$$

are treated as the effective sources so that wave equation (2) and (3) for the scattering random media become

$$\nabla \times \nabla \times \overline{E}_m(\overline{r}) - k_0^2\frac{\overline{\overline{\epsilon}}_{gm}}{\epsilon_0} \cdot \overline{E}_m(\overline{r}) = k_0^2\overline{\overline{Q}}_m(\overline{r}) \cdot \overline{E}_m(\overline{r}) \tag{5}$$

The permittivities in $\overline{\overline{\epsilon}}_{g1}$ and $\overline{\overline{\epsilon}}_{g2}$ are determined by the elimination of secular terms [17]. Physically, $\overline{\overline{\epsilon}}_{g1}$ and $\overline{\overline{\epsilon}}_{g2}$ are the effective permittivity tensors in the very low frequency limit where the scattering loss is negligible compared to the absorption loss [32].

In form of an integral equation, the total field in region $m = 0, 1, 2$ is the superposition of the mean field and the scattered field; explicitly,

$$\overline{E}_m(\overline{r}) = \overline{E}_m^{(0)}(\overline{r}) + k_0^2\sum_{n=1}^{2}\int_{V_n} d\overline{r}_n\, \overline{\overline{G}}_{mn}(\overline{r}, \overline{r}_n) \cdot \overline{\overline{Q}}_n(\overline{r}_n) \cdot \overline{E}_n(\overline{r}_n) \tag{6}$$

Mean field $\overline{E}_m^{(0)}(\overline{r})$ is the solution to the homogeneous wave equations where the effective sources vanish in the absence of the scatterers. As a particular solution to the inhomogeneous wave equations in the presence of the scatterers in region $n = 1,2$ occupying volume V_n, the scattered field in (6) is the integrals of the products between the effective source and dyadic Green's functions $\overline{\overline{G}}_{mn}(\overline{r},\overline{r}_n)$ defined by

$$\nabla \times \nabla \times \overline{\overline{G}}_{mn}(\overline{r},\overline{r}_n) - k_0^2 \frac{\overline{\overline{\epsilon}}_{gm}}{\epsilon_0} \cdot \overline{\overline{G}}_{mn}(\overline{r},\overline{r}_n) = \delta(\overline{r}-\overline{r}_n)\overline{\overline{I}} \tag{7}$$

where first subscript m in $\overline{\overline{G}}_{mn}(\overline{r},\overline{r}_n)$ denotes the observation region containing observation point $\overline{r}$, second subscript n stands for source region $n = 1,2$ containing source point $\overline{r}_n$, and $\delta(\overline{r}-\overline{r}_n)$ is the Dirac delta function. When $m \neq n$ signifying observation point $\overline{r}$ is outside source region n within which $\overline{r}_n$ is restricted, the Dirac delta function in the right-hand side of (7) vanishes. It is also obvious from (7) that an observation point in a scattering region can coincide with a source point in the same region $(m = n = 1,2)$ thus giving rise to the singularity of dyadic Green's function $\overline{\overline{G}}_{nn}(\overline{r},\overline{r}_n)$ which can be decomposed into a principal value part and a Dirac delta part

$$\overline{\overline{G}}_{nn}(\overline{r},\overline{r}_n) = PV\overline{\overline{G}}_{nn}(\overline{r},\overline{r}_n) - \delta(\overline{r}-\overline{r}_n)k_0^{-2}\overline{\overline{S}}_n\ , \quad n = 1,2 \tag{8}$$

Dyadic coefficient $\overline{\overline{S}}_n$ is conformed with the shape of the source exclusion volume and determined [illegible]ne condition of secular-term elimination [17]. With the decomposed Green's function of (8), the singular part in the integrand on the right-hand side of (6) for $m = n$ can be extracted and then combined with total field $\overline{E}_n(\overline{r})$ on the left-hand side to form external field $\overline{F}_n(\overline{r})$ in scattering region $n = 1,2$

$$\overline{F}_n(\overline{r}) = \left[\overline{\overline{I}} + \overline{\overline{S}}_n \cdot \overline{\overline{Q}}_n(\overline{r})\right] \cdot \overline{E}_n(\overline{r}) \tag{9}$$

In terms of external field $\overline{F}_n(\overline{r})$, the vector source of (4) can be redefined by introducing scatterer $\overline{\overline{\xi}}_n(\overline{r})$ such that

$$k_0^2\overline{\overline{\xi}}_n(\overline{r}) \cdot \overline{F}_n(\overline{r}) = k_0^2\overline{\overline{Q}}_n(\overline{r}) \cdot \overline{E}_n(\overline{r}) \tag{10}$$

It follows from (10) that scatterer $\overline{\overline{\xi}}_n(\overline{r})$ for the isotropic $(n = 1)$ and the anisotropic $(n = 2)$ random media are

$$\overline{\overline{\xi}}_n(\overline{r}) = \overline{\overline{Q}}_n(\overline{r}) \cdot \left[\overline{\overline{I}} + \overline{\overline{S}}_n \cdot \overline{\overline{Q}}_n(\overline{r})\right]^{-1} \tag{11}$$

By applying the distorted Born approximation [11,17,19,20] to (6) with the new definition of the sources in (30), the total field observed in region 0 is

$$\overline{E}_0(\overline{r}) = \overline{E}_0^{(0)}(\overline{r}) + k_0^2 \sum_{n=1}^{2} \int_{V_n} d\overline{r}_n \left\langle \overline{\overline{G}}_{0n}(\overline{r}, \overline{r}_n) \right\rangle \cdot \overline{\overline{\xi}}_n(\overline{r}_n) \cdot \left\langle \overline{F}_n(\overline{r}_n) \right\rangle \tag{12}$$

where isotropic effective permittivity $\overline{\overline{\epsilon}}_{eff1} = \epsilon_{eff1}\overline{\overline{I}}$ for region 1 and uniaxial permittivity $\overline{\overline{\epsilon}}_{eff2}$ for region 2 are used to calculate the mean dyadic Green's functions and the mean fields. The polarimetric scattering coefficients can then be obtained with the following correlation of the scattered field in (12)

$$\begin{aligned} \left\langle \overline{E}_{0s}(\overline{r}) \cdot \overline{E}_{0s}^*(\overline{r}) \right\rangle = \sum_{n=1}^{2} \sum_{i,j,k,l,m}^{x,y,z} k_0^4 \int_{V_n} d\overline{r}_n \int_{V_n} d\overline{r}_n^o \, C_{\xi njklm}(\overline{r}_n, \overline{r}_n^o) \\ \cdot \left[\left\langle G_{0nij}(\overline{r}, \overline{r}_n) \right\rangle \left\langle F_{nk}(\overline{r}_n) \right\rangle\right] \cdot \left[\left\langle G_{0nil}(\overline{r}, \overline{r}_n^o) \right\rangle \left\langle F_{nm}(\overline{r}_n^o) \right\rangle\right]^* \end{aligned} \tag{13}$$

For random media $n = 1$ and $n = 2$, $C_{\xi njklm}(\overline{r}_n, \overline{r}_n^o)$ in (13) is the $jklm$ element of fourth-rank correlation tensor $\overline{\overline{C}}_{\xi n}(\overline{r}_n, \overline{r}_n^o)$ defined as

$$C_{\xi njklm}(\overline{r}_n, \overline{r}_n^o) = \left\langle \xi_{njk}(\overline{r}_n) \xi_{nlm}^*(\overline{r}_n^o) \right\rangle \tag{14}$$

With specified correlation functions, the polarimetric scattering coefficients can thus be obtained after the effective permittivities of the random media are calculated as shown in the next section.

2.3 Effective Permittivities

The strong permittivity fluctuation theory [17] is used to derive the effective permittivities of the random media. The singularities of the dyadic Green's functions in the bilocal approximated Dyson's equations are accounted for and the low-frequency

approximation is applied to obtain the results for the isotropic and the anisotropic random media. The derivations are done in the frequency domain with the Fourier-transform method. The isotropic random medium is characterized with a correlation function of spherical form and the anisotropic random medium is described with a correlation function of spheroidal form. When the spheroidal form is reduced to spherical, the anisotropic result is confirmed with the isotropic case. Followed is the calculations of effective permittivities first for the isotropic and then for the anisotropic random media.

Consider an isotropic random medium composed of a host medium with permittivity ϵ_{b1} and randomly embedded scatterers with permittivity ϵ_{s1} and total fractional volume f_{s1} where subscript 1 is used for the isotropic random medium in accordance to the notation in Figure 2.2.1. By introducing auxiliary permittivity $\overline{\overline{\epsilon}}_{g1}$ into the wave equation as in (5), dyadic Green's function $\overline{\overline{G}}_{g1}(\bar{r},\bar{r}_1)$ satisfies the inhomogeneous differential equation of the form (7). Subscripts $g1$ is used here to indicate that $\overline{\overline{G}}_{g1}(\bar{r},\bar{r}_1)$ corresponds to a medium with permittivity ϵ_{g1}. To account for the singularity, $\overline{\overline{G}}_{g1}(\bar{r},\bar{r}_1) = \overline{\overline{G}}_{g1}(\bar{r}-\bar{r}_1)$ is decomposed as in (8) with $\overline{\overline{S}}_1 = S_1\overline{\overline{I}}$ for the Dirac delta part. By using the following definition for the Fourier transform

$$\overline{\overline{G}}_{g1}(\bar{r}) \equiv \frac{1}{8\pi^3}\int_{-\infty}^{\infty} d\bar{k}\, \overline{\overline{G}}_{g1}(\bar{k})\, e^{i\bar{k}\cdot\bar{r}} \tag{15}$$

the dyadic Green's function in the frequency domain is found to be

$$\overline{\overline{G}}_{g1}(\bar{k}) = \frac{\overline{\overline{I}}}{D(k)} - \frac{\bar{k}\,\bar{k}}{k_{g1}^2 D(k)} \quad \text{with} \quad \begin{cases} D(k) = k^2 - k_{g1}^2 \\ k_{g1}^2 = \omega^2\mu\epsilon_{g1} \end{cases} \tag{16}$$

Under the bilocal and the low-frequency approximations [17], the effective permittivity of the isotropic random medium is composed of a quasi-static part (ϵ_{g1}) and a correction part

$$\overline{\overline{\epsilon}}_{eff1} = \epsilon_{g1}\overline{\overline{I}} + \epsilon_0\left[\overline{\overline{I}} - \overline{\overline{\xi}}^{(0)}_{eff1}\cdot\overline{\overline{S}}_1\right]^{-1}\cdot\overline{\overline{\xi}}^{(0)}_{eff1} \tag{17}$$

The correction part in (17) physically accounts for the modification in the wave speed and attenuation due to the scattering effect of the scatterers. For $j,m = x,y,z$, the

jm element of $\overline{\overline{\xi}}^{(0)}_{eff1}$ is related to the Green's function (16) in the following manner

$$\left[\overline{\overline{\xi}}^{(0)}_{eff1}\right]_{jm} = \sum_{k,l}^{x,y,z} \Gamma^{(0)}_{\xi 1jklm} \left\{ k_0^2 \int_{-\infty}^{\infty} d\bar{k} \left[\overline{\overline{G}}_{g1}(\bar{k})\right]_{kl} \Phi_{\xi 1}(\bar{k}) + \left[\overline{\overline{S}}_1\right]_{kl} \right\} \tag{18}$$

To arrive at (18), the correlation function has been defined as

$$\Gamma_{\xi 1jklm}(\bar{r}_1, \bar{r}_1^{\circ}) = \langle \xi_{1jk}(\bar{r}_1) \xi_{1lm}(\bar{r}_1^{\circ}) \rangle \tag{19a}$$

and the random medium has been assumed to be statistically homogeneous so that (19a) can be written as

$$\Gamma_{\xi 1jklm}(\bar{r}_1, \bar{r}_1^{\circ}) = \Gamma_{\xi 1jklm}(\bar{r}_1 - \bar{r}_1^{\circ}) \equiv \Gamma^{(0)}_{\xi 1jklm} R_{\xi 1}(\bar{r}_1 - \bar{r}_1^{\circ}) \tag{19b}$$

where $R_{\xi 1}(\bar{r} = \bar{r}_1 - \bar{r}_1^{\circ})$ is the normalized correlation function such that $R_{\xi 1}(0)$ is equal to 1. In (18), $\Phi_{\xi 1}(\bar{k})$ is the Fourier transform of the normalized correlation function $R_{\xi 1}(\bar{r})$ defined as

$$\Phi_{\xi 1}(\bar{k}) \equiv \frac{1}{8\pi^3} \int_{-\infty}^{\infty} d\bar{r}\ R_{\xi 1}(\bar{r})\ e^{i\bar{k}\cdot\bar{r}} \tag{20}$$

In the isotropic random medium, $\overline{\overline{\xi}}_1(\bar{r}_1)$ is a scalar multiple of the unit dyadic $\overline{\overline{I}}$ and non-zero coefficient $\Gamma^{(0)}_{\xi 1jklm}$ are

$$\Gamma^{(0)}_{\xi 1jklm} = \langle \xi_{1jk}(\bar{r}_1) \xi_{1lm}(\bar{r}_1) \rangle \equiv \delta_{\xi 1}\ , \quad \begin{cases} k=j,\ l=m \\ j,m=x,y,z \end{cases} \tag{21}$$

For a spherically symmetric correlation function, it is seen from (17-21) that the effective permittivity of the isotropic random medium is independent of direction and expressed as a scalar multiple of $\overline{\overline{I}}$

$$\overline{\overline{\epsilon}}_{eff1} = \epsilon_{eff1} \overline{\overline{I}} = \left[\epsilon_{g1} + \frac{\epsilon_0 \delta_{\xi 1} (I_0 + S_1)}{1 - \delta_{\xi 1} (I_0 + S_1) S_1} \right] \overline{\overline{I}} \tag{22}$$

where I_0 is the integral of the product between a diagonal element of the dyadic Green's function and the correlation function in the frequency domain

$$I_0 = k_0^2 \int_0^{\infty} d\bar{k} \left[\overline{\overline{G}}_{g1}(\bar{k})\right]_{jj} \Phi_{\xi 1}(\bar{k}) \tag{23}$$

Due to the isotropy of the medium, any diagonal element ($jj = xx$, yy, or zz) of the dyadic Green's function (16) can be used in (23) to yield an identical result for I_0. For an isotropic random medium characterized by an exponential correlation function of spherical form with correlation length ℓ_1, $R_{\xi 1}(\overline{r})$ is expressed as

$$R_{\xi 1}(\overline{r}) = \exp\left(-\frac{r}{\ell_1}\right) \tag{24a}$$

whose Fourier transform is obtained by carrying out the integration (20) in the spherical coordinates to yield

$$\Phi_{\xi 1}(\overline{k}) = \frac{\ell_1^3}{\pi^2(1+k^2\ell_1^2)^2} \tag{24b}$$

With the use of (24b), the integration (23) is then carried out analytically by a change of variables into the spherical coordinates. The result for I_0 is

$$I_0 = \frac{\epsilon_0}{3\epsilon_{g1}}\left[-\frac{3\vartheta^2+1}{(\vartheta+1)^2} + i\frac{4\vartheta\sqrt{\vartheta}}{(\vartheta+1)^2}\right]_{\vartheta = k_{g1}^2\ell_1^2} \tag{25}$$

Coefficient S_1, which conforms with the shape of the source exclusion volume, can be determined by requiring the cancelation of the frequency dependent terms in (18) so that the secular term is eliminated. For the isotropic case, S_1 is thereby obtained

$$S_1 = -\lim_{\omega\to 0} I_0 = \frac{\epsilon_0}{3\epsilon_{g1}} \tag{26}$$

The elimination of the secular term also imposes the condition of zero-mean on the scatterer tensor

$$\left\langle \overline{\overline{\xi}}_1(\overline{r}) \right\rangle = 0 \tag{27}$$

Condition (27) and (26) together with definition (11) and (4) for $n = 1$ determine auxiliary permittivity $\overline{\overline{\epsilon}}_{g1}$ with the relation

$$\left(\frac{\epsilon_{b1}-\epsilon_{g1}}{\epsilon_{b1}+2\epsilon_{g1}}\right)(1-f_{s1}) + \left(\frac{\epsilon_{s1}-\epsilon_{g1}}{\epsilon_{s1}+2\epsilon_{g1}}\right) f_{s1} = 0 \tag{28}$$

When the value of ϵ_{g1} is obtained, variance $\delta_{\xi 1}$ is found from (21)

$$\delta_{\xi 1} = 9\frac{\epsilon_{g1}^2}{\epsilon_0^2}\left[\left(\frac{\epsilon_{b1}-\epsilon_{g1}}{\epsilon_{b1}+2\epsilon_{g1}}\right)^2(1-f_{s1}) + \left(\frac{\epsilon_{s1}-\epsilon_{g1}}{\epsilon_{s1}+2\epsilon_{g1}}\right)^2 f_{s1}\right] \tag{29}$$

In summary of the isotropic case, the isotropic effective permittivity is calculated with (22) where ϵ_{g1}, $\delta_{\xi 1}$, I_0, and S_1 are given by (28), (29), (23), and (26), respectively.

Consider now an anisotropic random medium composed of a host medium with permittivity ϵ_{b2} and embedded nonspherical scatterers with permittivity ϵ_{s2} and total fractional volume f_{s2}. The scatterers with a preferred alignment direction and an azimuthal symmetry effectively give rise to the uniaxial anisotropy of the random medium whose optic axis is the z' axis in Cartesian coordinate system $(\hat{x}', \hat{y}', \hat{z}')$ illustrated in Figure 2.2.2. The principle for deriving the anisotropic effective permittivity is the same as in the previous paragraph; however, the anisotropy of the medium needs be accounted for. In this case, an appropriate form of auxiliary permittivity $\overline{\overline{\epsilon}}_{g2}$ is

$$\overline{\overline{\epsilon}}_{g2} = \begin{bmatrix} \epsilon_{g2\rho'} & 0 & 0 \\ 0 & \epsilon_{g2\rho'} & 0 \\ 0 & 0 & \epsilon_{g2z'} \end{bmatrix} \tag{30}$$

Equation (30) is expressed in the primed coordinate system shown in Figure 2.2.2. This coordinate system is used to calculate the effective permittivity of the anisotropic random medium and a rotation transformation with tilt angle ψ is then applied to transform the result into unprimed Cartesian coordinate system $(\hat{x}, \hat{y}, \hat{z})$. Corresponding dyadic Green's function $\overline{\overline{G}}_{g2}(\overline{r}')$ is decomposed as in (8) with the Dirac delta part having uniaxial dyadic coefficient

$$\overline{\overline{S}}_2 = \begin{bmatrix} S_{2\rho'} & 0 & 0 \\ 0 & S_{2\rho'} & 0 \\ 0 & 0 & S_{2z'} \end{bmatrix} \tag{31}$$

According to the Fourier transform definition (15) where the subscript 1 is replaced by 2 and $\overline{r}$ and $\overline{k}$ are respectively changed to $\overline{r}'$ and $\overline{k}'$, dyadic Green's function

$\overline{\overline{G}}_{g2}(\overline{r}')$ has frequency-domain version $\overline{\overline{G}}_{g2}(\overline{k}')$ written as

$$\overline{\overline{G}}_{g2}(\overline{k}') = \frac{1}{(k_x'^2+k_y'^2)D_o(\overline{k}')}\begin{bmatrix} k_y'^2 & -k_x'k_y' & 0 \\ -k_x'k_y' & k_x'^2 & 0 \\ 0 & 0 & 0 \end{bmatrix} + \frac{1}{(k_x'^2+k_y'^2)D_e(\overline{k}')}\begin{bmatrix} k_x'^2 & k_x'k_y' & 0 \\ k_x'k_y' & k_y'^2 & 0 \\ 0 & 0 & \frac{k_{g2\rho'}^2}{k_{g2z'}^2}(k_x'^2+k_y'^2) \end{bmatrix} - \frac{\overline{k}'\overline{k}'}{k_{g2z'}^2 D_e(\overline{k}')} \tag{32}$$

where $D_o(\overline{k}')$, $D_e(\overline{k}')$, $k_{g2\rho'}^2$, and $k_{g2z'}^2$ are defined as follows

$$D_o(\overline{k}') = k_x'^2 + k_y'^2 + k_z'^2 - k_{g2\rho'}^2 \tag{33a}$$

$$D_e(\overline{k}') = k_z'^2 + \frac{k_{g2\rho'}^2}{k_{g2z'}^2}(k_x'^2 + k_y'^2 - k_{g2z'}^2) \tag{33b}$$

$$k_{g2\rho'}^2 = \omega^2\mu_0\epsilon_{g2\rho'}, \quad k_{g2z'}^2 = \omega^2\mu_0\epsilon_{g2z'} \tag{33c}$$

Similar to (17), the effective permittivity of the anisotropic random medium is composed of a quasi-static part and a scattering-effect part

$$\overline{\overline{\epsilon}}_{eff2}(\hat{r}') = \overline{\overline{\epsilon}}_{g2} + \epsilon_0\left[\overline{\overline{I}} - \overline{\overline{\xi}}_{eff2}^{(0)} \cdot \overline{\overline{S}}_2\right]^{-1} \cdot \overline{\overline{\xi}}_{eff2}^{(0)} \tag{34}$$

where $\hat{r}'$ indicates the primed coordinate system and the jm element of effective scatterer $\overline{\overline{\xi}}_{eff2}^{(0)}$ under the low-frequency approximation is of the form (37) with subscript 1 changed to 2 and $j,m = x',y',z'$

$$\left[\overline{\overline{\xi}}_{eff2}^{(0)}\right]_{jm} = \sum_{k,l}^{x',y',z'} \Gamma_{\xi 2jklm}^{(0)}\left\{k_0^2\int_{-\infty}^{\infty} d\overline{k}' \left[\overline{\overline{G}}_{g2}(\overline{k}')\right]_{kl}\Phi_{\xi 2}(\overline{k}') + \left[\overline{\overline{S}}_2\right]_{kl}\right\} \tag{35}$$

The statistically homogeneous anisotropic random medium is described with fourth-rank correlation tensor $\overline{\overline{\Gamma}}_{\xi 2}(\overline{r}_2', \overline{r}_2^{o\prime}) = \left\langle \overline{\overline{\xi}}_2(\overline{r}_2')\overline{\overline{\xi}}_2(\overline{r}_2^{o\prime})\right\rangle$ where $\overline{\overline{\xi}}_2(\overline{r}_2')$ is a diagonal tensor in the primed coordinates; thus, the non-zero elements of $\overline{\overline{\Gamma}}_{\xi 2}(\overline{r}_2', \overline{r}_2^{o\prime}) = \overline{\overline{\Gamma}}_{\xi 2}(\overline{r}_2' - \overline{r}_2^{o\prime})$ are

$$\Gamma_{\xi 2jklm}(\overline{r}') = \delta_{\xi 2\rho'} R_{\xi 2}(\overline{r}'), \quad jklm = \begin{cases} x'x'x'x', & x'x'y'y' \\ y'y'x'x', & y'y'y'y' \end{cases} \tag{36a}$$

$$\Gamma_{\xi 2jklm}(\overline{r}') = \delta_{\xi 2z'} R_{\xi 2}(\overline{r}'), \quad jklm = z'z'z'z' \tag{36b}$$

$$\Gamma_{\xi 2jklm}(\overline{r}') = \delta_{\xi 2c'} R_{\xi 2}(\overline{r}'), \quad jklm = \begin{cases} x'x'z'z', & y'y'z'z' \\ z'z'x'x', & z'z'y'y' \end{cases} \tag{36c}$$

where $\overline{r}' = \overline{r}_2' - \overline{r}_2^{o\prime}$ and element $\Gamma_{\xi 2jklm}(\overline{r}')$ is defined with a normalizing variance $\Gamma_{\xi 2jklm}(\overline{r}'=0) = \langle \xi_{2jk}(\overline{r}_2')\xi_{1lm}(\overline{r}_2')\rangle \equiv \Gamma^{(0)}_{\xi 2jklm}$ which can takes on the value of $\delta_{\xi 2\rho'}$, $\delta_{\xi 2z'}$, or $\delta_{\xi 2c'}$ such that $R_{\xi 2}(0) = 1$. For an azimuthally symmetric correlation function, it is observed from (30-36) that $\overline{\overline{\epsilon}}_{eff2}(\hat{r}')$ is uniaxial and expressed with the permittivity tensor

$$\overline{\overline{\epsilon}}_{eff2}(\hat{r}') = \begin{bmatrix} \epsilon_{eff2\rho'} & 0 & 0 \\ 0 & \epsilon_{eff2\rho'} & 0 \\ 0 & 0 & \epsilon_{eff2z'} \end{bmatrix} \tag{37a}$$

$$\begin{aligned} \epsilon_{eff2\rho'} &= \epsilon_{g2\rho'} + \frac{\epsilon_0 \delta_{\xi 2\rho'}(I_{\rho'} + S_{2\rho'})}{1 - \delta_{\xi 2\rho'}(I_{\rho'} + S_{2\rho'})S_{2\rho'}} \\ \epsilon_{eff2z'} &= \epsilon_{g2z'} + \frac{\epsilon_0 \delta_{\xi 2z'}(I_{z'} + S_{2z'})}{1 - \delta_{\xi 2z'}(I_{z'} + S_{2z'})S_{2z'}} \end{aligned} \tag{37b}$$

where $I_{z'}$ and $I_{\rho'}$ are the integrals in the frequency domain of the products between the corresponding diagonal element of the dyadic Green's function and normalized correlation function $\Phi_{\xi 2}(\overline{k}')$ defined as in (20) with the subscript 1 changed to 2 and $\overline{k}$ and $\overline{r}$ to $\overline{k}'$ and $\overline{r}'$. In the cylindrical coordinates, integral $I_{z'}$ and $I_{\rho'}$ are

$$\begin{aligned} I_{z'} = k_0^2 \int_0^{2\pi} d\phi' \int_0^{\infty} dk_\rho' k_\rho' \int_{-\infty}^{\infty} dk_z' (-k_{g2z'}^{-2}) \\ \cdot \left[\frac{k_z'^2 - k_{g2\rho'}^2}{k_z'^2 + k_\rho'^2(\epsilon_{g2\rho'}/\epsilon_{g2z'}) - k_{g2\rho'}^2} \right] \Phi_{\xi 2}(\overline{k}') \end{aligned} \tag{38a}$$

$$\begin{aligned} I_{\rho'} = k_0^2 \int_0^{2\pi} d\phi' \int_0^{\infty} dk_\rho' k_\rho' \int_{-\infty}^{\infty} dk_z' \\ \cdot \left[\frac{\sin^2\phi'}{k_z'^2 + k_\rho'^2 - k_{g2\rho'}^2} + \frac{(k_\rho'^{-2} - k_z'^{-2}) k_\rho'^2 \cos^2\phi'}{k_z'^2 + k_\rho'^2(\epsilon_{g2\rho'}/\epsilon_{g2z'}) - k_{g2\rho'}^2} \right] \Phi_{\xi 2}(\overline{k}') \end{aligned} \tag{38b}$$

For an anisotropic random medium characterized by an exponential correlation function of spheroidal form with correlation length $\ell_{2\rho'}$ and $\ell_{2z'}$, $R_{\xi 2}(\overline{r}')$ is expressed as

$$R_{\xi 2}(\overline{r}') = \exp\left(-\sqrt{\frac{x'^2 + y'^2}{\ell_{2\rho'}^2} + \frac{z'^2}{\ell_{2z'}^2}} \right) \tag{39a}$$

whose Fourier transform is obtained by carrying out the Fourier integration in the cylindrical coordinates or by applying the scaling theorem on (24b) to yield

$$\Phi_{\xi 2}(\overline{k}') = \frac{\ell_{2\rho'}^2 \ell_{2z'}}{\pi^2 (1 + k_\rho'^2 \ell_{2\rho'}^2 + k_z'^2 \ell_{2z'}^2)^2} \tag{39b}$$

With the use of (39b), the integrations in (38) can then be carried out analytically by effectuating the integrations over ϕ', using contour integration technique for the integrations over k_z', and then performing the integrations over k_ρ'. The result for $I_{z'}$ is determined as follows

$$I_{z'} = -\frac{2\epsilon_0}{\epsilon_{g2z'}}(\mathcal{I}_s + \mathcal{I}_d) \tag{40a}$$

$$\mathcal{I}_s = -\frac{\alpha\gamma_\ell^2\sqrt{\alpha\gamma_\ell^2}}{2a^2}\left[\frac{\sqrt{-\zeta}}{\vartheta_e} + \frac{\vartheta_e+\zeta}{\vartheta_e\sqrt{\vartheta_e}}\left(\frac{\pi}{2} - \tan^{-1}\frac{\sqrt{-\zeta}}{\sqrt{\vartheta_e}}\right)\right] \tag{40b}$$

$$\mathcal{I}_d = \frac{\alpha\gamma_\ell^2}{2a^2}\left[\frac{1+a\nu_{gz'}^2}{\vartheta_o} + \frac{\vartheta_o(a+2)-(b+a\nu_{gz'}^2)}{\vartheta_o\sqrt{\vartheta_o}}\left(\frac{\pi}{2} - \tan^{-1}\frac{1}{\sqrt{\vartheta_o}}\right)\right] \tag{40c}$$

$$a = \alpha\gamma_\ell^2 - 1\,, \quad \alpha = \frac{\epsilon_{g2z'}}{\epsilon_{g2\rho'}}\,, \quad \gamma_\ell = \frac{\ell_{2\rho'}}{\ell_{2z'}}\,, \quad \nu_{gz'}^2 = k_{g2\rho'}^2\ell_{2z'}^2 \tag{40d}$$

$$\zeta = \alpha\gamma_\ell^2\nu_{gz'}^2\,, \quad b = \frac{\alpha\gamma_\ell^2+\zeta}{a}\,, \quad \vartheta_o = b-1\,, \quad \vartheta_e = b+\zeta \tag{40e}$$

Integral $I_{\rho'}$ involves additional terms in the dyadic Green's function and the result is found to be

$$I_{\rho'} = \nu_{0\rho'}^2(\mathcal{I}_1^o - \mathcal{I}_2^o - \mathcal{I}_3^o) + \alpha\nu_{0\rho'}^2\left[(\mathcal{I}_1^e - \mathcal{I}_2^e - \mathcal{I}_3^e) + \frac{1}{\zeta}(\mathcal{I}_s + \mathcal{I}_d - \frac{1}{2})\right] \tag{41a}$$

$$\mathcal{I}_1^e = \frac{\alpha\gamma_\ell^2\sqrt{\alpha\gamma_\ell^2}}{2a^2\vartheta_e}\left[-\frac{\sqrt{-\zeta}}{b} + \frac{1}{\sqrt{\vartheta_e}}\left(\frac{\pi}{2} - \tan^{-1}\frac{\sqrt{-\zeta}}{\sqrt{\vartheta_e}}\right)\right] \tag{41b}$$

$$\mathcal{I}_2^e = \frac{1}{2a\vartheta_o}\left[1 - \frac{1}{\sqrt{\vartheta_o}}\left(\frac{\pi}{2} - \tan^{-1}\frac{1}{\sqrt{\vartheta_o}}\right)\right] \tag{41c}$$

$$\mathcal{I}_3^e = \frac{\alpha\gamma_\ell^2}{2a^2\vartheta_o}\left[-\frac{1}{b} + \frac{1}{\sqrt{\vartheta_o}}\left(\frac{\pi}{2} - \tan^{-1}\frac{1}{\sqrt{\vartheta_o}}\right)\right] \tag{41d}$$

$$\mathcal{I}_{1,2,3}^o = \mathcal{I}_{1,2,3}^e(\alpha = 1)\,, \quad \nu_{0\rho'} = k_0\ell_{2\rho'} \tag{41e}$$

Diagonal element $S_{g2\rho'}$ and $S_{g2z'}$ of dyadic coefficient $\overline{\overline{S}}_2$ in the singular part of the Green's function for the anisotropic medium are obtained by requiring the cancelation of the frequency dependent terms in (35) to eliminate the secular terms. Derived from

(35), (40), and (41), coefficient $S_{g2\rho'}$ and $S_{g2z'}$ are

$$S_{2\rho'} = -\lim_{\omega\to 0} I_{\rho'} = \frac{\epsilon_0}{2\epsilon_{g2\rho'} a\sqrt{a}}\left[(1+a)\tan^{-1}\sqrt{a} - \sqrt{a}\right] \tag{42a}$$

$$S_{2z'} = -\lim_{\omega\to 0} I_{z'} = \frac{\epsilon_0(1+a)}{\epsilon_{g2z'} a\sqrt{a}}\left[\sqrt{a} - \tan^{-1}\sqrt{a}\right] \tag{42b}$$

Similar to (27), the zero-mean condition is imposed on scatterer $\bar{\bar{\xi}}_2(\bar{r})$ for the elimination of the secular terms. This condition together with (42) and definition (11) and (4) for $n = 2$ in the primed coordinate system determine auxiliary permittivity $\bar{\bar{\epsilon}}_{g2}$ in the following manner

$$\frac{(\epsilon_{b2} - \epsilon_{g2\rho'})(1-f_{s2})}{\epsilon_0 + S_{2\rho'}(\epsilon_{b2} - \epsilon_{g2\rho'})} + \frac{(\epsilon_{s2} - \epsilon_{g2\rho'})f_{s2}}{\epsilon_0 + S_{2\rho'}(\epsilon_{s2} - \epsilon_{g2\rho'})} = 0 \tag{43a}$$

$$\frac{(\epsilon_{b2} - \epsilon_{g2z'})(1-f_{s2})}{\epsilon_0 + S_{2z'}(\epsilon_{b2} - \epsilon_{g2z'})} + \frac{(\epsilon_{s2} - \epsilon_{g2z'})f_{s2}}{\epsilon_0 + S_{2z'}(\epsilon_{s2} - \epsilon_{g2z'})} = 0 \tag{43b}$$

Numerical values of $\epsilon_{g2\rho'}$, $\epsilon_{g2z'}$, $S_{2\rho'}$, and $S_{2z'}$ are obtained by solving (42) and (43) iteratively. A suggested scheme for the iteration is to initially assign $\epsilon_{g2\rho'} = \epsilon_{g2z'} = \epsilon_{b2}$ then use (42) to find $S_{2\rho'}$ and $S_{2z'}$ which are subsequently employed to recalculate $\epsilon_{g2\rho'}$ and $\epsilon_{g2z'}$ with (62) rearranged as

$$\epsilon_{g2\rho'} = \epsilon_{b2} + \frac{f_{s2}(\epsilon_{s2} - \epsilon_{g2\rho'})}{(1-f_{s2})} \frac{\epsilon_0 + S_{2\rho'}(\epsilon_{b2} - \epsilon_{g2\rho'})}{\epsilon_0 + S_{2\rho'}(\epsilon_{s2} - \epsilon_{g2\rho'})} \tag{44a}$$

$$\epsilon_{g2z'} = \epsilon_{b2} + \frac{f_{s2}(\epsilon_{s2} - \epsilon_{g2z'})}{(1-f_{s2})} \frac{\epsilon_0 + S_{2z'}(\epsilon_{b2} - \epsilon_{g2z'})}{\epsilon_0 + S_{2z'}(\epsilon_{s2} - \epsilon_{g2z'})} \tag{44b}$$

The iteration is repeated until a required accuracy is achieved. Equation (44) indicates that small fractional volume f_{s2} leads to a fast conversion rate for the iterative solution and explains why the background permittivity has been chosen as the initial value for the auxiliary permittivities. After $\epsilon_{g2\rho'}$, $\epsilon_{g2z'}$, $S_{2\rho'}$, and $S_{2z'}$ are computed, variance $\delta_{\xi 2\rho'}$, $\delta_{\xi 2z'}$, and $\delta_{\xi 2z'}$ are found from (36)

$$\delta_{\xi 2\rho'} = \left[\frac{\epsilon_{b2} - \epsilon_{g2\rho'}}{\epsilon_0 + S_{2\rho'}(\epsilon_{b2} - \epsilon_{g2\rho'})}\right]^2 (1-f_{s2}) + \left[\frac{\epsilon_{s2} - \epsilon_{g2\rho'}}{\epsilon_0 + S_{2\rho'}(\epsilon_{s2} - \epsilon_{g2\rho'})}\right]^2 f_{s2} \tag{45a}$$

$$\delta_{\xi 2z'} = \left[\frac{\epsilon_{b2} - \epsilon_{g2z'}}{\epsilon_0 + S_{2z'}(\epsilon_{b2} - \epsilon_{g2z'})}\right]^2 (1-f_{s2}) + \left[\frac{\epsilon_{s2} - \epsilon_{g2z'}}{\epsilon_0 + S_{2z'}(\epsilon_{s2} - \epsilon_{g2z'})}\right]^2 f_{s2} \tag{45b}$$

In summary of the anisotropic case, the anisotropic effective permittivity tensor is calculated in the primed coordinate system of Figure 2.2.2 with (37) where $\epsilon_{g2\rho'}$, $\epsilon_{g2z'}$, $S_{2\rho'}$, and $S_{2z'}$ are obtained by iterating (44) and (42) and then $\delta_{\xi 2\rho'}$, $\delta_{\xi 2z'}$, $\delta_{\xi 2c'}$, $I_{\rho'}$, and $I_{z'}$ are determined by (45a-c), (41), and (40), respectively. To transform the result into the unprimed coordinate system, the following operation is applied

$$\bar{\bar{\epsilon}}_{eff2} = \bar{\bar{T}}_\psi \cdot \bar{\bar{\epsilon}}_{eff2}(\hat{r}') \cdot \bar{\bar{T}}_\psi^{-1} \quad \text{with} \quad \bar{\bar{T}}_\psi = \begin{bmatrix} 1 & 0 & 0 \\ 0 & \cos\psi & \sin\psi \\ 0 & -\sin\psi & \cos\psi \end{bmatrix} \tag{46}$$

where $\bar{\bar{T}}_\psi$ is the transformation matrix which rotates a vector by angle ψ from the primed coordinates to the unprimed coordinates. After the rotation, the anisotropic effective permittivity, which is a symmetric tensor in the $(\hat{x}, \hat{y}, \hat{z})$ system, is related to tilt angle ψ by

$$\bar{\bar{\epsilon}}_{eff2} = \begin{bmatrix} \epsilon_{eff2xx} & 0 & 0 \\ 0 & \epsilon_{eff2yy} & \epsilon_{eff2yz} \\ 0 & \epsilon_{eff2zy} & \epsilon_{eff2zz} \end{bmatrix} \tag{47a}$$

$$\begin{aligned} \epsilon_{eff2xx} &= \epsilon_{eff2\rho'}\,, \quad \epsilon_{eff2yz} = \epsilon_{eff2zy} \\ \epsilon_{eff2yz} &= (\epsilon_{eff2z'} - \epsilon_{eff2\rho'}) \cos\psi \sin\psi \\ \epsilon_{eff2yy} &= \epsilon_{eff2\rho'} \cos^2\psi + \epsilon_{eff2z'} \sin^2\psi \\ \epsilon_{eff2zz} &= \epsilon_{eff2\rho'} \sin^2\psi + \epsilon_{eff2z'} \cos^2\psi \end{aligned} \tag{47b}$$

In this section, the effective permittivities of the isotropic and anisotropic random media have been derived. It is necessary to note that the principal branch cut of square root $\sqrt{w}$ for complex number w has been chosen such that $-\pi < \arg w \leq \pi$ where $\arg w$ denotes the argument of w. Also, inverse tangent $\tan^{-1} w$ for complex number w is determined by

$$\tan^{-1} w = \frac{1}{2i} \ln w_a \quad \text{with} \quad w_a = \frac{1+iw}{1-iw} \tag{48}$$

where $\ln w_a$ is the natural logarithm of w_a on the principal Riemann sheet $|w_a| > 0$ and $-\pi < \arg w_a < \pi$.

Auxiliary permittivity ϵ_{g1} of the isotropic random medium as obtained is the same as the Polder and van Santen mixing formula [19]; thus, auxiliary permittivity ϵ_{g2} of the anisotropic random medium obtained in a similar manner can be considered as a more generalized version. Related to the auxiliary permittivity and the shape of the exclusion volume, the dyadic coefficient of the Dirac delta part in the Green's function is also derivable with a surface integration over a limiting equicorrelation surface and proved to satisfy the following condition [82]

$$2\frac{\epsilon_{g\rho}}{\epsilon_0}S_\rho + \frac{\epsilon_{gz}}{\epsilon_0}S_z = 1 \tag{49}$$

where $\epsilon_{g\rho} = \epsilon_{gz} = \epsilon_{g1}$ and $S_\rho = S_z = S_1$ for the isotropic case or $\epsilon_{g\rho} = \epsilon_{g2\rho'}$, $\epsilon_{gz} = \epsilon_{g2z'}$, $S_\rho = S_{2\rho'}$, and $S_z = S_{2z'}$ for the anisotropic case.

As mentioned earlier, the anisotropic effective permittivity becomes isotropic when the spheroidal correlation function is reduced to spherical. This is the case when $\ell_{2\rho'}$ approaches $\ell_{2z'}$ and it is trivial to show that

$$\lim_{\ell_{2\rho'}\to\ell_{2z'}} S_{2\rho'} = \lim_{\ell_{2\rho'}\to\ell_{2z'}} S_{2z'} \tag{50a}$$

$$\lim_{\ell_{2\rho'}\to\ell_{2z'}} \epsilon_{g2\rho'} = \lim_{\ell_{2\rho'}\to\ell_{2z'}} \epsilon_{g2z'} \tag{50b}$$

The limit (50a) has the form of (26) and consequently the variances in (45) have the same limit of the form (29) since $\epsilon_{g2\rho'}$ and $\epsilon_{g2z'}$ approach to the same limit as indicated in (50b). To prove that $I_{\rho'}$ and $I_{z'}$ have the same expression of the form (25) as $\ell_{2\rho'} \to \ell_{2z'}$, attention must be given to the afore chosen branch cuts. For instance, $\sqrt{-\zeta}$ is $-i\sqrt{\zeta}$ instead of $i\sqrt{\zeta}$; this is because $w = -\zeta \to -k_{g2\rho'}^2\ell_{2z'}^2$ as $\ell_{2\rho'} \to \ell_{2z'}$ and w is thus in the third quadrant of the complex w plane so that $\sqrt{w}$ is consequently in the fourth quadrant due to the chosen branch cut of the square root. The value of $\sqrt{-\zeta}$ so obtained is identical to $-i\sqrt{\zeta}$ and not to $i\sqrt{\zeta}$. The proof is then straight forward.

In deriving the effective permittivities, the low-frequency and the bilocal approximations have been used. The low-frequency approximation is valid if $k_{g1}\ell_1 \ll 1$

for the isotropic case or $k_{g2\rho'}\ell_{2\rho'} \ll 1$ and $k_{g2\rho'}\ell_{2z'} \ll 1$ for the anisotropic case. This approximation results in the ignorance of the spatial dispersive characteristics of the inhomogeneous media. In this case, the bilocal approximation further requires that $|[\overline{\overline{\xi}}^{(0)}_{effn}]_{jm}| \ll 1$ with $n = 1$ for the isotropic or $n = 2$ for the anisotropic case. This condition allows more simplification on the permittivity results (22) and (37) where the denominators can be approximated to be unity.

When the low-frequency condition is removed, the spatial dispersion of the random media is manifested in the dependence of the effective scatterers on wave vector $\overline{k}$ as

$$\left[\overline{\overline{\xi}}_{effn}(\overline{k})\right]_{jm} = \sum_{k,l}^{x',y',z'} \Gamma^{(0)}_{\xi njklm} \left\{ \frac{k_0^2}{2} \int_{-\infty}^{\infty} d\overline{k}' \left[\overline{\overline{G}}_{gn}(\overline{k}')\right]_{kl} \cdot \left[\Phi_{\xi n}(\overline{k}' - \overline{k}) + \Phi_{\xi n}(\overline{k}' + \overline{k})\right] + \left[\overline{\overline{S}}_n\right]_{kl} \right\} \tag{51}$$

The effective permittivities are still calculated with (17) or (34) with the effective scatterer (51) replacing the low-frequency version. In this case, the bilocal approximation is valid when $|[\overline{\overline{\xi}}_{effn}(\overline{k})]_{jm}| \ll 1$. From (17), (34), and (51), it is observed that the effective permittivities are even functions of wave vector $\overline{k}$ and can be expressed with symmetric tensors. The random media under consideration are therefore reciprocal as physically expected. Besides the above approximation, the use of the Fourier transform in this section implies that the media are unbounded in the calculations of the effective permittivities. In the next section, the effective permittivities is used to obtain the dyadic Green's function of the layer random medium which accounts for the multiple reflections, refractions, and transmissions at the medium interfaces.

2.4 Dyadic Green's Functions

In this section, the mean dyadic Green's Functions (DGFs), needed in the calculation of the scattered field correlation (13), is presented for the three-layer configuration. Rather than directly calculating $\left\langle \overline{\overline{G}}_{0n}(\overline{r}, \overline{r}_s) \right\rangle$ for observation point $\overline{r}$ in region 0 and

source point $\bar{r}_s$ in region n, $\langle \overline{\overline{G}}_{n0}(\bar{r},\bar{r}_s) \rangle$ are obtained for the source in region 0 and the observation in region n and the needed DGFs are then deduced from the symmetric relation

$$\langle \overline{\overline{G}}_{mn}(\bar{r},\bar{r}_s) \rangle = \langle \overline{\overline{G}}^{\mathsf{T}}_{nm}(\bar{r}_s,\bar{r}) \rangle \tag{52}$$

In this method [29,32,81], vector wave equations are first written for the DGFs subjected to the appropriate boundary conditions at the interfaces and radiation conditions at infinite distances above and below the interfaces. Next, the Cartesian coordinate systems corresponding to upgoing and downgoing waves in the layers are shown. The DGFs can then be solved in terms of transmission and reflection coefficients for the upgoing and downgoing waves. This procedure for obtaining the DGFs are detailed in the subsequent paragraphs.

Consider the source in region 0 at $\bar{r}_s$ above interface $z = 0$. The DGFs observed in regions $n = 0,1,2,3$ are governed by vector wave equations as follows

$$\nabla \times \nabla \times \langle \overline{\overline{G}}_{00}(\bar{r},\bar{r}_s) \rangle - k_0^2 \cdot \langle \overline{\overline{G}}_{00}(\bar{r},\bar{r}_s) \rangle = \delta(\bar{r}-\bar{r}_s)\overline{\overline{I}},\ z \geq 0 \tag{53a}$$

$$\nabla \times \nabla \times \langle \overline{\overline{G}}_{10}(\bar{r},\bar{r}_s) \rangle - k_0^2 \frac{\epsilon_{eff1}}{\epsilon_0} \cdot \langle \overline{\overline{G}}_{10}(\bar{r},\bar{r}_s) \rangle = 0,\ 0 \geq z \geq -d_1 \tag{53b}$$

$$\nabla \times \nabla \times \langle \overline{\overline{G}}_{20}(\bar{r},\bar{r}_s) \rangle - k_0^2 \frac{\overline{\overline{\epsilon}}_{eff2}}{\epsilon_0} \cdot \langle \overline{\overline{G}}_{20}(\bar{r},\bar{r}_s) \rangle = 0,\ -d_1 \geq z \geq -d_2 \tag{53c}$$

$$\nabla \times \nabla \times \langle \overline{\overline{G}}_{30}(\bar{r},\bar{r}_s) \rangle - k_0^2 \frac{\epsilon_3}{\epsilon_0} \cdot \langle \overline{\overline{G}}_{30}(\bar{r},\bar{r}_s) \rangle = 0,\ -d_2 \geq z \tag{53d}$$

The boundary conditions call for the continuity of $\hat{z} \times \langle \overline{\overline{G}}_{n0} \rangle$ and $\hat{z} \times \nabla \times \langle \overline{\overline{G}}_{n0} \rangle$ at the interfaces where the tangential electric and magnetic fields are continuous, respectively. The boundary conditions can be written explicitly as

$$\left.\begin{aligned} \hat{z} \times \langle \overline{\overline{G}}_{00}(\bar{r},\bar{r}_s) \rangle &= \hat{z} \times \langle \overline{\overline{G}}_{10}(\bar{r},\bar{r}_s) \rangle \\ \hat{z} \times \nabla \times \langle \overline{\overline{G}}_{00}(\bar{r},\bar{r}_s) \rangle &= \hat{z} \times \nabla \times \langle \overline{\overline{G}}_{10}(\bar{r},\bar{r}_s) \rangle \end{aligned}\right\} \text{ at } z = 0 \tag{54a}$$

$$\left.\begin{aligned} \hat{z} \times \langle \overline{\overline{G}}_{10}(\bar{r},\bar{r}_s) \rangle &= \hat{z} \times \langle \overline{\overline{G}}_{20}(\bar{r},\bar{r}_s) \rangle \\ \hat{z} \times \nabla \times \langle \overline{\overline{G}}_{10}(\bar{r},\bar{r}_s) \rangle &= \hat{z} \times \nabla \times \langle \overline{\overline{G}}_{20}(\bar{r},\bar{r}_s) \rangle \end{aligned}\right\} \text{ at } z = -d_1 \tag{54b}$$

$$\left.\begin{aligned} \hat{z} \times \langle \overline{\overline{G}}_{20}(\bar{r},\bar{r}_s) \rangle &= \hat{z} \times \langle \overline{\overline{G}}_{30}(\bar{r},\bar{r}_s) \rangle \\ \hat{z} \times \nabla \times \langle \overline{\overline{G}}_{20}(\bar{r},\bar{r}_s) \rangle &= \hat{z} \times \nabla \times \langle \overline{\overline{G}}_{30}(\bar{r},\bar{r}_s) \rangle \end{aligned}\right\} \text{ at } z = -d_2 \tag{54c}$$

To express the solutions for the DGFs physically in terms of upgoing and downgoing waves, Cartesian coordinate systems are defined to coincide with directions of electromagnetic fields and Poynting vectors. In the same manner as (1), coordinate system $(\hat{h}(k_{nz}^w), \hat{v}(k_{nz}^w), \hat{k}_n^w)$, corresponding to upgoing $(w = u)$ and downgoing $(w = d)$ waves in the isotropic media $(n = 0, 1, 3)$, are determined by

$$\hat{h}(k_{nz}^w) = \frac{\hat{z} \times \overline{k}_n^w}{\left|\hat{z} \times \overline{k}_n^w\right|}, \quad \hat{v}(k_{nz}^w) = \frac{\overline{k}_n^w \times \hat{h}(k_{nz}^w)}{\left|\overline{k}_n^w \times \hat{h}(k_{nz}^w)\right|} \tag{55a}$$

$$\hat{k}_n^w = \overline{k}_n^w / \left|\overline{k}_n^w\right| \quad \text{with} \quad \overline{k}_n^w = k_x \hat{x} + k_y \hat{y} + k_{nz}^w \hat{z} \tag{55b}$$

where the z components of the wave vectors are related as follows

$$k_{nz}^u = -k_{nz}^d = k_{nz} = \sqrt{k_n^2 - k_x^2 - k_y^2}, \quad \text{with} \quad k_n^2 = \begin{cases} \omega^2 \mu \epsilon_n, & n = 0, 3 \\ \omega^2 \mu \epsilon_{eff1}, & n = 1 \end{cases} \tag{56}$$

For the effective anisotropic medium $(n = 2)$ with optic axis $\hat{z}'$, the ordinary and extraordinary waves propagating in the upgoing and downgoing directions call for four different coordinate systems. Corresponding to the ordinary waves, coordinate system $(\hat{o}(k_{2z}^w), \hat{e}(k_{2z}^w), \hat{k}_2^w)$ are defined by

$$\hat{o}(k_{2z}^w) = \frac{\hat{z}' \times \overline{k}_2^w}{\left|\hat{z}' \times \overline{k}_2^w\right|}, \quad \hat{e}(k_{2z}^w) = \frac{\overline{k}_2^w \times \hat{o}(k_{2z}^w)}{\left|\overline{k}_2^w \times \hat{o}(k_{2z}^w)\right|} \tag{57a}$$

$$\hat{k}_2^w = \overline{k}_2^w / \left|\overline{k}_2^w\right| \quad \text{with} \quad \overline{k}_2^w = k_x \hat{x} + k_y \hat{y} + k_{2z}^w \hat{z} \tag{57b}$$

where the z components of the ordinary upgoing $(w = ou)$ and the ordinary downgoing $(w = od)$ wave vectors are

$$k_{2z}^{ou} = -k_{2z}^{od} = k_{2z}^o = \sqrt{k_2^2 - k_\rho^2} \quad \text{with} \quad k_2^2 = \omega^2 \mu \epsilon_{eff\,2xx} \tag{58}$$

Corresponding to the extraordinary waves in the anisotropic medium, coordinate system $(\hat{o}(k_{2z}^w), \hat{e}(k_{2z}^w), \hat{s}_2^w)$ are defined by

$$\hat{o}(k_{2z}^w) = \frac{\hat{z}' \times \overline{k}_2^w}{\left|\hat{z}' \times \overline{k}_2^w\right|}, \quad \hat{e}(k_{2z}^w) = \frac{\overline{s}_2^w \times \hat{o}(k_{2z}^w)}{\left|\overline{s}_2^w \times \hat{o}(k_{2z}^w)\right|}, \quad \hat{s}_2^w = \overline{s}_2^w / \left|\overline{s}_2^w\right| \tag{59}$$

where the extraordinary upgoing wave $(w = eu)$ and the extraordinary downgoing wave $(w = ed)$ vectors are determined by

$$\overline{k}_2^w = k_x\hat{x} + k_y\hat{y} + k_{2z}^w\hat{z} \quad \text{with} \quad w = eu, ed \tag{60a}$$

$$k_{2z}^{eu} = -\frac{\epsilon_{eff2yz}}{\epsilon_{eff2zz}}k_y + \frac{1}{\epsilon_{eff2zz}} \cdot \sqrt{k_2^2\epsilon_{eff2x'}\epsilon_{eff2zz} - k_x^2\epsilon_{eff2\rho'}\epsilon_{eff2zz} - k_y^2\epsilon_{eff2\rho'}\epsilon_{eff2x'}} \tag{60b}$$

$$k_{2z}^{ed} = -\frac{\epsilon_{eff2yz}}{\epsilon_{eff2zz}}k_y - \frac{1}{\epsilon_{eff2zz}} \cdot \sqrt{k_2^2\epsilon_{eff2x'}\epsilon_{eff2zz} - k_x^2\epsilon_{eff2\rho'}\epsilon_{eff2zz} - k_y^2\epsilon_{eff2\rho'}\epsilon_{eff2x'}} \tag{60c}$$

and unit ray vector $\hat{s}_2^w$ [81] of the extraordinary waves are parallel to

$$\overline{s}_2^w = \overline{\overline{\epsilon}}_{eff2} \cdot \overline{k}_2^w = \epsilon_{eff2xx}k_x\hat{x} + (\epsilon_{eff2yy}k_y + \epsilon_{eff2yz}k_{2z}^w)\hat{y} + (\epsilon_{eff2zy}k_y + \epsilon_{eff2zz}k_{2z}^w)\hat{z}\,, \quad \text{with} \quad w = eu, ed \tag{61}$$

The above definitions of the unit vectors are physically descriptive. Unit vector $\hat{h}$ is parallel to TE, $\hat{v}$ to TM, $\hat{o}$ to ordinary, and $\hat{e}$ to extraordinary wave polarizations. For wave vector $\overline{k}_n^w$, all the lateral components are $\overline{k}_\rho = \hat{x}k_x + \hat{y}k_y$ due to the phase matching condition and the z components are calculated from dispersion relations. Poynting vectors are all in the directions of wave vectors except for extraordinary waves whose Poynting vectors are in the directions of $\overline{s}_2^w$ given by (61).

In terms of upgoing and downgoing waves, solutions for the DGFs are

$$\begin{aligned}
\left\langle \overline{\overline{G}}_{00}(\overline{r}, \overline{r}_s) \right\rangle = \frac{i}{8\pi^2}\int_{-\infty}^{\infty}dk_x\int_{-\infty}^{\infty}dk_y\frac{e^{-i\overline{k}_0^d\cdot\overline{r}_s}}{k_{0z}} \\
\Big\{\ \hat{h}(k_{0z}^d)e^{i\overline{k}_0^d\cdot\overline{r}}\hat{h}(k_{0z}^d) \\
+ \left[R_{hh}(\overline{k}_\rho)\hat{h}(k_{0z}^u)e^{i\overline{k}_0^u\cdot\overline{r}} + R_{hv}(\overline{k}_\rho)\hat{v}(k_{0z}^u)e^{i\overline{k}_0^u\cdot\overline{r}}\right]\hat{h}(k_{0z}^d) \\
+ \hat{v}(k_{0z}^d)e^{i\overline{k}_0^d\cdot\overline{r}}\hat{v}(k_{0z}^d) \\
+ \left[R_{vh}(\overline{k}_\rho)\hat{h}(k_{0z}^u)e^{i\overline{k}_0^u\cdot\overline{r}} + R_{vv}(\overline{k}_\rho)\hat{v}(k_{0z}^u)e^{i\overline{k}_0^u\cdot\overline{r}}\right]\hat{v}(k_{0z}^d)\Big\} \\
z_s > z \geq 0
\end{aligned} \tag{62a}$$

$$\left\langle \overline{\overline{G}}_{10}(\overline{r},\overline{r}_s)\right\rangle = \frac{i}{8\pi^2}\int_{-\infty}^{\infty}dk_x\int_{-\infty}^{\infty}dk_y\frac{e^{-i\overline{k}_0^d\cdot\overline{r}_s}}{k_{0z}}$$
$$\Bigg\{\left[D_{1hh}(\overline{k}_\rho)\hat{h}(k_{1z}^d)e^{i\overline{k}_1^d\cdot\overline{r}}+D_{1hv}(\overline{k}_\rho)\hat{v}(k_{1z}^d)e^{i\overline{k}_1^d\cdot\overline{r}}\right]\hat{h}(k_{0z}^d)$$
$$+\left[U_{1hh}(\overline{k}_\rho)\hat{h}(k_{1z}^u)e^{i\overline{k}_1^u\cdot\overline{r}}+U_{1hv}(\overline{k}_\rho)\hat{v}(k_{1z}^u)e^{i\overline{k}_1^u\cdot\overline{r}}\right]\hat{h}(k_{0z}^d)$$
$$+\left[D_{1vh}(\overline{k}_\rho)\hat{h}(k_{1z}^d)e^{i\overline{k}_1^d\cdot\overline{r}}+D_{1vv}(\overline{k}_\rho)\hat{v}(k_{1z}^d)e^{i\overline{k}_1^d\cdot\overline{r}}\right]\hat{v}(k_{0z}^d)$$
$$+\left[U_{1vh}(\overline{k}_\rho)\hat{h}(k_{1z}^u)e^{i\overline{k}_1^u\cdot\overline{r}}+U_{1vv}(\overline{k}_\rho)\hat{v}(k_{1z}^u)e^{i\overline{k}_1^u\cdot\overline{r}}\right]\hat{v}(k_{0z}^d)\Bigg\}$$
$$0\geq z\geq -d_1 \tag{62b}$$

$$\left\langle \overline{\overline{G}}_{20}(\overline{r},\overline{r}_s)\right\rangle = \frac{i}{8\pi^2}\int_{-\infty}^{\infty}dk_x\int_{-\infty}^{\infty}dk_y\frac{e^{-i\overline{k}_0^d\cdot\overline{r}_s}}{k_{0z}}$$
$$\Bigg\{\left[D_{2ho}(\overline{k}_\rho)\hat{o}(k_{2z}^{od})e^{i\overline{k}_2^{od}\cdot\overline{r}}+D_{2he}(\overline{k}_\rho)\hat{e}(k_{2z}^{ed})e^{i\overline{k}_2^{ed}\cdot\overline{r}}\right]\hat{h}(k_{0z}^d)$$
$$+\left[U_{2ho}(\overline{k}_\rho)\hat{o}(k_{2z}^{ou})e^{i\overline{k}_2^{ou}\cdot\overline{r}}+U_{2he}(\overline{k}_\rho)\hat{e}(k_{2z}^{eu})e^{i\overline{k}_2^{eu}\cdot\overline{r}}\right]\hat{h}(k_{0z}^d)$$
$$+\left[D_{2vo}(\overline{k}_\rho)\hat{o}(k_{2z}^{od})e^{i\overline{k}_2^{od}\cdot\overline{r}}+D_{2ve}(\overline{k}_\rho)\hat{e}(k_{2z}^{ed})e^{i\overline{k}_2^{ed}\cdot\overline{r}}\right]\hat{v}(k_{0z}^d)$$
$$+\left[U_{2vo}(\overline{k}_\rho)\hat{o}(k_{2z}^{ou})e^{i\overline{k}_2^{ou}\cdot\overline{r}}+U_{2ve}(\overline{k}_\rho)\hat{e}(k_{2z}^{eu})e^{i\overline{k}_2^{eu}\cdot\overline{r}}\right]\hat{v}(k_{0z}^d)\Bigg\}$$
$$-d_1\geq z\geq -d_2 \tag{62c}$$

$$\left\langle \overline{\overline{G}}_{30}(\overline{r},\overline{r}_s)\right\rangle = \frac{i}{8\pi^2}\int_{-\infty}^{\infty}dk_x\int_{-\infty}^{\infty}dk_y\frac{e^{-i\overline{k}_0^d\cdot\overline{r}_s}}{k_{0z}}$$
$$\Bigg\{\left[T_{hh}(\overline{k}_\rho)\hat{h}(k_{3z}^d)e^{i\overline{k}_3^d\cdot\overline{r}}+T_{hv}(\overline{k}_\rho)\hat{v}(k_{3z}^d)e^{i\overline{k}_3^d\cdot\overline{r}}\right]\hat{h}(k_{0z}^d)$$
$$+\left[T_{vh}(\overline{k}_\rho)\hat{h}(k_{3z}^d)e^{i\overline{k}_3^d\cdot\overline{r}}+T_{vv}(\overline{k}_\rho)\hat{v}(k_{3z}^d)e^{i\overline{k}_3^d\cdot\overline{r}}\right]\hat{v}(k_{0z}^d)\Bigg\}$$
$$-d_2\geq z \tag{62d}$$

DGF coefficient R's, U's, D's, and T's can be calculated directly from the boundary conditions in (54). To facilitate the calculation and the interpretation, the matrix method [81] is used to express the DGF coefficients in terms of Fresnel reflection and transmission coefficients. These expressions are determined by considering amplitude vector $\overline{A}_n$ of upgoing waves and $\overline{B}_n$ of downgoing waves in region $n=0,1,2,3$. In this method, amplitude vectors of waves propagating away and toward each interface

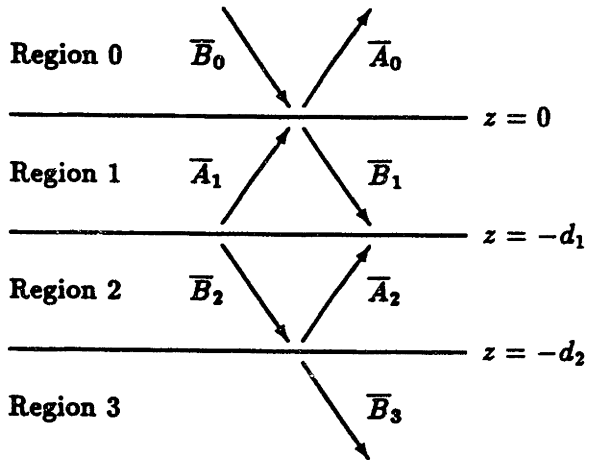

Figure 2.4.1 Amplitude vector $\overline{A}_n$ are for upgoing waves, $\overline{B}_n$ are for downgoing waves, and the arrows represent the propagation directions

as shown in Figure 2.4.1 are related with matrix equations

$$\begin{bmatrix} \overline{A}_0 \\ \overline{B}_1 \end{bmatrix} = \begin{bmatrix} \overline{\overline{R}}_{01} & \overline{\overline{T}}_{10} \\ \overline{\overline{T}}_{01} & \overline{\overline{R}}_{10} \end{bmatrix} \cdot \begin{bmatrix} \overline{B}_0 \\ \overline{A}_1 \end{bmatrix} \tag{63a}$$

$$\begin{bmatrix} \overline{A}_1 \\ \overline{B}_2 \end{bmatrix} = \begin{bmatrix} \overline{\overline{R}}_{12} & \overline{\overline{T}}_{21} \\ \overline{\overline{T}}_{12} & \overline{\overline{R}}_{21} \end{bmatrix} \cdot \begin{bmatrix} \overline{B}_1 \\ \overline{A}_2 \end{bmatrix} \tag{63b}$$

$$\begin{bmatrix} \overline{A}_2 \\ \overline{B}_3 \end{bmatrix} = \begin{bmatrix} \overline{\overline{R}}_{23} \\ \overline{\overline{T}}_{23} \end{bmatrix} \cdot \overline{B}_2 \tag{63c}$$

Observed from (62), the amplitude vectors are also connected to incident amplitude vector $\overline{B}_0$ by

$$\overline{A}_0 \equiv \overline{\overline{R}}_0 \cdot \overline{B}_0 = \begin{bmatrix} R_{hh}(\overline{k}_\rho) & R_{vh}(\overline{k}_\rho) \\ R_{hv}(\overline{k}_\rho) & R_{vv}(\overline{k}_\rho) \end{bmatrix} \cdot \overline{B}_0 \tag{64a}$$

$$\overline{B}_1 \equiv \overline{\overline{D}}_1 \cdot \overline{B}_0 = \begin{bmatrix} D_{1hh}(\overline{k}_\rho) & D_{1vh}(\overline{k}_\rho) \\ D_{1hv}(\overline{k}_\rho) & D_{1vv}(\overline{k}_\rho) \end{bmatrix} \cdot \overline{B}_0 \tag{64b}$$

$$\overline{A}_1 \equiv \overline{\overline{U}}_1 \cdot \overline{B}_0 = \begin{bmatrix} U_{1hh}(\overline{k}_\rho) & U_{1vh}(\overline{k}_\rho) \\ U_{1hv}(\overline{k}_\rho) & U_{1vv}(\overline{k}_\rho) \end{bmatrix} \cdot \overline{B}_0 \tag{64c}$$

$$\overline{B}_2 \equiv \overline{\overline{D}}_2 \cdot \overline{B}_0 = \begin{bmatrix} D_{2ho}(\overline{k}_\rho) & D_{2vo}(\overline{k}_\rho) \\ D_{2he}(\overline{k}_\rho) & D_{2ve}(\overline{k}_\rho) \end{bmatrix} \cdot \overline{B}_0 \tag{64d}$$

$$\overline{A}_2 \equiv \overline{\overline{U}}_2 \cdot \overline{B}_0 = \begin{bmatrix} U_{2ho}(\overline{k}_\rho) & U_{2vo}(\overline{k}_\rho) \\ U_{2he}(\overline{k}_\rho) & U_{2ve}(\overline{k}_\rho) \end{bmatrix} \cdot \overline{B}_0 \tag{64e}$$

$$\overline{B}_3 \equiv \overline{\overline{T}}_3 \cdot \overline{B}_0 = \begin{bmatrix} T_{hh}(\overline{k}_\rho) & T_{vh}(\overline{k}_\rho) \\ T_{hv}(\overline{k}_\rho) & T_{vv}(\overline{k}_\rho) \end{bmatrix} \cdot \overline{B}_0 \tag{64f}$$

Equation system (63) is readily solved for the downgoing and upgoing amplitude vectors in terms of $\overline{B}_0$ and the results are then compared to (64) to obtain the following DGF coefficient matrices

$$\overline{\overline{R}}_0 = \overline{\overline{R}}_{01} + \overline{\overline{T}}_{10} \cdot \left(\overline{\overline{R}}_{12} + \overline{\overline{T}}_{21} \cdot \overline{\overline{R}}_{23} \cdot \overline{\overline{\Gamma}} \cdot \overline{\overline{T}}_{12}\right) \cdot \overline{\overline{D}}_1 \tag{65a}$$

$$\overline{\overline{D}}_1 = \left[\overline{\overline{I}} - \overline{\overline{R}}_{10} \cdot \left(\overline{\overline{R}}_{12} + \overline{\overline{T}}_{21} \cdot \overline{\overline{R}}_{23} \cdot \overline{\overline{\Gamma}} \cdot \overline{\overline{T}}_{12}\right)\right]^{-1} \cdot \overline{\overline{T}}_{01} \tag{65b}$$

$$\overline{\overline{U}}_1 = \left[\overline{\overline{R}}_{12} + \overline{\overline{T}}_{21} \cdot \overline{\overline{R}}_{23} \cdot \overline{\overline{\Gamma}} \cdot \overline{\overline{T}}_{12}\right] \cdot \overline{\overline{D}}_1 \tag{65c}$$

$$\overline{\overline{D}}_2 = \overline{\overline{\Gamma}} \cdot \overline{\overline{T}}_{12} \cdot \overline{\overline{D}}_1 \tag{65d}$$

$$\overline{\overline{U}}_2 = \overline{\overline{R}}_{23} \cdot \overline{\overline{\Gamma}} \cdot \overline{\overline{T}}_{12} \cdot \overline{\overline{D}}_1 \tag{65e}$$

$$\overline{\overline{T}}_3 = \overline{\overline{T}}_{23} \cdot \overline{\overline{\Gamma}} \cdot \overline{\overline{T}}_{12} \cdot \overline{\overline{D}}_1 \tag{65f}$$

where $\overline{\overline{\Gamma}} = \left(\overline{\overline{I}} - \overline{\overline{R}}_{21} \cdot \overline{\overline{R}}_{23}\right)^{-1}$ and the reflection and transmission matrices are

$$\overline{\overline{R}}_{01} = \begin{bmatrix} R_{01hh} & 0 \\ 0 & R_{01vv} \end{bmatrix}, \quad \overline{\overline{R}}_{10} = \begin{bmatrix} R_{10hh} & 0 \\ 0 & R_{10vv} \end{bmatrix} \tag{66a}$$

$$\overline{\overline{T}}_{01} = \begin{bmatrix} T_{01hh} & 0 \\ 0 & T_{01vv} \end{bmatrix}, \quad \overline{\overline{T}}_{10} = \begin{bmatrix} T_{10hh} & 0 \\ 0 & T_{10vv} \end{bmatrix} \tag{66b}$$

$$\overline{\overline{R}}_{12} = \begin{bmatrix} e^{i2k_{1z}^u d_1} R_{12hh} & e^{i2k_{1z}^u d_1} R_{12vh} \\ e^{i2k_{1z}^u d_1} R_{12hv} & e^{i2k_{1z}^u d_1} R_{12vv} \end{bmatrix} \tag{66c}$$

$$\overline{\overline{R}}_{21} = \begin{bmatrix} e^{i(k_{2z}^{od} - k_{2z}^{ou}) d_1} R_{21oo} & e^{i(k_{2z}^{od} - k_{2z}^{eu}) d_1} R_{21eo} \\ e^{i(k_{2z}^{ed} - k_{2z}^{ou}) d_1} R_{21oe} & e^{i(k_{2z}^{ed} - k_{2z}^{eu}) d_1} R_{21ee} \end{bmatrix} \tag{66d}$$

$$\overline{\overline{T}}_{12} = \begin{bmatrix} e^{i(k_{2z}^{od} - k_{1z}^{d}) d_1} T_{12ho} & e^{i(k_{2z}^{od} - k_{1z}^{d}) d_1} T_{12vo} \\ e^{i(k_{2z}^{ed} - k_{1z}^{d}) d_1} T_{12he} & e^{i(k_{2z}^{ed} - k_{1z}^{d}) d_1} T_{12ve} \end{bmatrix} \tag{66e}$$

$$\overline{\overline{T}}_{21} = \begin{bmatrix} e^{i(k_{1z}^{u} - k_{2z}^{ou}) d_1} T_{21oh} & e^{i(k_{1z}^{u} - k_{2z}^{eu}) d_1} T_{21eh} \\ e^{i(k_{1z}^{u} - k_{2z}^{ou}) d_1} T_{21ov} & e^{i(k_{1z}^{u} - k_{2z}^{eu}) d_1} T_{21ev} \end{bmatrix} \tag{66f}$$

$$\overline{\overline{R}}_{23} = \begin{bmatrix} e^{i(k_{2z}^{ou} - k_{2z}^{od}) d_2} R_{23oo} & e^{i(k_{2z}^{ou} - k_{2z}^{ed}) d_2} R_{23eo} \\ e^{i(k_{2z}^{eu} - k_{2z}^{od}) d_2} R_{23oe} & e^{i(k_{2z}^{eu} - k_{2z}^{ed}) d_2} R_{23ee} \end{bmatrix} \tag{66g}$$

$$\overline{\overline{T}}_{23} = \begin{bmatrix} e^{i(k_{3z}^{d} - k_{2z}^{od}) d_2} T_{23oh} & e^{i(k_{3z}^{d} - k_{2z}^{ed}) d_2} T_{23eh} \\ e^{i(k_{3z}^{d} - k_{2z}^{od}) d_2} T_{23ov} & e^{i(k_{3z}^{d} - k_{2z}^{ed}) d_2} T_{23ev} \end{bmatrix} \tag{66h}$$

in which the exponents carry phase factors due to the locations of the interfaces and Fresnel reflection and transmission coefficient R's and T's are given in Appendix A. The above results vividly describe the physical processes of wave interaction in the layer media. For instance, amplitude vector $\overline{B}_2$ of downgoing waves in region 2 is spelled out from (64d) and (65d) as

$$\overline{B}_2 = \overline{\overline{\Gamma}} \cdot \overline{\overline{T}}_{12} \cdot \overline{\overline{D}}_1 \cdot \overline{B}_0 \tag{67}$$

which can be interpreted as the incident wave $\overline{B}_0$ from region 0 propagates down into region 1 $(\overline{\overline{D}}_1 \cdot \overline{B}_0)$, transmits through the interface between region 1 and region 2 $(\overline{\overline{T}}_{12} \cdot \overline{\overline{D}}_1 \cdot \overline{B}_0)$, and multiply reflects between the interfaces of region 2 $(\overline{\overline{\Gamma}} \cdot \overline{\overline{T}}_{12} \cdot \overline{\overline{D}}_1 \cdot \overline{B}_0)$. This completes the derivation of the DGFs corresponding to the source in region 0 in integral form (62).

For latter calculations of the scattering coefficients involving the effective sources in the scattering regions $(n = 1, 2)$, dyadic Green's function $\langle \overline{\overline{G}}_{01}(\overline{r}, \overline{r}_s) \rangle$ and $\langle \overline{\overline{G}}_{02}(\overline{r}, \overline{r}_s) \rangle$ need be obtained by applying the symmetry relation (52) requiring the transposition of the corresponding DGFs in the last paragraph and the sign changes of k_x and k_y respectively to $-k_x$ and $-k_y$. After the integrations are carried out with the two-dimensional saddle point method [67,81], the results for the DGFs in the radiation field are

$$\langle \overline{\overline{G}}_{0n}(\overline{r}, \overline{r}_s) \rangle = \frac{e^{ik_0 r}}{4\pi r} e^{-i\overline{k}_\rho \cdot \overline{\rho}_s} \overline{\overline{g}}_n(\overline{k}_\rho, z_s) , \quad n = 1, 2 \tag{68}$$

where $\overline{\rho}_s = \hat{x} x_s + \hat{y} y_s$ and dyadic coefficient $\overline{\overline{g}}_n(\overline{k}_\rho, z_s)$ are defined as

$$\begin{aligned}
\overline{\overline{g}}_1(\overline{k}_\rho, z_s) \equiv\ & \hat{h}(k_{0z}^u) \left[D_{1hh}(-\overline{k}_\rho) \hat{h}(k_{1z}^u) e^{-ik_{1z}^u z_s} - D_{1hv}(-\overline{k}_\rho) \hat{v}(k_{1z}^u) e^{-ik_{1z}^u z_s} \right] \\
& + \hat{h}(k_{0z}^u) \left[U_{1hh}(-\overline{k}_\rho) \hat{h}(k_{1z}^d) e^{-ik_{1z}^d z_s} - U_{1hv}(-\overline{k}_\rho) \hat{v}(k_{1z}^d) e^{-ik_{1z}^d z_s} \right] \\
& - \hat{v}(k_{0z}^u) \left[D_{1vh}(-\overline{k}_\rho) \hat{h}(k_{1z}^u) e^{-ik_{1z}^u z_s} - D_{1vv}(-\overline{k}_\rho) \hat{v}(k_{1z}^u) e^{-ik_{1z}^u z_s} \right] \\
& - \hat{v}(k_{0z}^u) \left[U_{1vh}(-\overline{k}_\rho) \hat{h}(k_{1z}^d) e^{-ik_{1z}^d z_s} - U_{1vv}(-\overline{k}_\rho) \hat{v}(k_{1z}^d) e^{-ik_{1z}^d z_s} \right]
\end{aligned} \tag{69a}$$

$$\begin{aligned}\overline{\overline{g}}_2(\overline{k}_\rho, z_s) \equiv\ & \hat{h}(k_{0z}^u)\left[D_{2ho}(-\overline{k}_\rho)\hat{o}(k_{2z}^{ou})e^{-ik_{2z}^{ou}z_s} - D_{2he}(-\overline{k}_\rho)\hat{e}(k_{2z}^{eu})e^{-ik_{2z}^{eu}z_s}\right] \\ & + \hat{h}(k_{0z}^u)\left[U_{2ho}(-\overline{k}_\rho)\hat{o}(k_{2z}^{od})e^{-ik_{2z}^{od}z_s} - U_{2he}(-\overline{k}_\rho)\hat{e}(k_{2z}^{ed})e^{-ik_{2z}^{ed}z_s}\right] \\ & - \hat{v}(k_{0z}^u)\left[D_{2vo}(-\overline{k}_\rho)\hat{o}(k_{2z}^{ou})e^{-ik_{2z}^{ou}z_s} - D_{2ve}(-\overline{k}_\rho)\hat{e}(k_{2z}^{eu})e^{-ik_{2z}^{eu}z_s}\right] \\ & - \hat{v}(k_{0z}^u)\left[U_{2vo}(-\overline{k}_\rho)\hat{o}(k_{2z}^{od})e^{-ik_{2z}^{od}z_s} - U_{2ve}(-\overline{k}_\rho)\hat{e}(k_{2z}^{ed})e^{-ik_{2z}^{ed}z_s}\right] \quad (69b)\end{aligned}$$

In summary, the DGFs are obtained in (69) where all the coefficients are determined by (64-66) and Appendix A. With the available DGFs, the scattering coefficients are derived in the next section.

2.5 Scattering Coefficients

The polarimetric backscattering coefficients are defined by (13) in Chapter 1 based on ensemble averages of scattered fields. As indicated in (13), the averages are calculated with spatial integrations over products of the DGFs, the mean fields, and the correlation functions. The DGFs have been obtained; next shown are the mean field and the correlation functions. The integrations are then carried out to derive the scattering coefficients.

The mean external fields in the scattering regions $(n = 1, 2)$ can be approximated as the corresponding homogeneous solutions to the wave equations

$$\nabla \times \nabla \times \left\langle \overline{F}_n(\overline{r}) \right\rangle - k_0^2 \frac{\overline{\overline{\epsilon}}_{effn}}{\epsilon_0} \left\langle \overline{F}_n(\overline{r}) \right\rangle = 0 \ , \quad n = 1, 2 \qquad (70)$$

which are solved subjected to the boundary conditions at interface $z = 0, -d_1, -d_2$. For incident field $\overline{E}_{0i} = \left[\hat{h}(k_{0zi})E_{hi} + \hat{v}(k_{0zi})E_{vi}\right]e^{i\overline{k}_{0i}\cdot\overline{r}}$, the mean fields can be written as

$$\left\langle \overline{F}_n(\overline{r}) \right\rangle = e^{\overline{k}_{\rho i}\cdot\overline{\rho}}\, \overline{P}_n(\overline{k}_{\rho i}, z) \ , \quad n = 1, 2 \qquad (71)$$

where subscript i indicates the incident wave, $\overline{\rho} = \hat{x}x + \hat{y}y$ is the lateral space, $\overline{k}_{\rho i} = \hat{x}k_{xi} + \hat{y}k_{yi} = k_0(\hat{x}\sin\theta_{0i}\cos\phi_{0i} + \hat{y}\sin\theta_{0i}\sin\phi_{0i})$ is the lateral component of incident wave vector $\overline{k}_{0i}$, and polarization vector $\overline{P}_n(\overline{k}_{\rho i}, z)$ are determined by

$$\begin{aligned}\overline{P}_1(\overline{k}_{\rho i}, z) \equiv\ & E_{hi}\left[D_{1hh}(\overline{k}_{\rho i})\hat{h}(k^d_{1zi})e^{ik^d_{1zi}z} + D_{1hv}(\overline{k}_{\rho i})\hat{v}(k^d_{1zi})e^{ik^d_{1zi}z}\right] \\ & + E_{hi}\left[U_{1hh}(\overline{k}_{\rho i})\hat{h}(k^u_{1zi})e^{ik^u_{1zi}z} + U_{1hv}(\overline{k}_{\rho i})\hat{v}(k^u_{1zi})e^{ik^u_{1zi}z}\right] \\ & + E_{vi}\left[D_{1vh}(\overline{k}_{\rho i})\hat{h}(k^d_{1zi})e^{ik^d_{1zi}z} + D_{1vv}(\overline{k}_{\rho i})\hat{v}(k^d_{1zi})e^{ik^d_{1zi}z}\right] \\ & + E_{vi}\left[U_{1vh}(\overline{k}_{\rho i})\hat{h}(k^u_{1zi})e^{ik^u_{1zi}z} + U_{1vv}(\overline{k}_{\rho i})\hat{v}(k^u_{1zi})e^{ik^u_{1zi}z}\right] \qquad (72a)\end{aligned}$$

$$\begin{aligned}\overline{P}_2(\overline{k}_{\rho i}, z) \equiv\ & E_{hi}\left[D_{2ho}(\overline{k}_{\rho i})\hat{o}(k^{od}_{2zi})e^{ik^{od}_{2zi}z} + D_{2he}(\overline{k}_{\rho i})\hat{e}(k^{ed}_{2zi})e^{ik^{ed}_{2zi}z}\right] \\ & + E_{hi}\left[U_{2ho}(\overline{k}_{\rho i})\hat{o}(k^{ou}_{2zi})e^{ik^{ou}_{2zi}z} + U_{2he}(\overline{k}_{\rho i})\hat{e}(k^{eu}_{2zi})e^{ik^{eu}_{2zi}z}\right] \\ & + E_{vi}\left[D_{2vo}(\overline{k}_{\rho i})\hat{o}(k^{od}_{2zi})e^{ik^{od}_{2zi}z} + D_{2ve}(\overline{k}_{\rho i})\hat{e}(k^{ed}_{2zi})e^{ik^{ed}_{2zi}z}\right] \\ & + E_{vi}\left[U_{2vo}(\overline{k}_{\rho i})\hat{o}(k^{ou}_{2zi})e^{ik^{ou}_{2zi}z} + U_{2ve}(\overline{k}_{\rho i})\hat{e}(k^{eu}_{2zi})e^{ik^{eu}_{2zi}z}\right] \qquad (72b)\end{aligned}$$

with z components of the wave vectors defined in the same manner as (56), (58), and (60b,c) by changing k^w_{nz}, k_x, and k_y respectively to k^w_{nzi}, k_{xi}, and k_{yi}.

The correlation functions are defined by (14) in the spatial domain. To facilitate the integration of (13), Fourier transforms of the correlation functions are introduced for the statistically homogeneous scattering media under consideration

$$C_{\xi njklm}(\overline{r}_n, \overline{r}^{\,\circ}_n) = \int_{-\infty}^{\infty} d\overline{\beta}\Phi_{njklm}(\overline{\beta})e^{-i\overline{\beta}\cdot(\overline{r}_n - \overline{r}^{\,\circ}_n)}\ , \quad n = 1, 2 \qquad (73)$$

For the isotropic random medium $(n = 1)$, the non-zero elements of spectral density $\Phi_{1jklm}(\overline{\beta})$ are simply

$$\Phi_1(\overline{\beta}) = \Phi_{1jjmm}(\overline{\beta}) = \delta_1\Phi_{\xi 1}(\overline{\beta}) \qquad (74)$$

where $\Phi_{\xi 1}(\overline{\beta})$ is defined as in (20) and functionally given by (24b) in conformity with the correlation function used to find the isotropic effective permittivity. For a two-constituent medium, variance δ_1 is

$$\delta_1 = 9\left|\frac{\epsilon_{g1}}{\epsilon_0}\right|^2\left[\left|\frac{\epsilon_{b1} - \epsilon_{g1}}{\epsilon_{b1} + 2\epsilon_{g1}}\right|^2(1 - f_{s1}) + \left|\frac{\epsilon_{s1} - \epsilon_{g1}}{\epsilon_{s1} + 2\epsilon_{g1}}\right|^2 f_{s1}\right] \qquad (75)$$

For the anisotropic random medium ($n = 2$), the correlation functions (73) specified in the untilted coordinate system $(\hat{x}, \hat{y}, \hat{z})$ are derived by applying the rotation transformation $\overline{\overline{T}}_\psi$ on scatterer $\overline{\overline{\xi}}_2(\overline{r}_2')$ in the tilted coordinate system $(\hat{x}', \hat{y}', \hat{z}')$ so that

$$\overline{\overline{\xi}}_2(\overline{r}_2) = \overline{\overline{T}}_\psi \cdot \overline{\overline{\xi}}_2(\overline{r}_2') \cdot \overline{\overline{T}}_\psi^{-1} = \begin{bmatrix} \xi_{2xx}(\overline{r}_2) & 0 & 0 \\ 0 & \xi_{2yy}(\overline{r}_2) & \xi_{2yz}(\overline{r}_2) \\ 0 & \xi_{2zy}(\overline{r}_2) & \xi_{2zz}(\overline{r}_2) \end{bmatrix} \tag{76}$$

where the elements of $\overline{\overline{\xi}}_2(\overline{r}_2)$ have the form of (47b) with ϵ_{eff2} replaced by ξ_2. The scatterer elements in the untilted coordinates are then used in (14) to find the anisotropic correlation functions whose spectral densities can be obtained from the following spectral densities defined in the tilted coordinates as

$$\Phi_{2\rho'}(\overline{\beta}') = \Phi_{2x'x'x'x'}(\overline{\beta}') = \delta_{2\rho'}\Phi_{\xi 2}(\overline{\beta}') \tag{77a}$$

$$\Phi_{2z'}(\overline{\beta}') = \Phi_{2z'z'z'z'}(\overline{\beta}') = \delta_{2z'}\Phi_{\xi 2}(\overline{\beta}') \tag{77b}$$

$$\Phi_{2c'}(\overline{\beta}') = \Phi_{2x'x'z'z'}(\overline{\beta}') = \delta_{2c'}\Phi_{\xi 2}(\overline{\beta}') \tag{77c}$$

where $\Phi_{\xi 2}(\overline{\beta}')$ is functionally determined by (39b) in conformity with the correlation function used to calculate the anisotropic effective permittivity. For the two-constituent anisotropic random medium, the variances in (77) are

$$\delta_{2\rho'} = \left|\frac{\epsilon_{b2}-\epsilon_{g2\rho'}}{\epsilon_0+S_{2\rho'}(\epsilon_{b2}-\epsilon_{g2\rho'})}\right|^2(1-f_{s2}) + \left|\frac{\epsilon_{s2}-\epsilon_{g2\rho'}}{\epsilon_0+S_{2\rho'}(\epsilon_{s2}-\epsilon_{g2\rho'})}\right|^2 f_{s2} \tag{78a}$$

$$\delta_{2z'} = \left|\frac{\epsilon_{b2}-\epsilon_{g2z'}}{\epsilon_0+S_{2z'}(\epsilon_{b2}-\epsilon_{g2z'})}\right|^2(1-f_{s2}) + \left|\frac{\epsilon_{s2}-\epsilon_{g2z'}}{\epsilon_0+S_{2z'}(\epsilon_{s2}-\epsilon_{g2z'})}\right|^2 f_{s2} \tag{78b}$$

$$\begin{aligned}\delta_{2c'} = {} & \left[\frac{\epsilon_{b2}-\epsilon_{g2\rho'}}{\epsilon_0+S_{2\rho'}(\epsilon_{b2}-\epsilon_{g2\rho'})}\right]\left[\frac{\epsilon_{b2}-\epsilon_{g2z'}}{\epsilon_0+S_{2z'}(\epsilon_{b2}-\epsilon_{g2z'})}\right]^*(1-f_{s2}) \\ & + \left[\frac{\epsilon_{s2}-\epsilon_{g2\rho'}}{\epsilon_0+S_{2\rho'}(\epsilon_{s2}-\epsilon_{g2\rho'})}\right]\left[\frac{\epsilon_{s2}-\epsilon_{g2z'}}{\epsilon_0+S_{2z'}(\epsilon_{s2}-\epsilon_{g2z'})}\right]^* f_{s2}\end{aligned} \tag{78c}$$

Due to the invariant property of the Fourier transform under the rotation transformation, spectral density $\Phi_{2jklm}(\overline{\beta})$ in the untilted coordinates can functionally be related to those given in (77) with

$$\Phi_{\xi 2}(\overline{\beta}) = \Phi_{\xi 2}(\beta_x' = \beta_x, \beta_y' = \beta_y\cos\psi - \beta_z\sin\psi, \beta_z' = \beta_y\sin\psi + \beta_z\cos\psi) \tag{79}$$

In the untilted coordinates, the rotation transformation together with the above invariant property give the anisotropic spectral densities

$$\Phi_{2jklm}(\overline{\beta}) = \delta_{2jklm}\Phi_{\xi 2}(\overline{\beta}) \tag{80}$$

where non-zero variance δ_{2jklm} are dependent on the tilt angle ψ as

$$\delta_{2xxxx} = \delta_{2\rho'} \tag{81a}$$

$$\delta_{2xxyy} = \delta^*_{2yyxx} = \delta_{2\rho'}\cos^2\psi + \delta_{2c'}\sin^2\psi \tag{81b}$$

$$\delta_{2xxyz} = \delta_{2xxzy} = \delta^*_{2yzxx} = \delta^*_{2zyxx} = (\delta_{2c'} - \delta_{2\rho'})\sin\psi\cos\psi \tag{81c}$$

$$\delta_{2xxzz} = \delta^*_{2zzxx} = \delta_{2\rho'}\sin^2\psi + \delta_{2c'}\cos^2\psi \tag{81d}$$

$$\delta_{2yyyy} = \delta_{2\rho'}\cos^4\psi + \delta_{2z'}\sin^4\psi + (\delta_{2c'} + \delta^*_{2c'})\sin^2\psi\cos^2\psi \tag{81e}$$

$$\begin{aligned}\delta_{2yyyz} &= \delta_{2yyzy} = \delta^*_{2yzyy} = \delta^*_{2zyyy} \\ &= (\delta_{2c'} - \delta_{2\rho'})\cos^3\psi\sin\psi + (\delta_{2z'} - \delta^*_{2c'})\sin^3\psi\cos\psi\end{aligned} \tag{81f}$$

$$\begin{aligned}\delta_{2yyzz} &= \delta^*_{2zzyy} \\ &= (\delta_{2\rho'} + \delta_{2z'})\sin^2\psi\cos^2\psi + \delta_{2c'}\cos^4\psi + \delta^*_{2c'}\sin^4\psi\end{aligned} \tag{81g}$$

$$\begin{aligned}\delta_{2yzyz} &= \delta_{2yzzy} = \delta_{2zyyz} = \delta_{2zyzy} \\ &= (\delta_{2\rho'} + \delta_{2z'} - \delta_{2c'} - \delta^*_{2c'})\sin^2\psi\cos^2\psi\end{aligned} \tag{81h}$$

$$\begin{aligned}\delta_{2yzzz} &= \delta_{2zyzz} = \delta^*_{2zzyz} = \delta^*_{2zzzy} \\ &= (\delta^*_{2c'} - \delta_{2\rho'})\sin^3\psi\cos\psi + (\delta_{2z'} - \delta_{2c'})\cos^3\psi\sin\psi\end{aligned} \tag{81i}$$

$$\delta_{2zzzz} = \delta_{2\rho'}\sin^4\psi + \delta_{2z'}\cos^4\psi + (\delta_{2c'} + \delta^*_{2c'})\sin^2\psi\cos^2\psi \tag{81j}$$

The correlation of the scattered field can now be found by substituting into (13) the dyadic Green's functions (68), the means fields (71), and the correlation functions (73). To enable the calculation of the scattering coefficients according to (13) in Chapter 1, correlations of the scattered field components are actualized in the manner of (14, Chapter 1)

$$\left\langle E_{\mu s}(\overline{r})E^*_{\nu s}(\overline{r})\right\rangle = \frac{E_{\tau i}E^*_{\kappa i}}{(4\pi r)^2}$$
$$\left\{k_0^4\int_{-\infty}^{\infty}d\overline{\beta}_\rho\int d\overline{\rho}_1\int d\overline{\rho}_1^{\circ}\; e^{i(\overline{k}_{\rho i}-\overline{k}_\rho-\overline{\beta}_\rho)\cdot\overline{\rho}_1}e^{-i(\overline{k}_{\rho i}-\overline{k}_\rho-\overline{\beta}_\rho)\cdot\overline{\rho}_1^{\circ}}\right.$$
$$\sum_{j,m}^{x,y,z}\int_{-\infty}^{\infty}d\beta_z\int_{-d_1}^{0}dz_1\int_{-d_1}^{0}dz_1^{\circ}\;\Phi_1(\overline{\beta})e^{-i\beta_z(z_1-z_1^{\circ})}$$
$$\cdot g_{1\mu j}(\overline{k}_\rho,z_1)\mathcal{F}_{1\tau j}(\overline{k}_{\rho i},z_1)g^*_{1\nu m}(\overline{k}_\rho,z_1^{\circ})\mathcal{F}^*_{1\kappa m}(\overline{k}_{\rho i},z_1^{\circ})$$
$$+k_0^4\int_{-\infty}^{\infty}d\overline{\beta}_\rho\int d\overline{\rho}_2\int d\overline{\rho}_2^{\circ}\;e^{i(\overline{k}_{\rho i}-\overline{k}_\rho-\overline{\beta}_\rho)\cdot\overline{\rho}_2}e^{-i(\overline{k}_{\rho i}-\overline{k}_\rho-\overline{\beta}_\rho)\cdot\overline{\rho}_2^{\circ}}$$
$$\sum_{j,k,l,m}^{x,y,z}\int_{-\infty}^{\infty}d\beta_z\int_{-d_2}^{-d_1}dz_2\int_{-d_2}^{-d_1}dz_2^{\circ}\;\Phi_{2jklm}(\overline{\beta})e^{-i\beta_z(z_2-z_2^{\circ})}$$
$$\left.\cdot g_{2\mu j}(\overline{k}_\rho,z_2)\mathcal{F}_{2\tau k}(\overline{k}_{\rho i},z_2)g^*_{2\nu l}(\overline{k}_\rho,z_2^{\circ})\mathcal{F}^*_{2\kappa m}(\overline{k}_{\rho i},z_2^{\circ})\right\} \tag{82}$$

where $\overline{\beta}=\overline{\beta}_\rho+\hat{z}\beta_z$, $\overline{\beta}_\rho=\hat{x}\beta_x+\hat{y}\beta_y$, subscript μ, ν, τ, and κ can be h or v, and DGF element $g_{n\mu j}(\overline{k}_\rho,z_n)$ and normalized mean field component $\mathcal{F}_{n\tau j}(\overline{k}_\rho,z_n)$ for $n=1,2$ and $\hat{j}=\hat{x},\hat{y},\hat{z}$ are defined as

$$g_{n\mu j}(\overline{k}_\rho,z_n)=\left[\hat{\mu}(k_{0z}^u)\cdot\overline{\overline{g}}_n(\overline{k}_\rho,z_n)\right]\cdot\hat{j} \tag{83a}$$
$$\mathcal{F}_{n\tau j}(\overline{k}_{\rho i},z_n)=E_{\tau i}^{-1}\left\langle\overline{F}_n(\overline{r}_n)\right\rangle\cdot\hat{j}\,\Big|_{E_{\nu i}=0} \tag{83b}$$

The integrations in (82) are carried out with the procedure in [4]: the integrals over $\overline{\rho}_n$ give Dirac delta function $4\pi^2\delta(\overline{k}_{\rho i}-\overline{k}_\rho-\overline{\beta}_\rho)$, the integrals over $\overline{\beta}_\rho$ then effectuate $\overline{\beta}_\rho=\overline{k}_{\rho i}-\overline{k}_\rho$, and the integrals over $\overline{\rho}_n^{\circ}$ form illuminated area A. Then (82) becomes

$$\left\langle E_{\mu s}(\overline{r})E^*_{\nu s}(\overline{r})\right\rangle = E_{\tau i}E^*_{\kappa i}\frac{k_0^4A}{4r^2}$$
$$\left\{\sum_{j,m}^{x,y,z}\int_{-\infty}^{\infty}d\beta_z\int_{-d_1}^{0}dz_1\int_{-d_1}^{0}dz_1^{\circ}\;\Phi_1(\overline{\beta}_\rho=\overline{k}_{\rho i}-\overline{k}_\rho,\beta_z)e^{-i\beta_z(z_1-z_1^{\circ})}\right.$$
$$\cdot g_{1\mu j}(\overline{k}_\rho,z_1)\mathcal{F}_{1\tau j}(\overline{k}_{\rho i},z_1)g^*_{1\nu m}(\overline{k}_\rho,z_1^{\circ})\mathcal{F}^*_{1\kappa m}(\overline{k}_{\rho i},z_1^{\circ})$$
$$+\sum_{j,k,l,m}^{x,y,z}\int_{-\infty}^{\infty}d\beta_z\int_{-d_2}^{-d_1}dz_2\int_{-d_2}^{-d_1}dz_2^{\circ}\;\Phi_{2jklm}(\overline{\beta}_\rho=\overline{k}_{\rho i}-\overline{k}_\rho,\beta_z)e^{-i\beta_z(z_2-z_2^{\circ})}$$
$$\left.\cdot g_{2\mu j}(\overline{k}_\rho,z_2)\mathcal{F}_{2\tau k}(\overline{k}_{\rho i},z_2)g^*_{2\nu l}(\overline{k}_\rho,z_2^{\circ})\mathcal{F}^*_{2\kappa m}(\overline{k}_{\rho i},z_2^{\circ})\right\} \tag{84}$$

It is observed from the forms of g's and $\mathcal{F}$'s that all the polarization vectors and coefficient D's and U's can be taken out of the integrations in (84). Retained inside the integrations are the spectral densities and the exponential terms which account for the upgoing and downgoing propagation of the mean fields and the scattered fields. Furthermore, $\phi_{0s} = \phi_{0i} + \pi$ and $\theta_{0s} = \theta_{0i}$ in the backscattering direction so that $\overline{k}_p = -\overline{k}_{pi}$ and $k_{nz}^w = k_{nzi}^w$ for wave type $w = u, d$ in region $n = 1$ or $w = ou, od, eo, ed$ in region $n = 2$. Also note that the z components of the upgoing and the downgoing wave vectors in region 1 differ only by a minus sign. Consequently, the following integrals are defined to simplify the calculation

$$\mathcal{I}_1^{abcd} \equiv \int_{-\infty}^{\infty} d\beta_x \Phi_1(2\overline{k}_{pi}, \beta_x) \int_{-d_1}^{0} dz_1 e^{-i(\beta_z - \kappa_{ab})z_1} \int_{-d_1}^{0} dz_1^o e^{i(\beta_z - \kappa_{cd})z_1^o} \tag{85a}$$

$$\text{with} : \begin{cases} \kappa_{ab} = (a+b)k_{1z} \; ; & a, b = -1, 1 \\ \kappa_{cd} = (c+d)k_{1z}^* \; ; & c, d = -1, 1 \end{cases} \tag{85b}$$

$$\mathcal{I}_{2jklm}^{pqrs} \equiv \int_{-\infty}^{\infty} d\beta_x \Phi_{2jklm}(2\overline{k}_{pi}, \beta_x) \int_{-d_2}^{-d_1} dz_2 e^{-i(\beta_z - \kappa_{pq})z_2} \int_{-d_2}^{-d_1} dz_2^o e^{i(\beta_z - \kappa_{rs})z_2^o} \tag{86a}$$

$$\text{with} : \begin{cases} \kappa_{pq} = -k_{2zi}^p + k_{2zi}^q \; ; & p, q = ou, od, eu, ed \\ \kappa_{rs} = -k_{2zi}^{r*} + k_{2zi}^{s*} \; ; & r, s = ou, od, eu, ed \end{cases} \tag{86b}$$

For the isotropic random medium, integral $\mathcal{I}_1^{abcd}$ involves 16 quantities since a, b, c, and d each has two possibilities of -1 and 1. The integrations over vertical space z_1 and z_1^o are readily carried out and the integration over β_x is performed with the residue theorem in the contour integration method. From Appendix D, the result for $\mathcal{I}_1^{abcd}$ is

$$\mathcal{I}_1^{abcd} = i\frac{2\delta_1}{\pi \ell_1} \left[\frac{e^{-i(\kappa_{ab} - \kappa_{cd})d_1}}{(\kappa_{ab} - \kappa_1)^2(\kappa_{ab} - \kappa_1^*)^2(\kappa_{ab} - \kappa_{cd})} + \frac{1}{(\kappa_{cd} - \kappa_1)^2(\kappa_{cd} - \kappa_1^*)^2(\kappa_{cd} - \kappa_{ab})} - \mathcal{P}_1(\kappa_1) - \mathcal{Q}_1(\kappa_1^*) \right] \tag{87a}$$

where $\kappa_1 = i\ell^{-1}\sqrt{1 + 4k_{pi}^2 \ell_1^2}$ and quantities $\mathcal{P}_1(\kappa_1)$ and $\mathcal{Q}_1(\kappa_1^*)$ are

$$\mathcal{P}_1(\kappa_1) = \frac{id_1 e^{i(\kappa_1 - \kappa_{ab})d_1}}{(2\kappa_1)^2(\kappa_1 - \kappa_{ab})(\kappa_1 - \kappa_{cd})} + \frac{1 - e^{i(\kappa_1 - \kappa_{ab})d_1} + e^{-i(\kappa_{ab} - \kappa_{cd})d_1}}{(2\kappa_1)^2(\kappa_1 - \kappa_{ab})(\kappa_1 - \kappa_{cd})}$$

$$\cdot \left[\frac{1}{\kappa_1}+\frac{1}{\kappa_1-\kappa_{ab}}+\frac{1}{\kappa_1-\kappa_{cd}}\right] \tag{87b}$$

$$\mathcal{Q}_1(\kappa_1^*)=\frac{id_1e^{-i(\kappa_1^*-\kappa_{cd})d_1}}{(2\kappa_1^*)^2(\kappa_1^*-\kappa_{ab})(\kappa_1^*-\kappa_{cd})} + \frac{e^{-i(\kappa_1^*-\kappa_{cd})d_1}}{(2\kappa_1^*)^2(\kappa_1^*-\kappa_{ab})(\kappa_1^*-\kappa_{cd})} \cdot \left[\frac{1}{\kappa_1^*}+\frac{1}{\kappa_1^*-\kappa_{ab}}+\frac{1}{\kappa_1^*-\kappa_{cd}}\right] \tag{87c}$$

For the anisotropic random medium, integral $\mathcal{I}_{2jklm}^{pqrs}$ involves 256 quantities since p, q, r, and s each has four possibilities of ou, od, eu, and ed. As in the isotropic case, the integrations over vertical space z_2 and z_2^o are readily carried out and the integration over β_z is performed with the residue theorem in the contour integration method. From Appendix D, the result for $\mathcal{I}_{2jklm}^{pqrs}$ is

$$\mathcal{I}_{2jklm}^{pqrs}=i\frac{2\delta_{2jklm}\ell_{2\rho'}^2\ell_{2z'}}{\pi\mathcal{L}_2^4}\left[\frac{e^{-i(\kappa_{pq}-\kappa_{rs})d_2}}{(\kappa_{pq}-\kappa_2)^2(\kappa_{pq}-\kappa_2^*)^2(\kappa_{pq}-\kappa_{rs})} + \frac{e^{i(\kappa_{rs}-\kappa_{pq})d_1}}{(\kappa_{rs}-\kappa_2)^2(\kappa_{rs}-\kappa_2^*)^2(\kappa_{rs}-\kappa_{pq})}-\mathcal{P}_2(\kappa_2)-\mathcal{Q}_2(\kappa_2^*)\right] \tag{88a}$$

in which the square of length $\mathcal{L}_2$ is $\mathcal{L}_2^2=\ell_{2\rho'}^2\sin^2\psi+\ell_{2z'}^2\cos^2\psi$, pole κ_2 is $\kappa_2=\mathcal{L}_2^{-2}\left[-k_{yi}(\ell_{2z'}^2-\ell_{2\rho'}^2)\sin(2\psi)+i\sqrt{(1+4k_{zi}^2\ell_{2\rho'}^2)\mathcal{L}_2^2+4k_{yi}^2\ell_{2\rho'}^2\ell_{2z'}^2}\right]$, and quantities $\mathcal{P}_2(\kappa_2)$ and $\mathcal{Q}_2(\kappa_2^*)$ are determined as follows

$$\mathcal{P}_2(\kappa_2)=\frac{i(d_2-d_1)e^{-i(\kappa_2-\kappa_{rs})d_1}e^{i(\kappa_2-\kappa_{pq})d_2}}{(2i\mathrm{Im}\kappa_2)^2(\kappa_2-\kappa_{pq})(\kappa_2-\kappa_{rs})} + \left[\frac{e^{-i(\kappa_{pq}-\kappa_{rs})d_1}+e^{-i(\kappa_{pq}-\kappa_{rs})d_2}}{(2i\mathrm{Im}\kappa_2)^2(\kappa_2-\kappa_{pq})(\kappa_2-\kappa_{rs})} - \frac{e^{-i(\kappa_2-\kappa_{rs})d_1}e^{i(\kappa_2-\kappa_{pq})d_2}}{(2i\mathrm{Im}\kappa_2)^2(\kappa_2-\kappa_{pq})(\kappa_2-\kappa_{rs})}\right] \cdot \left[\frac{1}{i\mathrm{Im}\kappa_2}+\frac{1}{\kappa_2-\kappa_{pq}}+\frac{1}{\kappa_2-\kappa_{rs}}\right] \tag{88b}$$

$$\mathcal{Q}_2(\kappa_2^*)=\frac{i(d_2-d_1)e^{i(\kappa_2^*-\kappa_{pq})d_1}e^{-i(\kappa_2^*-\kappa_{rs})d_2}}{(2i\mathrm{Im}\kappa_2^*)^2(\kappa_2^*-\kappa_{pq})(\kappa_2^*-\kappa_{rs})} + \frac{e^{i(\kappa_2^*-\kappa_{pq})d_1}e^{-i(\kappa_2^*-\kappa_{rs})d_2}}{(2i\mathrm{Im}\kappa_2^*)^2(\kappa_2^*-\kappa_{pq})(\kappa_2^*-\kappa_{rs})} \cdot \left[\frac{1}{i\mathrm{Im}\kappa_2^*}+\frac{1}{\kappa_2^*-\kappa_{pq}}+\frac{1}{\kappa_2^*-\kappa_{rs}}\right] \tag{88c}$$

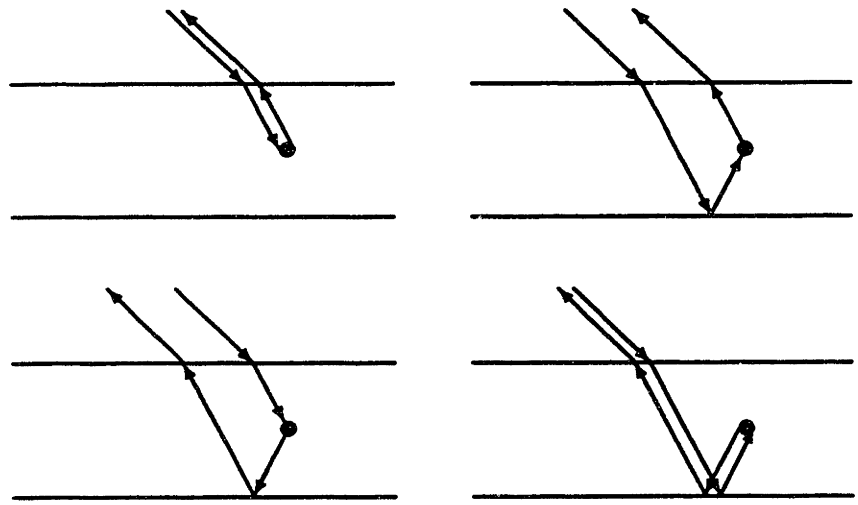

Figure 2.5.1 Wave scattering processes

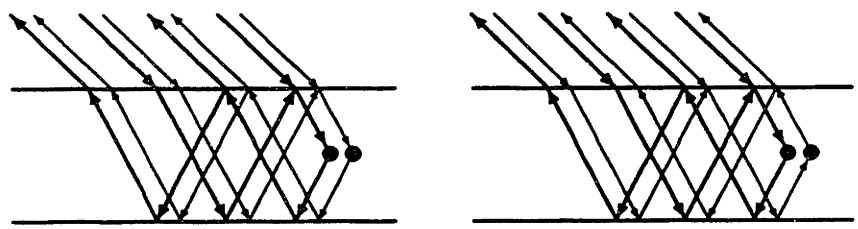

a Same directions b Opposite directions

Figure 2.5.2 Correlations of waves multiply interacting with the boundaries. Thin arrows represent complex conjugates of thick-arrow terms

The polarimetric backscattering coefficients are now obtained by applying results (87) and (88) to (84) and then making use of definition (13, Chapter 1). From the observation on the forms of the DGF and mean field coefficients, the scattering coefficients can be expressed conveniently as

$$\sigma_{\mu\tau\nu\kappa} = \pi k_0^4 \sum_{a,b,c,d}^{-1,1} \Psi_{1\mu\tau}^{ab} \Psi_{1\nu\kappa}^{cd*} \mathcal{I}_1^{abcd} + \pi k_0^4 \sum_{p,q,r,s}^{ou,od} \sum_{j,k,l,m}^{eu,ed} \sum_{}^{a,y,s} \Psi_{2\mu\tau,jk}^{pq} \Psi_{2\nu\kappa,lm}^{rs*} \mathcal{I}_{2jklm}^{pqrs} \tag{89}$$

where all coefficient Ψ's are given in Appendix B and C. The scattering coefficients

obtained in (89) is for the scattered field expressed in the scattered basis. To change to the incident basis, simply take the negative of $\sigma_{hvs\kappa}$ and $\sigma_{vvh\kappa}$. As calculated, the scattering coefficients are composed of 16 terms from the isotropic random medium and 256 terms from the anisotropic random medium. For the isotropic random medium, a scattered field can be an upgoing or a downgoing wave which is excited by an upgoing or a downgoing mean field as depicted in Figure 2.5.1. Therefore, there are 4 possibilities for the total scattered field and its correlation thus consists of 16 terms. For the anisotropic random medium, a scattered field can be an upgoing or a downgoing wave excited by an upgoing or a downgoing mean field and each wave type can be ordinary or extraordinary. Therefore, there are 16 possibilities for the total scattered field and thus its correlation consists of 256 terms. Furthermore, all multiple interactions between the waves and the boundaries are accounted for and all correlations of waves with same and different propagation directions are included. For instances, Figure 2.5.2a represents a correlation of waves multiply interacting with the boundaries and propagating in the same directions and Figure 2.5.2b illustrates a correlation of waves propagating in opposite directions.

In this section, the random medium model is formulated and the polarimetric backscattering coefficients are obtained under the distorted Born approximation with the strong permittivity fluctuation theory. In the next section, the model is applied to study the polarimetric backscattering properties from layer random media. Consideration is also given to the polarization signatures of the media and their relations to the corresponding covariance matrices are explained.

2.6 Results and Discussion

a. Two-layer Configuration

For geophysical media with a two-layer configuration, the three-layer model is ap-

plied with the top scattering layer removed by setting its thickness and variances to zero. The reduced model is used to investigate the polarimetric backscattering directly from an uncovered anisotropic random medium such as sea ice. Consider an electromagnetic wave at 9 GHz incident on a random medium composed of an ice background with permittivity $\epsilon_{2b} = (3.15 + i0.002)\epsilon_0$ and a 3.0%-volume fraction of vertically oriented ($\psi = 0$) brine inclusions with permittivity $\epsilon_{2s} = (38 + i41)\epsilon_0$ and correlation length $\ell_{2\rho'} = 0.5$ mm and $\ell_{2z'} = 1.5$ mm for which the strong fluctuation theory (SFT) gives the variances of $\delta_{2\rho'} = 1.48$, $\delta_{2z'} = 14.9$, and $\delta_{2c'} = 4.57 - i1.08$ and the uniaxial effective permittivity tensor with $\epsilon_{2\rho'} = (3.37 + i0.034)\epsilon_0$ and $\epsilon_{2z'} = (3.85 + i0.374)\epsilon_0$ as shown in Figure 2.6.1. The thickness of the random medium is 1.7 m and the permittivity of the underlying sea water is $\epsilon_3 = (45.0 + i40.0)\epsilon_0$. To point out the anisotropy effect on the polarimetric backscattering, a comparison is made with an isotropic random medium with the same parameters except $\ell_{2\rho'} = \ell_{2z'} = 0.5$ mm for which the SFT yields $\delta_{2\rho'} = \delta_{2z'} = \delta_{2c'} = 2.53$ and $\epsilon_{2r'} = \epsilon_{2z'} = (3.43 + i0.047)\epsilon_0$. For both the untilted anisotropic and the isotropic random media, cross term σ_{hv}, σ_{hhhv}, and σ_{hvvv} are zero under the first-order distorted Born approximation rendering the covariance matrix of the form

$$\overline{\overline{C}} = \begin{bmatrix} \sigma_{hh} & 0 & \sigma_{hhvv} \\ 0 & 0 & 0 \\ \sigma^*_{hhvv} & 0 & \sigma_{vv} \end{bmatrix} \quad \text{or} \quad \overline{\overline{C}} = \sigma \begin{bmatrix} 1 & 0 & \rho\sqrt{\gamma} \\ 0 & 0 & 0 \\ \rho^*\sqrt{\gamma} & 0 & \gamma \end{bmatrix} \tag{90}$$

Conventional backscattering coefficient σ_{hh} and σ_{vv} are plotted as a function of incident angle in Figure 2.6.2 for the two-layer untilted anisotropic (a) and the isotropic (b) cases. As observed from Figure 2.6.2, σ_{vv} crosses over σ_{hh} for the anisotropic case whereas, for the isotropic case, σ_{vv} is higher than σ_{hh} over the range of incident angles under consideration. The distinction of the conventional backscattering coefficients, σ_{vv} and σ_{hh}, associated with the two different random media is, however, not as obvious as that of the polarimetric correlation coefficient ρ as indicated in Figure 2.6.3 where the untilted anisotropic random medium manifests

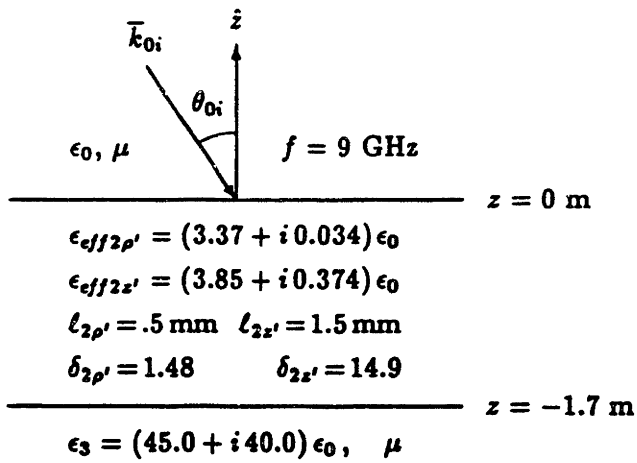

Figure 2.6.1 Parameters for the two-layer configuration

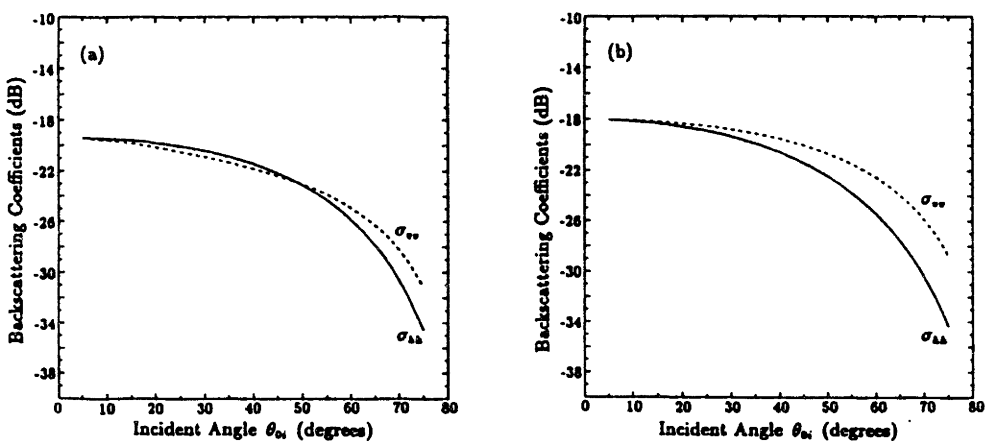

Figure 2.6.2 Conventional backscattering coefficients: (a) untilted anisotropic random medium, (b) isotropic random medium

its characteristics in ρ with magnitude and phase inversely related to the incident angle while the isotropic random medium ρ simply has the value of approximately 1.0 over the range of incident angles. These results can be explained based on the physical characteristics of the random media. In the anisotropic random medium, the effective complex wave vectors of the ordinary and the extraordinary waves are different; therefore, the h-polarized wave corresponding to the ordinary wave and the v-polarized wave corresponding to the extraordinary wave have different propagation velocities and attenuation rates which result in the separation of the scattering centers

of the two wave types. At normal incident angle, there is no distinction between the h and the v waves for the untilted random medium, the two waves are correlated, and thus the correlation coefficient ρ has the value of unity. As the incident angle is increased, the two waves become increasingly distinctive and less correlated; thus, the correlation coefficient takes on a complex value with decreased magnitude and phase. For the isotropic random medium, the distinction between the h and the v waves is only due to the boundary effect and the good correlation of two wave types leads to the correlation coefficient of value close to unity.

To illustrate the effect of the scatterers tilted in a preferred alignment direction, consider now the anisotropic random medium as described in the previous example but with non-zero tilt angle. For instance, let $\psi = 10°, 20°$ and $\phi_{0i} = 0°$. In this case, the correlation coefficient ρ also contains information about the tilting as shown in Figure 2.6.3. It is observed that the maximum magnitude of ρ is at normal incidence in the untilted case and moves to a larger incident angle as the tilted angle becomes larger. Also, the phase of ρ does not change sign for the case of $\psi = 0°$ whereas, in the tilted cases, the phase of ρ changes sign at the incident angle where the magnitude of ρ is maximum. Furthermore, it should be noted that the tilting results in non-zero cross terms and the corresponding covariance matrix become fully populated. As shown in this subsection, the covariance matrix describes the fully polarimetric scattering property of the remotely sensed media and thus can be used for the identification and the classification of terrain types.

b. Three-layer Configuration

To identify the effect of the covering top layer on the backscattering from the lower layer, the components of covariance matrices are compared between a two-layer configuration such as the bare sea ice in subsection 2.6a and a three-layer configuration such as the sea ice with snow cover. In Figure 2.6.4, the covering dry-snow layer is a low-loss isotropic random medium of thickness $d_1 = 0.1$ m composed of an air

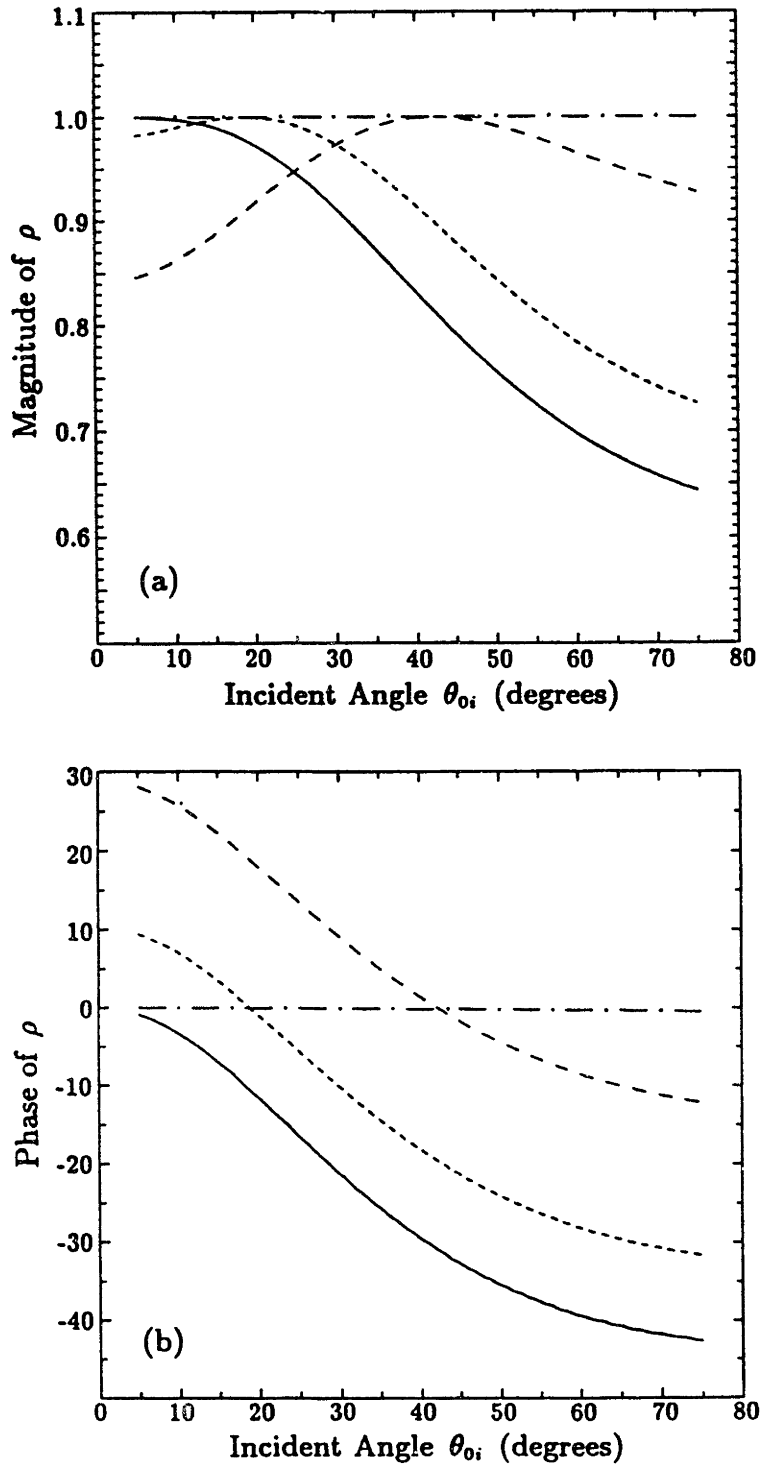

Figure 2.6.3 Correlation coefficients ρ : (a) magnitude, (b) phase. Dash-dot curves are for the isotropic, continuous for the untilted, short-dash for the 10°-tilted, and long-dash for the 20°-tilted random media

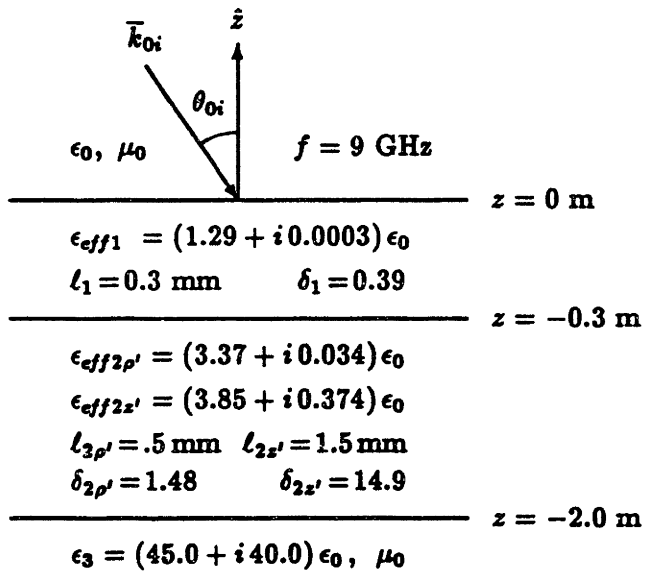

Figure 2.6.4 Parameters for the three-layer configuration

background with permittivity $\epsilon_{1b} = \epsilon_0$ and a 20%-volume fraction of ice particles with permittivity $\epsilon_{1s} = (3.15 + i0.002)\epsilon_0$ and correlation length $\ell_1 = 0.3$ mm for which the SFT gives the variance of $\delta_1 = 0.39$ and the isotropic effective permittivity of $\epsilon_{eff1} = (1.29 + i0.0003)\epsilon_0$; the middle and the underlying regions are, respectively, the sea ice with vertical brine inclusion over the sea water with the same physical parameters as in the two-layer configuration.

Displayed in Figure 2.6.5 are the plots of σ_{hh} and σ_{vv} as a function of incident angle for the two-layer and the three-layer configurations. The comparison shows that both σ_{hh} and σ_{vv} are enhanced due to the effect of the dry-snow cover whose ice particles introduce more backscattering. Moreover, the boundary effect is recognized in form of the oscillations on σ_{hh} and σ_{vv}. The oscillations can also be seen clearly on the phase of the correlation coefficient ρ in Figure 2.6.6b. As compared to the two-layer case, the absolute value of the phase of ρ for the three layer is smaller over the range of incident angle. Physically, this is due to the isotropic covering layer, which characteristically exhibits its isotropy in ρ with a small phase, partially

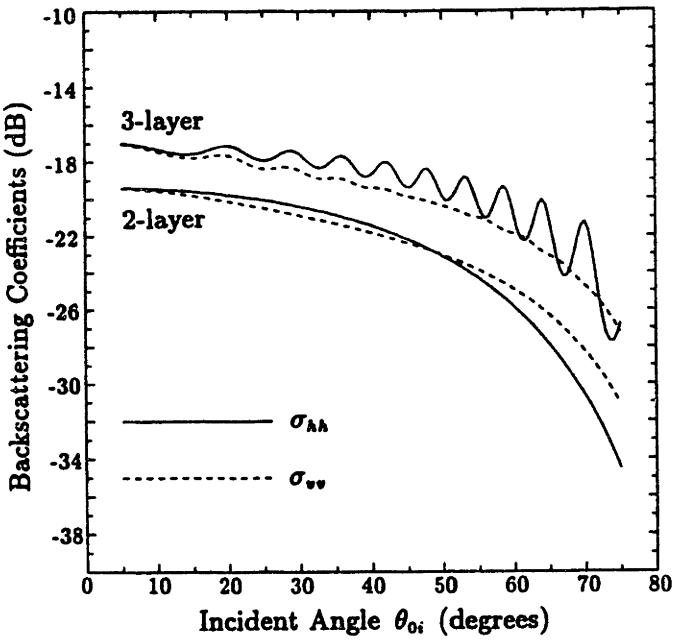

Figure 2.6.5 Conventional backscattering coefficients for the two-layer and three-layer configurations

masks the scattering effect of the lower anisotropic random medium. The magnitude of ρ, however, exhibits very weak oscillations while clearly retaining the almost same characteristics as observed directly from the two-layer configuration as seen in Figure 2.6.6b. Thus, the correlation coefficient ρ can carry information from both the covering low-loss isotropic layer and the lower tilted anisotropic layer in a rather distinctive manner. If the top layer is more lossy, both σ_{hh} and σ_{vv} can be diminished and the boundary-effect oscillations can be depressed. As illustrated, the three-layer model can account for the effect of the top scattering layer covering a geophysical medium whose characteristics can be recognized from the polarimetric covariance matrix.

c. Polarization Signatures

For given polarizations of the transmitter and the receiver, (11) can be used to synthesize the scattering coefficient which is similar to the polarization signature defined in [80]. When orientation angle $\alpha_i = \alpha_r = \alpha_c$ and $\beta_i = \beta_r = \beta_c$, the

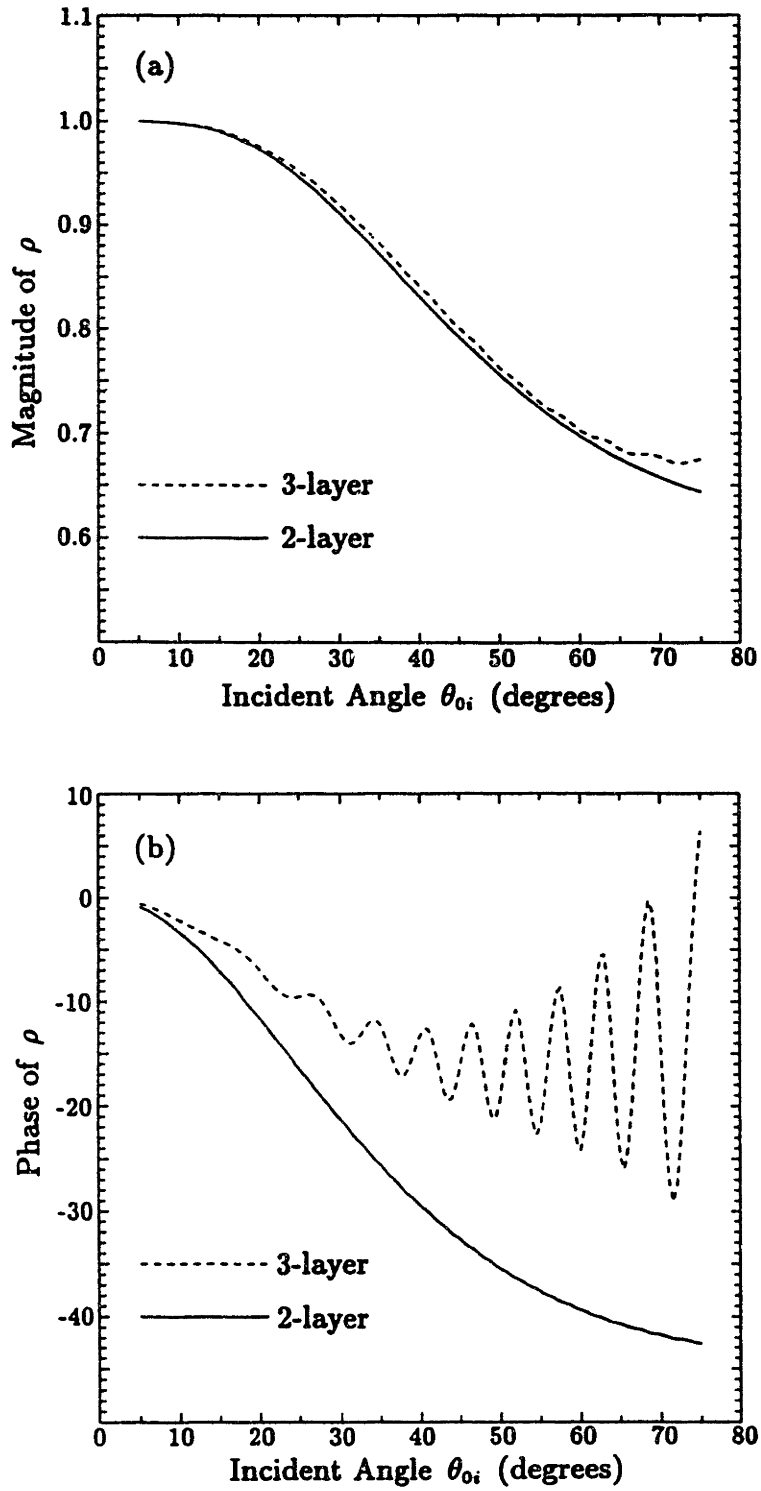

Figure 2.6.6 Correlation coefficients ρ: (a) magnitude, (b) phase. Continuous curves are for the two-layer and dash curves are for the three-layer configurations

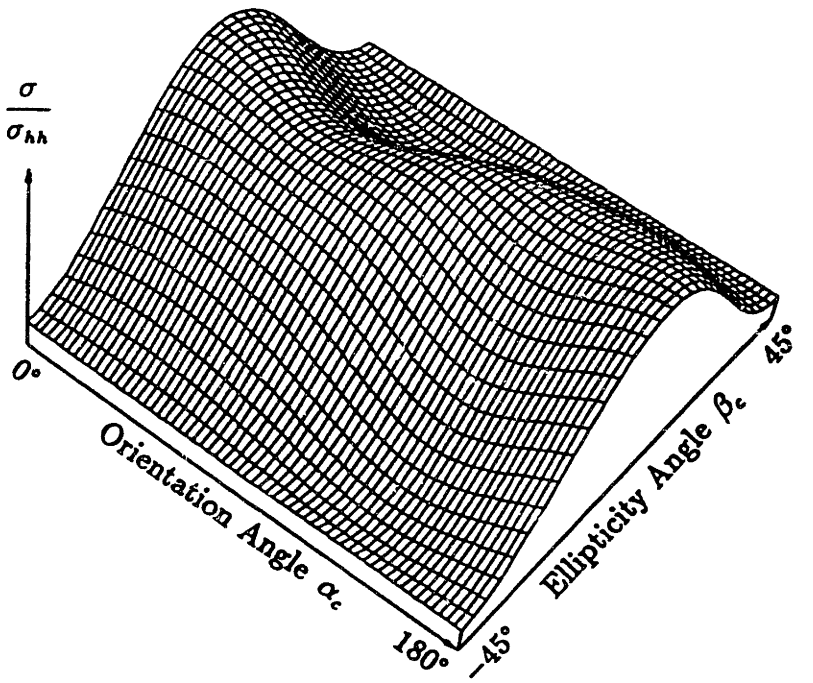

Figure 2.6.7 Copolarized signature normalized to σ_{hh} for the two-layer configuration at $\theta_{0i} = 40°$

copolarized signature can be displayed with a three-dimensional plot with the vertical axis for the normalized signature and the horizontal plane for α_c and β_c. In this subsection, the copolarized signature is shown for the bare sea ice and compared with that of the snow-covered sea ice. The forms of the displayed signatures and their relations to the corresponding covariance matrices will be explained.

Consider the 9-GHz wave incident at $\theta_{0i} = 40°$ on the sea ice with vertical brine inclusions. The corresponding covariance matrix is

$$\overline{\overline{C}} = 7.12 \times 10^{-3} \begin{bmatrix} 1 & 0 & (0.83\ \angle -29.5°)\sqrt{\gamma} \\ 0 & 0 & 0 \\ (0.83\ \angle +29.5°)\sqrt{\gamma} & 0 & \gamma = 0.915 \end{bmatrix} \tag{91}$$

The copolarized signature is shown in Figure 2.6.7 where the variation is seen in both α_c and β_c. To illustrate the variation in α_c, the copolarized signature normalized to σ_{hh} for linear polarization is plotted in Figure 2.6.8 where the normalized signature

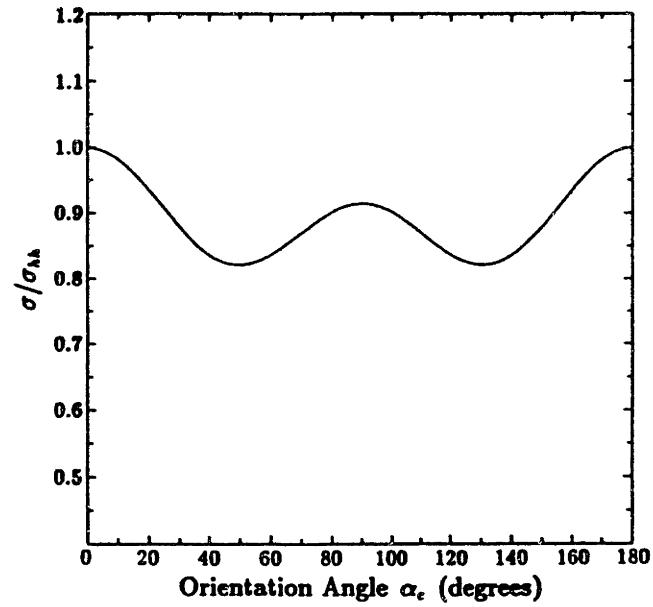

Figure 2.6.8 Linearly copolarized signature normalized to σ_{hh} for the two-layer configuration at $\theta_{0i} = 40°$

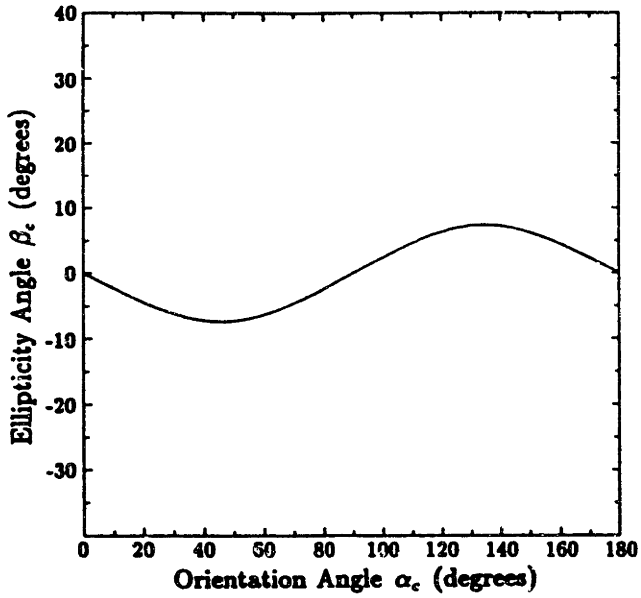

Figure 2.6.9 Signature distortion track of the two-layer configuration

at $\alpha = 90°$ has the value of 0.915 which is the ratio $\gamma = \sigma_{vv}/\sigma_{hh}$ in covariance matrix (91) and the undulation also depends on the correlation coefficient ρ. For the variation in β_e, the signature at a fixed value of α_e increases to a maximum

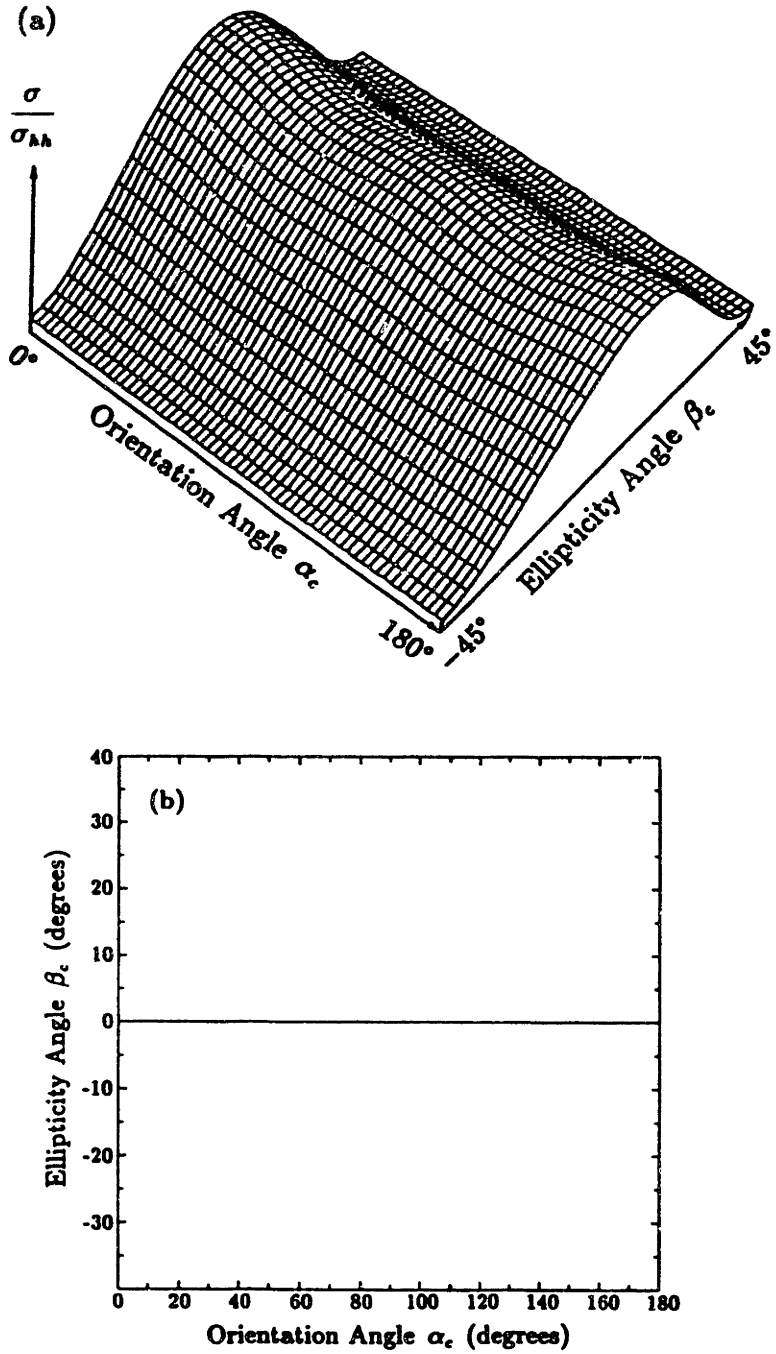

Figure 2.6.10 For the covariance matrix (91) with the phase of ρ set to zero: (a) Copolarized signature normalized to σ_{hh}, (b) Signature distortion track

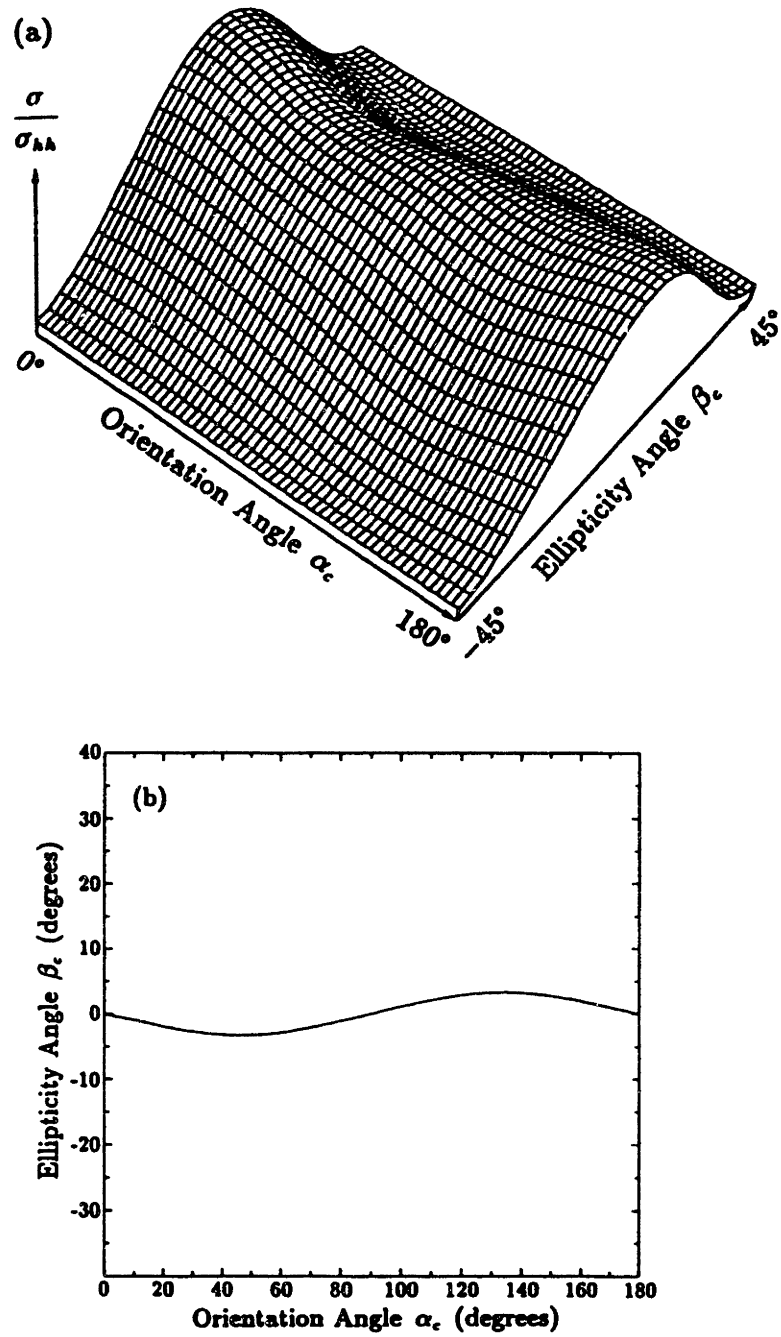

Figure 2.6.11 For the three-layer configuration: (a) Copolarized signature normalized to σ_{hh}, (b) Signature distortion track

and then decreases. The variation over the polarization plane (α_c, β_c) makes the signature look like being distorted. To describe this distortion, a "signature distortion track" is defined as the plot of β_c at which the signature is maximum as a function of α_c such that $\partial\sigma(\alpha_c, \beta_c)/\partial\beta_c = 0$. This plot tracks the locations of the local maxima of the copolarized signature over the polarization plane. The result of the signature distortion track for the bare sea ice is shown in Figure 2.6.9 which indicates that a maximum copolarized scattering coefficient can be obtained with an h $(\alpha_c = 0°, 180°)$ or v $(\alpha_c = 90°)$ polarization and with an elliptical polarization for other orientation angles. To explain the cause of the distortion, the phase of ρ in the covariance matrix (91) is artificially set to zero which consequently gives the signature in Figure 2.6.10a where the distortion disappears as seen in Figure 2.6.10b. Thus, the distortion is due to the non-zero phase of ρ which can come from the anisotropy of the random medium as discussed in subsection 2.6a. Furthermore, the distortion track is symmetric about the v polarization $(\alpha = 90°, \beta = 0°)$ due to the azimuthal symmetry of the untilted anisotropic random medium. Consider an azimuthally symmetric random medium whose polarimetric backscattering properties are characterized with a covariance matrix of the form [83]

$$\overline{\overline{C}} = \sigma_{hh} \begin{bmatrix} 1 & 0 & \rho\sqrt{\gamma} \\ 0 & e & 0 \\ \rho^*\sqrt{\gamma} & 0 & \gamma \end{bmatrix} \tag{92}$$

which is more general than (90). In this case, the distortion track equation is

$$\begin{aligned} \partial\sigma/\partial\beta_c = \sigma_{hh} \sin 2\beta_c \left[(\gamma - 1)\cos 2\alpha_c - (\gamma + 1 - 4e)\cos^2 2\alpha_c \cos 2\beta_c \right. \\ \left. - 2\sqrt{\gamma}\mathrm{Re}\rho \cos 2\beta_c (1 + \sin^2 2\alpha_c)\right] + 2\sigma_{hh}\sqrt{\gamma}\mathrm{Im}\rho \sin 2\alpha_c \cos 4\beta_c = 0 \end{aligned} \tag{93}$$

from which the properties of the signature distortion track can be deduced. If $\mathrm{Im}(\rho) = 0$, (93) has solution $\beta_c = 0$ for any given orientation angle α_c and the track is just the straight line at β_c of zero value signifying the disappearance of

the distortion. Also, the invariance of (93) under the change of α_c and β_c respectively to $(180° - \alpha_c)$ and $-\beta_c$ implies the symmetry about the v polarization $(\alpha_c = 90°, \beta_c = 0°)$. When $e = 0$ as in (90), these track properties still remain.

The pedestal is also observed in Figure 2.6.6. To explain the existence of the pedestal, the pedestal height is calculated from (11, Chapter 1) by setting $\beta_c = \pm 45°$ (circular polarizations) for the case of (92)

$$\sigma(\beta_c = \pm 45°)/\sigma_{hh} = e + \frac{1}{4}[(\gamma + 1) - 2\sqrt{\gamma}\mathrm{Re}\rho] \tag{94}$$

Obviously from (94), the pedestal height is composed of two terms: the first term e can come from the depolarization due to multiple scattering [83] and the second term can come from the anisotropy of the random medium. For the untilted anisotropic random medium under consideration, the pedestal height is therefore non-zero even thought the cross term e is not accounted for. In this case, the pedestal is due to the anisotropy and the boundary effects.

For the snow covered sea ice with the three-layer configuration in Figure 2.6.4, the covariance matrix at the incident angle of $\theta_{0i} = 40°$ is

$$\overline{\overline{C}} = 1.34 \times 10^{-2} \begin{bmatrix} 1 & 0 & (0.84\ \angle -13.2°)\sqrt{\gamma} \\ 0 & 0 & 0 \\ (0.84\ \angle +13.2°)\sqrt{\gamma} & 0 & \gamma = 0.85 \end{bmatrix} \tag{95}$$

The corresponding copolarized signature and the signature distortion track are displayed in Figure 2.6.11. Compared to the two-layer case, the three-layer signature is less distorted and the pedestal height is lower. This is due to the masking effect of the isotropic covering layer which renders the anisotropic characteristics of the lower scattering layer less pronounced.

Polarization signatures of random media with two and three layers have been shown in this subsection. The forms of the copolarized signatures and the pedestal heights are explained with the components of the covariance matrices from which the polarimetric scattering properties are readily recognized.

2.7 Summary

In this chapter, the fully polarimetric backscattering coefficients have been obtained from the layer model with spheroidal scatterers. The top layer is modelled as an isotropic random medium, the middle layer as an anisotropic random medium, and the underlying layer as a homogeneous medium. The strong fluctuation theory is used to calculated the effective permittivities of the scattering layers and the distorted Born approximation is applied to derive the scattered fields. The dyadic Green's functions are used in the calculations and the backscattering processes are explained. The model can be applied to the remote sensing of both bare and covered geophysical media as illustrated for the case of bare and snow covered sea ice. The physical information conveyed in the elements of the covariance matrices are discussed especially for the correlation coefficient ρ. The copolarization signatures for the layer random media are obtained with the Mueller matrices and explained with the scattering coefficients contained in the covariance matrices. Since the fully polarimetric scattering coefficients convey more information about the remotely sensed media as compared to the conventional scattering coefficients, the polarimetry provides a better means for the identification and classification of the geophysical media.

Chapter 3
Model with Random Spheroidal Scatterers

3.1 Introduction

In this chapter, the layer configuration with scattering regions containing randomly oriented spheroidal scatterers is considered. The scatterers are modeled with a spheroidal correlation function with random orientation described by a probability density function of the Eulerian rotation angles. The extended strong permittivity fluctuation theory [58] is used to calculate the effective permittivity and the distorted Born approximation is applied to obtain the polarimetric scattering coefficients. The model accounts for multiple interactions due to medium interfaces, coherent effects of wave propagation, and first-order cross-polarized returns.

The chapter is organized into six sections. Section 3.2 presents the derivation of the effective permittivity with the extended strong fluctuation theory for an inhomogeneous medium with embedded spheroidal scatterers having random orientation. Section 3.3 shows the calculation of the polarimetric scattering coefficients, under the distorted Born approximation, from the scattering regions in the layer configuration. Section 3.4 discusses the results for soybean monitored temporally from early to fully grown until late stages. Section 3.5 assesses the use of scattering coefficients for inversion of vegetation biomass and soil moisture. In the polarimetry aspect, physical insight provided by the theoretical model is used to explain the behavior

of the covariance matrices and the corresponding polarization signatures calculated with Mueller matrix. Finally, section 3.6 summarizes this chapter.

3.2 Effective Permittivity

In Chapter 2, spheroidal scatterers in the random medium have a preferred alignment described by a global correlation function with a fixed axial direction. For an inhomogeneous medium such as a vegetation canopy, the leaves, for example, can be oriented in a random manner. In this case, a correlation function corresponding locally to a scatterer is used in the derivation of the effective permittivity with the strong permittivity fluctuation theory extended to account for the random orientation of the scatterers. When the average process is performed over all orientation angles, the effective permittivity is isotropic as expected from the geometry of the random orientation.

Consider an inhomogeneous medium composed of a host medium with permittivity ϵ_b and embedded spheroidal scatterers with permittivity ϵ_s and total fractional volume f_s. By introducing auxiliary permittivity $\bar{\bar{\epsilon}}_g$ into the wave equation, dyadic Green's function $\overline{\overline{G}}_g(\bar{r},\bar{r}')$ satisfies the inhomogeneous differential equation of the form (5, Chapter 2) where the subscript m for the layer number is dropped. The singularity is accounted for by decomposing $\overline{\overline{G}}_g(\bar{r},\bar{r}') = \overline{\overline{G}}_g(\bar{r}-\bar{r}')$ into a principal value part and a Dirac delta part with dyadic coefficient $\overline{\overline{S}}$ the as in (8, Chapter 2). The effective permittivity of the random medium is composed of a quasi-static part and a scattering-effect part which accounts for the modification in the wave speed and attenuation [17,58]

$$\bar{\bar{\epsilon}}_{eff} = \bar{\bar{\epsilon}}_g + \epsilon_0\left[\overline{\overline{I}} - \bar{\bar{\xi}}_{eff}\cdot\left\langle\overline{\overline{S}}\right\rangle\right]^{-1}\cdot\bar{\bar{\xi}}_{eff} \tag{1}$$

where auxiliary permittivity $\bar{\bar{\epsilon}}_g$ and dyadic coefficient $\overline{\overline{S}}$ are determined by the condition of secular-term elimination, and the effective dyadic scatterer $\bar{\bar{\xi}}_{eff}$ under

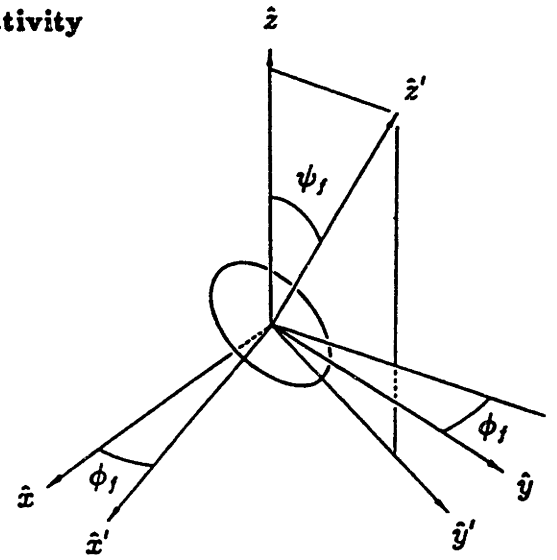

Figure 3.2.1 Geometry of a spheroidal scatterer

the low-frequency approximation is given by

$$\left[\overline{\overline{\xi}}_{eff}\right]_{jm} = \int_0^{\pi} d\psi_f \int_0^{2\pi} d\phi_f p(\psi_f, \phi_f) \sum_{k,l}^{x,y,z} \Gamma^{(0)}_{\ell jklm} \left\{ k_0^2 \int_{-\infty}^{\infty} d\overline{k}' \left[\overline{\overline{G}}_s(\overline{k}')\right]_{kl} \Phi_\ell(\overline{k}') + \left[\overline{\overline{S}}\right]_{kl} \right\} \Big|_{\psi_f, \phi_f} \tag{2}$$

in which $\Gamma^{(0)}_{\ell jklm}$ is the variance, $\overline{\overline{G}}_s$ is the isotropic Green's function (16, Chapter 2), Φ_ℓ is the Fourier transform of the normalized local correlation function, and $p(\psi_f, \phi_f)$ is the probability density function of Eulerian orientation angle ψ_f and ϕ_f illustrated in Figure 3.2.1. The effective permittivity as obtained is approximated by truncating the series in the renormalization method. The validity condition for the approximation is $\left|\left[\overline{\overline{\xi}}_{eff}\right]\right|_{jm} \ll 1$.

The spheroidal scatterer is described with a normalized local correlation function of the form

$$R_\ell(\overline{r}') = \exp\left(-\sqrt{\frac{x'^2 + y'^2}{\ell_{\rho'}^2} + \frac{z'^2}{\ell_{z'}^2}}\right) \tag{3}$$

with correlation length $\ell_{\rho'}$ and $\ell_{z'}$ in the local coordinates corresponding to the principal axes of the scatterer. The correlation lengths are related to the physical geometry of the scatterer and can be estimated from the size and the shape of the scatterer as shown in [58] for small scatterer and low fractional volume. This local correlation function can be used to describe a scatterer with needle-like or disc-like

shape. The Fourier transform Φ_ξ of (3) is the same as (39b, Chapter 2). For randomly oriented scatterers with no preferred direction, the probability density function of orientation is

$$p(\psi_f, \phi_f) = \sin\psi_f/(4\pi) \tag{4}$$

The derivation of the effective permittivity is similar to the procedure in Chapter 2 and the integrations over the Eulerian angles are straight forward [58]. Followed is the result showing how the effective permittivity is calculated. First, $\overline{\overline{\epsilon}}_g = \epsilon_g \overline{\overline{I}}$ and $\overline{\overline{S}} = diag(S_{\rho'}, S_{\rho'}, S_{z'})$ are obtained by iterating

$$f_s\left[2\xi_{\rho'}(\epsilon_s) + \xi_{z'}(\epsilon_s)\right] + (1 - f_s)\left[2\xi_{\rho'}(\epsilon_b) + \xi_{z'}(\epsilon_b)\right] = 0 \tag{5a}$$

$$S_{\rho'} = \frac{\epsilon_0}{2\epsilon_g a\sqrt{a}}\left[(1+a)\tan^{-1}\sqrt{a} - \sqrt{a}\right] \tag{5b}$$

$$S_{z'} = \frac{\epsilon_0(1+a)}{\epsilon_g a\sqrt{a}}\left[\sqrt{a} - \tan^{-1}\sqrt{a}\right] \tag{5c}$$

where the quantities $\xi_{\rho'}(\epsilon)$, $\xi_{z'}(\epsilon)$, and a are respectively defined as

$$\xi_{\rho'}(\epsilon) = \frac{\epsilon - \epsilon_g}{\epsilon_0 + S_{\rho'}(\epsilon - \epsilon_g)} \tag{6a}$$

$$\xi_{z'}(\epsilon) = \frac{\epsilon - \epsilon_g}{\epsilon_0 + S_{z'}(\epsilon - \epsilon_g)} \tag{6b}$$

$$a = \gamma^2 - 1 \quad \text{with} \quad \gamma = \frac{\ell_{\rho'}}{\ell_{z'}} \tag{6c}$$

the averaged dyadic coefficient $\left\langle \overline{\overline{S}} \right\rangle$ is then calculated from (6a) and (6b)

$$\left\langle \overline{\overline{S}} \right\rangle = \left(\frac{2}{3}S_{\rho'} + \frac{1}{3}S_{z'}\right)\overline{\overline{I}} = \frac{\epsilon_0}{3\epsilon_g}\overline{\overline{I}} \tag{7}$$

and finally the effective scatterer is determined by

$$\begin{aligned}\overline{\overline{\xi}}_{eff} = {} & f_s\left[\frac{2}{3}\xi^2_{\rho'}(\epsilon_s)\left(I_{\rho'} + S_{\rho'}\right) + \frac{1}{3}\xi^2_{z'}(\epsilon_s)\left(I_{z'} + S_{z'}\right)\right]\overline{\overline{I}} \\ & + (1 - f_s)\left[\frac{2}{3}\xi^2_{\rho'}(\epsilon_b)\left(I_{\rho'} + S_{\rho'}\right) + \frac{1}{3}\xi^2_{z'}(\epsilon_b)\left(I_{z'} + S_{z'}\right)\right]\overline{\overline{I}}\end{aligned} \tag{8}$$

in which $I_{z'}$ comes from the integration of the product between the correlation function and the $z'z'$-element of the dyadic Green's function

$$I_{z'} = -\frac{2k_0^2}{k_g^2}(\mathcal{I}_e + \mathcal{I}_d) \tag{9a}$$

$$\mathcal{I}_e = -\frac{\gamma^3}{2a^2}\left[\frac{\sqrt{-\zeta}}{\vartheta_e} + \frac{\vartheta_e+\zeta}{\vartheta_e\sqrt{\vartheta_e}}\left(\frac{\pi}{2} - \tan^{-1}\frac{\sqrt{-\zeta}}{\sqrt{\vartheta_e}}\right)\right] \tag{9b}$$

$$\mathcal{I}_d = \frac{\gamma^2}{2a^2}\left[\frac{1+a\nu_{gz'}^2}{\vartheta_o} + \frac{\vartheta_o(a+2)-(b+a\nu_{gz}^2)}{\vartheta_o\sqrt{\vartheta_o}}\left(\frac{\pi}{2} - \tan^{-1}\frac{1}{\sqrt{\vartheta_o}}\right)\right] \tag{9c}$$

$$\nu_{gz'}^2 = k_g^2\ell_{z'}^2, \quad \zeta = \gamma^2\nu_{gz'}^2, \quad b = \frac{\gamma^2+\zeta}{a}, \quad \vartheta_o = b-1, \quad \vartheta_e = b+\zeta \tag{9d}$$

and $I_{\rho'}$ comes from the integration of the product between the correlation function and the $\rho'\rho'$-element of the dyadic Green's function

$$I_{\rho'} = 2k_0^2\ell_{\rho'}^2(\mathcal{I}_1^o - \mathcal{I}_2^o - \mathcal{I}_3^o) + \frac{k_0^2}{k_g^2}(\mathcal{I}_e + \mathcal{I}_d - \frac{1}{2}) \tag{10a}$$

$$\mathcal{I}_1^o = \frac{\gamma^3}{2a^2\vartheta_e}\left[-\frac{\sqrt{-\zeta}}{b} + \frac{1}{\sqrt{\vartheta_e}}\left(\frac{\pi}{2} - \tan^{-1}\frac{\sqrt{-\zeta}}{\sqrt{\vartheta_e}}\right)\right] \tag{10b}$$

$$\mathcal{I}_2^o = \frac{1}{2a\vartheta_o}\left[1 - \frac{1}{\sqrt{\vartheta_o}}\left(\frac{\pi}{2} - \tan^{-1}\frac{1}{\sqrt{\vartheta_o}}\right)\right] \tag{10c}$$

$$\mathcal{I}_3^o = \frac{\gamma^2}{2a^2\vartheta_o}\left[-\frac{1}{b} + \frac{1}{\sqrt{\vartheta_o}}\left(\frac{\pi}{2} - \tan^{-1}\frac{1}{\sqrt{\vartheta_o}}\right)\right] \tag{10d}$$

As seen from the above expressions, the effective permittivity $\bar{\bar{\epsilon}}_{eff} = \epsilon_{eff}\bar{\bar{I}}$ is isotropic. In the next section, the effective permittivity is used to obtain the complete set of polarimetric backscattering coefficients under the distorted Born approximation by using dyadic Green's function (DGF) of the layer configuration.

3.3 Scattering Coefficients

The same layer configuration in Chapter 2 is used here except that the scatterers in both regions 1 and 2 are spheroidal and allowed to be randomly oriented. The polarimetric backscattering coefficients are defined by (13, Chapter 1) based on ensemble

averages of scattered fields. The averages are calculated with spatial integrations over products of the DGFs, the mean fields, and the correlation functions as follows

$$\begin{aligned}\left\langle \overline{E}_{0s}(\overline{r}) \cdot \overline{E}^{*}_{0s}(\overline{r}) \right\rangle = & \sum_{i,j,k,l,m}^{x,y,z} k_0^4 \int_0^{\pi} d\psi_f \int_0^{2\pi} d\phi_f p(\psi_f, \phi_f) \int_{V_1} d\overline{r}_1 \int_{V_1} d\overline{r}_1^{\circ} C_{\xi 1jklm}(\overline{r}_1, \overline{r}_1^{\circ}; \psi_f, \phi_f) \\ & \cdot \left[\left\langle G_{01ij}(\overline{r}, \overline{r}_1) \right\rangle \left\langle F_{1k}(\overline{r}_1) \right\rangle \right] \cdot \left[\left\langle G_{01il}(\overline{r}, \overline{r}_1^{\circ}) \right\rangle \left\langle F_{1m}(\overline{r}_1^{\circ}) \right\rangle \right]^{*} \\ & + \sum_{i,j,k,l,m}^{x,y,z} k_0^4 \int_0^{\pi} d\psi_f \int_0^{2\pi} d\phi_f p(\psi_f, \phi_f) \int_{V_2} d\overline{r}_2 \int_{V_2} d\overline{r}_2^{\circ} C_{\xi 2jklm}(\overline{r}_2, \overline{r}_2^{\circ}; \psi_f, \phi_f) \\ & \cdot \left[\left\langle G_{02ij}(\overline{r}, \overline{r}_2) \right\rangle \left\langle F_{2k}(\overline{r}_2) \right\rangle \right] \cdot \left[\left\langle G_{02il}(\overline{r}, \overline{r}_2^{\circ}) \right\rangle \left\langle F_{2m}(\overline{r}_2^{\circ}) \right\rangle \right]^{*} \end{aligned} \tag{11}$$

The DGFs and the mean fields are given in Chapter 2; the correlation functions need to be determined next. The integrations are then carried out to derive the scattering coefficients.

The correlation functions C's in (11) are defined in the spatial domain with

$$C_{\xi njklm}(\overline{r}_n, \overline{r}_n^{\circ}, \psi_f, \phi_f) = \left\langle \xi_{njk}(\overline{r}_n) \xi^{*}_{nlm}(\overline{r}_n^{\circ}) \middle| \psi_f(\overline{r}_n), \phi_f(\overline{r}_n) \right\rangle , \quad n = 1, 2 \tag{12}$$

To facilitate the integration of (11), Fourier transforms of the correlation functions are introduced for the statistically homogeneous scattering media under consideration

$$C_{\xi njklm}(\overline{r}_n, \overline{r}_n^{\circ}; \psi_f, \phi_f) = \int_{-\infty}^{\infty} d\overline{\beta} \Phi_{njklm}(\overline{\beta}) e^{-i\overline{\beta} \cdot (\overline{r}_n - \overline{r}_n^{\circ})} , \quad n = 1, 2 \tag{13}$$

which is expressed in the global coordinate system $(\hat{x}, \hat{y}, \hat{z})$ and related by the Eulerian rotation transformation (ϕ_f, ψ_f) to those in the local coordinate system $(\hat{x}', \hat{y}', \hat{z}')$

$$\Phi_{n\rho'}(\overline{\beta}') = \Phi_{nx'x'x'x'}(\overline{\beta}') = \delta_{n\rho'} \Phi_{\xi n}(\overline{\beta}') \tag{14a}$$

$$\Phi_{nz'}(\overline{\beta}') = \Phi_{nx'x'z'z'}(\overline{\beta}') = \delta_{nz'} \Phi_{\xi n}(\overline{\beta}') \tag{14b}$$

$$\Phi_{nc'}(\overline{\beta}') = \Phi_{nx'x'z'x'}(\overline{\beta}') = \delta_{nc'} \Phi_{\xi n}(\overline{\beta}') \tag{14c}$$

where $\Phi_{\xi n}(\overline{\beta}')$ is the Fourier transform of (3) and the variance δ_n's in (14) are

$$\delta_{n\rho'} = \left| \frac{\epsilon_{bn} - \epsilon_{gn}}{\epsilon_0 + S_{n\rho'}(\epsilon_{bn} - \epsilon_{gn})} \right|^2 (1 - f_{sn}) + \left| \frac{\epsilon_{sn} - \epsilon_{gn}}{\epsilon_0 + S_{n\rho'}(\epsilon_{sn} - \epsilon_{gn})} \right|^2 f_{sn} \tag{15a}$$

$$\delta_{nz'} = \left|\frac{\epsilon_{bn}-\epsilon_{gn}}{\epsilon_0+S_{nz'}(\epsilon_{bn}-\epsilon_{gn})}\right|^2(1-f_{sn})+\left|\frac{\epsilon_{sn}-\epsilon_{gn}}{\epsilon_0+S_{nz'}(\epsilon_{sn}-\epsilon_{gn})}\right|^2 f_{sn} \tag{15b}$$

$$\begin{aligned}\delta_{nc'} = &\left[\frac{\epsilon_{bn}-\epsilon_{gn}}{\epsilon_0+S_{n\rho'}(\epsilon_{bn}-\epsilon_{gn})}\right]\left[\frac{\epsilon_{bn}-\epsilon_{gn}}{\epsilon_0+S_{nz'}(\epsilon_{bn}-\epsilon_{gn})}\right]^*(1-f_{sn})\\ &+\left[\frac{\epsilon_{sn}-\epsilon_{gn}}{\epsilon_0+S_{n\rho'}(\epsilon_{sn}-\epsilon_{gn})}\right]\left[\frac{\epsilon_{sn}-\epsilon_{gn}}{\epsilon_0+S_{nz'}(\epsilon_{sn}-\epsilon_{gn})}\right]^* f_{sn}\end{aligned} \tag{15c}$$

Due to the invariant property of the Fourier transform under the rotation transformation, spectral density $\Phi_{njklm}(\overline{\beta})$ in the global coordinates can functionally be related to those given in (14) with

$$\begin{aligned}\Phi_{\xi n}(\overline{\beta}) = \Phi_{\xi n}(&\beta'_x = \beta_x\cos\phi_f + \beta_y\sin\phi_f,\\ &\beta'_y = -\beta_x\sin\phi_f\cos\psi_f + \beta_y\cos\phi_f\cos\psi_f - \beta_z\sin\psi_f,\\ &\beta'_z = -\beta_x\sin\phi_f\sin\psi_f + \beta_y\cos\phi_f\sin\psi_f + \beta_z\cos\psi_f)\end{aligned} \tag{16}$$

In the global coordinates, the rotation transformation together with the above invariant property give the spectral densities of the form

$$\Phi_{njklm}(\overline{\beta}) = \delta_{njklm}\Phi_{\xi n}(\overline{\beta}) \tag{17}$$

where variance δ_{njklm} are dependent on angle ϕ_f and ψ_f as

$$\delta_{njklm} = \delta_{n\rho'}T_{\rho jk}T_{\rho lm} + \delta_{nc'}T_{\rho jk}T_{zlm} + \delta^*_{nc'}T_{zjk}T_{\rho lm} + \delta_{n\rho'}T_{zjk}T_{zlm} \tag{18}$$

in which matrix $\overline{\overline{T}}_\rho$ and $\overline{\overline{T}}_z$ are defined as follows

$$\overline{\overline{T}}_z = \overline{\overline{I}} - \overline{\overline{T}}_\rho \tag{19a}$$

$$\overline{\overline{T}}_\rho = \begin{bmatrix} \cos^2\phi_f + \sin^2\phi_f\cos^2\psi_f & \sin\phi_f\cos\phi_f\sin^2\psi_f & \sin\phi_f\sin\psi_f\cos\psi_f \\ \sin\phi_f\cos\phi_f\sin^2\psi_f & \sin^2\phi_f + \cos^2\phi_f\cos^2\psi_f & -\cos\phi_f\sin\psi_f\cos\psi_f \\ \sin\phi_f\sin\psi_f\cos\psi_f & -\cos\phi_f\sin\psi_f\cos\psi_f & \sin^2\psi_f \end{bmatrix} \tag{19b}$$

The correlation of the scattered field can now be found by substituting into (11) the dyadic Green's functions of the layer medium, the means fields, and the

correlation functions. From the observation on the forms of the DGF and mean field coefficients, the scattering coefficients can be expressed conveniently as

$$\sigma_{\mu\tau\nu\kappa} = \pi k_0^4 \int_0^{\pi} d\psi_f \int_0^{2\pi} d\phi_f p(\psi_f, \phi_f) \sum_{a,b,c,d}^{-1,1} \sum_{j,k,l,m}^{x,y,z} \Psi_{1\mu\tau,jk}^{ab} \Psi_{1\nu\kappa,lm}^{cd*} \mathcal{I}_{1jklm}^{abcd}$$
$$+ \pi k_0^4 \int_0^{\pi} d\psi_f \int_0^{2\pi} d\phi_f p(\psi_f, \phi_f) \sum_{p,q,r,s}^{d,u} \sum_{j,k,l,m}^{x,y,z} \Psi_{2\mu\tau,jk}^{pq} \Psi_{2\nu\kappa,lm}^{rs*} \mathcal{I}_{2jklm}^{pqrs} \tag{20}$$

Note that region 2 now becomes isotropic due to the random orientation of the scatterers. Thus, the ordinary and extraordinary waves degenerate into one characteristic wave either going down (d) or up (u) and the coefficients Ψ_2's are derived from those in Chapter 2 by letting $\epsilon_{eff2} = \epsilon_{eff2\rho'} = \epsilon_{eff2z'}$. For region 1, coefficient Ψ_2's are simply

$$\Psi_{1\mu\tau,jk}^{ab} = S_{1\mu,j}^{a} I_{1\tau,k}^{b} \tag{21}$$

in which coefficient vector $\overline{I}_{1\tau}^{b}$ from the mean field are given by

$$\overline{I}_{1h}^{-1} = D_{1hh}(\overline{k}_{\rho i})\hat{h}(k_{1zi}^{d}) + D_{1hv}(\overline{k}_{\rho i})\hat{v}(k_{1zi}^{d}) \tag{22a}$$

$$\overline{I}_{1h}^{+1} = U_{1hh}(\overline{k}_{\rho i})\hat{h}(k_{1zi}^{u}) + U_{1hv}(\overline{k}_{\rho i})\hat{v}(k_{1zi}^{u}) \tag{22b}$$

$$\overline{I}_{1v}^{-1} = D_{1vv}(\overline{k}_{\rho i})\hat{v}(k_{1zi}^{d}) + D_{1vh}(\overline{k}_{\rho i})\hat{h}(k_{1zi}^{d}) \tag{22c}$$

$$\overline{I}_{1v}^{+1} = U_{1vv}(\overline{k}_{\rho i})\hat{v}(k_{1zi}^{u}) + U_{1vh}(\overline{k}_{\rho i})\hat{h}(k_{1zi}^{u}) \tag{22d}$$

and coefficient vector $\overline{S}_{1\mu}^{a}$ from the Green's function are given by

$$\overline{S}_{1h}^{-1} = D_{1hh}(-\overline{k}_{\rho})\hat{h}(k_{1zi}^{u}) - D_{1hv}(-\overline{k}_{\rho})\hat{v}(k_{1zi}^{u}) \tag{23a}$$

$$\overline{S}_{1h}^{+1} = U_{1hh}(-\overline{k}_{\rho})\hat{h}(k_{1zi}^{d}) - U_{1hv}(-\overline{k}_{\rho})\hat{v}(k_{1zi}^{d}) \tag{23b}$$

$$\overline{S}_{1v}^{-1} = D_{1vv}(-\overline{k}_{\rho})\hat{v}(k_{1zi}^{u}) - D_{1vh}(-\overline{k}_{\rho})\hat{h}(k_{1zi}^{u}) \tag{23c}$$

$$\overline{S}_{1v}^{+1} = U_{1vv}(-\overline{k}_{\rho})\hat{v}(k_{1zi}^{d}) - U_{1vh}(-\overline{k}_{\rho})\hat{h}(k_{1zi}^{d}) \tag{23d}$$

The integrations $\mathcal{I}_{1jklm}^{abcd}$ and $\mathcal{I}_{2jklm}^{pqrs}$ are carried out with the method described in Chapter 2. The result for $\mathcal{I}_{1jklm}^{abcd}$ is

$$\mathcal{I}_{1jklm}^{abcd} = i\frac{2\delta_{1jklm}\ell_{1\rho'}^2\ell_{1z'}}{\pi\mathcal{L}_1^4}\left[\frac{e^{-i(\kappa_{ab}-\kappa_{cd})d_1}}{(\kappa_{ab}-\kappa_1)^2(\kappa_{ab}-\kappa_1^*)^2(\kappa_{ab}-\kappa_{cd})}\right.$$
$$\left. + \frac{1}{(\kappa_{cd}-\kappa_1)^2(\kappa_{cd}-\kappa_1^*)^2(\kappa_{cd}-\kappa_{ab})} - \mathcal{P}_1(\kappa_1) - \mathcal{Q}_1(\kappa_1^*)\right] \tag{24a}$$

in which the square of length $\mathcal{L}_1$ is $\mathcal{L}_1^2 = \ell_{1\rho'}^2 \sin^2\psi_f + \ell_{1z'}^2 \cos^2\psi_f$, pole κ_1 is $\kappa_1 = \mathcal{L}_1^{-2}\left[-k_{\phi y}(\ell_{1z'}^2 - \ell_{1\rho'}^2)\sin(\psi_f)\cos(\psi_f) + i\sqrt{(1+k_{\phi x}^2\ell_{1\rho'}^2)\mathcal{L}_1^2 + k_{\phi y}^2\ell_{1\rho'}^2\ell_{1z'}^2}\right]$, with $k_{\phi x} = k_{\rho i}\cos(\phi_i - \phi_f) - k_{\rho s}\cos(\phi_s - \phi_f)$ and $k_{\phi y} = k_{\rho i}\sin(\phi_i - \phi_f) - k_{\rho s}\sin(\phi_s - \phi_f)$ and quantities $\mathcal{P}_1(\kappa_1)$ and $\mathcal{Q}_1(\kappa_1^*)$ are determined as follows

$$\begin{aligned}\mathcal{P}_1(\kappa_1) = {} & \frac{id_1 e^{i(\kappa_1-\kappa_{ab})d_1}}{(2i\mathrm{Im}\kappa_1)^2(\kappa_1-\kappa_{ab})(\kappa_1-\kappa_{cd})} \\ & + \frac{1 - e^{i(\kappa_1-\kappa_{ab})d_1} + e^{-i(\kappa_{ab}-\kappa_{cd})d_1}}{(2i\mathrm{Im}\kappa_1)^2(\kappa_1-\kappa_{ab})(\kappa_1-\kappa_{cd})} \\ & \cdot \left[\frac{1}{i\mathrm{Im}\kappa_1} + \frac{1}{\kappa_1-\kappa_{ab}} + \frac{1}{\kappa_1-\kappa_{cd}}\right] \end{aligned} \tag{24b}$$

$$\begin{aligned}\mathcal{Q}_1(\kappa_1^*) = {} & \frac{id_1 e^{-i(\kappa_1^*-\kappa_{cd})d_1}}{(2i\mathrm{Im}\kappa_1^*)^2(\kappa_1^*-\kappa_{ab})(\kappa_1^*-\kappa_{cd})} \\ & + \frac{e^{-i(\kappa_1^*-\kappa_{cd})d_1}}{(2i\mathrm{Im}\kappa_1^*)^2(\kappa_1^*-\kappa_{ab})(\kappa_1^*-\kappa_{cd})} \\ & \cdot \left[\frac{1}{i\mathrm{Im}\kappa_1^*} + \frac{1}{\kappa_1^*-\kappa_{ab}} + \frac{1}{\kappa_1^*-\kappa_{cd}}\right] \end{aligned} \tag{24c}$$

The result for $\mathcal{I}_{2jklm}^{pqrs}$ from region 2 is

$$\begin{aligned}\mathcal{I}_{2jklm}^{pqrs} = {} & i\frac{2\delta_{2jklm}\ell_{2\rho'}^2\ell_{2z'}}{\pi\mathcal{L}_2^4}\left[\frac{e^{-i(\kappa_{pq}-\kappa_{rs})d_2}}{(\kappa_{pq}-\kappa_2)^2(\kappa_{pq}-\kappa_2^*)^2(\kappa_{pq}-\kappa_{rs})}\right. \\ & \left. + \frac{e^{i(\kappa_{rs}-\kappa_{pq})d_1}}{(\kappa_{rs}-\kappa_2)^2(\kappa_{rs}-\kappa_2^*)^2(\kappa_{rs}-\kappa_{pq})} - \mathcal{P}_2(\kappa_2) - \mathcal{Q}_2(\kappa_2^*)\right] \end{aligned} \tag{25a}$$

in which the square of length $\mathcal{L}_2$ is $\mathcal{L}_2^2 = \ell_{2\rho'}^2 \sin^2\psi_f + \ell_{2z'}^2 \cos^2\psi_f$, pole κ_2 is $\kappa_2 = \mathcal{L}_2^{-2}\left[-k_{\phi y}(\ell_{2z'}^2 - \ell_{2\rho'}^2)\sin(\psi_f)\cos(\psi_f) + i\sqrt{(1+k_{\phi x}^2\ell_{2\rho'}^2)\mathcal{L}_2^2 + k_{\phi y}^2\ell_{2\rho'}^2\ell_{2z'}^2}\right]$, and quantities $\mathcal{P}_2(\kappa_2)$ and $\mathcal{Q}_2(\kappa_2^*)$ are determined as follows

$$\begin{aligned}\mathcal{P}_2(\kappa_2) = {} & \frac{i(d_2-d_1)e^{-i(\kappa_2-\kappa_{rs})d_1}e^{i(\kappa_2-\kappa_{pq})d_2}}{(2i\mathrm{Im}\kappa_2)^2(\kappa_2-\kappa_{pq})(\kappa_2-\kappa_{rs})} \\ & + \left[\frac{e^{-i(\kappa_{pq}-\kappa_{rs})d_1} + e^{-i(\kappa_{pq}-\kappa_{rs})d_2}}{(2i\mathrm{Im}\kappa_2)^2(\kappa_2-\kappa_{pq})(\kappa_2-\kappa_{rs})}\right. \\ & \left. - \frac{e^{-i(\kappa_2-\kappa_{rs})d_1}e^{i(\kappa_2-\kappa_{pq})d_2}}{(2i\mathrm{Im}\kappa_2)^2(\kappa_2-\kappa_{pq})(\kappa_2-\kappa_{rs})}\right] \\ & \cdot \left[\frac{1}{i\mathrm{Im}\kappa_2} + \frac{1}{\kappa_2-\kappa_{pq}} + \frac{1}{\kappa_2-\kappa_{rs}}\right] \end{aligned} \tag{25b}$$

$$Q_2(\kappa_2^*) = \frac{i(d_2-d_1)e^{i(\kappa_2^*-\kappa_{ps})d_1}e^{-i(\kappa_2^*-\kappa_{rs})d_2}}{(2i\mathrm{Im}\kappa_2^*)^2(\kappa_2^*-\kappa_{pq})(\kappa_2^*-\kappa_{rs})}$$
$$+\frac{e^{i(\kappa_2^*-\kappa_{ps})d_1}e^{-i(\kappa_2^*-\kappa_{rs})d_2}}{(2i\mathrm{Im}\kappa_2^*)^2(\kappa_2^*-\kappa_{pq})(\kappa_2^*-\kappa_{rs})}$$
$$\cdot\left[\frac{1}{i\mathrm{Im}\kappa_2^*}+\frac{1}{\kappa_2^*-\kappa_{pq}}+\frac{1}{\kappa_2^*-\kappa_{rs}}\right] \tag{25c}$$

The remaining integrations over ϕ_f and ψ_f can be carried out numerically in general or analytically in the low-frequency case. The scattering coefficients obtained in (20) is for the scattered field expressed in the scattered basis which can be changed to incident basis by taking the negative of $\sigma_{hr\nu\kappa}$ and $\sigma_{\nu rh\kappa}$. Furthermore, the scattering effects of the rough boundaries at the medium interfaces are estimated by incoherently adding the total contribution from the rough surface scattering taking into account the propagation loss through the medium; formulas for rough surface scattering are in [32,81].

In this section, the effective permittivity is derived with the extended strong fluctuation theory and the polarimetric backscattering coefficients are obtained under the distorted Born approximation. In the next section, the model is applied to study the polarimetric scattering properties from vegetation. Polarization signatures and their relations to the corresponding covariance matrices are also investigated.

3.4 Results and Discussion

a. Azimuthal Symmetry

For an azimuthally symmetric random medium, cross term $\sigma_{hhh\nu}$ and $\sigma_{h\nu\nu\nu}$ are zero rendering the covariance matrix of the form

$$\overline{\overline{C}} = \begin{bmatrix} \sigma_{hh} & 0 & \sigma_{hh\nu\nu} \\ 0 & \sigma_{h\nu} & 0 \\ \sigma_{hh\nu\nu}^* & 0 & \sigma_{\nu\nu} \end{bmatrix} \quad \text{or} \quad \overline{\overline{C}} = \sigma \begin{bmatrix} 1 & 0 & \rho\sqrt{\gamma} \\ 0 & e & 0 \\ \rho^*\sqrt{\gamma} & 0 & \gamma \end{bmatrix} \tag{26}$$

The model presented in this chapter gives non-zero cross term $\sigma_{h\nu}$ under the first-order distorted Born approximation. This result is due to the nonspherical shape of

the scatterers. However, higher-order contribution to σ_{hv} is neglected.

The covariance matrix of the form (26) is considered for terrain media with a two-layer configuration such as azimuthally symmetric vegetation over soil. In this case, the three-layer model is applied with one of the scattering regions removed by setting the layer thickness and the fluctuation variances to zero. The model is used to investigate the polarimetric backscattering directly from an agricultural field such as soybean for which scattering data and detail ground truth are available.

b. Conventional Backscattering

The soybean data are provided by Dr. T. Le Toan of *Centre d'Etude Spatiale des Rayonnements*. Backscattering coefficients σ_{hh}, σ_{vv}, and σ_{hv} of wave frequency 5.3 GHz and 0-50° incident angle together with ground truth were measured at 10 different growth stages of the soybean from 17 July to 30 September 1986. The scattering configuration of the soybean canopy is illustrated in Figure 3.4.1 for the parameters taken on 8-07-86. The ground truth data are summarized in Table 3.4.1 including: canopy height d in meter (m), volumetric water content m_v of the canopy in kilogram per cubic meter (kg/m^3), vegetation fractional volume f_s in percent (%), volumetric water content m_s of the underlying soil in percent (%), rms height σ_s and surface correlation length ℓ_s of the assumed Gaussian rough soil surface in centimeter (cm).

From table 3.4.1, it is observed that the rough soil surface slope tends to be smoother while m_v and f_s increase then decrease as the soybean grows. However, the water content f_w in vegetation approximated by $f_w = m_v/(10f_s)$ (for m_v in kg/m^3 and f_s in %) linearly decreases with time indicating that the older soybean is less moist. From the ground truth, leaf and soil dielectric constants are estimated from [84] and [85], respectively. The correlation lengths ℓ_ρ and ℓ_z in Table 3.4.2 for disc-like leaves together with the ground truth are input in the model to obtain the theoretical results.

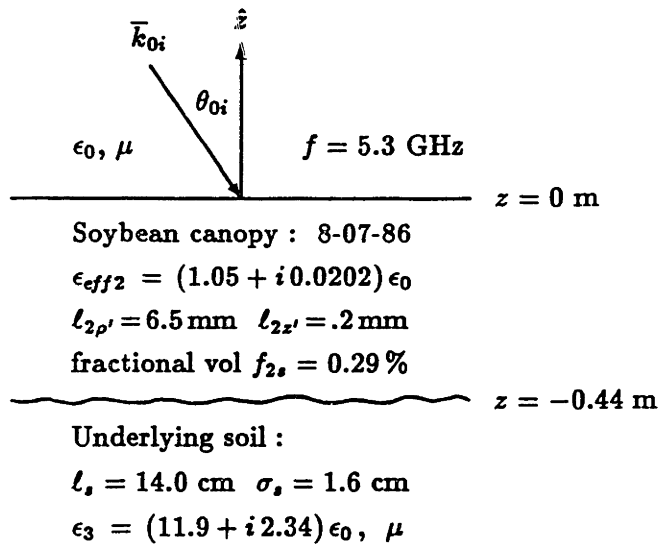

Figure 3.4.1 Scattering configuration of soybean canopy

Date	d (m)	m_v (kg/m^3)	f_s (%)	m_s (%)	σ_s (cm)	ℓ_s (cm)
7-17-86	0.200	0.93	0.11	28.0	1.7	14
7-25-86	0.290	1.41	0.18	21.0	1.7	14
8-07-86	0.440	1.99	0.29	26.0	1.6	14
8-14-86	0.520	3.92	0.60	32.0	1.6	14
8-20-86	0.590	5.23	0.87	15.8	1.5	13
8-28-86	0.680	4.59	0.89	33.4	1.4	13
9-03-86	0.745	4.15	0.88	19.8	1.3	12
9-12-86	0.825	2.84	0.68	12.0	1.2	12
9-19-86	0.790	2.10	0.50	29.6	1.2	12
9-30-86	0.735	1.11	0.29	25.0	1.2	12

Table 3.4.1 Ground truth data for soybean

Date	7-17	7-25	8-07	8-14	8-20	8-28	9-03	9-12	9-19	9-30
ℓ_ρ	7.5	7.5	6.5	5.5	4.5	3.5	3.2	5.0	5.8	7.5
ℓ_z	0.10	0.10	0.20	0.30	0.30	0.25	0.30	0.40	0.40	0.40

Table 3.4.2 Correlation lengths for soybean (in mm)

The comparisons for conventional backscattering coefficients of the soybean are shown in Figures 3.4.2-3.4.11 over the range of incident angles from 0° to 50° and in Figure 3.4.12 at 20° incident angle over the growth time. For copolarized returns σ_{hh} and σ_{vv}, the theoretical and experimental results are in good agreement. By comparing the contributions from the scattering due to the soybean canopy and the scattering due to the rough soil surface, the trend observed in σ_{hh} and σ_{vv} can be interpreted physically. At small incident angles, the rough surface scattering contribution is important when the total attenuation of the soybean, especially at low vegetation fractional volume, allows the soil surface to be seen by the wave. The rough surface contribution, however, rapidly diminishes as the incident angle increases. At larger incident angles, the volume scattering due to the soybean canopy becomes dominant and the copolarized returns slowly decrease as the incident angle increases. These scattering mechanisms explain why the returns are high near normal incident angle, decrease rather quickly up to incident angle about 20°, and slowly decrease as the incident angle increases to 50°. However, the theoretical predictions are higher on the first and last dates where the vegetation fractional volumes are low. In those cases, the rough surface characterization with rms height σ_s and surface correlation length ℓ_s are sensitive to the backscattering coefficients which can vary as much as ± 1.5 dB when σ_s and ℓ_s change within $\pm 10\%$ of the measured values as shown in Figures 3.4.13 and 3.4.14. For cross polarized return σ_{hv}, the theoretical values are lower than the experimental data. This is due to the fact that scatterers with elongated shape such as stems and higher-order contribution to the cross term are neglected in the calculation of volume, surface, and volume-surface scattering. An interesting observation is the high correlation between fractional volume and the lateral correlation length ℓ_ρ of the disc-like leaf shape. The correlation coefficient is -0.966 indicating the inverse relation between the two parameters.

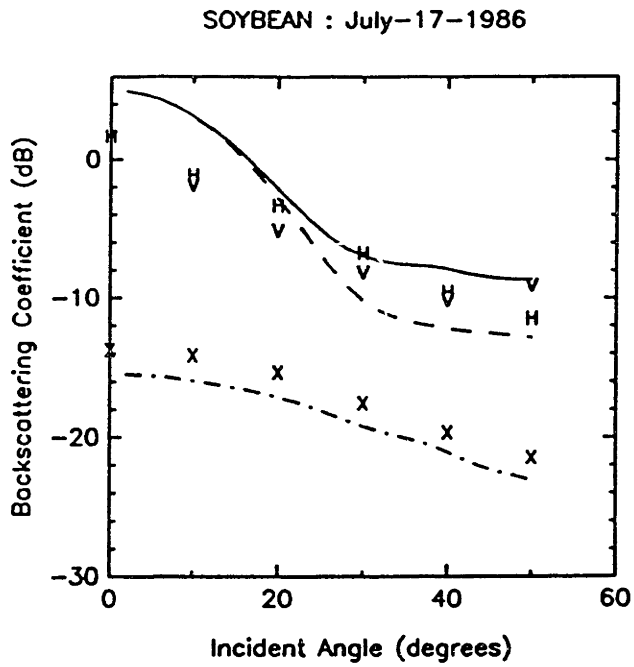

Figure 3.4.2 Backscattering coefficients of the soybean canopy : H and continuous curve for σ_{hh}, V and dash curve for σ_{vv}, and X and dash-dot curve for σ_{hv}; letters are for experimental data and curves for theoretical results

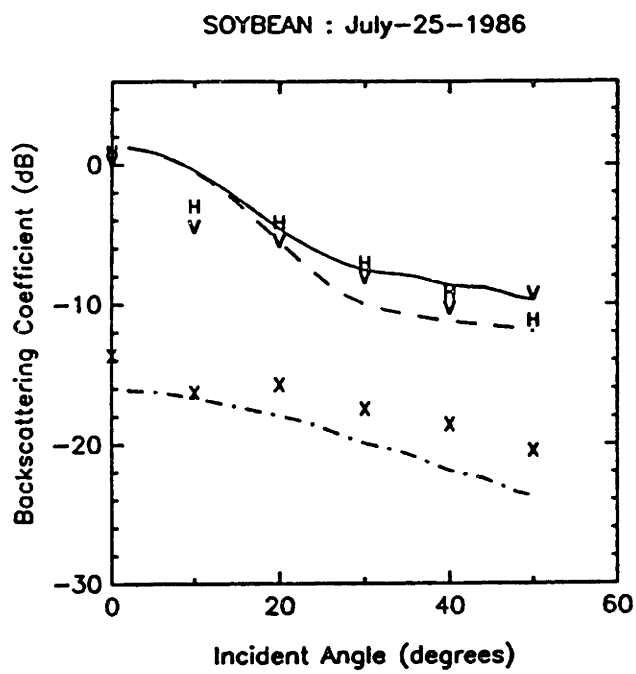

Figure 3.4.3 Backscattering coefficients of the soybean canopy : H and continuous curve for σ_{hh}, V and dash curve for σ_{vv}, and X and dash-dot curve for σ_{hv}; letters are for experimental data and curves for theoretical results

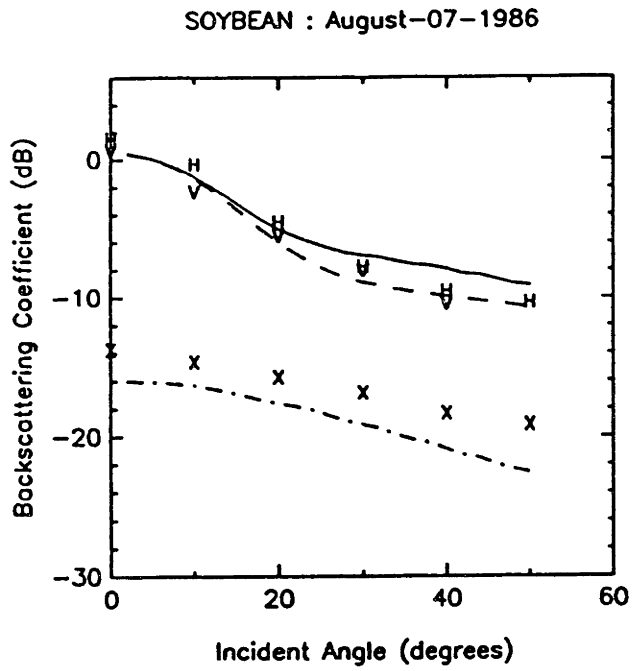

Figure 3.4.4 Backscattering coefficients of the soybean canopy : H and continuous curve for σ_{hh}, V and dash curve for σ_{vv}, and X and dash-dot curve for σ_{hv}; letters are for experimental data and curves for theoretical results

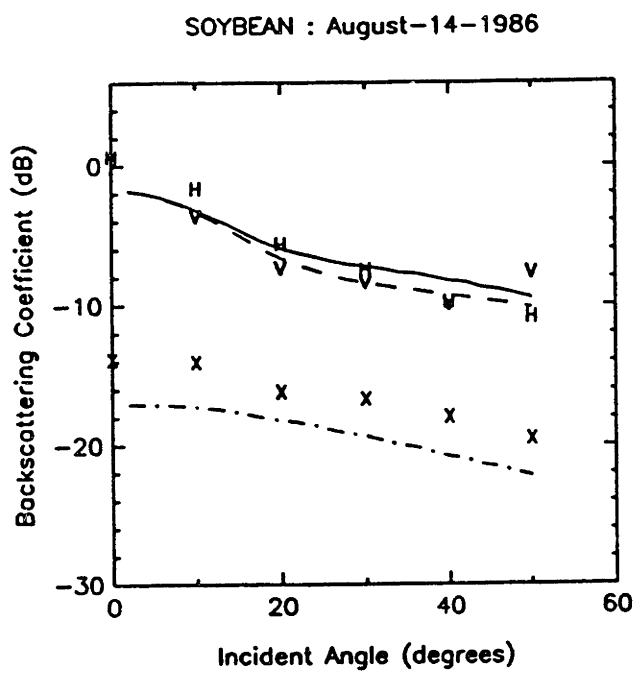

Figure 3.4.5 Backscattering coefficients of the soybean canopy : H and continuous curve for σ_{hh}, V and dash curve for σ_{vv}, and X and dash-dot curve for σ_{hv}; letters are for experimental data and curves for theoretical results

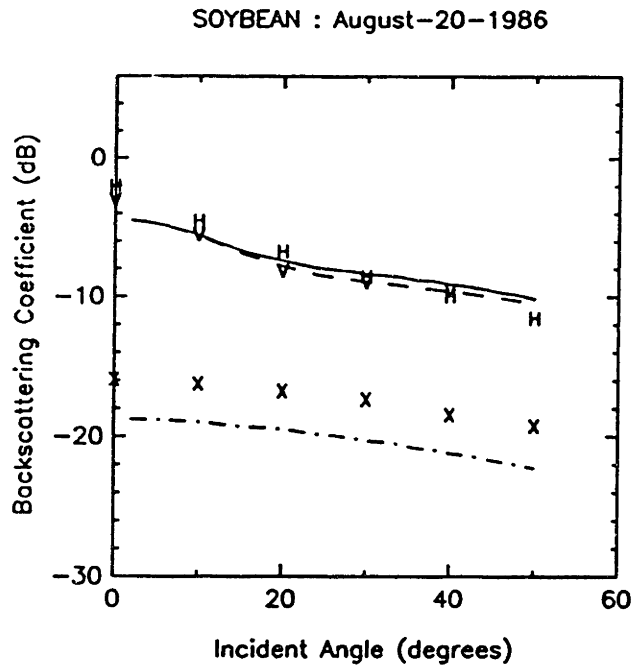

Figure 3.4.6 Backscattering coefficients of the soybean canopy : H and continuous curve for σ_{hh}, V and dash curve for σ_{vv}, and X and dash-dot curve for σ_{hv}; letters are for experimental data and curves for theoretical results

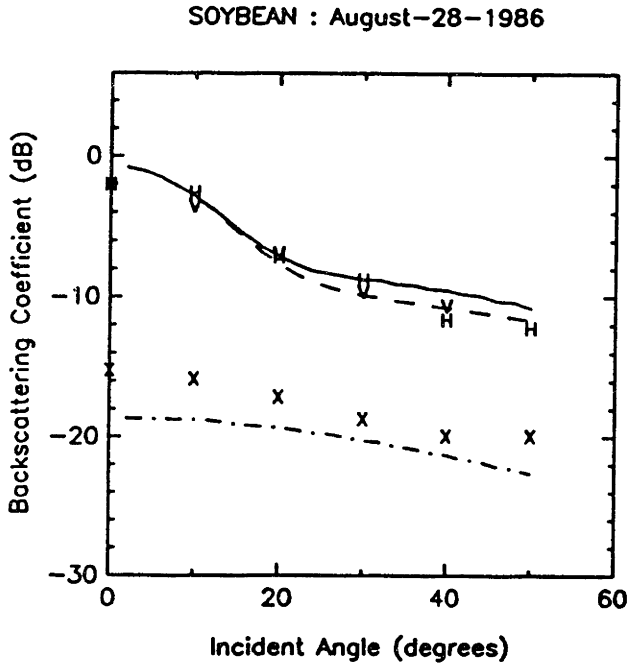

Figure 3.4.7 Backscattering coefficients of the soybean canopy : H and continuous curve for σ_{hh}, V and dash curve for σ_{vv}, and X and dash-dot curve for σ_{hv}; letters are for experimental data and curves for theoretical results

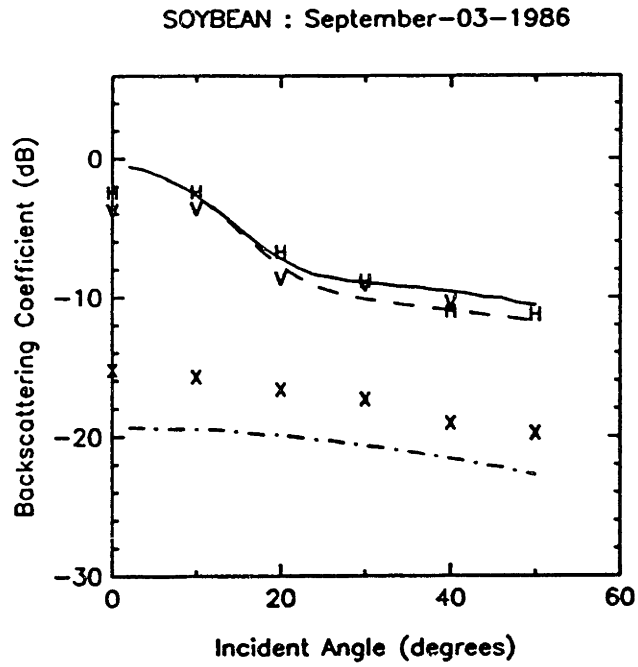

Figure 3.4.8 Backscattering coefficients of the soybean canopy : H and continuous curve for σ_{hh}, V and dash curve for σ_{vv}, and X and dash-dot curve for σ_{hv}; letters are for experimental data and curves for theoretical results

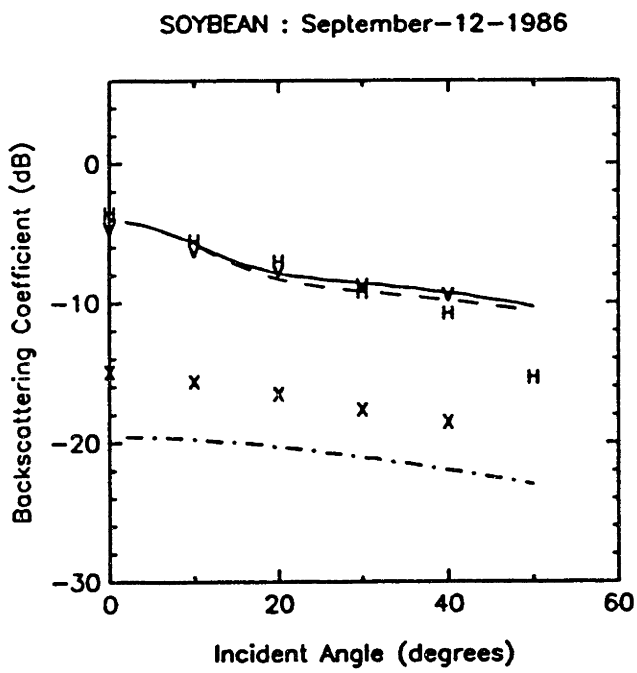

Figure 3.4.9 Backscattering coefficients of the soybean canopy : H and continuous curve for σ_{hh}, V and dash curve for σ_{vv}, and X and dash-dot curve for σ_{hv}; letters are for experimental data and curves for theoretical results

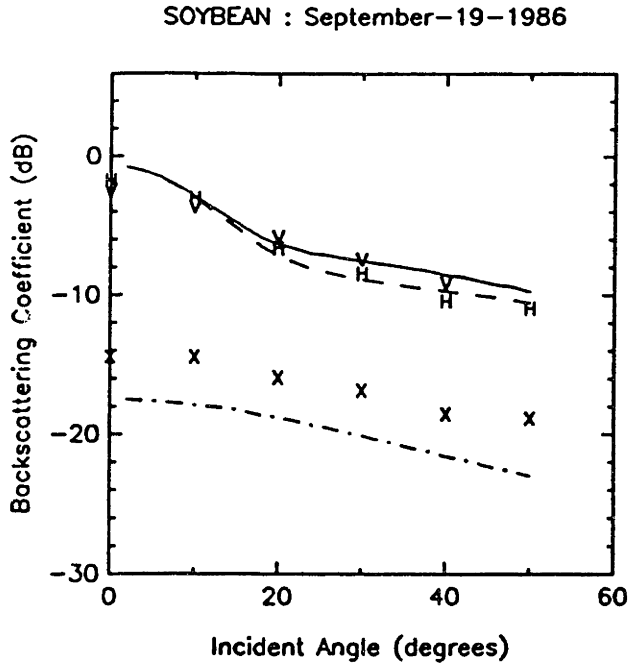

Figure 3.4.10 Backscattering coefficients of the soybean canopy : H and continuous curve for σ_{hh}, V and dash curve for σ_{vv}, and X and dash-dot curve for σ_{hv}; letters are for experimental data and curves for theoretical results

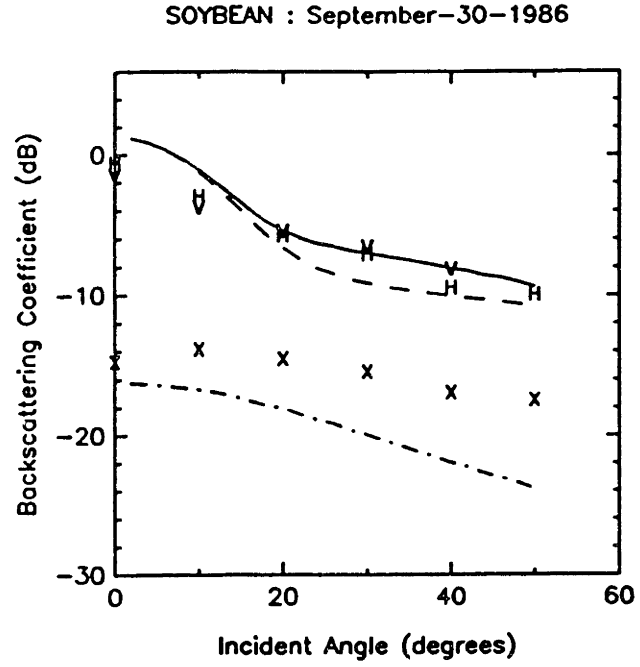

Figure 3.4.11 Backscattering coefficients of the soybean canopy : H and continuous curve for σ_{hh}, V and dash curve for σ_{vv}, and X and dash-dot curve for σ_{hv}; letters are for experimental data and curves for theoretical results

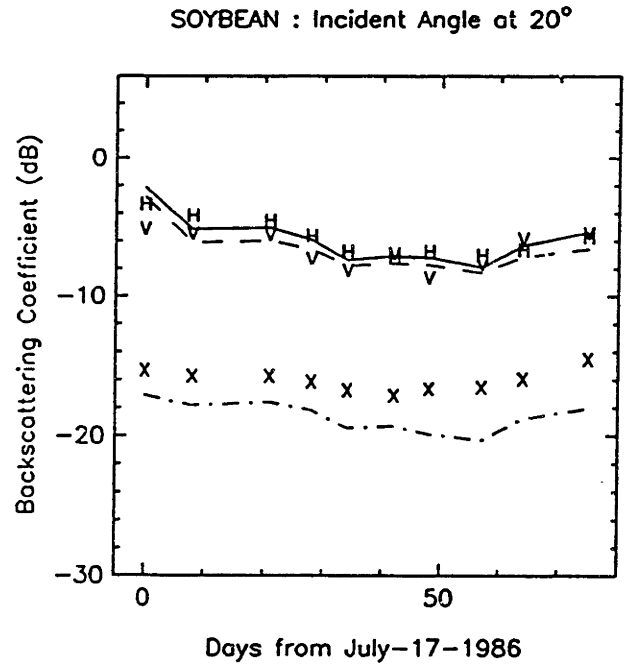

Figure 3.4.12 Backscattering coefficients of the soybean canopy : H and continuous curve for σ_{hh}, V and dash curve for σ_{vv}, and X and dash-dot curve for σ_{hv}; letters are for experimental data and curves for theoretical results

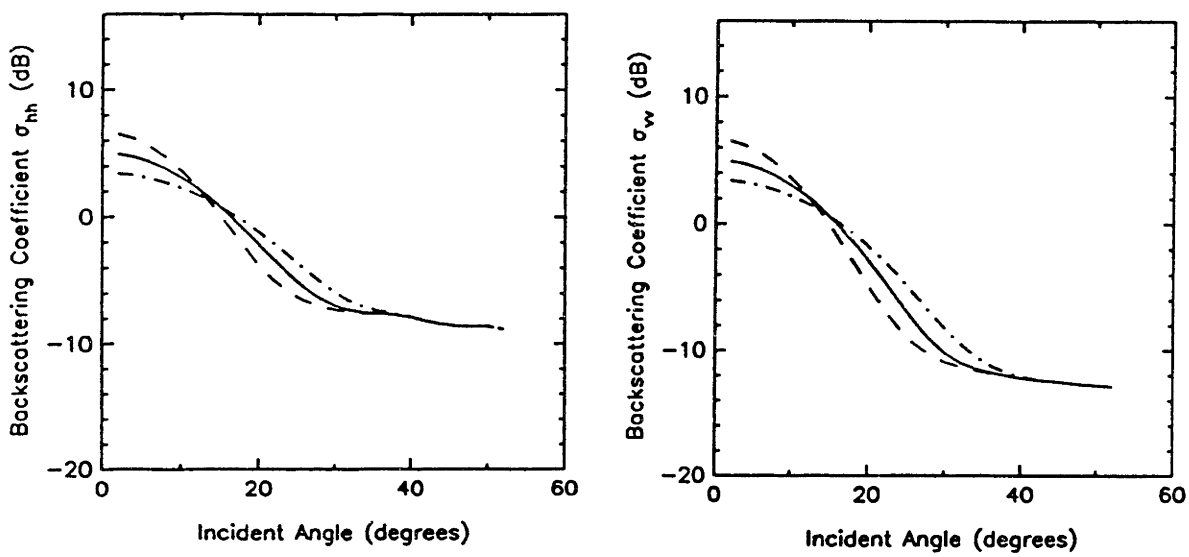

Figure 3.4.13 Sensitivity of backscattering coefficients (7-17) : continuous curve uses measured values of rough soil surface, dash and dash-dot curve the rough surface values varied within ±10%

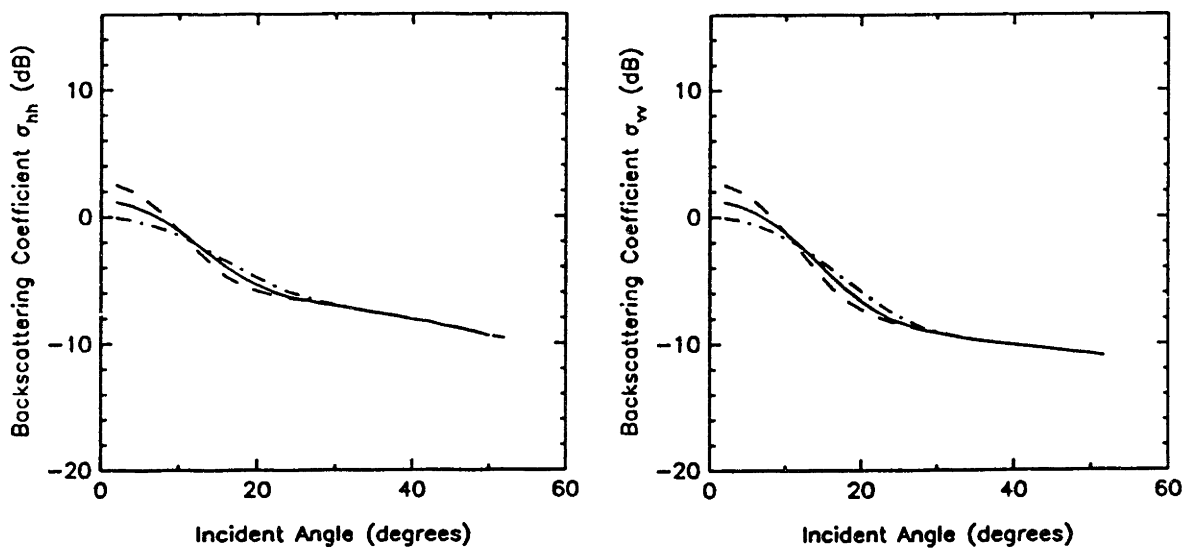

Figure 3.4.14 Sensitivity of backscattering coefficients (9-30) : continuous curve uses measured values of rough soil surface, dash and dash-dot curve the rough surface values varied within ±10%

c. Polarimetric Backscattering

To investigate the polarimetric scattering properties, the physical parameters of the soybean are used as input to the model to calculate the correlation coefficient ρ between the copolarized returns and to simulate the polarization signature of the soybean with the Mueller matrix.

As an example, the polarimetric backscattering of the soybean at the growth stage of 8-07-86 is studied in this section. At incident angle of 40° where the scattering from the soybean canopy is dominant, the covariance matrix is

$$\overline{\overline{C}} = 0.16 \begin{bmatrix} 1 & 0 & (0.70\ \angle -1.2°)\sqrt{\gamma} \\ 0 & e = 0.050 & 0 \\ (0.70\ \angle +1.2°)\sqrt{\gamma} & 0 & \gamma = 0.63 \end{bmatrix} \tag{27}$$

From (27), the magnitude of ρ is 0.70 and the phase is $-1.2°$. The magnitude of

ρ is obviously lower than unity; this is an indication of the nonspherical shape of the scatterers. If the scatterers have spherical shape, the magnitude of ρ will be close to 1 [Chapter 2]. The small phase of ρ, in this case, indicates that the effective permittivity of the soybean has the isotropic characteristics which allows the h and the v waves to propagate with the same speed and attenuation rate and thus does not result in the separation of scattering centers of the wave types. Therefore, the distinction between the two wave types is mainly due to the boundary effect giving rise to the small phase of ρ.

The elements of the covariance matrix (27) are used to calculate the Mueller matrix which is used in (11, Chapter 1) to obtain the signature of the soybean. The copolarized signature is shown in Figure 3.4.15 which exhibits local maxima at h and v polarizations and the symmetry about the v polarization manifesting the azimuthal symmetry of the soybean. The signature also shows the existence of the pedestal, contributed by the cross term e and the imbalance between $(\gamma + 1)$ and $2\sqrt{\gamma}\mathrm{Re}\rho$ [Chapter 2], which is physically due to the nonspherical shape of the scatterers. Another feature of the copolarized signature is the signature distortion track (SDT) defined as the curve of β whose value corresponds to the local maximum return for a given α. The SDT is a description of how the signature is distorted. The corresponding signature distortion track (SDT) of the signature in Figure 3.4.15 is plotted in Figure 3.4.16 revealing very weak distortion due to the small phase of ρ as a result of the random medium isotropy. As illustrated, the fully polarimetric scattering coefficient convey information about physical and structural properties of the random medium. For all other growth stages, the corresponding copolarized signatures will be simulated in the next section.

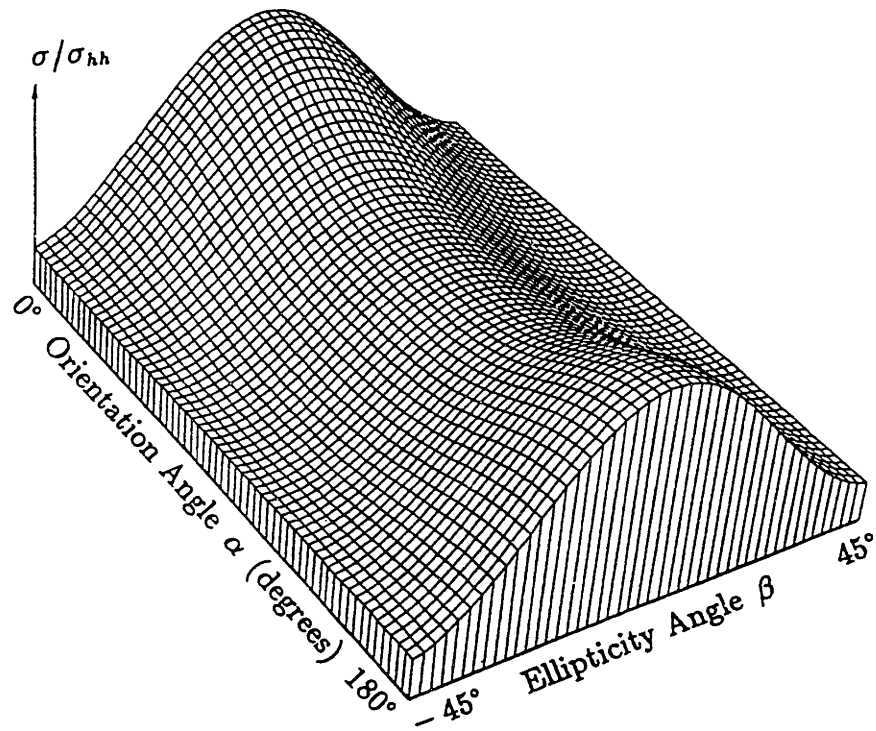

Figure 3.4.15 Copolarization signature of soybean at 40° incidence (8-07)

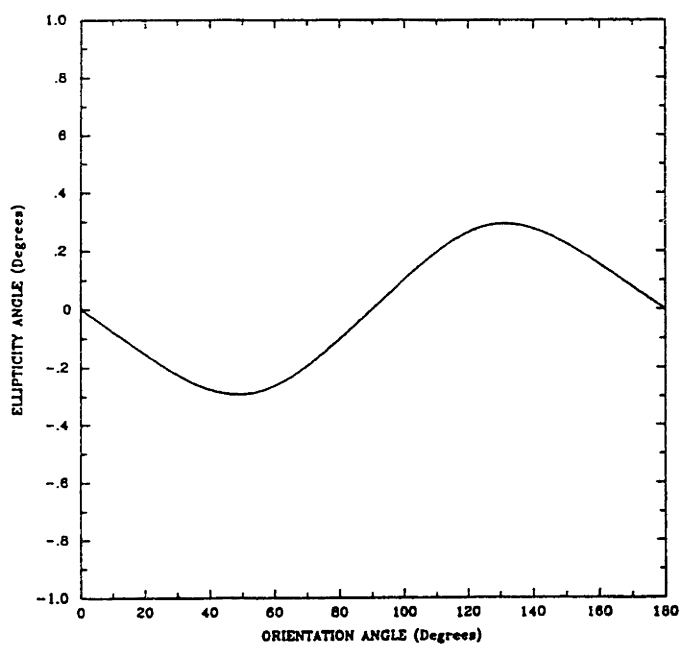

Figure 3.4.16 Signature distortion track of soybean at 40° incidence (8-07)

3.5 Assessment for Inversion

In the last section, the theoretical results are shown to compare well with backscattering data for soybean from early to late growth stage. In this section, a set of input data will be prepared based on the trend of the physical parameters observed in the measurements. Then, the data will be input into the random medium model to simulate the backscattering coefficients for soybean under various radar configurations and soybean conditions. As an approach towards inversion problem for soil moisture and/or vegetation fractional volume (biomass), the simulation will be used to investigate the optimum radar configuration and determine the soybean condition under which the interested physical parameters are invertible. First, the trends observed during the growth of soybean are taken into account to prepare a set of input parameters for use in the simulation. Then a radar configuration is investigated for application in the inversion application. Next, the simulation results of backscattering coefficients are calculated from the model with the biophysical input parameters to look for suitable vegetation condition. Furthermore, polarization signature simulation over different growth stages of the soybean is studied to acquire structural information of the vegetation.

a. Observations on Biophysical Parameters

For vegetation canopy such as soybean, biophysical parameters are interrelated; therefore, their trends in the growth of the vegetation must be imposed on the simulation to obtain physically meaningful results. With that purpose, the soybean parameters are studied in this section.

The temporal ground truth of the soybean in Table 3.4.1 shows that the vegetation fractional volume f_v increases to a maximum value and then decreases. This trend is illustrated in Figure 3.5.1 with the measured data represented by the dot circles and the continuous fitting curves which will be used later for the simulation of

backscattering coefficients. Since the fractional volume of the soybean is temporally double-valued, it is useful to classify the growth stage into: young stage before the soybean attains the maximum fractional volume, fully grown when the volume is maximum, and old stage afterwards.

By using the relation $f_w = m_v/(10f_s)$ (for m_v in kg/m^3 and f_s in %), the volumetric water content in soybean is found to decreases linearly as the soybean grows. This moisture reduction is clearly seen in Figure 3.5.2 where the dot circles are from measured data and the negatively inclined line is the linear fitting. From the fits of f_s and m_v, temporal curve for volumetric water content m_v of the soybean canopy is obtained and compared with measured data as shown in Figure 3.5.3.

As mentioned in the previous section, the correlation length ℓ_ρ and the vegetation fractional volume f_s are highly correlated with the negative correlation coefficient of -0.966 indicating their inverse relation graphed in Figure 3.5.4 with dot-circle measured data and the fitting line. Then, this line together with f_s from young to old stage are used to deduce the temporal ℓ_ρ curve to compare with the data in Figure 3.5.5. The correlation length ℓ_z, corresponding to the effective thickness of the leaves, tends to increase with time as observed in Figure 3.5.6.

From Figure 3.5.7, the soybean height grows linearly until an old stage then decreases. For the soil roughness, the general trend reveals a temporal smoothening effect as seen from Figure 3.5.8. The soil moisture, however, is rather random (see Figure 3.5.9) and does not show any correlation with other biophysical parameters. Thus, the soil moisture can be treated as an independent variable.

In summary, each biophysical parameter of the soybean follows a trend as the vegetation grows. The trends and interrelation of the parameters are fitted with curves which will be used later for simulation to account for the temporal and interrelated variations of the soybean canopy. Due to the random behavior, the soil moisture can be used as an independent parameter.

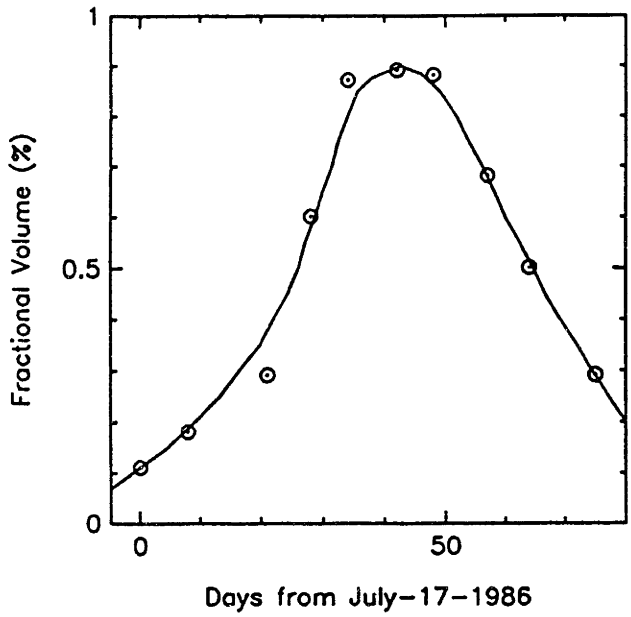

Figure 3.5.1 Temporal variation of soybean fractional volume (f_s) : dot circles are for data and the continuous curve is the fitting

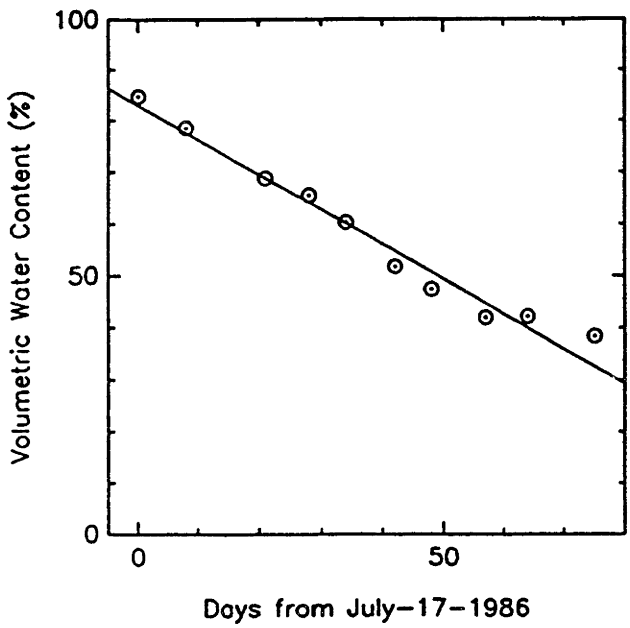

Figure 3.5.2 Temporal moisture reduction in soybean (f_w) : dot circles are for data and the continuous curve is the fitting

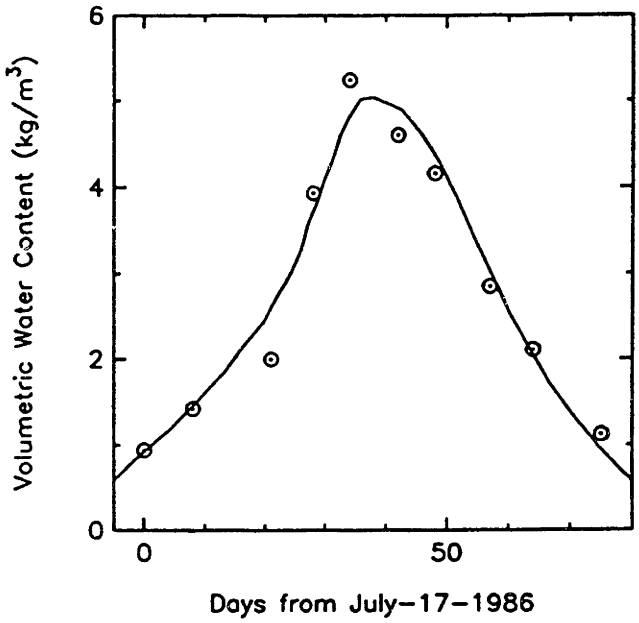

Figure 3.5.3 Temporal variation of soybean canopy water content (m_v) : dot circles are for data and the continuous curve is the fitting

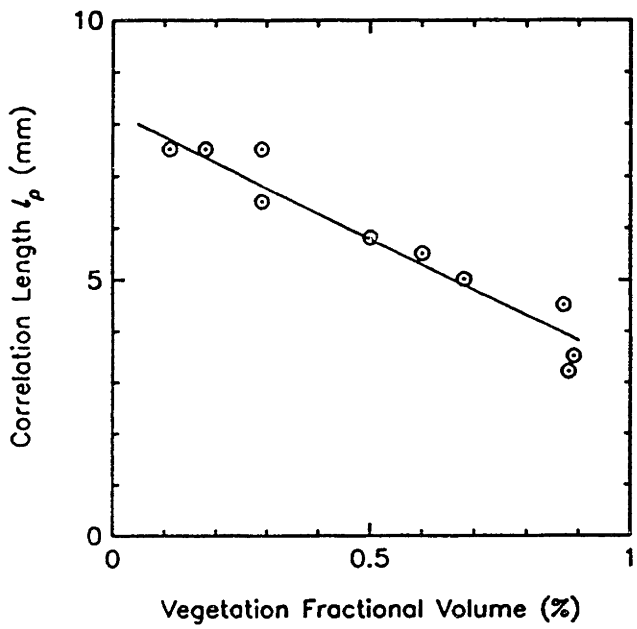

Figure 3.5.4 Relation of correlation length ℓ_p and vegetation fractional volume f_v : dot circles are for data and the continuous curve is the fitting

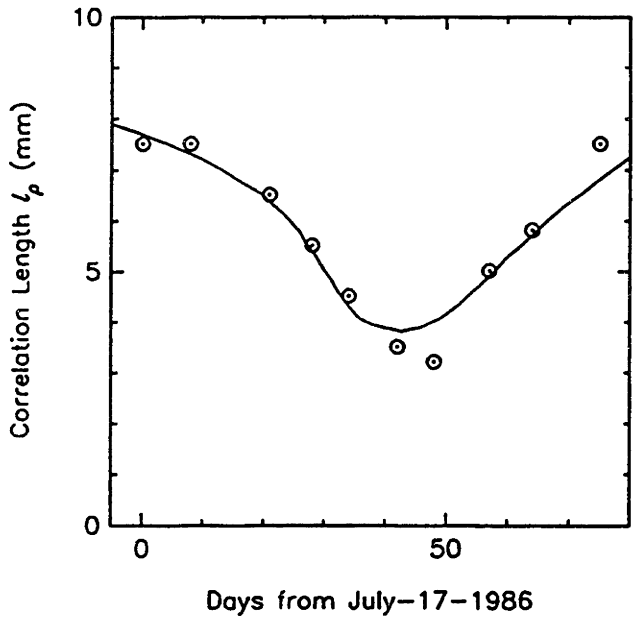

Figure 3.5.5 Temporal variation of correlation length ℓ_ρ : dot circles are for data and the continuous curve is the fitting

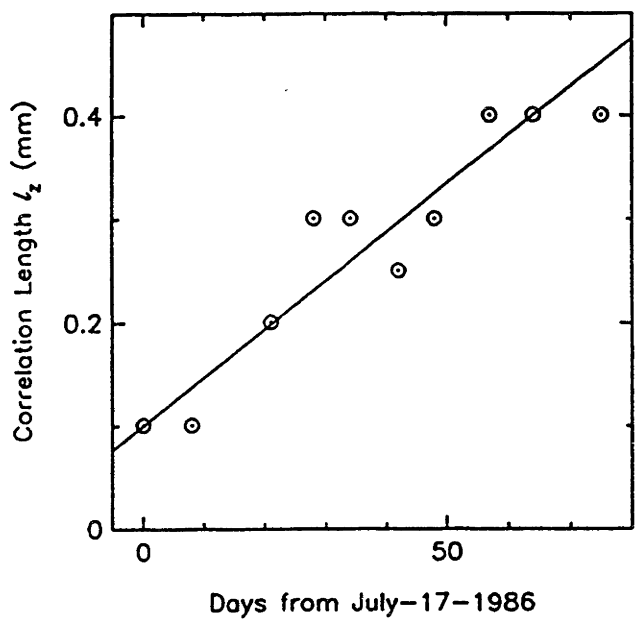

Figure 3.5.6 Temporal variation of correlation length ℓ_z : dot circles are for data and the continuous curve is the fitting

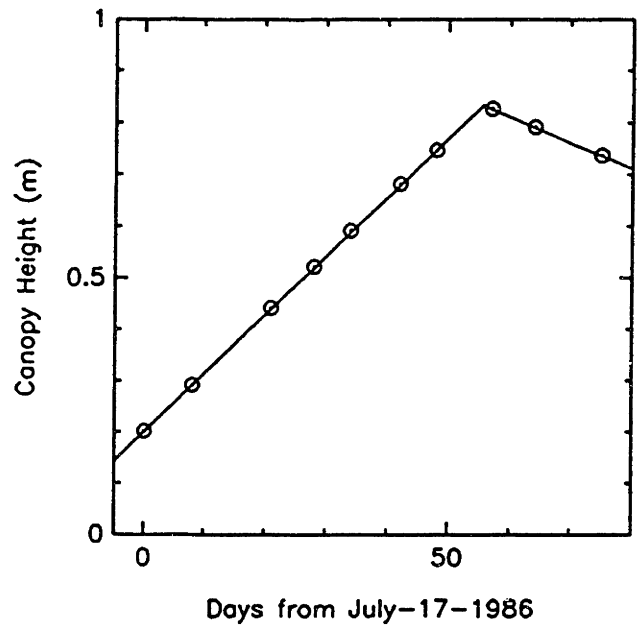

Figure 3.5.7 Temporal variation of canopy height d : dot circles are for data and the continuous curve is the fitting

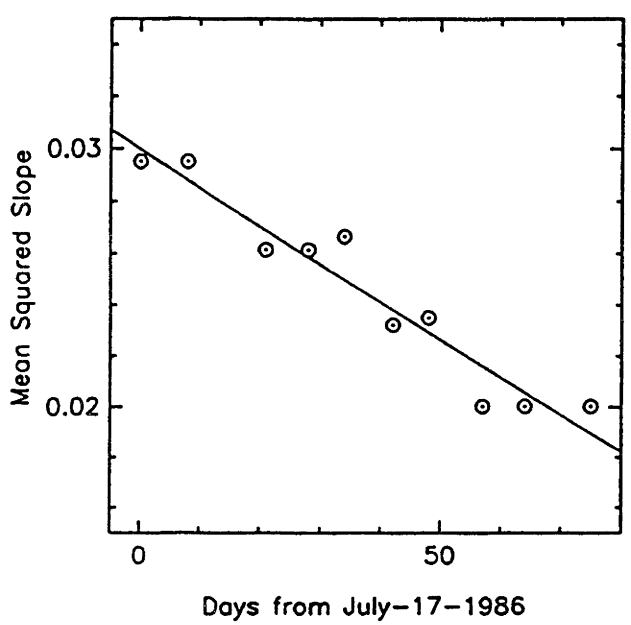

Figure 3.5.8 Temporal smoothening effect on soil surface : dot circles are for data and the continuous curve is the fitting

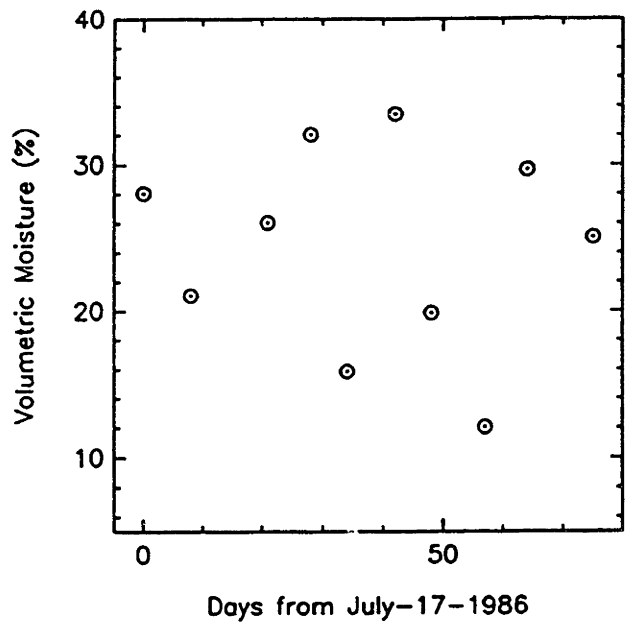

Figure 3.5.9 Random behavior of soil moisture (m_v): dot circles are measurements

b. Radar Configuration for Inversion

In this section, the conventional backscattering coefficients are simulated for the range of incident angles from 0 to 50° to determine which polarizations and incident angles can be use for inversion of soil moisture. The simulation is carried out by using the input parameters of the first date 7-17-86 (early stage) and the last date (late stage) from Tables 3.4.1 and 3.4.2 and volumetric soil moisture is varied from 2% to 30%. Those dates are chosen because the soybean is not so dense that the underlying soil can be seen by the wave. The cross polarized returns σ_{hv} are low and require accurate measurement and calibration; thus, the copolarized returns, which are more sensitive to the soil moisture, are more suitable for the inversion. The simulation of σ_{hh} and σ_{vv} are plotted in Figure 3.5.10 for the early stage and Figure 3.5.11 for the late stage. The results show that as soil moisture increases the backscattering coefficients increase. At incident angles larger than 15°, σ_{hh} has higher sensitivity to

the soil moisture than σ_{vv} does. This is because the soil boundary has stronger effect on σ_{hh} that σ_{vv}. At incident angles smaller than 15°, σ_{hh} and σ_{vv} have similar behavior due to more similar boundary effect on both types of returns. Furthermore, the returns are more sensitive to the soil moisture than at the larger incident angle due to the shorter effective wave path in the lossy soybean canopy. Thus, both σ_{hh} and σ_{vv} at small incident angles are more useful for the inversion. However, near normal incident angles are not necessarily better. The sensitivity study on the soil roughness condition in the previous section indicates that incident angles between 10° and 15° are less susceptible to the soil roughness condition. With consideration of the inversion, the incident angle of 10° is chosen for either σ_{hh} or σ_{vv} for further simulation under different vegetation conditions in the next subsection.

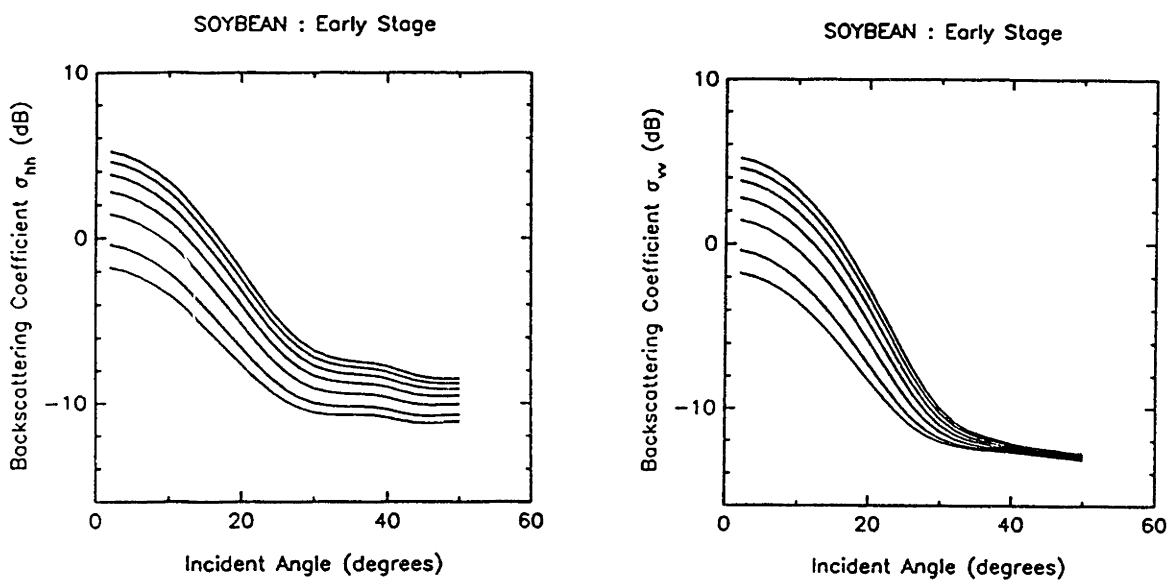

Figure 3.5.10 Simulation for early stage soybean : volumetric soil moisture is $m_v = 2, 5, 10, 15, 20, 25, 30\%$ respectively corresponding to curves from bottom to top

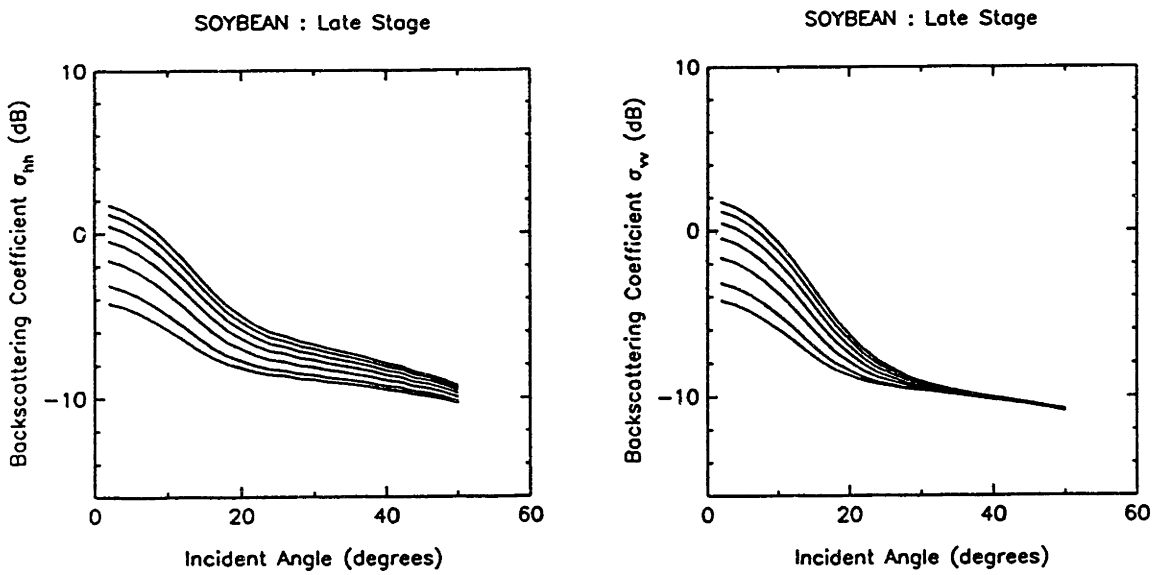

Figure 3.5.11 Simulation for late stage soybean : volumetric soil moisture is $m_v = 2, 5, 10, 15, 20, 25, 30\%$ respectively corresponding to curves from bottom to top

c. Vegetation Condition for Inversion

In this section, the input parameters obtained with the curves from subsection 3.5a and the radar configuration chosen in subsection 3.5b are used to simulate backscattering coefficients of various soybean condition under the constrains of temporal and interrelated biophysical variations. This simulation is to determine which growth stage of the soybean is sensitive to the soil moisture and thus can be used to obtain simulated data for acquiring empirical formulas in the application to the inversion problem. The simulation is done according to the growth stages of the soybean: from the early stage, throughout the young stage, up to the fully grown soybean, and throughout the old stage to the late stage. The backscattering coefficients σ_{hh} and σ_{vv} are simulated as functions of vegetation fractional volume f_v and volumetric soil moisture content m_v and presented in two different formats in Figure 3.5.12 for the younger soybean and Figure 3.5.13 for the older soybean. The results suggest that

the early young stage and the late old stage when the vegetation fractional volume is than 0.3% are sensitive to the soil moisture and the simulated data can be used to obtain the empirical formulas. At the suggested low fractional volume and low incident angles, the scattering coefficients, however, depend on both the fractional volume and soil moisture. The simulations in Figures 3.5.16-3.5.19 show that, at 40° incidence, σ_{vv} depends only on fractional volume and therefore favorable for inversion of the fractional volume. Then the results can be used with data at low incident angles to retrieve soil moisture.

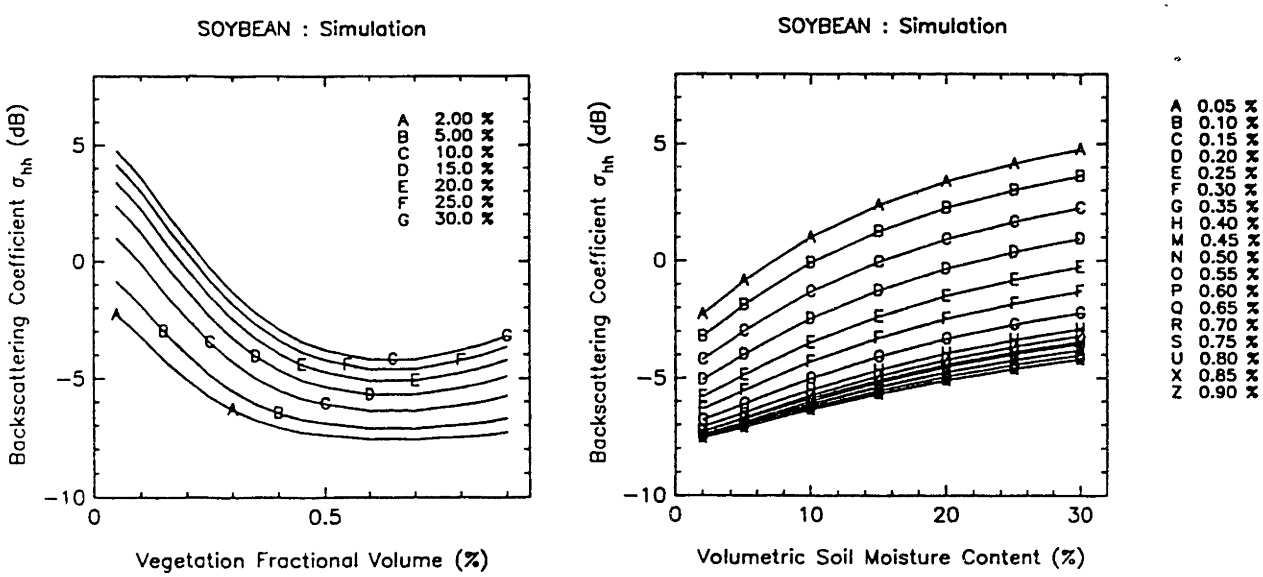

Figure 3.5.12 Simulation of σ_{hh} for young soybean at 10° incident angle

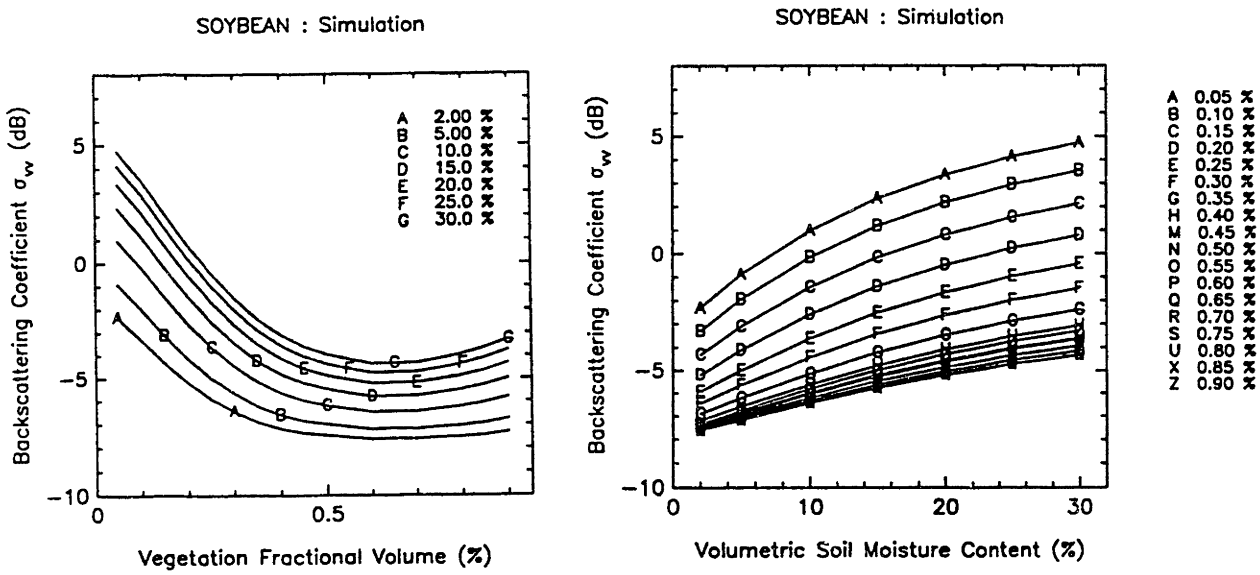

Figure 3.5.13 Simulation of σ_{vv} for young soybean at 10° incident angle

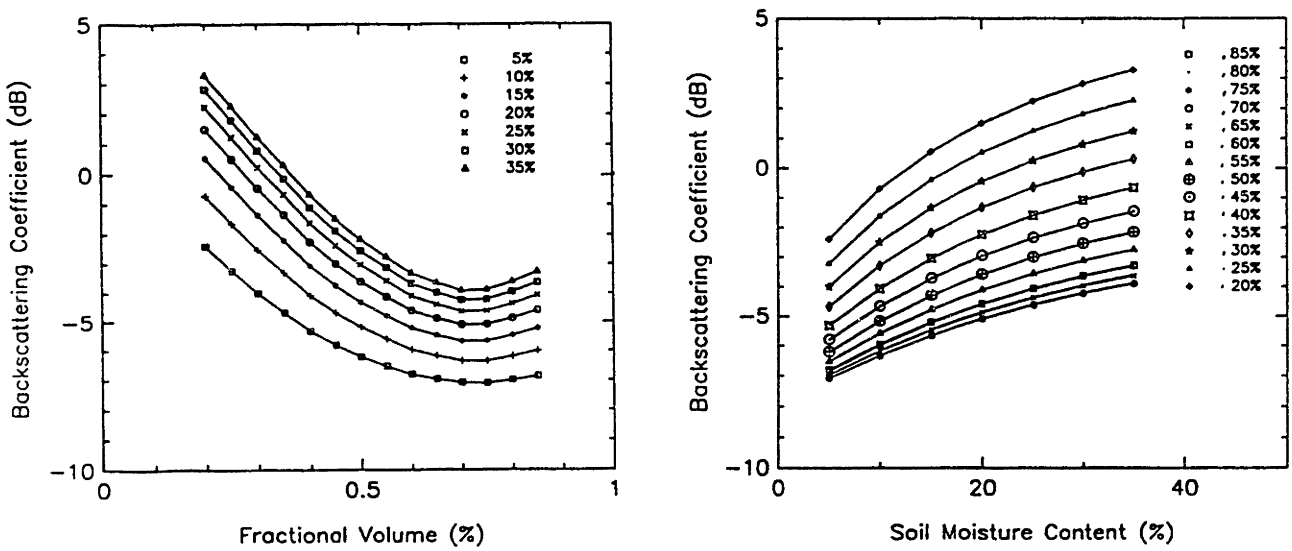

Figure 3.5.14 Simulation of σ_{hh} for old soybean at 10° incident angle

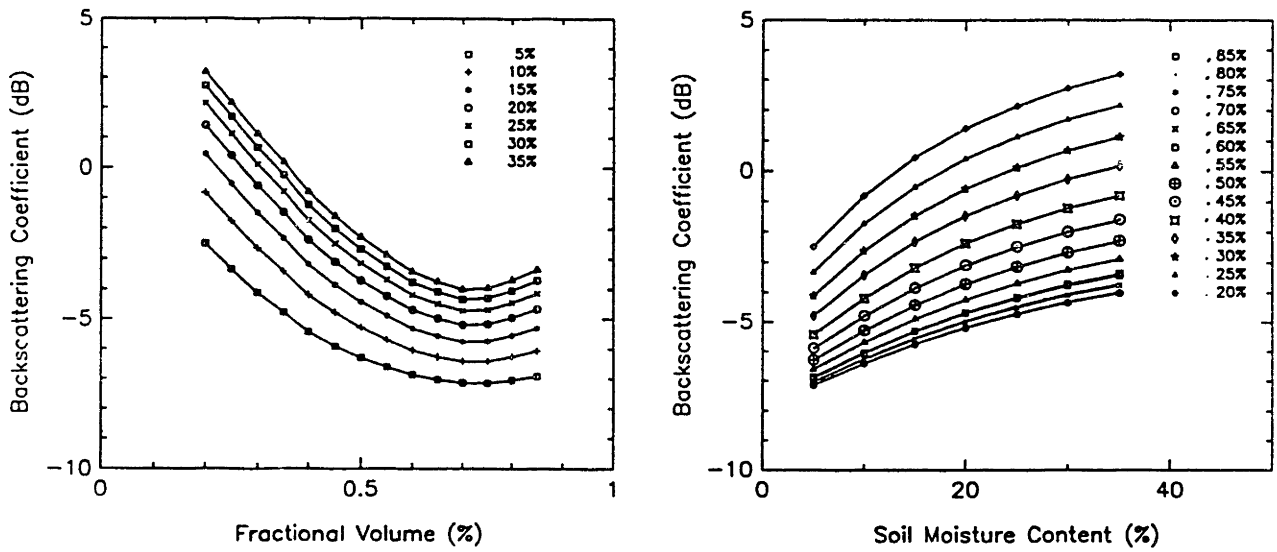

Figure 3.5.15 Simulation of σ_{vv} for old soybean at 10° incident angle

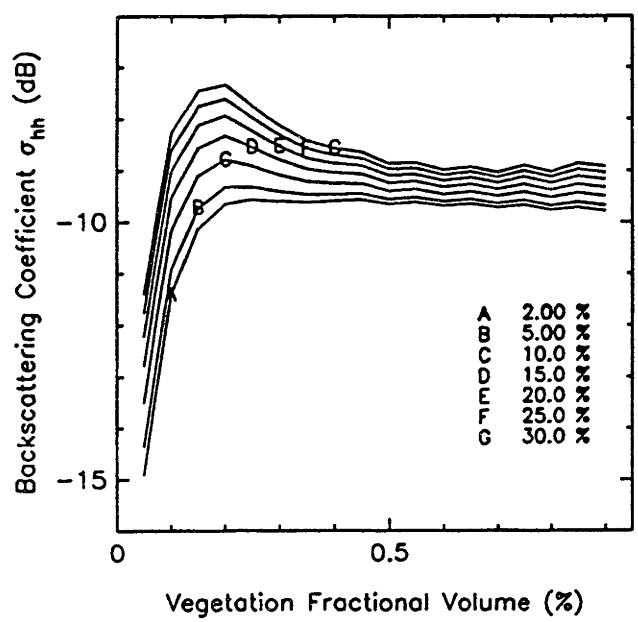

Figure 3.5.16 Simulation of σ_{hh} for young soybean at 40° incident angle

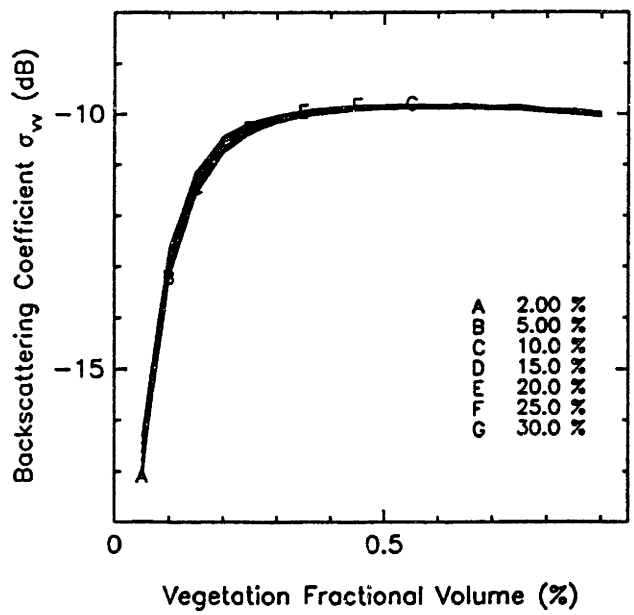

Figure 3.5.17 Simulation of σ_{vv} for young soybean at 40° incident angle

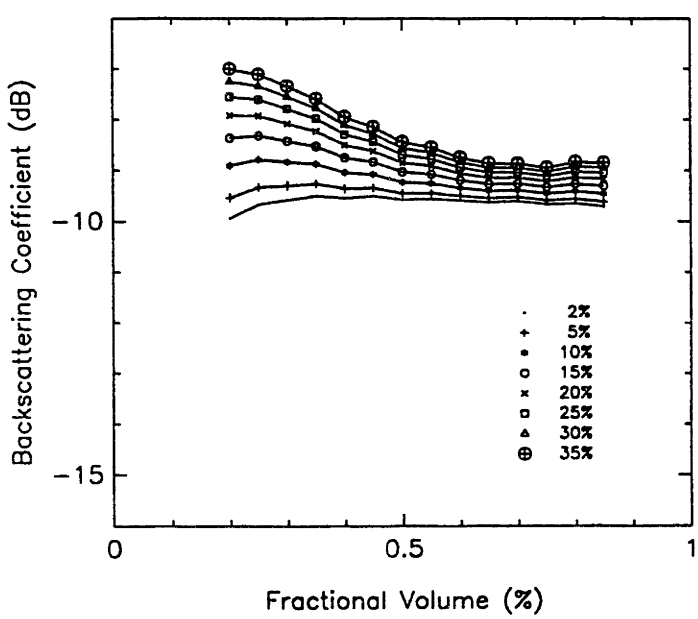

Figure 3.5.18 Simulation of σ_{hh} for old soybean at 40° incident angle

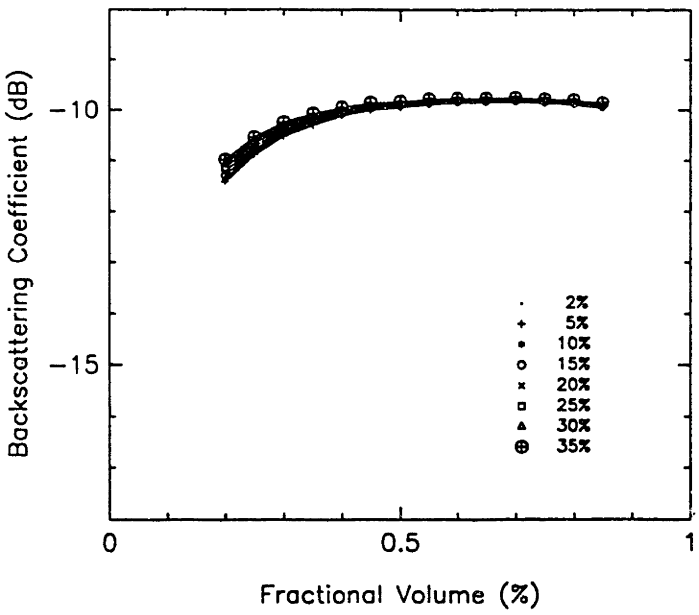

Figure 3.5.19 Simulation of σ_{vv} for old soybean at 40° incident angle

d. Polarization Signatures of Soybean

To study the polarimetric scattering properties, the physical parameters of the soybean are used as input to the model to calculate the polarization signatures (40° incident angle) of the soybean at 10 different growth stages shown in Figure 3.5.20 from mid-July to the end of September 1986. The first observation is that all the signatures have a pedestal; this is due to the non-spherical shape of the soybean leaves. Another observation is that the signatures have almost no distortion; this indicates the azimuthal symmetry of soybean canopy. The signatures also show lower saddle when the soybean fractional volume is lower especially on the first and last dates; this is an indication of whether the wave can reach the soil surface. Thus from the polarization signatures of the soybean, structural information on the soybean canopy can be obtained.

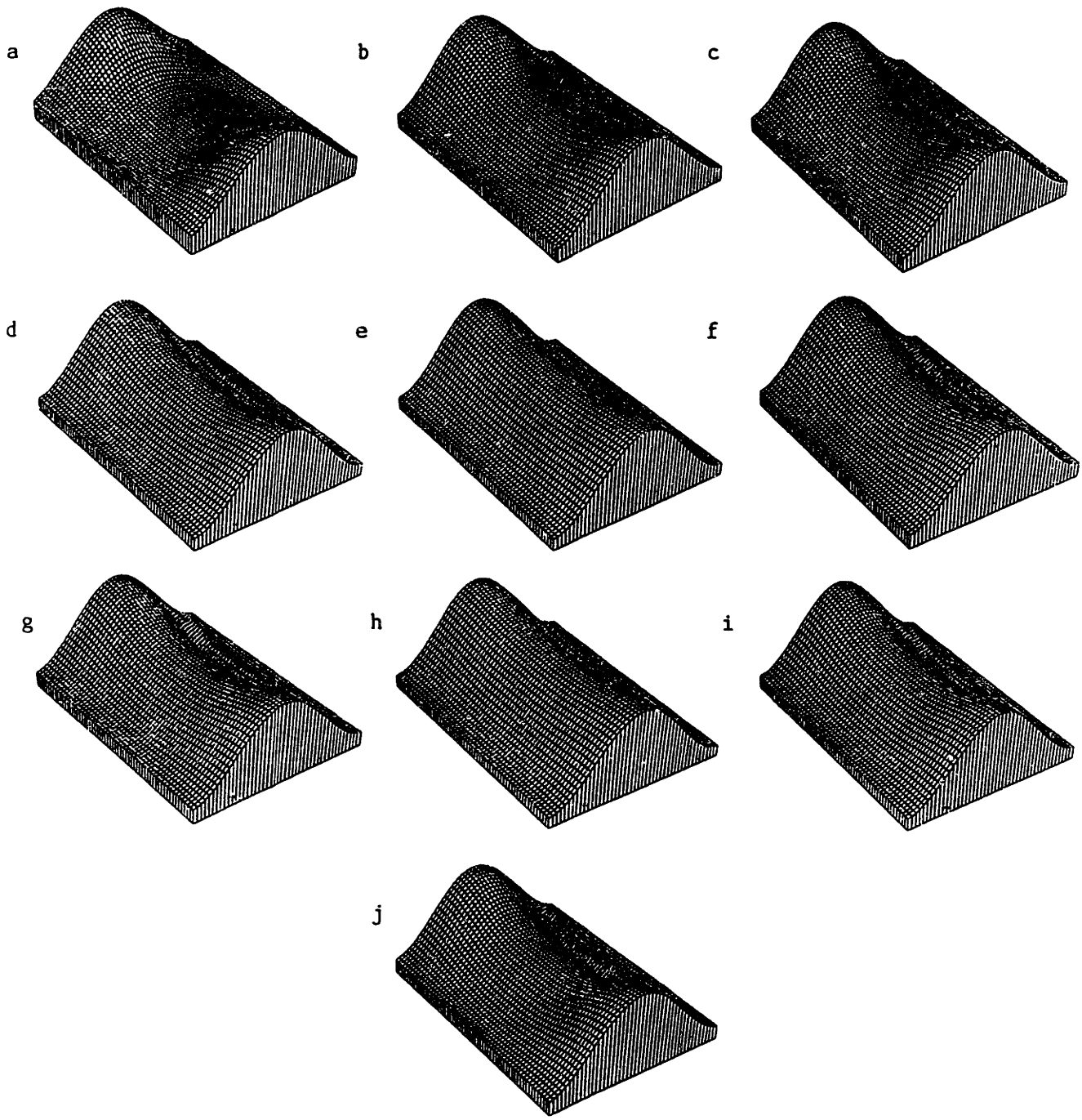

Figure 3.5.20 Copolarized signatures of soybean at 10 different growth stages in chronological order from a to j: In each plot, the long horizontal axis is for orientation angle α [0, 180°], the short horizontal axis for ellipticity angle β [−45°, 45°], and the vertical axis for normalized signature (also see Fig. 4.3 in Chapter 3)

3.6 Summary

In this chapter, the fully polarimetric backscattering coefficients have been obtained with the layer random medium model. The extended strong fluctuation theory is used to calculated the effective permittivities of the scattering layers and the distorted Born approximation is applied to derive the scattered fields. The dyadic Green's functions are used in the calculations and the backscattering processes are explained. The model is applied to explain the backscattering from a soybean canopy. The leaves are considered to have disc-like shape with random orientation. The information conveyed in the elements of the covariance matrix is discussed especially for the correlation coefficient ρ. The copolarized signatures for the layer random media are obtained with the Mueller matrix and explained in the context of polarimetric scattering coefficients. The complete set of polarimetric coefficients convey additional information on the remotely sensed vegetation as compared to the conventional scattering coefficients and thus provide a better means for identification and classification.

Further comparisons with polarimetric scattering data together with ground truth will provide more affirmative validation of the existing models. For vegetation with more complicate physical and structural properties, further model development is necessary to incorporate the complexity. Experimental data are therefore necessitated to validate the new theoretical developments. For fully polarimetry, measured polarimetric scattering coefficients with accurate calibration need be obtained to compare with theoretical results. Sensitivity study using validated model will provide directions for application to inversion of vegetation parameters.

In the last section, the random medium model is used to simulate backscattering coefficients for application to inversion. The temporal and interrelation of biophysical parameters are studied and taken into consideration in the simulation. The results indicate that σ_{hh} and σ_{vv} at incident angles between 10° and 15° under

early young stage or late old stage of the soybean with vegetation fractional volume less than 10% can be used for inversion of soil moisture. The simulated copolarized signatures at various growth stages of the soybean also reveal structural information of the canopy.

Chapter 4
Model with Random Ellipsoidal Scatterers

4.1 Introduction

In this chapter, the layer configuration with scattering regions containing ellipsoidal scatterers is considered. The scatterers are modeled with an ellipsoidal correlation function with the orientation described by a probability density function of the Eulerian rotation angles. The orientation of the scatterers is vertically aligned and azimuthally random. The strong permittivity fluctuation theory is extended to calculate the effective permittivity and the distorted Born approximation is applied to obtain the polarimetric scattering coefficients. The model is then applied to remote sensing of sea ice.

The chapter is organized into six sections. In the next section, the effective permittivity of the inhomogeneous medium is derived with the extended strong fluctuation theory. Section 4.3 presents the calculation of the polarimetric scattering coefficients, under the distorted Born approximation, from the scattering regions in the layer configuration. Section 4.4 shows the comparison between the theoretical results and experimental measurements in the microwave frequency range for first-year sea ice. Section 4.5 simulates polarization signatures and discusses polarimetric scattering properties of sea ice. The chapter is finally summarized in section 4.6.

4.2 Effective Permittivity

In an inhomogeneous medium such as sea ice, sea water is trapped in an ice medium in form of brine inclusions which are usually ellipsoidal. The ice tends to grow vertically downward rendering the ellipsoidal inclusions aligned preferably in the vertical direction. In the absence of sea current, the minor axes of the ellipsoids are horizontal random as seen in Figure 4.2.1. A correlation function corresponding locally to a scatterer is used in the derivation of the effective permittivity with the strong permittivity fluctuation theory extended to account for the horizontally random orientation of the scatterers. When the average process is performed over orientation angle ϕ_f shown in Figure 4.2.2, the effective permittivity is a uniaxial tensor with vertical optic axis describing the azimuthal symmetry of the inhomogeneous medium.

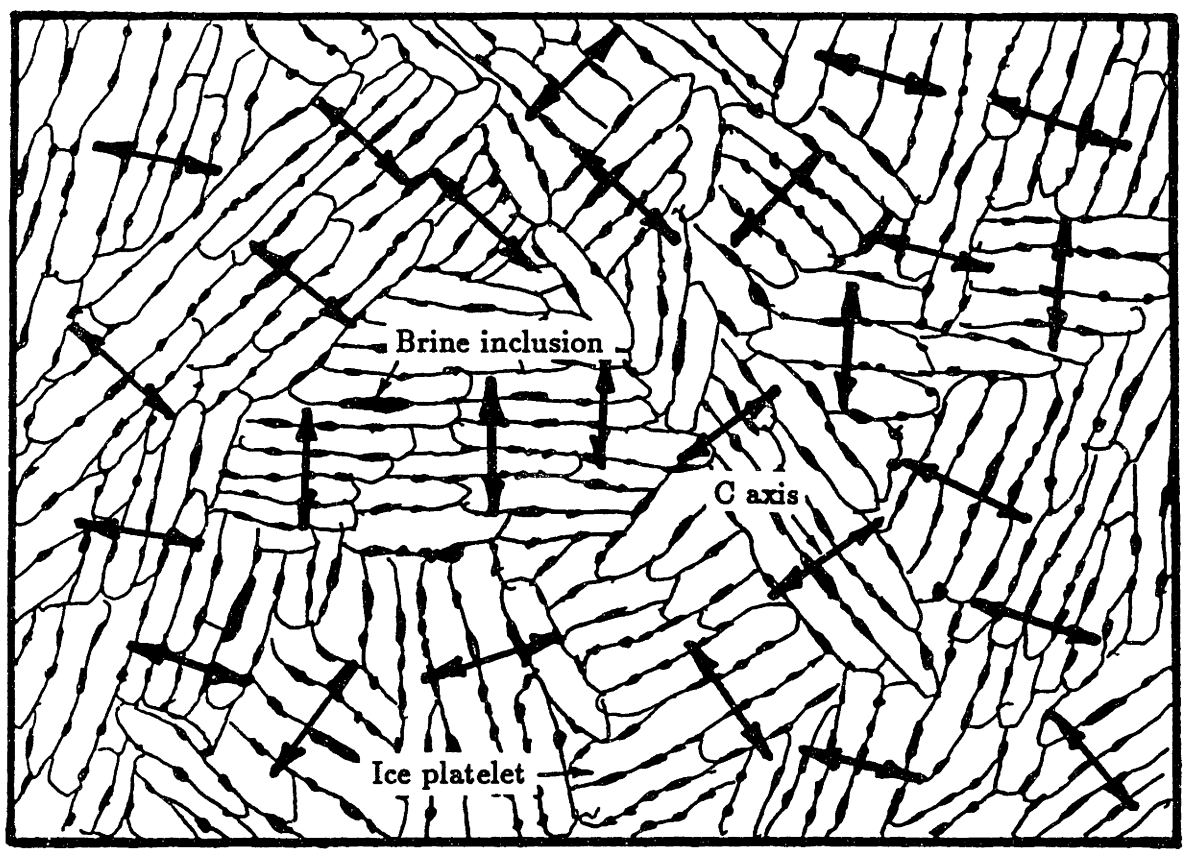

Figure 4.2.1 Drawing of a horizontal section of sea ice : the double-headed arrows denote the azimuthal orientations of the ellipsoidal brine inclusions

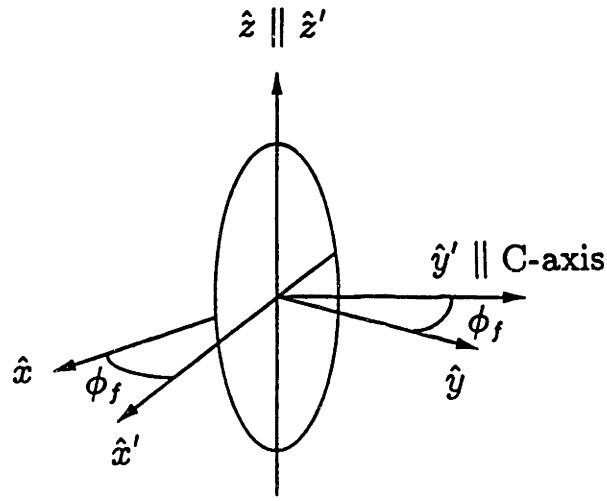

Figure 4.2.2 Geometry of an ellipsoidal scatterer

Let ϵ_b be the permittivity of the host medium and ϵ_s be the permittivity of the embedded ellipsoidal scatterers occupying a total fractional volume of f_s. Similar to the method in Chapter 3, auxiliary permittivity $\overline{\overline{\epsilon}}_g$ is introduced into the wave equation for latter consideration of the singularity in dyadic Green's function $\overline{\overline{G}}_g(\bar{r},\bar{r}')$. The singularity is accounted for by decomposing $\overline{\overline{G}}_g(\bar{r},\bar{r}') = \overline{\overline{G}}_g(\bar{r}-\bar{r}')$ into a principal value part and a Dirac delta part with dyadic coefficient $\overline{\overline{S}}$ which, in this case, is a diagonal tensor with three distinctive diagonal elements $S_{x'}$, $S_{y'}$, and $S_{z'}$ in the local coordinates (x',y',z') which is related to the global coordinates (x,y,z) by the Eulerian rotation tensor

$$\overline{\overline{T}} = \begin{bmatrix} \cos\phi_f & \sin\phi_f & 0 \\ -\sin\phi_f & \cos\phi_f & 0 \\ 0 & 0 & 1 \end{bmatrix} \tag{1}$$

The effective permittivity of the inhomogeneous medium is composed of a quasi-static part and a scattering-effect part which accounts for the modification in the wave speed and attenuation

$$\overline{\overline{\epsilon}}_{eff} = \overline{\overline{\epsilon}}_g + \epsilon_0 \left[\overline{\overline{I}} - \overline{\overline{\xi}}_{eff} \cdot \left\langle \overline{\overline{S}} \right\rangle\right]^{-1} \cdot \overline{\overline{\xi}}_{eff} \tag{2}$$

where auxiliary permittivity $\bar{\bar{\epsilon}}_g$ and dyadic coefficient $\bar{\bar{S}}$ are determined by the condition of secular-term elimination, and the effective dyadic scatterer $\bar{\bar{\xi}}_{eff}$ under the low-frequency approximation is given by

$$\left[\bar{\bar{\xi}}_{eff}\right]_{jm} = \int_0^{2\pi} d\phi_f \, p(\phi_f) \sum_{k,l}^{x,y,z} \Gamma^{(0)}_{\xi jklm} \left\{ k_0^2 \int_{-\infty}^{\infty} d\bar{k}' \left[\bar{\bar{G}}_g(\bar{k}')\right]_{kl} \Phi_\xi(\bar{k}') + \left[\bar{\bar{S}}_2\right]_{kl} \right\} \Big|_{\phi_f} \tag{3}$$

in which $\Gamma^{(0)}_{\xi jklm}$ is the variance, $\bar{\bar{G}}_g$ is the isotropic Green's function (32, Chapter 2) which is invariant under the azimuthal Eulerian rotation (2), Φ_ξ is the Fourier transform of the normalized local correlation function, and $p(\phi_f)$ is the probability density function of orientation angle ϕ_f. As obtained, the effective permittivity is approximated by truncating the series in the renormalization method. The validity condition for the approximation is $\left|\left[\bar{\bar{\xi}}_{eff}(\bar{k})\right]\right|_{jm} \ll 1$.

The ellipsoidal scatterer is described with a normalized local correlation function of the form

$$R_\xi(\bar{r}') = \exp\left(-\sqrt{\frac{x'^2}{\ell_{x'}^2} + \frac{y'^2}{\ell_{y'}^2} + \frac{z'^2}{\ell_{z'}^2}}\right) \tag{4a}$$

with correlation length $\ell_{x'}$, $\ell_{y'}$, and $\ell_{z'}$ in the local coordinates corresponding to the minor, the meridian, and the major axes of the scatterer. In this model, the correlation lengths are related to the effective size and shape of the scatterers. This local correlation function is more general and reducible to spheroidal or spherical shape. Derived from (4), the Fourier transform Φ_ξ is

$$\Phi_\xi(\bar{k}') = \frac{\ell_{x'}\ell_{y'}\ell_{z'}}{\pi^2(1 + k_x'^2\ell_{x'}^2 + k_y'^2\ell_{y'}^2 + k_z'^2\ell_{z'}^2)^2} \tag{4b}$$

For the horizontally random orientation with no preference in azimuthal direction, the probability density function of orientation is simply

$$p(\phi_f) = 1/(2\pi) \tag{5}$$

To calculate the effective permittivity according to (2), $\bar{\bar{\epsilon}}_g$ and $\langle\bar{\bar{S}}\rangle$ need be determined. Due to the global azimuthal symmetry, auxiliary permittivity $\bar{\bar{\epsilon}}_g$ in the

coordinate (x, y, z) has the uniaxial form

$$\bar{\bar{\epsilon}}_g = \begin{bmatrix} \epsilon_{g\rho} & 0 & 0 \\ 0 & \epsilon_{g\rho} & 0 \\ 0 & 0 & \epsilon_{gz} \end{bmatrix} \tag{6}$$

whose elements are subjected to the condition $\langle \bar{\bar{\xi}} \rangle = 0$

$$\langle \bar{\bar{\xi}} \rangle = \int_0^{2\pi} d\phi_f \; p(\phi_f) \bar{\bar{T}}^{-1} \cdot \left\langle \begin{bmatrix} \xi_{x'} & 0 & 0 \\ 0 & \xi_{y'} & 0 \\ 0 & 0 & \xi_{z'} \end{bmatrix} \right\rangle \cdot \bar{\bar{T}}$$

$$= \frac{1}{2} \left\langle \begin{bmatrix} \xi_{x'} + \xi_{y'} & 0 & 0 \\ 0 & \xi_{x'} + \xi_{y'} & 0 \\ 0 & 0 & 2\xi_{z'} \end{bmatrix} \right\rangle = 0 \tag{7}$$

In (7), local quantities $\xi_{x'}$, $\xi_{y'}$, and $\xi_{z'}$ are related to the elements of $\bar{\bar{S}}$ by

$$\xi_{x'}(\epsilon) = \frac{\epsilon - \epsilon_{g\rho}}{\epsilon_0 + S_{x'}(\epsilon - \epsilon_{g\rho})} \tag{8a}$$

$$\xi_{y'}(\epsilon) = \frac{\epsilon - \epsilon_{g\rho}}{\epsilon_0 + S_{y'}(\epsilon - \epsilon_{g\rho})} \tag{8b}$$

$$\xi_{z'}(\epsilon) = \frac{\epsilon - \epsilon_{gz}}{\epsilon_0 + S_{z'}(\epsilon - \epsilon_{gz})} \tag{8c}$$

where ϵ can takes on the value of ϵ_s in a scatterer or ϵ_b in the background medium. By combining (7) and (8), $\epsilon_{g\rho}$ and ϵ_{gz} can be written as

$$\epsilon_{g\rho} = \epsilon_b + f_s \frac{\epsilon_s - \epsilon_{g\rho}}{1 - f_s} \frac{2\epsilon_0 + (S_{x'} + S_{y'})(\epsilon_s - \epsilon_{g\rho})}{2\epsilon_0 + (S_{x'} + S_{y'})(\epsilon_b - \epsilon_{g\rho})} \frac{\epsilon_0 + S_{x'}(\epsilon_b - \epsilon_{g\rho})}{\epsilon_0 + S_{x'}(\epsilon_s - \epsilon_{g\rho})} \frac{\epsilon_0 + S_{y'}(\epsilon_b - \epsilon_{g\rho})}{\epsilon_0 + S_{y'}(\epsilon_s - \epsilon_{g\rho})} \tag{9a}$$

$$\epsilon_{gz} = \epsilon_b + f_s \frac{\epsilon_s - \epsilon_{gz}}{1 - f_s} \frac{\epsilon_0 + S_{z'}(\epsilon_b - \epsilon_{gz})}{\epsilon_0 + S_{z'}(\epsilon_s - \epsilon_{gz})} \tag{9b}$$

The average dyadic coefficient $\langle \bar{\bar{S}} \rangle$ in the global coordinates is obtained by the averaging integration over the probability density function of orientation

$$\langle \bar{\bar{S}} \rangle = \int_0^{2\pi} d\phi_f \; p(\phi_f) \bar{\bar{T}}^{-1} \cdot \begin{bmatrix} S_{x'} & 0 & 0 \\ 0 & S_{y'} & 0 \\ 0 & 0 & S_{z'} \end{bmatrix} \cdot \bar{\bar{T}}$$

$$= \frac{1}{2}\begin{bmatrix} S_{x'} + S_{y'} & 0 & 0 \\ 0 & S_{x'} + S_{y'} & 0 \\ 0 & 0 & 2S_{z'} \end{bmatrix} = \begin{bmatrix} S_\rho & 0 & 0 \\ 0 & S_\rho & 0 \\ 0 & 0 & S_z \end{bmatrix} \tag{10}$$

where $S_{x'}$, $S_{y'}$, and $S_{z'}$ are derived from the secular elimination condition [17] which renders

$$S_{x'} = \int_0^{2\pi} d\phi \, \frac{\epsilon_0 \gamma_x^2 \cos^2\phi}{2\pi \epsilon_{g\rho} a\sqrt{a}} \left[(1+a)\tan^{-1}\sqrt{a} - \sqrt{a}\right] \tag{11a}$$

$$S_{y'} = \int_0^{2\pi} d\phi \, \frac{\epsilon_0 \gamma_y^2 \sin^2\phi}{2\pi \epsilon_{g\rho} a\sqrt{a}} \left[(1+a)\tan^{-1}\sqrt{a} - \sqrt{a}\right] \tag{11b}$$

$$S_{z'} = \int_0^{2\pi} d\phi \, \frac{\epsilon_0 (1+a)}{2\pi \epsilon_{gz} a\sqrt{a}} \left[\sqrt{a} - \tan^{-1}\sqrt{a}\right] \tag{11c}$$

where the integrations over ϕ can be carried out numerically and a, γ_x, and γ_y are defined as

$$a = \alpha\gamma^2 - 1, \quad \alpha = \frac{\epsilon_{gz}}{\epsilon_{g\rho}} \tag{12a}$$

$$\gamma = \frac{1}{\ell_{x'}} \left(\frac{\cos^2\phi}{\ell_{x'}^2} + \frac{\sin^2\phi}{\ell_{y'}^2}\right)^{-\frac{1}{2}} \tag{12b}$$

$$\gamma_x = \frac{1}{\ell_{x'}} \left(\frac{\cos^2\phi}{\ell_{x'}^2} + \frac{\sin^2\phi}{\ell_{y'}^2}\right)^{-\frac{1}{2}} \tag{12c}$$

$$\gamma_y = \frac{1}{\ell_{y'}} \left(\frac{\cos^2\phi}{\ell_{x'}^2} + \frac{\sin^2\phi}{\ell_{y'}^2}\right)^{-\frac{1}{2}} \tag{12d}$$

Also due to the azimuthal symmetry, the effective scatterer tensor ξ_{eff} has the uniaxial form

$$\bar{\bar{\xi}}_{eff} = \begin{bmatrix} \xi_{eff\rho} & 0 & 0 \\ 0 & \xi_{eff\rho} & 0 \\ 0 & 0 & \xi_{effz} \end{bmatrix} \tag{13}$$

which is obtained by substituting the Green's function, the correlation function, and the probability density function of orientation into (3). The integration method has been discussed in Chapter 2 and 3. Followed is how to calculate $\bar{\bar{\xi}}_{eff}$:

$$\xi_{eff\rho} = \frac{1}{2}\left[\delta_{\xi x'}(I_{x'} + S_{x'}) + \delta_{\xi y'}(I_{y'} + S_{y'})\right] \tag{14a}$$

$$\xi_{effz} = \delta_{\xi z'}(I_{z'} + S_{z'}) \tag{14b}$$

The variance δ_ξ's in (14) are determined by

$$\delta_{\xi x'} = \left[\frac{\epsilon_b - \epsilon_{g\rho}}{\epsilon_0 + S_{x'}(\epsilon_b - \epsilon_{g\rho})}\right]^2 (1-f_s) + \left[\frac{\epsilon_s - \epsilon_{g\rho}}{\epsilon_0 + S_{x'}(\epsilon_s - \epsilon_{g\rho})}\right]^2 f_{s2} \tag{15a}$$

$$\delta_{\xi y'} = \left[\frac{\epsilon_b - \epsilon_{g\rho}}{\epsilon_0 + S_{y'}(\epsilon_b - \epsilon_{g\rho})}\right]^2 (1-f_s) + \left[\frac{\epsilon_s - \epsilon_{g\rho}}{\epsilon_0 + S_{y'}(\epsilon_s - \epsilon_{g\rho})}\right]^2 f_{s2} \tag{15b}$$

$$\delta_{\xi z'} = \left[\frac{\epsilon_b - \epsilon_{gz}}{\epsilon_0 + S_{z'}(\epsilon_b - \epsilon_{gz})}\right]^2 (1-f_s) + \left[\frac{\epsilon_s - \epsilon_{gz}}{\epsilon_0 + S_{z'}(\epsilon_s - \epsilon_{gz})}\right]^2 f_s \tag{15c}$$

To complete the derivation of the anisotropic effective permittivity, expressions for $I_{x'}$, $I_{y'}$, and $I_{z'}$ are found. The result for $I_{z'}$ is

$$I_{z'} = \int_0^{2\pi} d\phi \, \frac{-\epsilon_0}{\pi \epsilon_{gz'}} (\mathcal{I}_\phi^s + \mathcal{I}_\phi^d) \tag{16a}$$

$$\mathcal{I}_\phi^s = -\frac{\alpha\gamma^2\sqrt{\alpha\gamma^2}}{2a^2}\left[\frac{\sqrt{-\zeta}}{\vartheta_e} + \frac{\vartheta_e + \zeta}{\vartheta_e\sqrt{\vartheta_e}}\left(\frac{\pi}{2} - \tan^{-1}\frac{\sqrt{-\zeta}}{\sqrt{\vartheta_e}}\right)\right] \tag{16b}$$

$$\mathcal{I}_\phi^d = \frac{\alpha\gamma^2}{2a^2}\left[\frac{1+a\nu_{gz'}^2}{\vartheta_o} + \frac{\vartheta_o(a+2) - (b+a\nu_{gz'}^2)}{\vartheta_o\sqrt{\vartheta_o}}\left(\frac{\pi}{2} - \tan^{-1}\frac{1}{\sqrt{\vartheta_o}}\right)\right] \tag{16c}$$

$$\nu_{gz'}^2 = k_{g\rho}^2 \ell_{z'}^2, \quad k_{g\rho}^2 = \omega^2\mu_0\epsilon_{g\rho}, \quad \zeta = \alpha\gamma^2\nu_{gz'}^2 \tag{16d}$$

$$b = \frac{\alpha\gamma^2 + \zeta}{a}, \quad \vartheta_o = b - 1, \quad \vartheta_e = b + \zeta \tag{16e}$$

For $I_{x'}$, the result is expressed as follows

$$I_{x'} = \int_0^{2\pi} d\phi \, \frac{k_0^2}{\pi}\left(\ell_{y'}^2\gamma_y^4 \sin^2\phi \; I_\phi^o + \ell_{x'}^2\gamma_x^4 \cos^2\phi \; I_\phi^e\right) \tag{17a}$$

$$I_\phi^e = \alpha\left[(\mathcal{I}_1^e - \mathcal{I}_2^e - \mathcal{I}_3^e) + \frac{1}{\zeta}(\mathcal{I}_s + \mathcal{I}_d - \frac{1}{2})\right] \tag{17b}$$

$$I_\phi^o = \mathcal{I}_1^o - \mathcal{I}_2^o - \mathcal{I}_3^o \tag{17c}$$

$$\mathcal{I}_1^e = \frac{\alpha\gamma^2\sqrt{\alpha\gamma^2}}{2a^2\vartheta_e}\left[-\frac{\sqrt{-\zeta}}{b} + \frac{1}{\sqrt{\vartheta_e}}\left(\frac{\pi}{2} - \tan^{-1}\frac{\sqrt{-\zeta}}{\sqrt{\vartheta_e}}\right)\right] \tag{17d}$$

$$\mathcal{I}_2^e = \frac{1}{2a\vartheta_o}\left[1 - \frac{1}{\sqrt{\vartheta_o}}\left(\frac{\pi}{2} - \tan^{-1}\frac{1}{\sqrt{\vartheta_o}}\right)\right] \tag{17e}$$

$$\mathcal{I}_3^e = \frac{\alpha\gamma^2}{2a^2\vartheta_o}\left[-\frac{1}{b} + \frac{1}{\sqrt{\vartheta_o}}\left(\frac{\pi}{2} - \tan^{-1}\frac{1}{\sqrt{\vartheta_o}}\right)\right] \tag{17f}$$

$$\mathcal{I}_1^o = \mathcal{I}_1^e(\alpha = 1), \quad \mathcal{I}_2^o = \mathcal{I}_2^e(\alpha = 1), \quad \mathcal{I}_3^o = \mathcal{I}_3^e(\alpha = 1) \tag{17g}$$

From the symmetry, $I_{y'}(\ell_{x'},\ell_{y'},\ell_{z'}) = I_{x'}(\ell_{y'},\ell_{x'},\ell_{z'})$. Explicitly, the result for $I_{y'}$ is

$$I_{y'} = \int_0^{2\pi} d\phi\ \frac{k_0^2}{\pi}\left(\ell_{x'}^2\gamma_x^4\cos^2\phi\ I_\phi^o + \ell_{y'}^2\gamma_y^4\sin^2\phi\ I_\phi^e\right) \tag{18}$$

Substituting $\bar{\bar{\epsilon}}_g$, $\langle\overline{\overline{S}}\rangle$, and $\bar{\bar{\xi}}_{eff}$ in (2) yields the uniaxial effective permittivity tensor $\bar{\bar{\epsilon}}_{eff}$ whose lateral and vertical elements are, respectively

$$\epsilon_{eff\rho} = \epsilon_{g\rho} + \epsilon_0\xi_{eff\rho}/(1 - S_\rho\xi_{eff\rho}) \tag{19a}$$

$$\epsilon_{effz} = \epsilon_{gz} + \epsilon_0\xi_{effz}/(1 - S_z\xi_{effz}) \tag{19b}$$

As seen from the above expressions, effective permittivity $\bar{\bar{\epsilon}}_{eff}$ is anisotropic with optic axis in the vertical direction. In the next section, the anisotropic effective permittivity is used in the derivation of the polarimetric backscattering coefficients under the distorted Born approximation with Green's function (DGF) of the layer configuration.

4.3 Scattering Coefficients

The layer configuration in Chapter 2 is used here except that the scatterers in the random media are more general in terms of shapes and orientations. The scatterers in region 1 are allowed to be randomly oriented spheroids as described in Chapter 3. In region 2, the scatterers are ellipsoids vertically aligned and randomly oriented in azimuthal directions. Definition (13, Chapter 1) is used to calculate polarimetric backscattering coefficients with ensemble averages of scattered fields. The averages are calculated with spatial integrations over products of the DGFs, the mean fields, and the correlation functions as follows

$$\begin{aligned}\left\langle \overline{E}_{0s}(\overline{r})\cdot\overline{E}_{0s}^*(\overline{r})\right\rangle = &\sum_{i,j,k,l,m}^{x,y,z} k_0^4\int_0^\pi d\psi_f\int_0^{2\pi} d\phi_f\ p_1(\psi_f,\phi_f)\int_{V_1} d\overline{r}_1\int_{V_1} d\overline{r}_1^o\, C_{\xi 1jklm}(\overline{r}_1,\overline{r}_1^o;\psi_f,\phi_f)\\ &\cdot\left[\left\langle G_{01ij}(\overline{r},\overline{r}_1)\right\rangle\left\langle F_{1k}(\overline{r}_1)\right\rangle\right]\cdot\left[\left\langle G_{01il}(\overline{r},\overline{r}_1^o)\right\rangle\left\langle F_{1m}(\overline{r}_1^o)\right\rangle\right]^*\\ &+\sum_{i,j,k,l,m}^{x,y,z} k_0^4\int_0^{2\pi} d\phi_f\ p_2(\phi_f)\int_{V_2} d\overline{r}_2\int_{V_2} d\overline{r}_2^o\, C_{\xi 2jklm}(\overline{r}_2,\overline{r}_2^o;\phi_f)\\ &\cdot\left[\left\langle G_{02ij}(\overline{r},\overline{r}_2)\right\rangle\left\langle F_{2k}(\overline{r}_2)\right\rangle\right]\cdot\left[\left\langle G_{02il}(\overline{r},\overline{r}_2^o)\right\rangle\left\langle F_{2m}(\overline{r}_2^o)\right\rangle\right]^*\end{aligned} \tag{20}$$

The DGFs and the mean fields have been obtained in Chapter 2; the correlation functions need to be determined next. The integrations are then effectuated to derive the scattering coefficients.

The correlation functions C's in (20) are defined by (12, Chapter 2) for region 1. In region 2, the correlation functions in the global spatial domain are

$$C_{\xi 2jklm}(\overline{r}_2, \overline{r}_2^o, \phi_f) = \left\langle \xi_{2jk}(\overline{r}_2)\xi_{2lm}^*(\overline{r}_2^o)\middle|\phi_f(\overline{r}_2)\right\rangle \tag{21}$$

To facilitate the integration of (20), Fourier transforms of the correlation functions are introduced for the statistically homogeneous scattering media under consideration

$$C_{\xi 2jklm}(\overline{r}_2, \overline{r}_2^o, \phi_f) = \int_{-\infty}^{\infty} d\overline{\beta}\Phi_{2jklm}(\overline{\beta})e^{-i\overline{\beta}\cdot(\overline{r}_2-\overline{r}_2^o)} \tag{22}$$

which is expressed in the global coordinate system $(\hat{x}, \hat{y}, \hat{z})$ and related by the Eulerian rotation transformation $\overline{\overline{T}}$ (1) to the following non-zero correlations in the local coordinate system $(\hat{x}', \hat{y}', \hat{z}')$

$$\Phi_{2x'x'}(\overline{\beta}') = \Phi_{2x'x'x'x'}(\overline{\beta}') = \delta_{2x'x'}\Phi_{\xi 2}(\overline{\beta}') \tag{23a}$$

$$\Phi_{2x'y'}(\overline{\beta}') = \Phi_{2x'x'y'y'}(\overline{\beta}') = \delta_{2x'y'}\Phi_{\xi 2}(\overline{\beta}') \tag{23b}$$

$$\Phi_{2x'z'}(\overline{\beta}') = \Phi_{2x'x'z'z'}(\overline{\beta}') = \delta_{2x'z'}\Phi_{\xi 2}(\overline{\beta}') \tag{23c}$$

$$\Phi_{2y'x'}(\overline{\beta}') = \Phi_{2y'y'x'x'}(\overline{\beta}') = \delta_{2y'x'}\Phi_{\xi 2}(\overline{\beta}') \tag{23d}$$

$$\Phi_{2y'y'}(\overline{\beta}') = \Phi_{2y'y'y'y'}(\overline{\beta}') = \delta_{2y'y'}\Phi_{\xi 2}(\overline{\beta}') \tag{23e}$$

$$\Phi_{2y'z'}(\overline{\beta}') = \Phi_{2y'y'z'z'}(\overline{\beta}') = \delta_{2y'z'}\Phi_{\xi 2}(\overline{\beta}') \tag{23f}$$

$$\Phi_{2z'x'}(\overline{\beta}') = \Phi_{2z'z'x'x'}(\overline{\beta}') = \delta_{2z'x'}\Phi_{\xi 2}(\overline{\beta}') \tag{23g}$$

$$\Phi_{2z'y'}(\overline{\beta}') = \Phi_{2z'z'y'y'}(\overline{\beta}') = \delta_{2z'y'}\Phi_{\xi 2}(\overline{\beta}') \tag{23h}$$

$$\Phi_{2z'z'}(\overline{\beta}') = \Phi_{2z'z'z'z'}(\overline{\beta}') = \delta_{2z'z'}\Phi_{\xi 2}(\overline{\beta}') \tag{23i}$$

where $\Phi_{\xi 2}(\overline{\beta}')$ given in (4b) is the Fourier transform of (4a) and the variance δ_2's in (23) are

$$\delta_{2x'x'} = \left|\frac{\epsilon_{b2}-\epsilon_{g2\rho}}{\epsilon_0+S_{2x'}(\epsilon_{b2}-\epsilon_{g2\rho})}\right|^2(1-f_{s2})+\left|\frac{\epsilon_{s2}-\epsilon_{g2\rho}}{\epsilon_0+S_{2x'}(\epsilon_{s2}-\epsilon_{g2\rho})}\right|^2 f_{s2} \tag{24a}$$

$$\delta_{2y'y'}=\left|\frac{\epsilon_{b2}-\epsilon_{g2\rho}}{\epsilon_0+S_{2y'}(\epsilon_{b2}-\epsilon_{g2\rho})}\right|^2(1-f_{s2})+\left|\frac{\epsilon_{s2}-\epsilon_{g2\rho}}{\epsilon_0+S_{2y'}(\epsilon_{s2}-\epsilon_{g2\rho})}\right|^2 f_{s2} \tag{24b}$$

$$\delta_{2z'z'}=\left|\frac{\epsilon_{b2}-\epsilon_{g2z}}{\epsilon_0+S_{2z'}(\epsilon_{b2}-\epsilon_{g2z})}\right|^2(1-f_{s2})+\left|\frac{\epsilon_{s2}-\epsilon_{g2z}}{\epsilon_0+S_{2z'}(\epsilon_{s2}-\epsilon_{g2z})}\right|^2 f_{s2} \tag{24c}$$

$$\begin{aligned}\delta_{2x'y'}=&\left[\frac{\epsilon_{b2}-\epsilon_{g2\rho}}{\epsilon_0+S_{2x'}(\epsilon_{b2}-\epsilon_{g2\rho})}\right]\left[\frac{\epsilon_{b2}-\epsilon_{g2\rho}}{\epsilon_0+S_{2y'}(\epsilon_{b2}-\epsilon_{g2\rho})}\right]^*(1-f_{s2})\\&+\left[\frac{\epsilon_{s2}-\epsilon_{g2\rho}}{\epsilon_0+S_{2x'}(\epsilon_{s2}-\epsilon_{g2\rho})}\right]\left[\frac{\epsilon_{s2}-\epsilon_{g2\rho}}{\epsilon_0+S_{2y'}(\epsilon_{s2}-\epsilon_{g2\rho})}\right]^* f_{s2}=\delta^*_{2y'x'}\end{aligned} \tag{24d}$$

$$\begin{aligned}\delta_{2x'z'}=&\left[\frac{\epsilon_{b2}-\epsilon_{g2\rho}}{\epsilon_0+S_{2x'}(\epsilon_{b2}-\epsilon_{g2\rho})}\right]\left[\frac{\epsilon_{b2}-\epsilon_{g2z}}{\epsilon_0+S_{2z'}(\epsilon_{b2}-\epsilon_{g2z})}\right]^*(1-f_{s2})\\&+\left[\frac{\epsilon_{s2}-\epsilon_{g2\rho}}{\epsilon_0+S_{2x'}(\epsilon_{s2}-\epsilon_{g2\rho})}\right]\left[\frac{\epsilon_{s2}-\epsilon_{g2z}}{\epsilon_0+S_{2z'}(\epsilon_{s2}-\epsilon_{g2z})}\right]^* f_{s2}=\delta^*_{2z'x'}\end{aligned} \tag{24e}$$

$$\begin{aligned}\delta_{2y'z'}=&\left[\frac{\epsilon_{b2}-\epsilon_{g2\rho}}{\epsilon_0+S_{2y'}(\epsilon_{b2}-\epsilon_{g2\rho})}\right]\left[\frac{\epsilon_{b2}-\epsilon_{g2z}}{\epsilon_0+S_{2z'}(\epsilon_{b2}-\epsilon_{g2z})}\right]^*(1-f_{s2})\\&+\left[\frac{\epsilon_{s2}-\epsilon_{g2\rho}}{\epsilon_0+S_{2y'}(\epsilon_{s2}-\epsilon_{g2\rho})}\right]\left[\frac{\epsilon_{s2}-\epsilon_{g2z}}{\epsilon_0+S_{2z'}(\epsilon_{s2}-\epsilon_{g2z})}\right]^* f_{s2}=\delta^*_{2z'y'}\end{aligned} \tag{24f}$$

Based on the invariant property of the Fourier transform under the rotation transformation, spectral density $\Phi_{2jklm}(\overline{\beta})$ in the global coordinates can functionally be related to those given in (24) with

$$\begin{aligned}\Phi_{\xi 2}(\overline{\beta})=\Phi_{\xi 2}(\beta'_x&=\beta_x\cos\phi_f+\beta_y\sin\phi_f,\\ \beta'_y&=-\beta_x\sin\phi_f+\beta_y\cos\phi_f,\\ \beta'_z&=\beta_z)\end{aligned} \tag{25}$$

In the global coordinates, the rotation transformation together with the above invariant property cast the anisotropic spectral densities into the form

$$\Phi_{2jklm}(\overline{\beta})=\delta_{2jklm}\Phi_{\xi 2}(\overline{\beta}) \tag{26}$$

where variance δ_{2jklm} are dependent on the Eulerian angle ϕ_f as

$$\delta_{2jklm}=(\delta_{2x'x'}T_{xxjk}+\delta_{2y'x'}T_{yyjk}+\delta_{2z'x'}T_{zzjk})\,T_{xxlm}$$

$$+ (\delta_{2x'y'} T_{xxjk} + \delta_{2y'y'} T_{yyjk} + \delta_{2z'y'} T_{zzjk})\, T_{yylm}$$

$$+ (\delta_{2x'z'} T_{xxjk} + \delta_{2y'z'} T_{yyjk} + \delta_{2z'z'} T_{zzjk})\, T_{zzlm} \tag{27}$$

The Eulerian rotation has been applied to arrived at (27) where T's are elements of the following transforming tensors

$$\overline{\overline{T}}_{xx} = \begin{bmatrix} \cos^2\phi_f & \sin\phi_f\cos\phi_f & 0 \\ \sin\phi_f\cos\phi_f & \sin^2\phi_f & 0 \\ 0 & 0 & 0 \end{bmatrix} \tag{28a}$$

$$\overline{\overline{T}}_{yy} = \begin{bmatrix} \sin^2\phi_f & -\sin\phi_f\cos\phi_f & 0 \\ -\sin\phi_f\cos\phi_f & \cos^2\phi_f & 0 \\ 0 & 0 & 0 \end{bmatrix} \tag{28b}$$

$$\overline{\overline{T}}_{zz} = \begin{bmatrix} 0 & 0 & 0 \\ 0 & 0 & 0 \\ 0 & 0 & 1 \end{bmatrix} = \overline{\overline{I}} - \overline{\overline{T}}_{xx} - T_{yy} \tag{28c}$$

By substituting the above correlation functions, the dyadic Green's functions of the layer medium, and the mean fields into (20), the correlations of the scattered field can now be found. Rearranging all the coefficients from the DGF and mean fields, the scattering coefficients can be written as

$$\sigma_{\mu\tau\nu\kappa} = \pi k_0^4 \int_0^{\pi} d\psi_f \int_0^{2\pi} d\phi_f \; p_1(\psi_f, \phi_f) \sum_{a,b,c,d}^{-1,1} \sum_{j,k,l,m}^{x,y,z} \Psi^{ab}_{1\mu\tau,jk} \Psi^{cd*}_{1\nu\kappa,lm} \mathcal{I}^{abcd}_{1jklm}$$

$$+ \pi k_0^4 \int_0^{2\pi} d\phi_f \; p_2(\phi_f) \sum_{p,q,r,s}^{\substack{ou,od \\ eu,ed}} \sum_{j,k,l,m}^{x,y,z} \Psi^{pq}_{2\mu\tau,jk} \Psi^{rs*}_{2\nu\kappa,lm} \mathcal{I}^{pqrs}_{2jklm} \tag{29}$$

As mentioned previously, region 2 contains scatterers with preferred vertical alignment which effectively render the medium anisotropic. The ordinary and extraordinary waves going down and up give rise to 216 terms in the second terms of (26) as discussed in Chapter 2. All coefficient Ψ_2's as well as $\mathcal{I}^{abcd}_{1jklm}$ have been derived in the previous chapters. For $\mathcal{I}^{pqrs}_{2jklm}$, the result is

$$\mathcal{I}^{pqrs}_{2jklm} = i \frac{2\delta_{2jklm} \ell_{2x'} \ell_{2y'} \ell_{2z'}}{\pi \mathcal{L}_2^4} \left[\frac{e^{-i(\kappa_{pq} - \kappa_{rs})d_2}}{(\kappa_{pq} - \kappa_2)^2 (\kappa_{pq} - \kappa_2^*)^2 (\kappa_{pq} - \kappa_{rs})} \right.$$

$$\left. + \frac{e^{i(\kappa_{rs} - \kappa_{pq})d_1}}{(\kappa_{rs} - \kappa_2)^2 (\kappa_{rs} - \kappa_2^*)^2 (\kappa_{rs} - \kappa_{pq})} - \mathcal{P}_2(\kappa_2) - \mathcal{Q}_2(\kappa_2^*) \right] \tag{30}$$

where the functional form of $\mathcal{P}_2(\kappa_2)$ and $\mathcal{Q}_2(\kappa_2^*)$ are respectively given in (25b-c, Chapter 3) with length $\mathcal{L}_2 = \ell_{2x'}$. In this case, pole κ_2 is

$$\kappa_2 = i\mathcal{L}_2^{-1}\sqrt{1 + k_{\phi x}^2 \ell_{2x'}^2 + k_{\phi y}^2 \ell_{2y'}^2} \tag{31}$$

The remaining integrations over Eulerian angles can be carried out numerically. When low-frequency condition is valid, the integrations are done analytically (see Chapter 5). It is worth noting again that (29) expresses the scattering coefficients in the scattered basis which can be transformed to incident basis by changing the sign of $\sigma_{h\tau v\kappa}$ and $\sigma_{v\tau h\kappa}$. The scattering effect of the rough boundaries at the medium interfaces can also be estimated by incoherently adding the total contribution from the rough surface scattering with consideration of the propagation loss to calculate the scattering coefficients. Compared with the model in Chapter 2 for the case of vertically oriented spheroids, the new model gives higher co-polarized backscattering coefficients due to higher total cross section of the ellipsoids for the same fractional volume. Another difference is that the new model provides non-zero cross-polarized backscattering in the first-order distorted Born term whereas the former can only account for the cross-polarized return in the second or higher order term when the spheroids are vertically oriented.

In this section, the strong fluctuation theory is extended to calculate the effective permittivity of an inhomogeneous medium containing ellipsoidal scatterers. The ellipsoids are aligned in the vertical direction but randomly oriented in azimuthal directions. Effectively, the inhomogeneous medium becomes uniaxial with vertical optic axis. To calculate the polarimetric backscattering coefficients, the distorted Born approximation is invoked and the dyadic Green's function for the layer configuration including the anisotropic layer is used. In the next section, the theoretical results are compared with experimental data for sea ice. The model is then applied to study the polarimetric scattering properties and polarization signatures from different ice types.

4.4 Results and Discussion

a. Data Comparisons

In this subsection, theoretical results are compared with experimental measurements for backscattering coefficients at 9 GHz as a function of incident angle. The scattering configuration is illustrated in Figure 4.4.1: layer 1 is air, layer 2 is sea ice, and layer 3 is sea water. The radar backscatter data were taken for the thick first-year sea ice near Point Barrow, AK [86]. The ice layer was 1.65-m thick and contained brine inclusions. From ground-truth data, it has been inferred [87] that the brine had a permittivity of $\epsilon_{s1} = (38+41)\epsilon_0$ and occupied a fractional volume of $f_{s1} = 4.5\%$. The background ice permittivity was estimated to be $\epsilon_{b1} = (3.15 + i0.002)\epsilon_0$ and the permittivity of sea water to be $\epsilon_2 = (45 + i40)\epsilon_0$. With correlation length $\ell_{1x'} = 0.70$ mm, $\ell_{1x'} = 0.25$ mm, and $\ell_{1z'} = 1.20$ mm, the theoretical results match well with the experimental data, as shown in Figure 4.2.2, for co-polarized backscattering coefficient σ_{hh} and σ_{vv} at large incident angles and cross-polarized backscattering coefficient σ_{vh} over the range of incident angles.

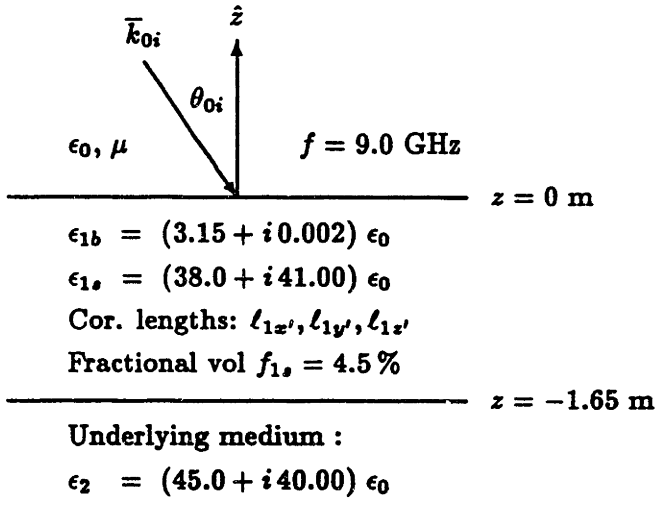

Figure 4.4.1 Scattering configuration of sea ice with flat surface

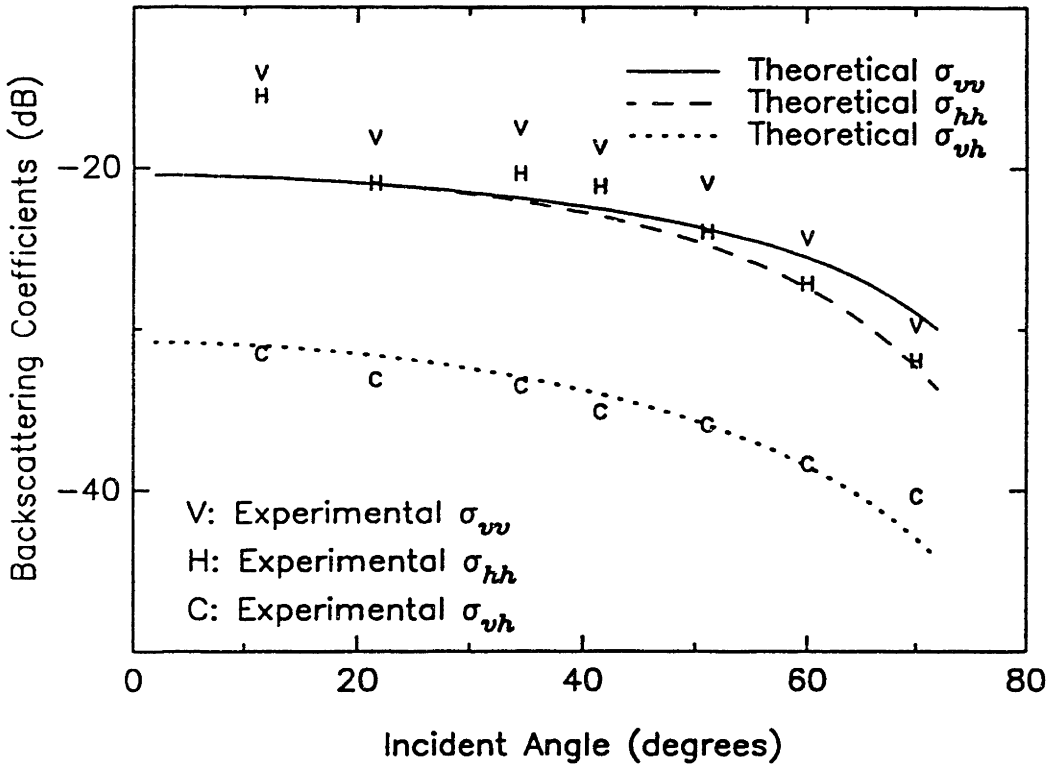

Figure 4.4.2 Backscattering from thick first-year sea ice with flat surface

The disagreement in the co-polarized backscattering coefficients at small incident angle is due to the scattering from rough surface. In the configuration of Figure 4.4.1 the upper boundary has been assumed to be flat and the rough surface scattering has been ignored. To account for the surface effect, the top interface is now considered to be a Gaussian rough surface described with standard deviation $\sigma_s = 0.60$ mm and correlation length $\ell_s = 1.5$ cm as depicted in Figure 4.4.3. The rough surface contribution is incoherently added to the volume scattering. The comparison between theoretical and experimental results for the co-polarized returns is much improved at the low incident angles as seen in Figure 4.4.4. For this surface, the additional contribution to the cross-polarized return is small and is actually ignored in the Kirchhoff model applied in this case. The cross-polarized return therefore remains unchanged.

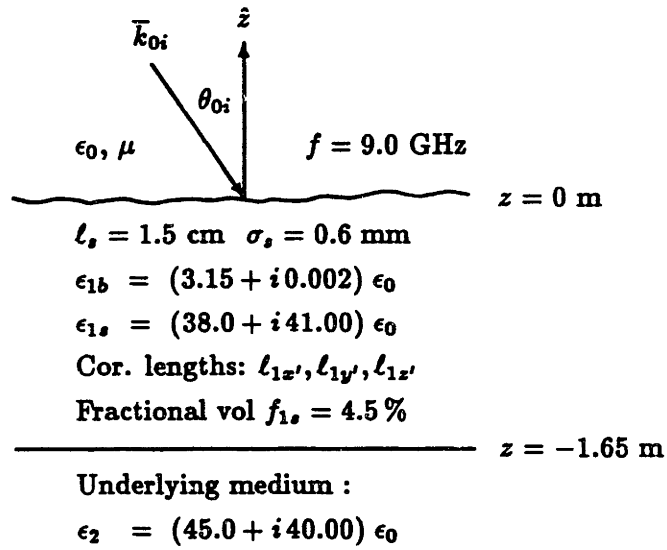

Figure 4.4.3 Scattering configuration of sea ice with rough surface

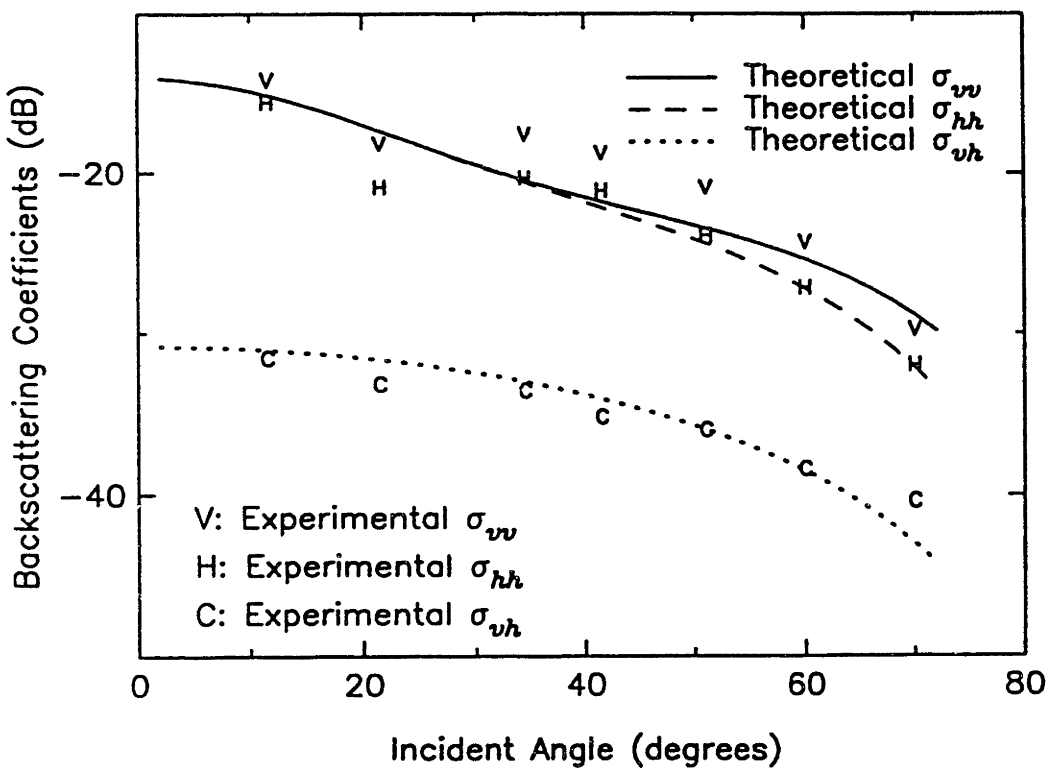

Figure 4.4.4 Backscattering from thick first-year sea ice with rough surface

The results have shown that the scattering from the brine inclusions is dominant at large incident angles while the contribution from the rough surface is important at small incident angles for co-polarized returns. The cross-polarized return due to the inclusions comes from the first-order term under the distorted Born approximation in this model. The spheroidal model in Chapter 2 would result in a zero value of cross-polarized backscattering coefficient σ_{vh} under the first-order approximation in this case because the scatterers are vertically aligned. The previous model, however, can give rise to significant value of σ_{vh} when the alignment direction of the scatterers is tilted off the vertical direction. As a difference between the two models, the vertical ellipsoid model predicts a decreasing trend in σ_{vh} as the incident angles increases as seen in Figures 4.4.2 and 4.4.4 whereas the tilted spheroidal model indicates a maximum σ_{vh} at certain incident angle depending on the tilt and the azimuthal incident angles. The fully polarimetric measurements were not made in the experiment. To study the polarimetric scattering properties of sea ice, the model will be used to simulate polarimetric data and signatures as discussed in the next subsection.

b. Polarimetric Simulation

Due to the azimuthal symmetry and non-zero σ_{vh} in this model, the covariance matrix ... have the form of (92, Chapter 2). To investigate how the covariance matrix and the corresponding polarization signature relates to and conveys information regarding different ice types, polarimetric data are simulated for three different cases of sea ice described in Figures 4.4.5-4.4.7. In Figure 4.4.5, the parameters are chosen to simulate first-year sea ice. Figure 4.4.6 shows the sea ice covered under a layer of dry snow. In Figure 4.4.7, the top part of the ice contains air bubbles, as seen in multi-year sea ice, and the lower part contains brine inclusion with lower fractional volume.

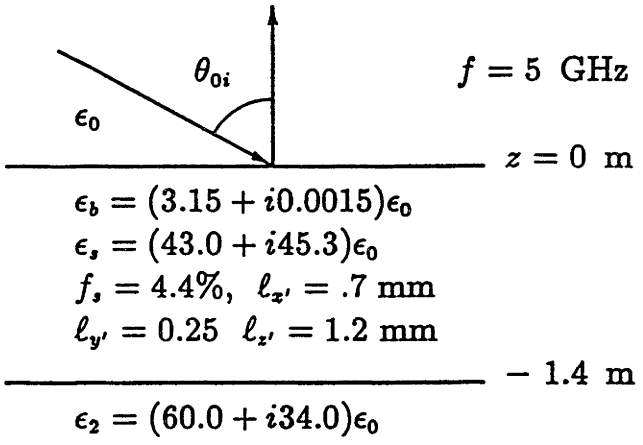

Figure 4.4.5 Scattering configuration of Case 1

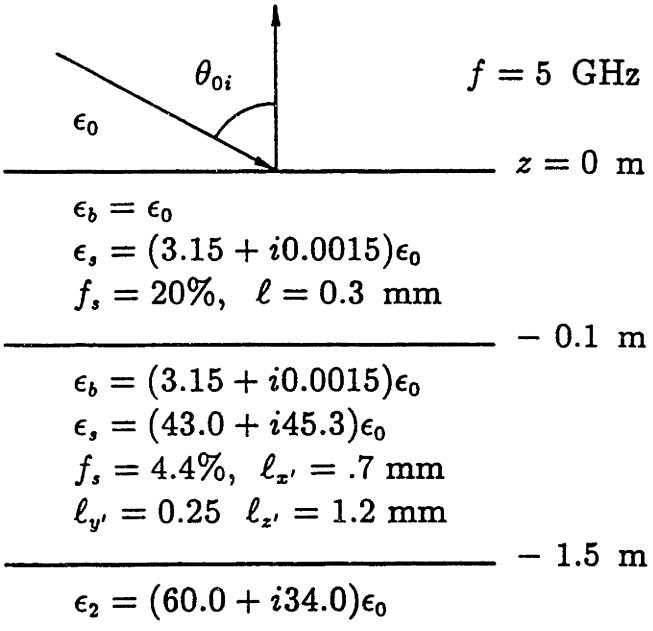

Figure 4.4.6 Scattering configuration of Case 2

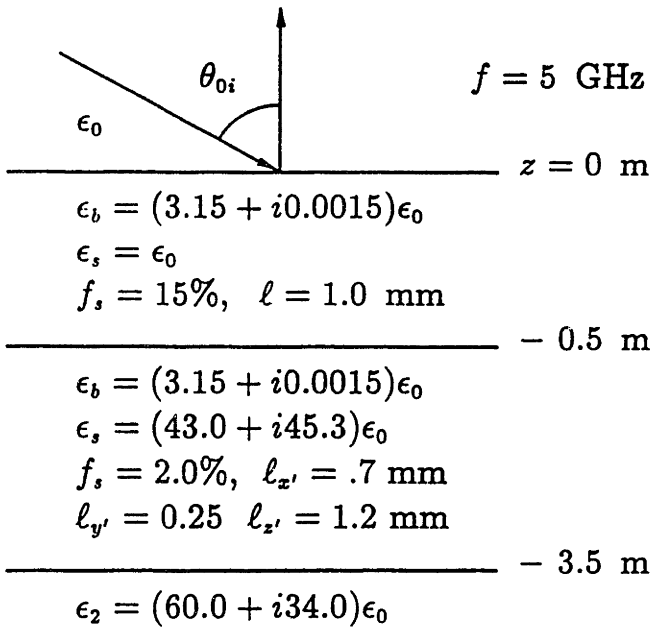

Figure 4.4.7 Scattering configuration of Case 3

The conventional backscattering coefficients for the three cases are compared in Figure 4.4.8. Case 2 gives higher returns than Case 1 since the snow layer introduces more low-loss scatterers and affects the transmission and reflection at the boundaries whose effect is responsible for the oscillations in the curves. Case 3 yields much higher returns as compared to the other two cases due to the low loss and the scattering effect of the air bubbles. Other than the differences in the absolute intensity levels, the behavior of the conventional backscattering coefficients generally follow the decreasing trend with increasing incident angles. Figure 4.4.9 presents the results for the magnitude and phases of the correlation coefficient ρ between the vertical and horizontal returns. In the magnitude of ρ, Case 2 follows rather closely the same characteristics as in Case 1 since the loss of the dry snow cover is still low enough for the wave to "see" the lower ice layer which is the same as in Case 1. Case 3 has $|\rho|$ close to 1 due to the dominant isotropic property of the top part of the ice. The phase of ρ reveals a clear distinction between the ice in Case 3 and the ice in Cases 1 and 2 with and without the snow cover. In such manner, the polarimetric element ρ conveys further information related to the structure of the sea ice.

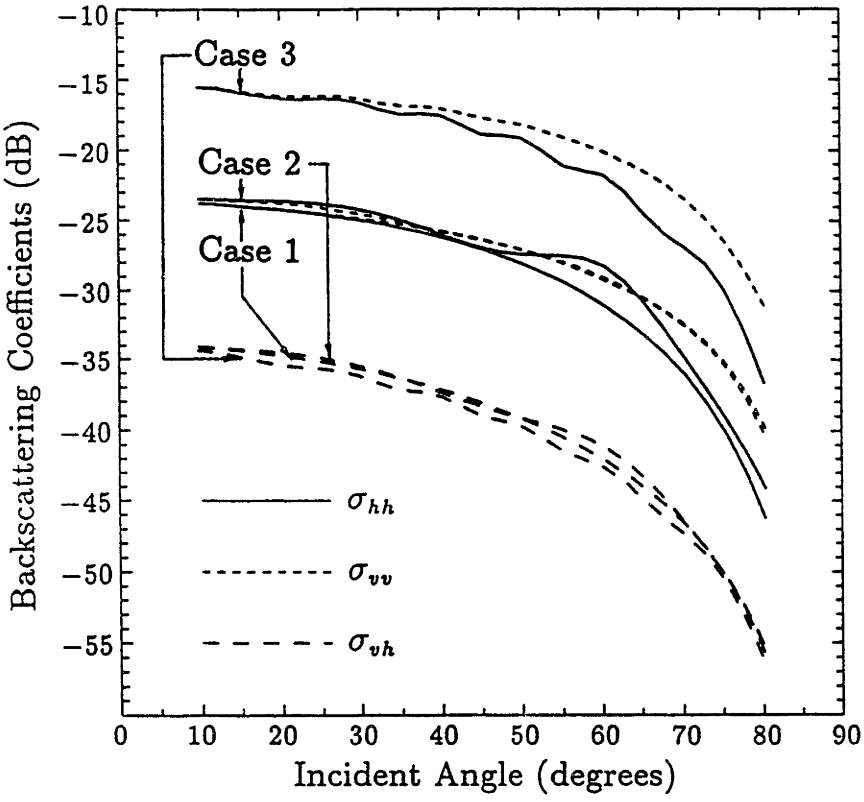

Figure 4.4.8 Conventional backscattering coefficients

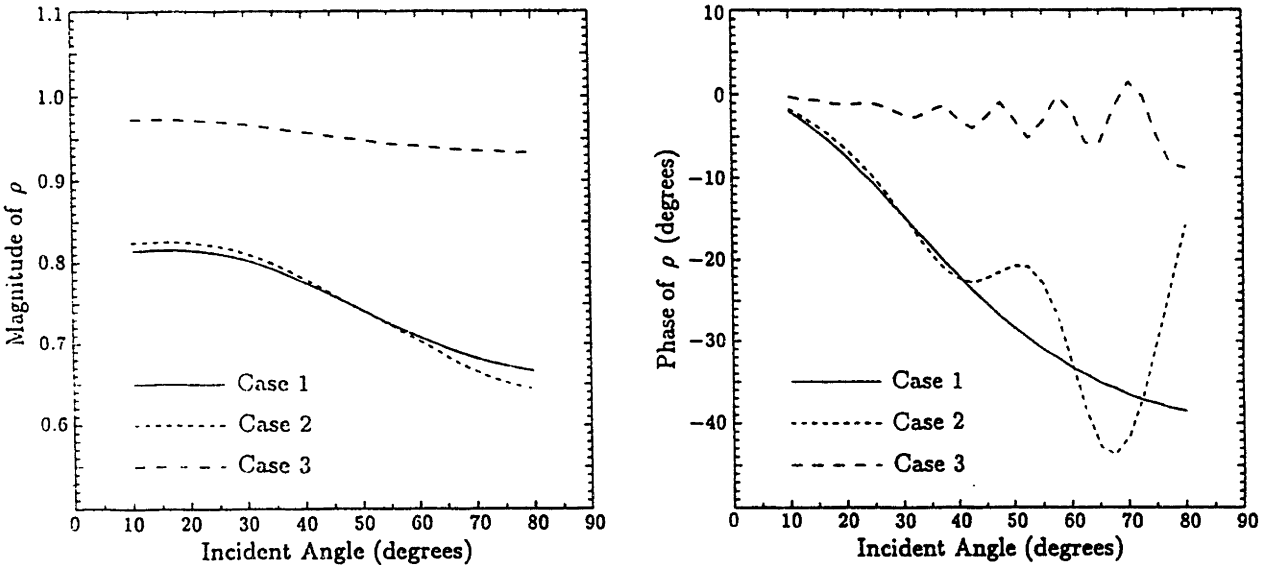

Figure 4.4.9 Correlation coefficient between vertical and horizontal returns

The co-polarization signatures of the ice are synthesized in Figure 4.4.10, 4.4.11, and 4.4.12 for Cases 1, 2, and 3, respectively. The signatures are shaped by the characteristics of the sea ice. All signatures are symmetrical around the mid-point of the polarization surface (corresponding to vv polarization); this is a manifestation of the azimuthal symmetry. Case 1 and 2 have pedestal higher than Case 3 due to the stronger depolarization effect of the ellipsoidal brine inclusions in the ice for the former cases. The signatures of Case 1 and 2 are also more distorted than Case 3. This is because the h and v waves, corresponding to the ordinary and extraordinary waves, in the anisotropic ice propagate at different speed and suffer different attenuation resulting in the separation of the scattering centers of the wave types which causes a large phase in ρ. As discussed in Chapter 2, it is the phase of ρ that gives rise to the distortion in the polarization signatures. The polarization signatures thereby reveal the characteristics of the remotely sensed media.

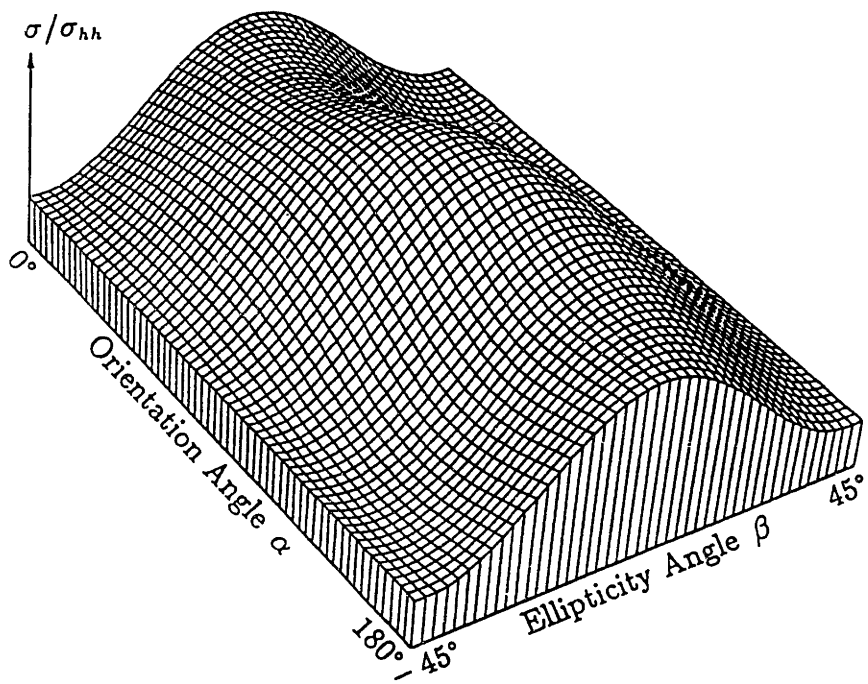

Figure 4.4.10 Co-polarized signature of the ice in Case 1

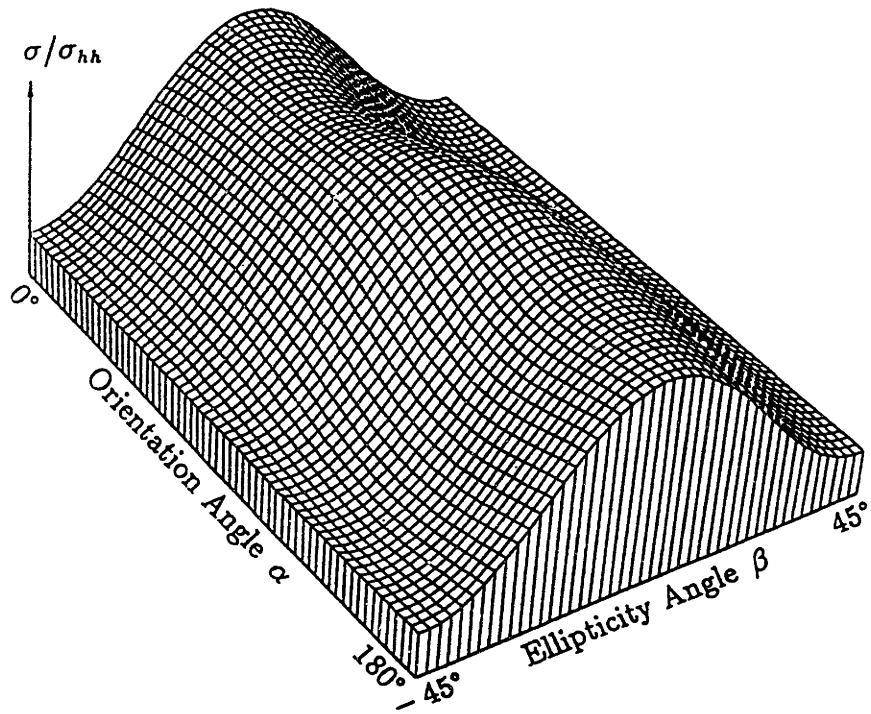

Figure 4.4.11 Co-polarized signature of the ice in Case 2

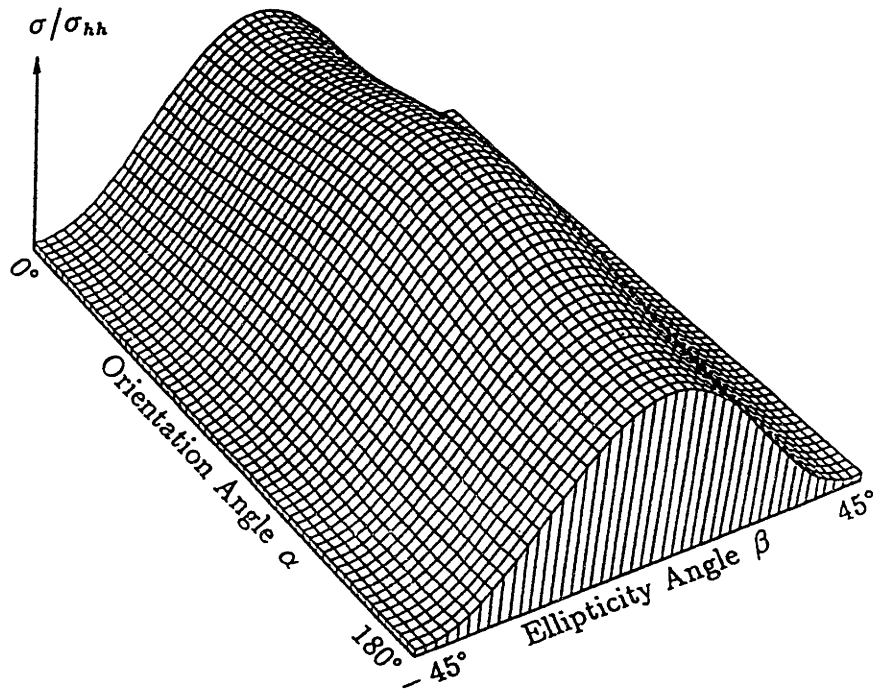

Figure 4.4.12 Co-polarized signature of the ice in Case 3

3.6 Summary

In this chapter, the model with ellipsoidal scatterers have been considered. The ellipsoids are aligned vertically and oriented randomly in azimuthal directions. The derivations of the effective permittivity with the extended strong fluctuation theory and the polarimetric scattering coefficients under the distorted Born approximation are presented. In this model, the cross-polarized return is obtained from the first-order distorted Born approximation. The theoretical results compare well with the measured data for thick first-year sea ice and the scattering mechanisms are explained. From the polarimetric simulation, it is shown that covariance matrices as well as polarization signatures convey further information regarding the characteristics and structure of the media as compared to the conventional backscattering coefficients. The model, however, only accounts for one type of scatterers in a host medium with two-phase mixing. Multi species model will be presented in the next chapter.

Chapter 5
Model with Multiple Species of Scatterers

5.1 Introduction

Geophysical media usually contain inhomogeneities of more than one types with different sizes, shapes, and permittivities. This chapter presents the layer configuration with scattering regions containing many species of scatterers. Each species can have size and shape distinctive from the others. Furthermore, the inhomogeneous media are multi-phase mixing since permittivities of the species can be different. The scatterers are modeled with correlation functions having spherical, spheroidal, or ellipsoidal form and random orientations. The model is then used to derive the effective permittivity and the polarimetric scattering coefficients.

The chapter is organized into six sections. Section 5.2 studies the scatterer correlation to determine the modeling correlation functions. Section 5.3 presents the derivation of the effective permittivity with the extended strong fluctuation theory for the multi-species medium. Section 5.4 shows the calculation of the polarimetric scattering coefficients under the distorted Born approximation. Section 5.5 discusses effects of scatterer shapes and multiple species on effective permittivities, backscattering coefficients, and polarimetric correlation coefficients. The chapter is finally summarized in section 5.6.

5.2 Scatterer Correlation

In the previous chapters, the inhomogeneous medium is composed of a host medium and one type of scatterers. In more general cases, multiple species need be included in the model to account for different types of scatterers. To describe the species in the theoretical model, an examination of the scatterer correlation is necessary to determine the correlation functions.

Consider an inhomogeneous medium composed of two different types of scatterers (species 1 and 2) in a background medium (species 3). The permittivity of species i is ϵ_i and the corresponding fractional volume is f_i. It is obvious that

$$f_1 + f_2 + f_3 = 1 \tag{1}$$

An arrow of arbitrary length r_0 is used to measure the probability p_{ij} of finding the arrow head in species j while the tail is fixed in species i [87,88]. Since the arrow head has to be in one species or the others, probability p_{ij} must satisfy the following equations

$$p_{11} + p_{12} + p_{13} = 1 \tag{2a}$$

$$p_{21} + p_{22} + p_{23} = 1 \tag{2b}$$

$$p_{31} + p_{32} + p_{33} = 1 \tag{2c}$$

It is also observed that fixing the tail in species i to find the head in species j is equivalent to fixing the tail in species j to find the head in species i. This leads to the following conditions of equivalence

$$f_1 p_{12} = f_2 p_{21} \tag{3a}$$

$$f_2 p_{23} = f_3 p_{32} \tag{3b}$$

$$f_3 p_{31} = f_1 p_{13} \tag{3c}$$

In (2) and (3), there are 3 unknown and 6 equations. The following three quantities are therefore chosen to complete the system of equations for determining p_{ij}

$$p_{12} = f_2 \Upsilon_{12}(\bar{r}_0) \tag{4a}$$

$$p_{23} = f_3 \Upsilon_{23}(\bar{r}_0) \tag{4b}$$

$$p_{31} = f_1 \Upsilon_{31}(\bar{r}_0) \tag{4c}$$

where $\Upsilon_{ij}(\bar{r}_0)$ is called the dissimilar function defined by the ratio of p_{ij} $(i \neq j)$ to the fractional volume f_j for a given vector $\bar{r}_0$. Letting $\Upsilon_{ij}(\bar{r}_0) = \Upsilon_{ji}(\bar{r}_0)$ and making use of (3) render

$$p_{21} = f_1 \Upsilon_{21}(\bar{r}_0) \tag{5a}$$

$$p_{32} = f_2 \Upsilon_{32}(\bar{r}_0) \tag{5b}$$

$$p_{13} = f_3 \Upsilon_{13}(\bar{r}_0) \tag{5c}$$

The probability p_{ij} discussed above is now used in the formalism of the strong fluctuation theory to investigate the correlation of the scatterers. With the auxiliary permittivity tensor denoted by $\bar{\bar{\epsilon}}_g$, local fluctuating tensor $\bar{\bar{\xi}}_i$ of species i is then defined with dyadic coefficient $\bar{\bar{S}}_i$ corresponding to exclusion volume of species i

$$\bar{\bar{\xi}}_i = \bar{\bar{\xi}}\,(\bar{r} \in \text{species } i) = \frac{\epsilon_i - \epsilon_g}{\epsilon_0} \left[\bar{\bar{I}} + \bar{\bar{S}}_i \cdot \frac{\epsilon_i \bar{\bar{I}} - \bar{\bar{\epsilon}}_g}{\epsilon_0} \right]^{-1} \tag{6}$$

whose correlation can be expressed in the binomial form as [89]

$$\begin{aligned} \left\langle \xi_{jk}(0) \xi_{lm}(\bar{r}_0) \right\rangle = {} & f_1 \left(p_{11} \xi_{1jk} \xi_{1lm} + p_{12} \xi_{1jk} \xi_{2lm} + p_{13} \xi_{1jk} \xi_{3lm} \right) \\ & + f_2 \left(p_{21} \xi_{2jk} \xi_{1lm} + p_{22} \xi_{2jk} \xi_{2lm} + p_{23} \xi_{2jk} \xi_{3lm} \right) \\ & + f_3 \left(p_{31} \xi_{3jk} \xi_{1lm} + p_{32} \xi_{3jk} \xi_{2lm} + p_{33} \xi_{3jk} \xi_{3lm} \right) \end{aligned} \tag{7}$$

In matrix form, the scatterer correlation (7) can be written as

$$\begin{aligned} \left\langle \xi_{jk}(0) \xi_{lm}(\bar{r}_0) \right\rangle = {} & \begin{bmatrix} \xi_{1jk} & \xi_{2jk} & \xi_{3jk} \end{bmatrix} \cdot \begin{bmatrix} f_1 p_{11} & f_1 p_{12} & f_1 p_{13} \\ f_2 p_{21} & f_2 p_{22} & f_2 p_{23} \\ f_3 p_{31} & f_3 p_{32} & f_3 p_{33} \end{bmatrix} \cdot \begin{bmatrix} \xi_{1lm} \\ \xi_{2lm} \\ \xi_{3lm} \end{bmatrix} \\ & - \begin{bmatrix} \xi_{1jk} & \xi_{2jk} & \xi_{3jk} \end{bmatrix} \cdot \begin{bmatrix} f_1 f_1 & f_1 f_2 & f_1 f_3 \\ f_2 f_1 & f_2 f_2 & f_2 f_3 \\ f_3 f_1 & f_3 f_2 & f_3 f_3 \end{bmatrix} \cdot \begin{bmatrix} \xi_{1lm} \\ \xi_{2lm} \\ \xi_{3lm} \end{bmatrix} \end{aligned} \tag{8a}$$

$$= [\xi_{1jk} \quad \xi_{2jk} \quad \xi_{3jk}] \cdot \begin{bmatrix} R_{11}(\bar{r}_0) & R_{12}(\bar{r}_0) & R_{13}(\bar{r}_0) \\ R_{21}(\bar{r}_0) & R_{22}(\bar{r}_0) & R_{23}(\bar{r}_0) \\ R_{31}(\bar{r}_0) & R_{32}(\bar{r}_0) & R_{33}(\bar{r}_0) \end{bmatrix} \cdot \begin{bmatrix} \xi_{1lm} \\ \xi_{2lm} \\ \xi_{3lm} \end{bmatrix} \tag{8b}$$

where the second term in (8a) does not affect the result due to the condition of secular elimination [17] which requires

$$f_1\xi_{1jk} + f_2\xi_{2jk} + f_3\xi_{3jk} = 0 \tag{9}$$

Equation (8b) is a result of the following definition of $R_{ij}(\bar{r}_0)$

$$R_{ij}(\bar{r}_0) = f_i p_{ij} - f_i f_j \tag{10}$$

which, from (1) and the properties of p_{ij}, is subjected to the conditions

$$R_{ij}(\bar{r}_0) = R_{ji}(\bar{r}_0) \quad \text{and} \quad \sum_{j=1}^{3} R_{ij}(\bar{r}_0) = 0 \tag{11}$$

Explicitly, $R_{ij}(\bar{r}_0)$ is expressed in terms of the fractional volumes and $\Upsilon_{ij}(\bar{r}_0)$ as

$$R_{11}(\bar{r}_0) = f_1 f_2 (1 - \Upsilon_{12}(\bar{r}_0)) + f_1 f_3 (1 - \Upsilon_{13}(\bar{r}_0)) \tag{12a}$$

$$R_{22}(\bar{r}_0) = f_2 f_1 (1 - \Upsilon_{21}(\bar{r}_0)) + f_2 f_3 (1 - \Upsilon_{23}(\bar{r}_0)) \tag{12b}$$

$$R_{33}(\bar{r}_0) = f_3 f_1 (1 - \Upsilon_{31}(\bar{r}_0)) + f_3 f_2 (1 - \Upsilon_{32}(\bar{r}_0)) \tag{12c}$$

$$R_{12}(\bar{r}_0) = -f_1 f_2 (1 - \Upsilon_{12}(\bar{r}_0)) \tag{12d}$$

$$R_{13}(\bar{r}_0) = -f_1 f_3 (1 - \Upsilon_{13}(\bar{r}_0)) \tag{12e}$$

$$R_{23}(\bar{r}_0) = -f_2 f_3 (1 - \Upsilon_{23}(\bar{r}_0)) \tag{12f}$$

The components of the scatterer corelation can now be related to the $R_{ij}(\bar{r}_0)$ by

$$\begin{aligned} \left\langle \xi_{jk}(0)\xi_{lm}(\bar{r}_0) \right\rangle &= \xi_{1jk}\xi_{1lm}R_{11}(\bar{r}_0) + \xi_{2jk}\xi_{2lm}R_{22}(\bar{r}_0) + \xi_{3jk}\xi_{3lm}R_{33}(\bar{r}_0) \\ &+ \frac{1}{2}(\xi_{1jk}\xi_{2lm} + \xi_{2jk}\xi_{1lm})(R_{33}(\bar{r}_0) - R_{22}(\bar{r}_0) - R_{11}(\bar{r}_0)) \\ &+ \frac{1}{2}(\xi_{2jk}\xi_{3lm} + \xi_{3jk}\xi_{2lm})(R_{11}(\bar{r}_0) - R_{22}(\bar{r}_0) - R_{33}(\bar{r}_0)) \\ &+ \frac{1}{2}(\xi_{1jk}\xi_{3lm} + \xi_{3jk}\xi_{1lm})(R_{22}(\bar{r}_0) - R_{11}(\bar{r}_0) - R_{33}(\bar{r}_0)) \end{aligned} \tag{13}$$

When the fractional volumes of the inhomogeneities are low (i.e. $f_1, f_2 \ll f_3$), the correlation between two different types of inhomogeneities is ignored and (12a-c) can be approximated as

$$R_{11}(\bar{r}_0) \approx f_1 f_3 \left(1 - \Upsilon_{13}(\bar{r}_0)\right) \tag{14a}$$

$$R_{22}(\bar{r}_0) \approx f_2 f_3 \left(1 - \Upsilon_{23}(\bar{r}_0)\right) \tag{14b}$$

$$R_{33}(\bar{r}_0) \approx R_{11}(\bar{r}_0) + R_{22}(\bar{r}_0) \tag{14c}$$

Defining $R_{i\xi}(\bar{r}_0) = (1 - \Upsilon_{i3}(\bar{r}_0))$ and substituting (14) and (13) yields

$$\begin{aligned}\left\langle \xi_{jk}(0)\xi_{lm}(\bar{r}_0)\right\rangle \approx\ & f_1 f_3 \left(\xi_{1jk} - \xi_{3jk}\right)\left(\xi_{1lm} - \xi_{3lm}\right) R_{1\xi}(\bar{r}_0) \\ & + f_2 f_3 \left(\xi_{2jk} - \xi_{3jk}\right)\left(\xi_{2lm} - \xi_{3lm}\right) R_{2\xi}(\bar{r}_0)\end{aligned} \tag{15}$$

For a medium containing N types of scatterers with permittivity ϵ_i, and fractional volume f_i, in a background medium with ϵ_b and f_b, scatterer correlation (15) is generalized into

$$\left\langle \xi_{jk}(0)\xi_{lm}(\bar{r}_0)\right\rangle = \sum_{i=1}^{N} f_i f_b \left(\xi_{ijk} - \xi_{bjk}\right)\left(\xi_{ilm} - \xi_{blm}\right) R_{i\xi}(\bar{r}_0) \tag{16}$$

where ξ_{blm} is defined with (6) for $\epsilon_i = \epsilon_b$ and $S_i = S_b$. Note that (16) is reduced to the formulas of two-phase mixing in [17,58]. In the low fractional approximation, (16) indicates how the correlation functions for different species of the scatterers are related to form the overall correlation $\left\langle \xi_{jk}(0)\xi_{lm}(\bar{r}_0)\right\rangle$. This form will be used in the next section to derive the effective permittivity of the inhomogeneous medium with multiple species.

5.3 Effective Permittivity

The effective permittivity of the random medium is composed of a quasi-static part and a scattering-effect part corresponding to the first and second term, respectively, in the following expression

$$\bar{\bar{\epsilon}}_{eff} = \bar{\bar{\epsilon}}_g + \epsilon_0 \left[\bar{\bar{I}} - \bar{\bar{\xi}}_{eff} \cdot \left\langle \bar{\bar{S}} \right\rangle\right]^{-1} \cdot \bar{\bar{\xi}}_{eff} \tag{17}$$

where auxiliary permittivity $\overline{\overline{\epsilon}}_g$ and dyadic coefficient $\overline{\overline{S}}$ are determined by the condition of secular-term elimination, and the effective dyadic scatterer $\overline{\overline{\xi}}_{eff}$ under the low-frequency approximation is given by

$$\left[\overline{\overline{\xi}}_{eff}\right]_{jm} = \sum_{i=1}^{N} \int_0^{2\pi} d\gamma \int_0^{\pi} d\beta \int_0^{2\pi} d\alpha \; p(\alpha,\beta,\gamma) \sum_{k,l}^{x,y,z} \Gamma^{(0)}_{i\xi jklm} \left\{ k_0^2 \int_{-\infty}^{\infty} d\overline{k}' \left[\overline{\overline{G}}_g(\overline{k}')\right]_{kl} \Phi_{i\xi}(\overline{k}') + \left[\overline{\overline{S}}\right]_{kl} \right\} \Big|_{\alpha,\beta,\gamma} \tag{18}$$

in which subscript i stands for species i, $p(\alpha,\beta,\gamma)$ is the probability density function of orientation, $\overline{\overline{G}}_g$ is the isotropic Green's function (16, Chapter 2), $\Phi_{i\xi}$ is the Fourier transform of the normalized local correlation function, and $\Gamma^{(0)}_{i\xi jklm}$ is the local variance of species i defined as

$$\Gamma^{(0)}_{i\xi jklm}(\hat{r}') = f_{i\alpha} f_{b} \left(\xi_{ijk} - \xi_{bjk}\right)\left(\xi_{ilm} - \xi_{blm}\right) \tag{19}$$

As obtained, the effective permittivity is an approximation and the validity condition is $\left|\left[\overline{\overline{\xi}}_{eff}\right]\right|_{jm} \ll 1$.

The method to derive the effective permittivity has been discussed in the previous chapter for spherical and randomly oriented spheroidal scatterers. Here, the derivation for multiple species including randomly oriented ellipsoidal scatterers is considered. The principal coordinate system (x',y',z') of a local ellipsoid is related to the global coordinate system (x,y,z) by Eulerian angle α, β, and γ as illustrated in Figure 5.3.1. The rotation α $(0<\alpha<2\pi)$ is about z' axis, β $(0<\beta<\pi)$ about y_1 axis, and γ $(0<\gamma<2\pi)$ about z_2 axis are described with the following relations

$$\begin{bmatrix} x_1 \\ y_1 \\ z_1 \end{bmatrix} = \overline{\overline{T}}_{\alpha} \cdot \begin{bmatrix} x' \\ y' \\ z' \end{bmatrix} = \begin{bmatrix} \cos\alpha & \sin\alpha & 0 \\ -\sin\alpha & \cos\alpha & 0 \\ 0 & 0 & 1 \end{bmatrix} \cdot \begin{bmatrix} x' \\ y' \\ z' \end{bmatrix} \tag{20a}$$

$$\begin{bmatrix} x_2 \\ y_2 \\ z_2 \end{bmatrix} = \overline{\overline{T}}_{\beta} \cdot \begin{bmatrix} x_1 \\ y_1 \\ z_1 \end{bmatrix} = \begin{bmatrix} \cos\beta & 0 & -\sin\beta \\ 0 & 1 & 0 \\ \sin\beta & 0 & \cos\beta \end{bmatrix} \cdot \begin{bmatrix} x_1 \\ y_1 \\ z_1 \end{bmatrix} \tag{20b}$$

$$\begin{bmatrix} x \\ y \\ z \end{bmatrix} = \overline{\overline{T}}_\gamma \cdot \begin{bmatrix} x_2 \\ y_2 \\ z_2 \end{bmatrix} = \begin{bmatrix} \cos\gamma & \sin\gamma & 0 \\ -\sin\gamma & \cos\gamma & 0 \\ 0 & 0 & 1 \end{bmatrix} \cdot \begin{bmatrix} x_2 \\ y_2 \\ z_2 \end{bmatrix} \tag{20c}$$

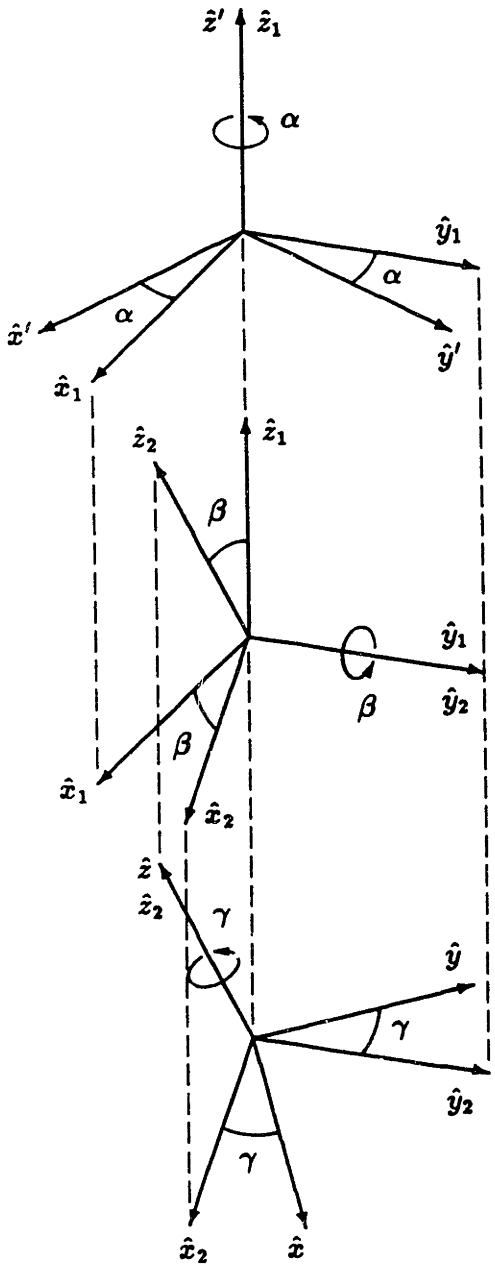

(a)

$$\overline{\overline{T}}_\alpha = \begin{bmatrix} \cos\alpha & \sin\alpha & 0 \\ -\sin\alpha & \cos\alpha & 0 \\ 0 & 0 & 1 \end{bmatrix}$$

(b)

$$\overline{\overline{T}}_\beta = \begin{bmatrix} \cos\beta & 0 & -\sin\beta \\ 0 & 1 & 0 \\ \sin\beta & 0 & \cos\beta \end{bmatrix}$$

(c)

$$\overline{\overline{T}}_\gamma = \begin{bmatrix} \cos\gamma & \sin\gamma & 0 \\ -\sin\gamma & \cos\gamma & 0 \\ 0 & 0 & 1 \end{bmatrix}$$

Figure 5.3.1 Eulerian angles : (a) α is the rotation angle about z' axis, (b) β is the rotation angle about y_1 axis, and (c) γ is the rotation angle about z_2 axis

and the resultant Eulerian transformation which rotates the global to the scatterer coordinates is

$$\begin{bmatrix} x' \\ y' \\ z' \end{bmatrix} = \overline{\overline{T}} \cdot \begin{bmatrix} x \\ y \\ z \end{bmatrix} = \left[\overline{\overline{T}}_\gamma \cdot \overline{\overline{T}}_\beta \cdot \overline{\overline{T}}_\alpha\right]^{-1} \cdot \begin{bmatrix} x \\ y \\ z \end{bmatrix} =$$

$$\begin{bmatrix} \cos\gamma\cos\beta\cos\alpha - \sin\gamma\sin\alpha & -\sin\gamma\cos\beta\cos\alpha - \cos\gamma\sin\alpha & \sin\beta\cos\alpha \\ \cos\gamma\cos\beta\sin\alpha + \sin\gamma\cos\alpha & -\sin\gamma\cos\beta\sin\alpha + \cos\gamma\cos\alpha & \sin\beta\sin\alpha \\ -\cos\gamma\sin\beta & \sin\gamma\sin\beta & \cos\beta \end{bmatrix} \cdot \begin{bmatrix} x \\ y \\ z \end{bmatrix} \tag{21}$$

To find ϵ_g, the condition of secular elimination $\left\langle \overline{\overline{\xi}}(\overline{r}) \right\rangle = 0$ is imposed

$$\left\langle \overline{\overline{\xi}}(\overline{r}) \right\rangle = \int_0^{2\pi} d\gamma \int_0^{\pi} d\beta \int_0^{2\pi} d\alpha \; p(\alpha,\beta,\gamma) \; \overline{\overline{T}}^{-1} \cdot \left[f_b \overline{\overline{\xi}}_b + \sum_{i=1}^{N} f_{is} \overline{\overline{\xi}}_i \right] \cdot \overline{\overline{T}} \tag{22}$$

For random orientation of non-spherical scatterers, the probability density function of orientation is

$$p(\alpha,\beta,\gamma) = \sin\beta/(8\pi^2) \tag{23}$$

which renders $\overline{\overline{\epsilon}}_g$ isotropic and, as shown in Appendix E, casts condition (22) into

$$\frac{1}{3}\left[f_b \left(\xi_{bx'} + \xi_{by'} + \xi_{bz'}\right) + \sum_{i=1}^{N} f_{is} \left(\xi_{ix'} + \xi_{iy'} + \xi_{iz'}\right) \right] = 0 \tag{24}$$

In (24), ξ's are defined by (6) and explicitly written in the local coordinates as

$$\xi_{ix'}(\epsilon) = \xi_{ix'x'}(\epsilon) = \frac{\epsilon - \epsilon_g}{\epsilon_0 + S_{ix'}(\epsilon - \epsilon_g)} \tag{25a}$$

$$\xi_{iy'}(\epsilon) = \xi_{iy'y'}(\epsilon) = \frac{\epsilon - \epsilon_g}{\epsilon_0 + S_{iy'}(\epsilon - \epsilon_g)} \tag{25b}$$

$$\xi_{iz'}(\epsilon) = \xi_{iz'z'}(\epsilon) = \frac{\epsilon - \epsilon_g}{\epsilon_0 + S_{iz'}(\epsilon - \epsilon_g)} \tag{25c}$$

where $i = 1, 2, ..., N$ for the scatterer species or $i = b$ for the background; ϵ can takes on the value of ϵ_{is} in a scatterer of species i or ϵ_b in the background medium.

The dyadic coefficient $\overline{\overline{S}}_i$ for spherical and spheroidal scatterers have been derived in the previous chapters. For ellipsoidal correlation function of the form

$$R_{i\xi}(\overline{r}') = \exp\left(-\sqrt{\frac{x'^2}{\ell_{ix'}^2} + \frac{y'^2}{\ell_{iy'}^2} + \frac{z'^2}{\ell_{iz'}^2}} \right) \tag{26a}$$

in which correlation length $\ell_{ix'}$, $\ell_{iy'}$, and $\ell_{iz'}$ are in the local coordinates corresponding to the minor, the meridian, and the major axes of an ellipsoidal scatterer of species i. The corresponding Fourier transform $\Phi_{i\xi}$ is

$$\Phi_{i\xi}(\overline{k}') = \frac{\ell_{ix'}\ell_{iy'}\ell_{iz'}}{\pi^2(1 + k_x'^2\ell_{ix'}^2 + k_y'^2\ell_{iy'}^2 + k_z'^2\ell_{iz'}^2)^2} \tag{26b}$$

With the above correlation function, element $S_{ix'}$, $S_{iy'}$, and $S_{iz'}$ are derived from the secular elimination condition and the symmetry of the ellipsoid. The results are

$$S_{iz'}(\ell_{ix'}, \ell_{iy'}, \ell_{iz'}) = \int_0^{2\pi} d\phi \, \frac{\epsilon_0(1 + a_i)}{2\pi\epsilon_g a_i\sqrt{a_i}} [\sqrt{a_i} - \tan^{-1}\sqrt{a_i}] \tag{27a}$$

$$S_{iy'}(\ell_{ix'}, \ell_{iy'}, \ell_{iz'}) = S_{iz'}(\ell_{ix'}, \ell_{iz'}, \ell_{iy'}) \tag{27b}$$

$$S_{ix'}(\ell_{ix'}, \ell_{iy'}, \ell_{iz'}) = S_{iz'}(\ell_{iz'}, \ell_{iy'}, \ell_{ix'}) \tag{27c}$$

where the integrations over ϕ can be carried out numerically and a_i and γ_i are defined as

$$a_i = \gamma_i^2 - 1 \tag{28a}$$

$$\gamma_i = \left(\frac{\cos^2\phi}{\gamma_{ix'}^2} + \frac{\sin^2\phi}{\gamma_{iy'}^2}\right)^{-\frac{1}{2}} \tag{28b}$$

$$\gamma_{ix'} = \frac{\ell_{ix'}}{\ell_{iz'}}, \quad \gamma_{iy'} = \frac{\ell_{iy'}}{\ell_{iz'}} \tag{28c}$$

For the background medium, the dyadic coefficient $\overline{\overline{S}}_b$ is just the average of the species components

$$\overline{\overline{S}}_b = \left(\sum_{i=1}^{N} f_{is}\overline{\overline{S}}_i\right)\left(\sum_{i=1}^{N} f_{is}\right)^{-1} \tag{29}$$

Then, the average dyadic coefficient $\langle\overline{\overline{S}}\rangle$ in (17) is determined by

$$\langle\overline{\overline{S}}\rangle = \sum_{i=1}^{N,b} f_{is}\int_0^{2\pi} d\gamma \int_0^{\pi} d\beta \int_0^{2\pi} d\alpha \; p(\alpha,\beta,\gamma)\,\overline{\overline{T}}^{-1} \cdot \begin{bmatrix} S_{ix'} & 0 & 0 \\ 0 & S_{iy'} & 0 \\ 0 & 0 & S_{iz'} \end{bmatrix} \cdot \overline{\overline{T}}$$

$$= \frac{f_b}{3}(S_{bx'} + S_{bz'} + S_{bz'})\overline{\overline{I}} + \sum_{i=1}^{N}\frac{f_{is}}{3}(S_{ix'} + S_{iz'} + S_{iz'})\overline{\overline{I}} = S\overline{\overline{I}} \tag{30}$$

Equations (24) and (30) are used to solve for ϵ_g and S's with an iteration method.

The effective scatterer $\overline{\overline{\xi}}_{eff}$ is next obtained to calculate the effective permittivity according to (17). First, consider the variances in expression (18) for $\overline{\overline{\xi}}_{eff}$. To facilitate the derivation, the following principal variances are defined in the local coordinates based on (19)

$$\delta_{i\xi j'k'} = \delta_{i\xi k'j'} = f_{is} f_b \left(\xi_{ij'} - \xi_{bj'}\right)\left(\xi_{ik'} - \xi_{bk'}\right) \tag{31}$$

In the global coordinates, the Eulerian transformation rotates the variances to

$$\begin{aligned}\Gamma^{(0)}_{i\xi jklm} = {} & \delta_{i\xi x'x'} a_{xjk} a_{xlm} + \delta_{i\xi x'y'} a_{xjk} a_{ylm} + \delta_{i\xi x'z'} a_{xjk} a_{zlm} \\ & + \delta_{i\xi y'x'} a_{yjk} a_{xlm} + \delta_{i\xi y'y'} a_{yjk} a_{ylm} + \delta_{i\xi y'z'} a_{yjk} a_{zlm} \\ & + \delta_{i\xi z'x'} a_{zjk} a_{xlm} + \delta_{i\xi z'y'} a_{zjk} a_{ylm} + \delta_{i\xi z'z'} a_{zjk} a_{zlm}\end{aligned} \tag{32}$$

where a_{jkl}'s have been defined in Appendix E. Now, let the quantity in the brackets in (18) be

$$\eta_{ijm}(\hat{r}') = k_0^2 \int_{-\infty}^{\infty} d\overline{k}' \left[\overline{\overline{G}}_g(\overline{k}')\right]_{kl} \Phi_{i\xi}(\overline{k}') + \left[\overline{\overline{S}}_i\right]_{kl} \tag{33}$$

In the local coordinates, $\overline{\overline{\eta}}_i(\hat{r}')$ is a diagonal tensor whose elements are

$$\eta_{ij'j'} = \eta_{ij'} = I_{ij'} + S_{ij'}, \quad j' = x', y', z' \tag{34}$$

where $I_{ij'}$ involves the integration of dyadic Green's function and correlation function. The results for $I_{iz'}$ is

$$I_{iz'} = \int_0^{2\pi} d\phi \, \frac{-\epsilon_0}{\pi \epsilon_g} (\mathcal{I}^s_{i\phi} + \mathcal{I}^d_{i\phi}) \tag{35a}$$

$$\mathcal{I}^s_{i\phi} = -\frac{\gamma_i^3}{2a_i^2}\left[\frac{\sqrt{-\zeta}}{\vartheta_e} + \frac{\vartheta_e + \zeta}{\vartheta_e \sqrt{\vartheta_e}}\left(\frac{\pi}{2} - \tan^{-1}\frac{\sqrt{-\zeta}}{\sqrt{\vartheta_e}}\right)\right] \tag{35b}$$

$$\mathcal{I}^d_{i\phi} = \frac{\gamma_i^2}{2a_i^2}\left[\frac{1 + a_i \nu_{gz'}^2}{\vartheta_o} + \frac{\vartheta_o(a_i+2) - (b + a_i \nu_{gz'}^2)}{\vartheta_o \sqrt{\vartheta_o}}\left(\frac{\pi}{2} - \tan^{-1}\frac{1}{\sqrt{\vartheta_o}}\right)\right] \tag{35c}$$

$$\nu_{gz'}^2 = k_g^2 \ell_{iz'}^2, \quad k_g^2 = \omega^2 \mu_0 \epsilon_g, \quad \zeta = \gamma_i^2 \nu_{gz'}^2 \tag{35d}$$

$$b = \frac{\gamma_i^2 + \zeta}{a_i}, \quad \vartheta_o = b - 1, \quad \vartheta_e = b + \zeta \tag{35e}$$

The symmetry of the ellipsoid is used to find $I_{iy'}$ and $I_{iz'}$ which are simply

$$I_{iy'}(\ell_{ix'}, \ell_{iy'}, \ell_{iz'}) = I_{iz'}(\ell_{ix'}, \ell_{iz'}, \ell_{iy'}) \tag{36}$$

$$I_{ix'}(\ell_{ix'}, \ell_{iy'}, \ell_{iz'}) = I_{iz'}(\ell_{iz'}, \ell_{iy'}, \ell_{ix'}) \tag{37}$$

To rotate $\overline{\overline{\eta}}_i(\hat{r}')$ into the global coordinates, the Eulerian transformation is applied. The elements of $\overline{\overline{\eta}}_i(\hat{r})$ in the global coordinates are

$$\eta_{ikl} = \eta_{ix'}a_{xkl} + \eta_{iy'}a_{ykl} + \eta_{iz'}a_{zkl} = \eta_{ilk} \tag{38}$$

Variance Γ in (32) and quantity η in (38) are combined to define

$$\begin{aligned}\xi^{(0)}_{ijm} = \sum_{k,l}^{x,y,z} \Gamma^{(0)}_{i\xi jklm}\eta_{ikl} = \sum_{u,v,w}^{x,y,z} \delta_{i\xi u'v'}\eta_{iw'} \\ \Big(a_{uxj}a_{vzm}a_{wxx} + a_{uxj}a_{vym}a_{wxy} + a_{uxj}a_{vzm}a_{wxz} \\ + a_{uyj}a_{vzm}a_{wyx} + a_{uyj}a_{vym}a_{wyy} + a_{uyj}a_{vzm}a_{wyz} \\ + a_{uzj}a_{vzm}a_{wzx} + a_{uzj}a_{vym}a_{wzy} + a_{uzj}a_{vzm}a_{wzz}\Big)\end{aligned} \tag{39}$$

After the integration over the Eulerian angles, the effective scatterer tensor for species i from (39) becomes

$$\overline{\overline{\xi}}_{i\,eff} = \int_0^{2\pi} d\gamma \int_0^{\pi} d\beta \int_0^{2\pi} d\alpha\; p(\alpha,\beta,\gamma)\; \overline{\overline{\xi}}^{(0)}_i = \frac{1}{3}\left(\delta_{i\xi x'x'}\eta_{ix'} + \delta_{i\xi y'y'}\eta_{iy'} + \delta_{i\xi z'z'}\eta_{iz'}\right)\overline{\overline{I}} \tag{40}$$

Another method to find (40) is to carry out all tensor operations involving Γ's and η's in the local coordinates and then rotate the result into the global coordinates where Appendix E is readily applicable to arrive at (40). Substituting (40) in (18) and using the result in (17) yields elements of the effective permittivity

$$\overline{\overline{\epsilon}}_{eff} = \left[\epsilon_g + \frac{\epsilon_o}{3}\sum_{i=1}^{N}\left(\delta_{i\xi x'x'}\eta_{ix'} + \delta_{i\xi y'y'}\eta_{iy'} + \delta_{i\xi z'z'}\eta_{iz'}\right)\right]\overline{\overline{I}} \tag{41}$$

The effective permittivity, as indicated in (41), is isotropic due to the random orientation of the scatterer species. The above result for the effective permittivity of an inhomogeneous medium containing many species will reduce to the result of

single scatterer species in the previous chapters. In the next section, the effective permittivity is used to obtain the complete set of polarimetric backscattering coefficients under the distorted Born approximation and the Green's function of the layer configuration.

5.4 Scattering Coefficients

The same layer configuration in Chapter 2 is used except that regions 1 and 2 hosts multiple species of scatterers which are ellipsoidal and randomly oriented. The polarimetric backscattering coefficients are defined by (13, Chapter 1) with ensemble averages of scattered fields. The averages are calculated with spatial integrations over products of the DGFs, the mean fields, and the correlation functions as follows

$$\begin{aligned}\left\langle \overline{E}_{0s}(\overline{r}) \cdot \overline{E}^{*}_{0s}(\overline{r}) \right\rangle = & \sum_{t=1}^{N_1} \sum_{i,j,k,l,m}^{x,y,z} k_0^4 \int_0^{2\pi} d\gamma \int_0^{\pi} d\beta \int_0^{2\pi} d\alpha \; p(\alpha,\beta,\gamma) \\ & \cdot \int_{V_1} d\overline{r}_1 \int_{V_1} d\overline{r}_1^{\,o} \, C_{t\xi 1jklm}(\overline{r}_1, \overline{r}_1^{\,o}; \alpha, \beta, \gamma) \\ & \cdot \left[\left\langle G_{01ij}(\overline{r}, \overline{r}_1) \right\rangle \left\langle F_{1k}(\overline{r}_1) \right\rangle \right] \cdot \left[\left\langle G_{01il}(\overline{r}, \overline{r}_1^{\,o}) \right\rangle \left\langle F_{1m}(\overline{r}_1^{\,o}) \right\rangle \right]^{*} \\ & + \sum_{t=1}^{N_2} \sum_{i,j,k,l,m}^{x,y,z} k_0^4 \int_0^{2\pi} d\gamma \int_0^{\pi} d\beta \int_0^{2\pi} d\alpha \; p(\alpha,\beta,\gamma) \\ & \cdot \int_{V_2} d\overline{r}_2 \int_{V_2} d\overline{r}_2^{\,o} \, C_{t\xi 2jklm}(\overline{r}_2, \overline{r}_2^{\,o}; \alpha, \beta, \gamma) \\ & \cdot \left[\left\langle G_{02ij}(\overline{r}, \overline{r}_2) \right\rangle \left\langle F_{2k}(\overline{r}_2) \right\rangle \right] \cdot \left[\left\langle G_{02il}(\overline{r}, \overline{r}_2^{\,o}) \right\rangle \left\langle F_{2m}(\overline{r}_2^{\,o}) \right\rangle \right]^{*} \end{aligned} \tag{42}$$

where t stands for the scatterer species t, N_1 is the number of species in region 1, and N_2 the number of species in region 2. The DGFs and the mean fields are given in Chapter 2. The correlation functions need to be determined next to derive the scattering coefficients.

The correlation functions C's in (42) are defined in the spatial domain with

$$C_{t\xi njklm}(\overline{r}_n, \overline{r}_n^{\,o}; \alpha, \beta, \gamma) = \left\langle \xi_{tnjk}(\overline{r}_n) \xi^{*}_{tnlm}(\overline{r}_n^{\,o}) \middle| \alpha(\overline{r}_n), \beta(\overline{r}_n), \gamma(\overline{r}_n) \right\rangle , \quad n = 1,2 \tag{43}$$

In (43), n represents region $n = 1,2$. To facilitate the integration in (42), Fourier

transforms of the correlation functions are introduced

$$C_{t\xi njklm}(\overline{r}_n, \overline{r}_n^o; \alpha, \beta, \gamma) = \int_{-\infty}^{\infty} d\overline{\beta} \Phi_{tnjklm}(\overline{\beta}) e^{-i\overline{\beta}\cdot(\overline{r}_n - \overline{r}_n^o)}, \quad n = 1, 2 \tag{44}$$

which is expressed in the global coordinate system $(\hat{x}, \hat{y}, \hat{z})$ and related by the rotation transformation with Eulerian angles (α, β, γ) to those in the local coordinate system $(\hat{x}', \hat{y}', \hat{z}')$. Φ_{tnjklm} is a product of a variance part and a functional part written as

$$\Phi_{tnjklm}(\overline{\beta}) = \Gamma_{tnjklm} \Phi_{t\xi n}(\overline{\beta}) \tag{45}$$

Variance Γ_{tnjklm} are defined the local coordinates as in (19) but the last term in the product is complex conjugated, namely

$$\Gamma_{tnjklm}(\hat{r}') = f_{ins} f_{bn} \left(\xi_{tnjk} - \xi_{bnjk}\right) \left(\xi_{tnlm} - \xi_{bnlm}\right)^* \tag{46}$$

After the Eulerian rotation to the global coordinates, Γ_{tnjklm} becomes

$$\begin{aligned}
\Gamma_{tnjklm} &= \sum_{u,v}^{x,y,z} \delta_{tnuv} a_{ujk} a_{vlm} \\
&= \delta_{tnx'x'} a_{xjk} a_{xlm} + \delta_{tnx'y'} a_{xjk} a_{ylm} + \delta_{tnx'z'} a_{xjk} a_{zlm} \\
&+ \delta_{tny'x'} a_{yjk} a_{xlm} + \delta_{tny'y'} a_{yjk} a_{ylm} + \delta_{tny'z'} a_{yjk} a_{zlm} \\
&+ \delta_{tnz'x'} a_{zjk} a_{xlm} + \delta_{tnz'y'} a_{zjk} a_{ylm} + \delta_{tnz'z'} a_{zjk} a_{zlm}
\end{aligned} \tag{47}$$

where the principal variances δ's in the local coordinates are

$$\delta_{tnj'k'} = \delta^*_{tnk'j'} = f_{ins} f_{bn} \left(\xi_{tnj'} - \xi_{bnj'}\right) \left(\xi_{tnk'} - \xi_{bnk'}\right)^* \tag{48}$$

When the integration of probability density function of random orientation is applied to the variances in (47), the averaged variance, for latter consideration, is defined as

$$\Delta_{tnjklm} = \sum_{u,v}^{x,y,z} \delta_{tnuv} \int_0^{2\pi} d\gamma \int_0^{\pi} d\beta \int_0^{2\pi} d\alpha \; p(\alpha, \beta, \gamma) \; a_{ujk} a_{vlm} \tag{49}$$

There are 729 integrations over the Eulerian angles in (49) among those 540 integrations turn out to be zero. The non-zero results are reported in Appendix F.

With the above correlation functions, the correlation of the scattered fields can now be determined to calculate the polarimetric scattering coefficients. All integrations in (42) can be carried out analytically except the triple integration over the Eulerian angles which may be intensive in computer time for numerical solution. Under the low-frequency approximation, analytical solution, which is very fast in computer time, is obtained and the result is expressed as

$$\sigma_{\mu\tau\nu\kappa} = \pi k_0^4 \sum_{t=1}^{N_1} \sum_{a,b,c,d}^{-1,1} \sum_{j,k,l,m}^{x,y,z} \Psi_{1\mu\tau,jk}^{ab} \Psi_{1\nu\kappa,lm}^{cd*} W_{t1jklm}^{abcd} + \pi k_0^4 \sum_{t=1}^{N_2} \sum_{p,q,r,s}^{d,u} \sum_{j,k,l,m}^{x,y,z} \Psi_{2\mu\tau,jk}^{pq} \Psi_{2\nu\kappa,lm}^{rs*} W_{t2jklm}^{pqrs} \tag{50}$$

Coefficient Ψ's have been derived earlier. For region 1, quantity W_{t1jklm}^{abcd} in (50) is

$$W_{t1jklm}^{abcd} = \int_0^{2\pi} d\gamma \int_0^{\pi} d\beta \int_0^{2\pi} d\alpha \; p(\alpha,\beta,\gamma) \; \Gamma_{t1jklm} I_{t1}^{abcd} \tag{51}$$

where the integral I_{t1}^{abcd} is approximated under the low frequency condition as

$$\begin{aligned} I_{t1}^{abcd} &= \int_{-\infty}^{\infty} d\beta_z \; \Phi_{t1\xi}(2\overline{k}_{pi}, \beta_z) \int_{-d1}^{0} dz_1 \; e^{-i(\beta_z - \kappa_{ab})z_1} \int_{-d1}^{0} dz_1^o \; e^{i(\beta_z - \kappa_{cd})z_1^o} \\ &\approx 2\pi i \Phi_{t1\xi}(0) \left[\frac{e^{-i(\kappa_{ab} - \kappa_{cd})d_1} - 1}{\kappa_{ab} - \kappa_{cd}} \right] \end{aligned} \tag{52}$$

From (49), (51), and (52), it is seen that W_{t1jklm}^{abcd} is simply

$$W_{t1jklm}^{abcd} = \Delta_{t1jklm} I_{t1}^{abcd} \tag{53}$$

Similarly for region 2, the quantity W_{t2jklm}^{abcd} in (50) is

$$W_{t2jklm}^{pqrs} = \int_0^{2\pi} d\gamma \int_0^{\pi} d\beta \int_0^{2\pi} d\alpha \; p(\alpha,\beta,\gamma) \; \Gamma_{t2jklm} I_{t2}^{pqrs} \tag{54}$$

where the integral I_{t2}^{pqrs} under the low frequency approximation is

$$\begin{aligned} I_{t2}^{pqrs} &= \int_{-\infty}^{\infty} d\beta_z \; \Phi_{t2\xi}(2\overline{k}_{pi}, \beta_z) \int_{-d2}^{-d1} dz_2 \; e^{-i(\beta_z - \kappa_{pq})z_2} \int_{-d2}^{-d1} dz_2^o \; e^{i(\beta_z - \kappa_{rs})z_2^o} \\ &= 2\pi i \Phi_{t2\xi}(0) \left[\frac{e^{-i(\kappa_{pq} - \kappa_{rs})d_2} - e^{-i(\kappa_{pq} - \kappa_{rs})d_1}}{\kappa_{pq} - \kappa_{rs}} \right] \end{aligned} \tag{55}$$

Then from (49), (54), and (55), it is recognized that W_{t2jklm}^{pqrs} is

$$W_{t2jklm}^{pqrs} = \Delta_{t2jklm} I_{t2}^{pqrs} \tag{56}$$

Note that the above results for the polarimetric scattering coefficients are expressed in the scattered basis. Both scattering regions in this configuration contain multiple species of ellipsoidal and the layers are isotropic due to the random orientation. This concludes the derivation.

In the last two sections, the effective permittivity and the polarimetric scattering coefficients have been obtained. In the next section, the model is applied to study the polarimetric scattering properties from vegetation. Effects of scatterer shape and multiple species are considered.

5.5 Results and Discussions

a. Effect of Scatterer Shapes

The model in this chapter accounts for various shapes which can be spherical, prolate or oblate spheroidal, or ellipsoidal in general. For an inhomogeneous medium with a fixed number of scatterers and fractional volume, the shape of the scatterers is a significant factor on the effective permittivity and the scattering coefficients of the medium. The shape of ice grains in snow is particularly subjected to temperature and environmental variations. To study the effect of the scatterer shape, consider a layer medium described in Figure 5.5.1. The scattering region consists of an air background and embedded scatterers of 20% fractional volume and permittivity $\epsilon_{1s} = (3.15 + i\,0.002)\epsilon_0$ for ice at 5 GHz. The underlying medium has a permittivity of $\epsilon_2 = (6.0 + i\,0.6)\epsilon_0$ which is in the permittivity range for soil.

Four different shapes of the scatterers are investigated: spherical, prolate spheroidal, oblate spheroidal, and ellipsoidal. The fractional volume and the number of scatterers are kept the same in all cases and the non-spherical scatterers are ran-

domly oriented. For the ellipsoidal shape, the longest correlation length is taken to be equal to that of the prolate spheroidal shape, the shortest correlation length is the same as that of the oblate spheroid, and the meridian correlation is chosen by setting the surface area (defined by the two longer correlation lengths) identical to that of the oblate spheroid. The correlation lengths and the calculated effective permittivities corresponding to the various shapes are reported in Table 5.5.1. It is seen that the effective permittivity is increasing when the scatterer shape varies from spherical, to prolate spheroidal, and then to oblate spheroidal forms. The permittivity results for the ellipsoids and oblate spheroids are similar due to the similar cross sections of the scatterers in the two cases.

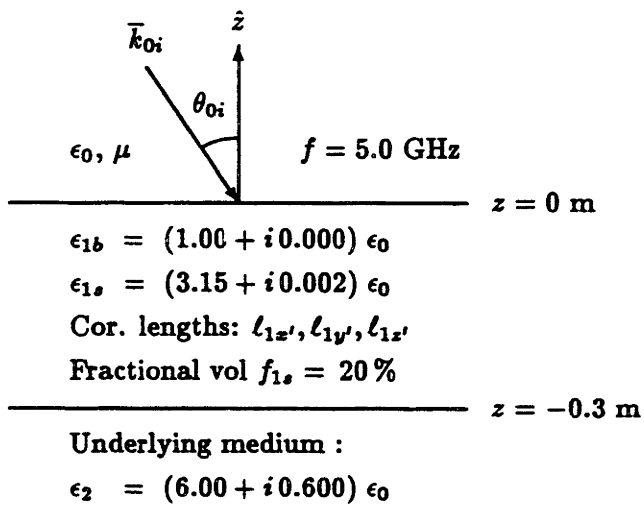

Figure 5.5.1 Scattering configuration

Shape	$\ell_{1x'}$	$\ell_{1y'}$	$\ell_{1z'}$	ϵ_{eff1}
Spherical	0.15 mm	0.15 mm	0.15 mm	$(1.29 + i\,1.95 \times 10^{-4})\,\epsilon_0$
Prolate	0.05 mm	0.05 mm	1.35 mm	$(1.31 + i\,2.27 \times 10^{-4})\,\epsilon_0$
Oblate	0.58 mm	0.58 mm	0.01 mm	$(1.33 + i\,2.63 \times 10^{-4})\,\epsilon_0$
Ellipsoidal	1.35 mm	0.25 mm	0.01 mm	$(1.32 + i\,2.64 \times 10^{-4})\,\epsilon_0$

Table 5.5.1 Correlation lengths and effective permittivities

The differences in the scatterer shape are also manifested in the scattering coefficients. Shown in Figure 5.5.2 are the copolarized backscattering coefficients where the oscillations are due to the boundary effect as discussed in Chapter 2. The copolarized backscattering increases as the scatterer cross section increases from the spherical, to prolate, and then to oblate spheroidal form. The copolarization results for the ellipsoidal and the oblate spheroidal forms are therefore similar. For cross-polarized returns, the spherical case gives zero value under the first-order distorted Born approximation. Cross-polarized backscattering coefficients for non-spherical scatterers are plotted as a function of incident angles in Figure 5.5.3. The oblate spheroids provides the highest returns while the ellipsoids and the prolate spheroids have similar cross-polarization effect due to the same size in their longest correlation lengths. As illustrated, the ellipsoids behave as a hybrid between the oblate and the prolate spheroids.

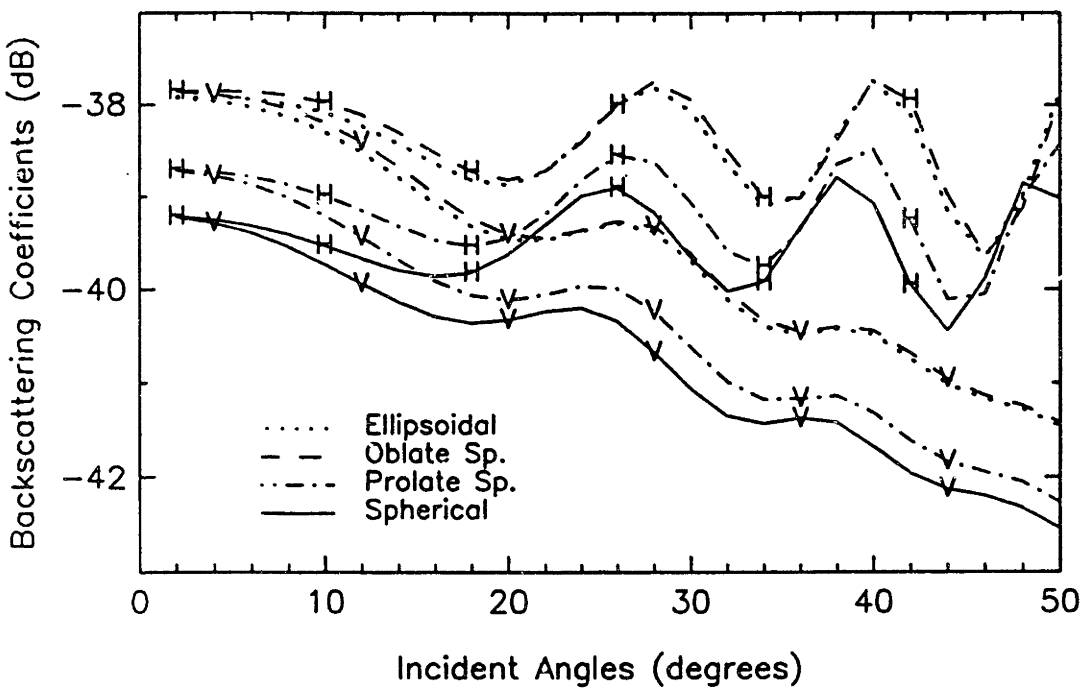

Figure 5.5.2 Copolarized backscattering coefficients : $H = \sigma_{hh}$ and $V = \sigma_{vv}$

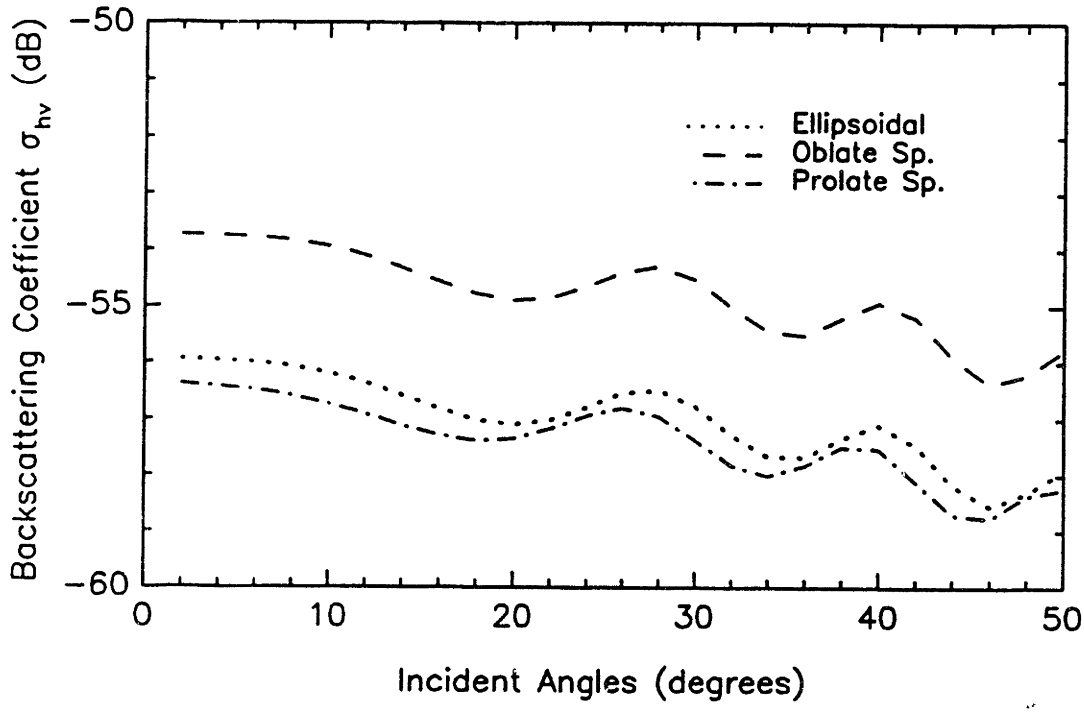

Figure 5.5.3 Cross-polarized backscattering coefficients

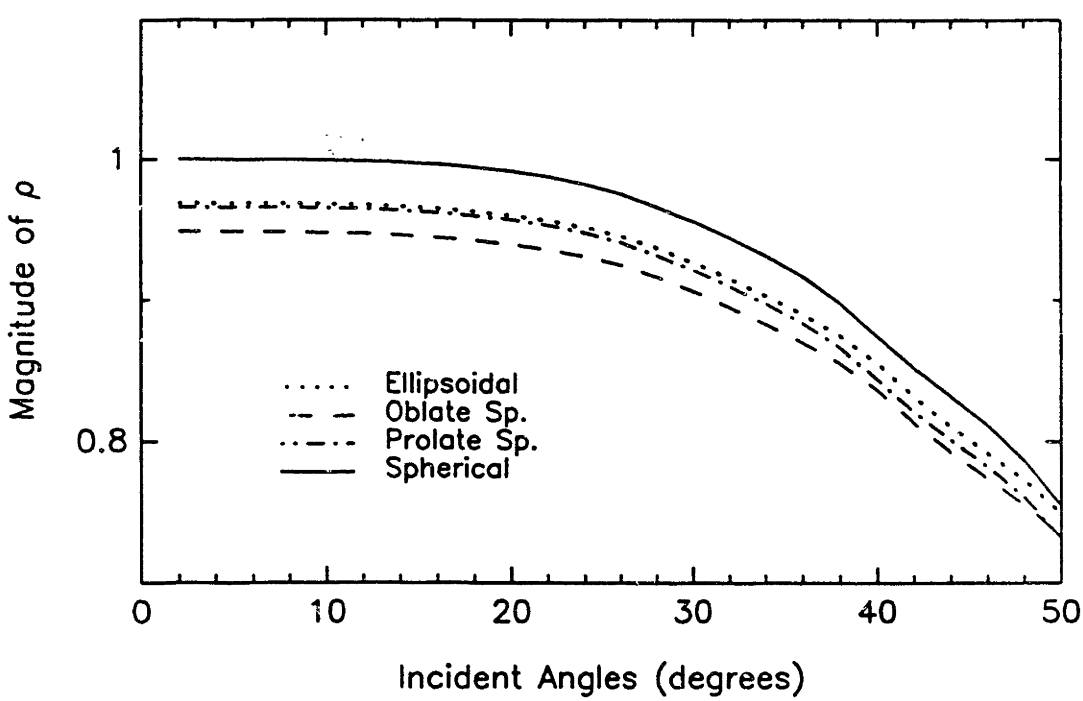

Figure 5.5.4 Magnitudes of correlation coefficient ρ

The common feature in all of the cases for the different shapes are the effective isotropy of the inhomogeneous medium. For non-spherical scatterers, the medium is rendered isotropic by random orientation with no preferred direction. The scattering centers of horizontal and vertical waves are therefore not separated as opposed to the anisotropic medium in Chapter 2. This results in correlation coefficient ρ, defined by (18b) in Chapter 1, between the h and v waves with a small phase. The magnitudes of ρ plotted in Figure 5.5.4 show a similar variation as a function of incident angles for the different shapes of the scatterers.

b. Effect of Multiple Species

In Chapter 3, the soybean canopy is modeled effectively with disc-like scatterers and the effect of needle-like scatterers has been ignored. The multi-species model in this chapter includes the coexistence of the disc-like and needle-like scatterers. In this case, the effect of the multiple species is studied with the configuration described in Figure 5.5.5 which corresponds to the soybean on 9-03-86 in Chapter 3. Now, needle-like scatterers are introduced into the canopy by allocating part of the total fractional volume to the new scatterer species whose permittivity is taken to be the same as that of the disc-like scatterers. The needle-like form is depicted by a prolate spheroidal shape with correlation lengths of 0.3 mm and 5.0 mm. Three cases are considered here: Case 1 has 100% oblate spheroids, Case 2 has 85% oblate and 15% prolate, and Case 3 has 70% oblate and 30% prolate spheroids. The calculated effective permittivities in Table 5.5.2 indicate an increase as more needle-like scatterers are introduced.

Backscattering coefficients decrease, as seen in Figure 5.5.6, for increasing needle-like species which renders the scatterer total cross section smaller. Again due to the effective isotropy, the phase of correlation coefficient ρ is small for the cases under consideration. While the magnitude of ρ for different mixtures are similar as indicated in Figure 5.5.7, intensity ratio $e = \sigma_{hv}/\sigma_{hh}$ is higher for a mixture

containing more needle-like scatterers as shown in Figure 5.5.8. This will result in a copolarized signature with higher pedestal signifying a stronger depolarization effect.

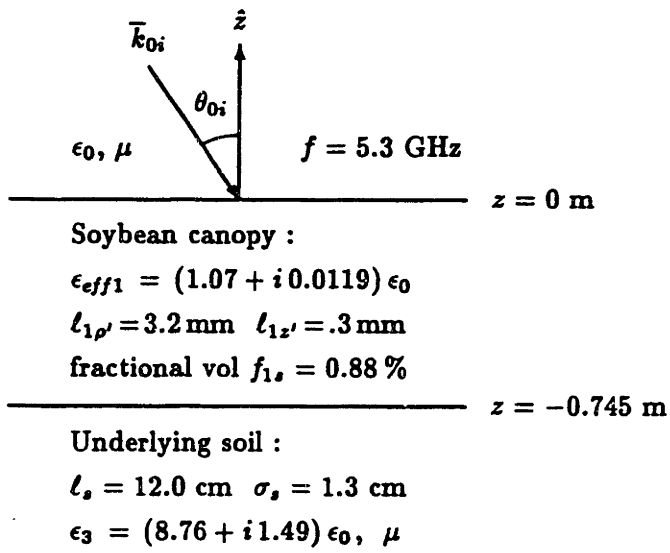

Figure 5.5.5 Scattering configuration

	Oblate	Prolate	ϵ_{eff1}
Case 1	100 %	0 %	$(1.070 + i\,0.0119)\,\epsilon_0$
Case 2	85 %	15 %	$(1.072 + i\,0.0134)\,\epsilon_0$
Case 3	70 %	30 %	$(1.074 + i\,0.0148)\,\epsilon_0$

Table 5.5.2 Species mixing and effective permittivities

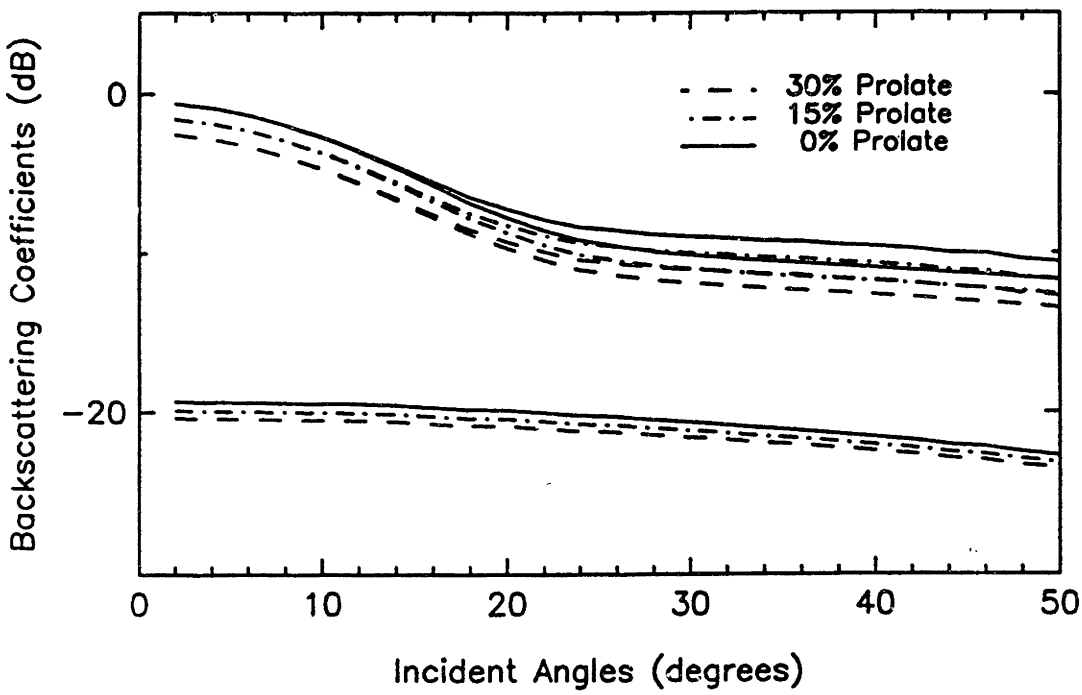

Figure 5.5.6 Copolarized backscattering coefficients : for each mixture, the top curve is for σ_{hh}, middle for σ_{vv}, and bottom for σ_{hv}

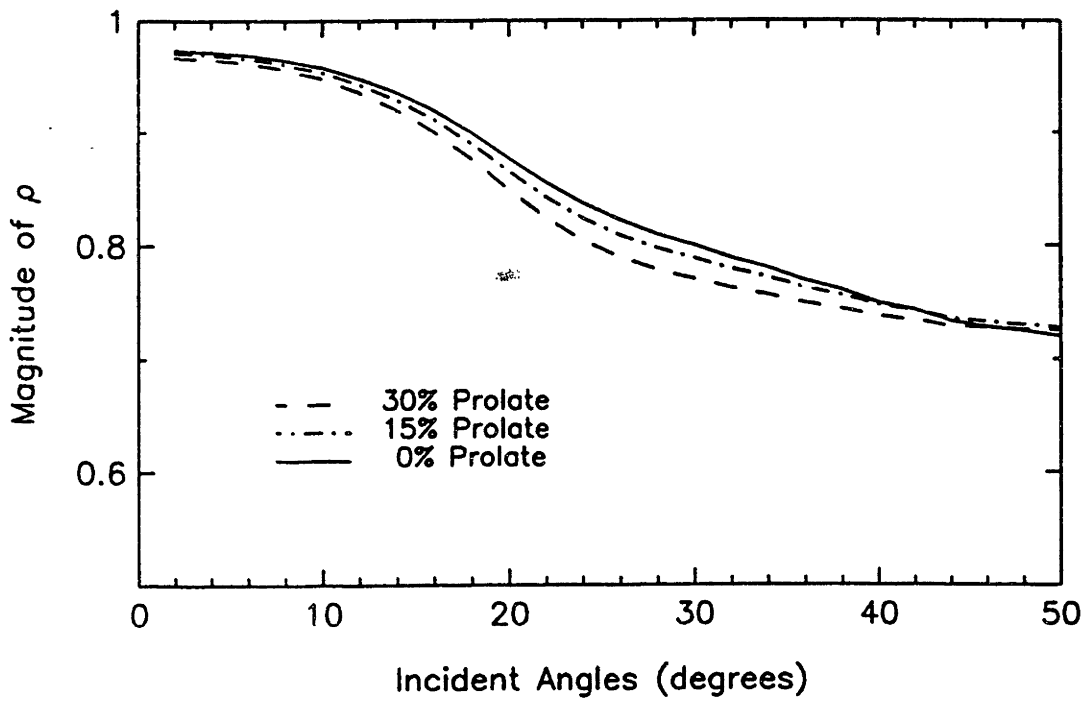

Figure 5.5.7 Magnitudes of correlation coefficient ρ

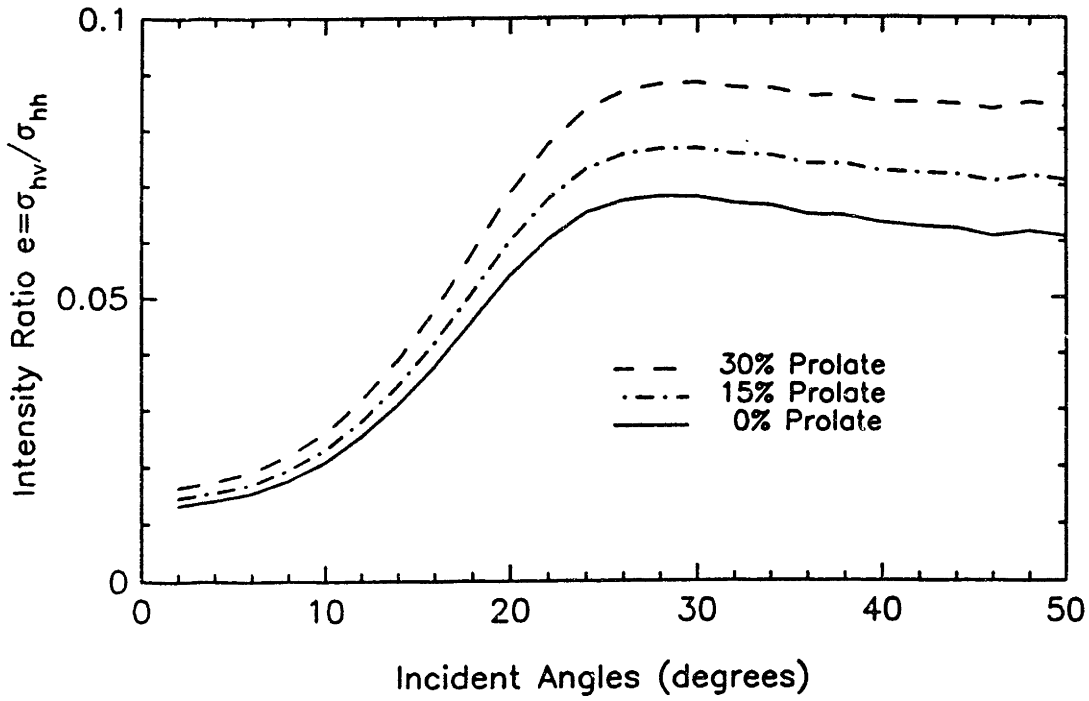

Figure 5.5.8 Intensity ratio $e = \sigma_{hv}/\sigma_{hh}$

5.6 Summary

In this chapter, a layer model with scattering regions containing multiple species of scatterers has been presented. The species are allowed to have different size, shape, and permittivity. After the scatterer correlation is analyzed, the effective permittivity of the multi-species medium is derived with the extended strong fluctuation theory. The polarimetric scattering coefficients is then calculated under the distorted Born approximation. The model indicates that non-spherical scatterers with larger cross section give higher permittivity and backscattering. For a mixture of oblate (disc-like) and prolate (needle-like) spheroids, the depolarization effect is stronger when the disc-like portion is increased. The model laid out in this chapter paves the way for an extension to account for more complexity of geophysical media where the multiple species can have size and shape distributions considered in the next chapter.

Chapter 6
Model with Size and Shape Distributions

6.1 Introduction

Inhomogeneities in geophysical media are multifarious. The model presented in this chapter accounts for the complexity of the multi-phase inhomogeneities with multiple species characterized by orientation, size, and shapes distributions. The orientation distribution of scatterers has been considered in previous chapters. The size variety of scatterers in a species is described in terms of the number density or the fractional volume as a function of normalized volumetric sizes. The shape variation affects electromagnetic properties of the inhomogeneous media in a nonlinear manner. To depict the various shapes of scatterers in a species, the scatterers with similar shape are classified into a shape division treated as a subspecies. The model is then used to derive the effective permittivity and polarimetric scattering coefficients.

The chapter is composed of six sections. Section 6.2 presents the derivation of the effective permittivity with the extended strong fluctuation theory for the multi-species medium with orientation, size, and shape distributions. Section 6.3 shows the calculation of the polarimetric scattering coefficients under the distorted Born approximation. Section 6.4 adapts the model specifically to sea ice whose thermal variation in structure and constituent characteristics are taken into consideration. Section 6.5 compares the theoretical and experimental results, explains the physical

mechanisms causing the thermal variation observed in sea ice, and studies the sensitivities of the model input parameters. Section 6.6 finally summarizes the chapter.

6.2 Effective Permittivity

Geophysical media contain scatterers with complex properties. The multiple species model in the last chapter need to be further developed to account for preferred alignment, size and shape distributions of the scatterers. In this section, the strong fluctuation theory is extended to derive the effective permittivity of the multi-species medium with given orientation, size, and shape distributions.

Consider an inhomogeneous medium composed of a background and a number of scatterer species. A species is temporarily defined as a set of scatterers with same permittivity. Auxiliary permittivity $\bar{\bar{\epsilon}}_g$ (quasi-static part) and dyadic coefficient $\bar{\bar{S}}$ are solved by iteration method from a set of nonlinear equations. From previous chapters, it is observed that dyadic coefficient $\bar{\bar{S}}$, representing the singularity, does depend on the ratios of correlation lengths; i.e., the scatterer shape. Thus, it is necessary to classify scatterers in each species into divisions treated as subspecies; each contains scatterers of similar shape. To simply the matter, a species is now redefined as a set of scatterers with the same permittivity *and* same shape. While $\bar{\bar{\epsilon}}_g$ depends only on correlation length ratios, the scattering-correction part of the effective permittivity does, however, depend on the scatterer size. The variation in size of the scatterers in a species can therefore be accounted for with an integration over the scatterer size distribution in the calculation of the scattering-correction part.

Let ϵ_b be the permittivity of the background medium containing N scatterer species. The scatterers are ellipsoids with vertical alignment and random azimuthal orientation. Permittivity $\epsilon_{i,}$ is for species i occupying a fractional volume $f_{i,}$ in the mixture. The effective permittivity of the inhomogeneous medium is composed of a quasi-static part and a scattering-effect part corresponding to the first and second

term, respectively, in the following expression

$$\bar{\bar{\epsilon}}_{eff} = \bar{\bar{\epsilon}}_g + \epsilon_0 \left[\bar{\bar{I}} - \bar{\bar{\xi}}_{eff} \cdot \left\langle \bar{\bar{S}} \right\rangle\right]^{-1} \cdot \bar{\bar{\xi}}_{eff} \tag{1}$$

where auxiliary permittivity $\bar{\bar{\epsilon}}_g$ and dyadic coefficient $\bar{\bar{S}}$ will be derived from the condition of secular-term elimination, and the effective dyadic scatterer $\bar{\bar{\xi}}_{eff}$ under the low-frequency approximation is

$$\left[\bar{\bar{\xi}}_{eff}\right]_{jm} = \sum_{i(s)=1}^{N} \int_{v_i} dv \int_0^{2\pi} d\gamma \int_0^{\pi} d\beta \int_0^{2\pi} d\alpha \; p_i(\alpha,\beta,\gamma) \sum_{k,l}^{x,y,z} \Gamma^{(0)}_{i\xi jklm} \left\{ k_0^2 \int_{-\infty}^{\infty} d\bar{k}' \left[\bar{\bar{G}}_g(\bar{k}')\right]_{kl} \Phi_{i\xi}(\bar{k}') + \left[\bar{\bar{S}}_i\right]_{kl} \right\} \Big|_{v,\alpha,\beta,\gamma} \tag{2}$$

where subscript i denotes species $i(s)$ which depends on the scatterer shape. The normalized volumetric size v is defined as the ratio of the volume of a scatterer under consideration over the volume of the smallest scatterer of the same permittivity *regardless of shape*. The integration over dv accounts for the size distribution in the size range v_i of the scatterers in species i. Quantity $p_i(\alpha,\beta,\gamma)$ is the probability density function of orientation given by (5, Chapter 4). $\bar{\bar{G}}_g$ is the anisotropic Green's function determined by (32, Chapter 2). $\Phi_{i\xi}$ is the Fourier transform of the normalized local correlation function. Local variance of species i is $\Gamma^{(0)}_{i\xi jklm}$ defined as

$$\Gamma^{(0)}_{i\xi jklm}(\hat{r}') = f_{is}(v) f_b \left(\xi_{ijk} - \xi_{bjk}\right)\left(\xi_{ilm} - \xi_{blm}\right) \tag{3}$$

Note that fractional volume $f_{is}(v)$ of species i is a function of the normalized volumetric size v.

To derive the effective permittivity, the method in Chapter 4 for anisotropic medium is combined with the method in Chapter 5 for multi-species mixture. The condition of secular elimination $\left\langle \bar{\bar{\xi}}(\bar{r}) \right\rangle = 0$ is imposed to find $\bar{\bar{\epsilon}}_g = diag(\epsilon_{g\rho}, \epsilon_{g\rho}, \epsilon_{gz})$

$$\left\langle \bar{\bar{\xi}}(\bar{r}) \right\rangle = \int_0^{2\pi} d\gamma \int_0^{\pi} d\beta \int_0^{2\pi} d\alpha \; p(\alpha,\beta,\gamma) \; \bar{\bar{T}}^{-1} \cdot \left[f_b \bar{\bar{\xi}}_b + \sum_{i=1}^{N} f_{is} \bar{\bar{\xi}}_i \right] \cdot \bar{\bar{T}} = 0 \tag{4}$$

Carrying out the integration over the Eulerian orientation angles yields

$$f_b \left(\xi_{bx'} + \xi_{by'}\right) + \sum_{i=1}^{N} f_i \left(\xi_{ix'} + \xi_{iy'}\right) = 0 \tag{5a}$$

$$f_b \xi_{bz'} + \sum_{i=1}^{N} f_i \xi_{iz'} = 0 \tag{5b}$$

In (5), ξ's are related to coefficient S's and written in the local coordinates as

$$\xi_{ix'}(\epsilon) = \xi_{ix'x'}(\epsilon) = \frac{\epsilon - \epsilon_{g\rho}}{\epsilon_0 + S_{ix'}(\epsilon - \epsilon_{g\rho})} \tag{6a}$$

$$\xi_{iy'}(\epsilon) = \xi_{iy'y'}(\epsilon) = \frac{\epsilon - \epsilon_{g\rho}}{\epsilon_0 + S_{iy'}(\epsilon - \epsilon_{g\rho})} \tag{6b}$$

$$\xi_{iz'}(\epsilon) = \xi_{iz'z'}(\epsilon) = \frac{\epsilon - \epsilon_{gz}}{\epsilon_0 + S_{iz'}(\epsilon - \epsilon_{gz})} \tag{6c}$$

where $i = 1, 2, ..., N$ for the scatterer species or $i = b$ for the background; ϵ can takes on the value of ϵ_{is} in a scatterer of species i or ϵ_b in the background medium. Dyadic coefficient $\overline{\overline{S}}_i$ for ellipsoidal scatterer has been derived in Chapter 4 and the result for species i is

$$S_{ix'} = \int_0^{2\pi} d\phi \, \frac{\epsilon_0 \gamma_{ix}^2 \cos^2\phi}{2\pi \epsilon_{g\rho} a_i \sqrt{a_i}} \left[(1 + a_i) \tan^{-1}\sqrt{a_i} - \sqrt{a_i}\right] \tag{7a}$$

$$S_{iy'} = \int_0^{2\pi} d\phi \, \frac{\epsilon_0 \gamma_{iy}^2 \sin^2\phi}{2\pi \epsilon_{g\rho} a_i \sqrt{a_i}} \left[(1 + a_i) \tan^{-1}\sqrt{a_i} - \sqrt{a_i}\right] \tag{7b}$$

$$S_{iz'} = \int_0^{2\pi} d\phi \, \frac{\epsilon_0 (1 + a_i)}{2\pi \epsilon_{gz} a_i \sqrt{a_i}} \left[\sqrt{a_i} - \tan^{-1}\sqrt{a_i}\right] \tag{7c}$$

where the integrations over ϕ are carried out numerically and a_i, γ_{ix}, and γ_{iy} are

$$a_i = \alpha \gamma_i^2 - 1\,, \quad \alpha = \frac{\epsilon_{gz}}{\epsilon_{g\rho}} \tag{8a}$$

$$\gamma_i = \frac{1}{\ell_{ix'}} \left(\frac{\cos^2\phi}{\ell_{ix'}^2} + \frac{\sin^2\phi}{\ell_{iy'}^2}\right)^{-\frac{1}{2}} \tag{8b}$$

$$\gamma_{ix} = \frac{1}{\ell_{ix'}} \left(\frac{\cos^2\phi}{\ell_{ix'}^2} + \frac{\sin^2\phi}{\ell_{iy'}^2}\right)^{-\frac{1}{2}} \tag{8c}$$

$$\gamma_{iy} = \frac{1}{\ell_{iy'}} \left(\frac{\cos^2\phi}{\ell_{ix'}^2} + \frac{\sin^2\phi}{\ell_{iy'}^2}\right)^{-\frac{1}{2}} \tag{8d}$$

Taking the average of the species $\overline{\overline{S}}_i$ renders dyadic coefficient $\overline{\overline{S}}_b$ for the background medium

$$\overline{\overline{S}}_b = \left(\sum_{i=1}^{N} f_i \overline{\overline{S}}_i\right) \left(\sum_{i=1}^{N} f_i\right)^{-1} \tag{9}$$

Then, the average dyadic coefficient $\langle \overline{\overline{S}} \rangle$ in (1) is determined by

$$\langle \overline{\overline{S}} \rangle = \sum_{i=1}^{N,b} f_{is} \int_0^{2\pi} d\gamma \int_0^{\pi} d\beta \int_0^{2\pi} d\alpha \, p_i(\alpha,\beta,\gamma) \, \overline{\overline{T}}^{-1} \cdot \begin{bmatrix} S_{ix'} & 0 & 0 \\ 0 & S_{iy'} & 0 \\ 0 & 0 & S_{iz'} \end{bmatrix} \cdot \overline{\overline{T}}$$

$$= \sum_{i=1}^{N,b} \frac{f_{is}}{2} \begin{bmatrix} S_{ix'} + S_{iy'} & 0 & 0 \\ 0 & S_{ix'} + S_{iy'} & 0 \\ 0 & 0 & 2S_{iz'} \end{bmatrix} = \begin{bmatrix} S_\rho & 0 & 0 \\ 0 & S_\rho & 0 \\ 0 & 0 & S_z \end{bmatrix} \tag{10}$$

for $f_{bs} = f_b$. Then ϵ_g's and S's are solved from the above equations with an iteration method.

To complete the derivation of the effective permittivity, the effective scatterer needs be obtained. Due to the azimuthal symmetry, effective scatterer tensor $\overline{\overline{\xi}}_{eff}$ takes on the uniaxial form

$$\overline{\overline{\xi}}_{eff} = \begin{bmatrix} \xi_{eff\rho} & 0 & 0 \\ 0 & \xi_{eff\rho} & 0 \\ 0 & 0 & \xi_{effz} \end{bmatrix} \tag{11}$$

which is defined by (2) from which the following results are acquired

$$\xi_{eff\rho} = \frac{1}{2} \sum_{i(s)=1}^{N} \int_{v_i} dv \left[\delta_{i\xi x'} \left(I_{ix'} + S_{ix'} \right) + \delta_{i\xi y'} \left(I_{iy'} + S_{iy'} \right) \right] \tag{12a}$$

$$\xi_{effz} = \sum_{i(s)=1}^{N} \int_{v_i} dv \delta_{i\xi z'} \left(I_{iz'} + S_{iz'} \right) \tag{12b}$$

Variance $\delta_{i\xi}$'s in (12) are related to fractional volumes and local scatterer by

$$\delta_{i\xi j'} = f_{is} f_b \left(\xi_{ij'} - \xi_{bj'} \right) \left(\xi_{ij'} - \xi_{bj'} \right) \tag{13}$$

Quantity I's in (12) is the integrations of products between Green's function elements and the correlation function. For ellipsoids with vertical alignment and random azimuthal orientation, the results for I's of scatterer species i can be summarized as follows:

(a) For z' element

$$I_{iz'} = \int_0^{2\pi} d\phi \, \frac{-\epsilon_0}{\pi \epsilon_{gz'}} (\mathcal{I}_{i\phi}^s + \mathcal{I}_{i\phi}^d) \tag{14a}$$

$$\mathcal{I}^e_{i\phi} = -\frac{\alpha\gamma_i^2\sqrt{\alpha\gamma_i^2}}{2a_i^2}\left[\frac{\sqrt{-\zeta}}{\vartheta_e} + \frac{\vartheta_e+\zeta}{\vartheta_e\sqrt{\vartheta_e}}\left(\frac{\pi}{2} - \tan^{-1}\frac{\sqrt{-\zeta}}{\sqrt{\vartheta_e}}\right)\right] \tag{14b}$$

$$\mathcal{I}^d_{i\phi} = \frac{\alpha\gamma^2}{2a_i^2}\left[\frac{1+a_i\nu_{gz'}^2}{\vartheta_o} + \frac{\vartheta_o(a_i+2)-(b+a_i\nu_{gz'}^2)}{\vartheta_o\sqrt{\vartheta_o}}\left(\frac{\pi}{2} - \tan^{-1}\frac{1}{\sqrt{\vartheta_o}}\right)\right] \tag{14c}$$

$$\nu_{gz'}^2 = k_{g\rho}^2\ell_{iz'}^2, \quad k_{g\rho}^2 = \omega^2\mu_0\epsilon_{g\rho}, \quad \zeta = \alpha\gamma_i^2\nu_{gz'}^2 \tag{14d}$$

$$b = \frac{\alpha\gamma_i^2+\zeta}{a_i}, \quad \vartheta_o = b-1, \quad \vartheta_e = b+\zeta \tag{14e}$$

(b) For x' element

$$I_{ix'} = \int_0^{2\pi} d\phi\, \frac{k_0^2}{\pi}\left(\ell_{iy'}^2\gamma_{iy}^4\sin^2\phi\, I^o_{i\phi} + \ell_{ix'}^2\gamma_{ix}^4\cos^2\phi\, I^e_{i\phi}\right) \tag{15a}$$

$$I^e_{i\phi} = \alpha\left[(\mathcal{I}^e_1 - \mathcal{I}^e_2 - \mathcal{I}^e_3) + \frac{1}{\zeta}(\mathcal{I}_s + \mathcal{I}_d - \frac{1}{2})\right] \tag{15b}$$

$$I^o_{i\phi} = \mathcal{I}^o_1 - \mathcal{I}^o_2 - \mathcal{I}^o_3 \tag{17c}$$

$$\mathcal{I}^e_1 = \frac{\alpha\gamma_i^2\sqrt{\alpha\gamma_i^2}}{2a_i^2\vartheta_e}\left[-\frac{\sqrt{-\zeta}}{b} + \frac{1}{\sqrt{\vartheta_e}}\left(\frac{\pi}{2} - \tan^{-1}\frac{\sqrt{-\zeta}}{\sqrt{\vartheta_e}}\right)\right] \tag{15d}$$

$$\mathcal{I}^e_2 = \frac{1}{2a_i\vartheta_o}\left[1 - \frac{1}{\sqrt{\vartheta_o}}\left(\frac{\pi}{2} - \tan^{-1}\frac{1}{\sqrt{\vartheta_o}}\right)\right] \tag{15e}$$

$$\mathcal{I}^e_3 = \frac{\alpha\gamma_i^2}{2a_i^2\vartheta_o}\left[-\frac{1}{b} + \frac{1}{\sqrt{\vartheta_o}}\left(\frac{\pi}{2} - \tan^{-1}\frac{1}{\sqrt{\vartheta_o}}\right)\right] \tag{15f}$$

$$\mathcal{I}^o_1 = \mathcal{I}^e_1(\alpha=1), \quad \mathcal{I}^o_2 = \mathcal{I}^e_2(\alpha=1), \quad \mathcal{I}^o_3 = \mathcal{I}^e_3(\alpha=1) \tag{15g}$$

(c) For y' element

$$I_{iy'} = \int_0^{2\pi} d\phi\, \frac{k_0^2}{\pi}\left(\ell_{ix'}^2\gamma_{ix}^4\cos^2\phi\, I^o_{i\phi} + \ell_{iy'}^2\gamma_{iy}^4\sin^2\phi\, I^e_{i\phi}\right) \tag{16}$$

Substituting $\bar{\bar{\epsilon}}_g$, $\langle\bar{\bar{S}}\rangle$, and $\bar{\bar{\xi}}_{eff}$ in (1) finally yields the uniaxial effective permittivity tensor $\bar{\bar{\epsilon}}_{eff} = diag(\epsilon_{eff\rho}, \epsilon_{eff\rho}, \epsilon_{effz})$ whose lateral and vertical elements are, respectively

$$\epsilon_{eff\rho} = \epsilon_{g\rho} + \epsilon_0\xi_{eff\rho}/(1 - S_\rho\xi_{eff\rho}) \tag{17a}$$

$$\epsilon_{effz} = \epsilon_{gz} + \epsilon_0\xi_{effz}/(1 - S_z\xi_{effz}) \tag{17b}$$

Depending on the structure and characteristics of the multi-species medium, the size and the shape distributions can be measured by using digitized section images [90].

The local correlation lengths corresponding to a scatterers can also be estimated by setting the correlation volume to be equal to the volume of the scatterer with the same axial ratios [88]. For an ellipsoid with major semi-axis a, meridian semi-axis b, and minor semi-axis c, relations with correlation lengths are

$$\ell_{ix'}\ell_{iy'}\ell_{iz'} = cba(6)^{-1/3}, \quad \ell_{iy'}/\ell_{ix'} = b/c, \quad \ell_{iz'}/\ell_{ix'} = a/c \tag{18}$$

The expressions in (17) indicate that effective permittivity $\bar{\bar{\epsilon}}_{eff}$ is anisotropic with an optic axis in the vertical direction due to the azimuthal symmetry. The derivation has been done for ellipsoidal scatterers which is more general and can be reduced to the spheroidal or the spherical case. In the next section, the anisotropic effective permittivity is used in the derivation of the polarimetric backscattering coefficients under the distorted Born approximation for a layer configuration.

6.3 Scattering Coefficients

A layer configuration with four different regions as illustrated in Figure 2.2.1 is considered here. Region 0 and region 4 are homogenous. Region 1 is a multi-species isotropic medium. Region 2 also contains multiple species of scatterers and becomes anisotropic due to the vertical alignment of scatterers. The polarimetric backscattering coefficients are defined by (13, Chapter 1) based on ensemble averages of scattered fields expressed as follows

$$\begin{aligned}
\left\langle \overline{E}_{0s}(\overline{r}) \cdot \overline{E}^{*}_{0s}(\overline{r}) \right\rangle = & \sum_{t(s)=1}^{N_1} \sum_{i,j,k,l,m}^{x,y,z} k_0^4 \int_{v_t} dv \int_0^{2\pi} d\gamma \int_0^{\pi} d\beta \int_0^{2\pi} d\alpha \; p_{t1}(\alpha,\beta,\gamma) \\
& \cdot \int_{V_1} d\overline{r}_1 \int_{V_1} d\overline{r}_1^{\circ} \, C_{t\xi 1jklm}(\overline{r}_1, \overline{r}_1^{\circ}; v, \alpha, \beta, \gamma) \\
& \cdot \left[\left\langle G_{01ij}(\overline{r}, \overline{r}_1) \right\rangle \left\langle F_{1k}(\overline{r}_1) \right\rangle \right] \cdot \left[\left\langle G_{01il}(\overline{r}, \overline{r}_1^{\circ}) \right\rangle \left\langle F_{1m}(\overline{r}_1^{\circ}) \right\rangle \right]^{*} \\
& + \sum_{t(s)=1}^{N_2} \sum_{i,j,k,l,m}^{x,y,z} k_0^4 \int_{v_t} dv \int_0^{2\pi} d\gamma \int_0^{\pi} d\beta \int_0^{2\pi} d\alpha \; p_{t2}(\alpha,\beta,\gamma) \\
& \cdot \int_{V_2} d\overline{r}_2 \int_{V_2} d\overline{r}_2^{\circ} \, C_{t\xi 2jklm}(\overline{r}_2, \overline{r}_2^{\circ}; v, \alpha, \beta, \gamma) \\
& \cdot \left[\left\langle G_{02ij}(\overline{r}, \overline{r}_2) \right\rangle \left\langle F_{2k}(\overline{r}_2) \right\rangle \right] \cdot \left[\left\langle G_{02il}(\overline{r}, \overline{r}_2^{\circ}) \right\rangle \left\langle F_{2m}(\overline{r}_2^{\circ}) \right\rangle \right]^{*}
\end{aligned} \tag{19}$$

where $t(s)$ denotes scatterer species t which depends on the scatterer shape, N_1 is the number of species in region 1, and N_2 the number of species in region 2. Green's functions and mean fields are calculated with effective permittivities and results have been given in previous chapters.

In (19), correlation function C's are defined in the spatial domain with

$$C_{t\xi njklm}(\overline{r}_n, \overline{r}_n^o; v, \alpha, \beta, \gamma) = \left\langle \xi_{tnjk}(\overline{r}_n) \xi^*_{tnlm}(\overline{r}_n^o) \middle| v(\overline{r}_n), \alpha(\overline{r}_n), \beta(\overline{r}_n), \gamma(\overline{r}_n) \right\rangle , \quad n = 1,2 \tag{20}$$

where n represents region $n = 1,2$. To facilitate the integration in (19), Fourier transforms of the correlation functions are introduced

$$C_{t\xi njklm}(\overline{r}_n, \overline{r}_n^o; v, \alpha, \beta, \gamma) = \int_{-\infty}^{\infty} d\overline{\beta} \Phi_{tnjklm}(\overline{\beta}) e^{-i\overline{\beta}\cdot(\overline{r}_n - \overline{r}_n^o)} , \quad n = 1,2 \tag{21}$$

which is expressed in the global coordinate system $(\hat{x}, \hat{y}, \hat{z})$ and related by the rotation transformation with Eulerian angles (α, β, γ) to those in the local coordinate system $(\hat{x}', \hat{y}', \hat{z}')$. Note that, for ellipsoids with vertical alignment and random azimuthal orientation, only rotation α is necessary. Spectral density Φ_{tnjklm} can be written in terms of a variance and a normalized functional form as

$$\Phi_{tnjklm}(\overline{\beta}) = \Gamma_{tnjklm} \Phi_{t\xi n}(\overline{\beta}) \tag{22}$$

Variance Γ_{tnjklm} of species t and region n are defined the local coordinates with

$$\Gamma_{tnjklm}(\hat{\tau}') = f_{ins} f_{bn} \left(\xi_{tnjk} - \xi_{tbjk}\right) \left(\xi_{tnlm} - \xi_{silm}\right)^* \tag{23}$$

By applying the appropriate rotation to the variances and using the invariance of Fourier transform under rotation transformation, the correlation functions can be written in the global coordinates to calculate the scattering coefficients.

Polarimetric backscattering coefficients for the layer configuration can be cast into the form

$$\sigma_{\mu\tau\nu\kappa} = \pi k_0^4 \sum_{t(s)=1}^{N_1} \sum_{a,b,c,d}^{-1,1} \sum_{j,k,l,m}^{x,y,z} \Psi^{ab}_{1\mu\tau,jk} \Psi^{cd*}_{1\nu\kappa,lm} W^{abcd}_{t1jklm}$$
$$+ \pi k_0^4 \sum_{t(s)=1}^{N_1} \sum_{p,q,r,s}^{ou,od \atop eu,ed} \sum_{j,k,l,m}^{x,y,z} \Psi^{pq}_{2\mu\tau,jk} \Psi^{rs*}_{2\nu\kappa,lm} W^{pqrs}_{t2jklm} \tag{24}$$

Coefficient Ψ's have been obtained in previous chapters. For region 1, the quantity W^{abcd}_{t1jklm} in (24) is

$$W^{abcd}_{t1jklm} = \int_{v_t} dv \int_0^{2\pi} d\gamma \int_0^{\pi} d\beta \int_0^{2\pi} d\alpha \; p_{t1}(\alpha,\beta,\gamma)\, \Gamma_{t1jklm} I^{abcd}_{t1} \tag{25}$$

which has been considered in Chapter 3 for spheroids and Chapter 5 for ellipsoids. Similarly for region 2, the quantity W^{pqrs}_{t2jklm} in (24) is

$$W^{pqrs}_{t2jklm} = \int_{v_t} dv \int_0^{2\pi} d\gamma \int_0^{\pi} d\beta \int_0^{2\pi} d\alpha \; p_{t2}(\alpha,\beta,\gamma)\, \Gamma_{t2jklm} I^{pqrs}_{t2} \tag{26}$$

where the integral I^{pqrs}_{t2} for ellipsoids of species t in region 2 is

$$\begin{aligned} I^{pqrs}_{t2jklm} = i\frac{2\delta_{t2jklm}\ell_{t2x'}\ell_{t2y'}\ell_{t2z'}}{\pi\mathcal{L}^4_{t2}} \Bigg[& \frac{e^{-i(\kappa_{pq}-\kappa_{rs})d_2}}{(\kappa_{pq}-\kappa_2)^2(\kappa_{pq}-\kappa_2^*)^2(\kappa_{pq}-\kappa_{rs})} \\ & + \frac{e^{i(\kappa_{rs}-\kappa_{pq})d_1}}{(\kappa_{rs}-\kappa_2)^2(\kappa_{rs}-\kappa_2^*)^2(\kappa_{rs}-\kappa_{pq})} - \mathcal{P}_2(\kappa_2) - \mathcal{Q}_2(\kappa_2^*) \Bigg] \end{aligned} \tag{27a}$$

where $\mathcal{P}_2(\kappa_2)$ and $\mathcal{Q}_2(\kappa_2^*)$ are determined by

$$\begin{aligned} \mathcal{P}_2(\kappa_2) = {} & \frac{i(d_2-d_1)e^{-i(\kappa_2-\kappa_{rs})d_1}e^{i(\kappa_2-\kappa_{pq})d_2}}{(2i\mathrm{Im}\kappa_2)^2(\kappa_2-\kappa_{pq})(\kappa_2-\kappa_{rs})} \\ & + \Bigg[\frac{e^{-i(\kappa_{pq}-\kappa_{rs})d_1}+e^{-i(\kappa_{pq}-\kappa_{rs})d_2}}{(2i\mathrm{Im}\kappa_2)^2(\kappa_2-\kappa_{pq})(\kappa_2-\kappa_{rs})} \\ & - \frac{e^{-i(\kappa_2-\kappa_{rs})d_1}e^{i(\kappa_2-\kappa_{pq})d_2}}{(2i\mathrm{Im}\kappa_2)^2(\kappa_2-\kappa_{pq})(\kappa_2-\kappa_{rs})}\Bigg] \\ & \cdot \left[\frac{1}{i\mathrm{Im}\kappa_2}+\frac{1}{\kappa_2-\kappa_{pq}}+\frac{1}{\kappa_2-\kappa_{rs}}\right] \end{aligned} \tag{27b}$$

$$\begin{aligned} \mathcal{Q}_2(\kappa_2^*) = {} & \frac{i(d_2-d_1)e^{i(\kappa_2^*-\kappa_{pq})d_1}e^{-i(\kappa_2^*-\kappa_{rs})d_2}}{(2i\mathrm{Im}\kappa_2^*)^2(\kappa_2^*-\kappa_{pq})(\kappa_2^*-\kappa_{rs})} \\ & + \frac{e^{i(\kappa_2^*-\kappa_{pq})d_1}e^{-i(\kappa_2^*-\kappa_{rs})d_2}}{(2i\mathrm{Im}\kappa_2^*)^2(\kappa_2^*-\kappa_{pq})(\kappa_2^*-\kappa_{rs})} \\ & \cdot \left[\frac{1}{i\mathrm{Im}\kappa_2^*}+\frac{1}{\kappa_2^*-\kappa_{pq}}+\frac{1}{\kappa_2^*-\kappa_{rs}}\right] \end{aligned} \tag{27c}$$

with length $\mathcal{L}_{t2} = \ell_{t2x'}$ and pole κ_2 given by

$$\kappa_2 = i\mathcal{L}^{-1}_{t2}\sqrt{1+k^2_{\phi a}\ell^2_{t2x'}+k^2_{\phi y}\ell^2_{t2y'}} \tag{28}$$

For the ellipsoids, only rotation α is necessary and the triple integration over Eulerian angles reduced to one which can be carried out numerically together with the integration over size v. The above results for the polarimetric scattering coefficients are in the scattered basis which can be transformed to the incident basis if necessary. In the next section, the model is specifically adapted to model sea ice with consideration of thermal variation in the medium structure and the constituent characteristics.

6.4 Model for Sea Ice

Sea ice is a multi-species medium with multi-phase mixing. The background is ice grown in columnar form as observed in congelation ice in many cases with horizontal crystallographic C axes. When there is no directional force, such as sea current, exerted during the growth process, the C axes are randomly oriented in azimuthal directions. The background ice are actually ice platelets which sandwich sea water in ellipsoidal pockets called brine inclusions. In addition, there are air bubbles embedded in the ice. Sea ice is also very dynamic in thermal variation. When the temperature changes, the ice structure varies and the constituent characteristics such as fractional volume and permittivity also vary. The model developed in the previous sections of this chapter is now specifically adapted to sea ice by using orientation, size, and shape distributions of scatterers and incorporating the thermodynamics of sea ice.

a. Size Distribution

Due to high permittivity of the saline water at microwave frequencies, brine inclusions have a strong effect on electromagnetic properties of sea ice. The size distribution of the inclusions has been reported to follow the power law [26]. Consider a power-law distribution for number density n of scatterers with size v described by

$$n = n_0 v^{-2p} \tag{29}$$

where p is the power-law index and n_0 is the number density of brine inclusions of

smallest size. The normalized volumetric size has been defined in section 6.2 as the ratio of volume v_s of an inclusion over the volume v_{s0} of the smallest one; namely,

$$v = v_s/v_{s0} = f_s/(nv_{s0}) \tag{30}$$

in which f_s (let's temporarily drop the species subscript) is the fractional volume of inclusions with volume v_s. From (30), the size distribution can also be represented by fractional volume as

$$f_s(v) = n_0 v_{s0} v^{1-2p} = f_{s0} v^{1-2p} \tag{31}$$

for f_{s0} being the fractional volume of the smallest inclusions. The size distribution is thus specified when f_{s0} and p are determined. This can be done when the total fractional volume, the minimum, average, and maximum sizes of the brine inclusions are measured.

Average volumetric size v_a can be obtained by measuring the sizes of every inclusions then taking the average. Mathematically, this process is described by

$$v_a = \frac{1}{f_{sM} - f_{s0}} \int_{f_{s0}}^{f_{sM}} df_s v(f_s) = \frac{1}{f_{sM} - f_{s0}} \int_{f_{s0}}^{f_{sM}} df_s \left(\frac{f_s}{f_{s0}}\right)^{1/(1-2p)} \tag{32}$$

Another method of measuring the average volumetric size is to take the ratio of the total fractional volume f_{sT} over the total number density n_T of the brine inclusions normalized to the smallest volume v_{s0}; i.e.,

$$v_a = \frac{f_{sT}}{n_T v_{s0}} \tag{33a}$$

where the the total number density n_T is calculated by

$$n_T = \int_1^{v_M} dv n(v) = \int_1^{v_M} dv n_0 v^{-2p} \tag{33b}$$

Both (32) and (33) give the same result for the average volumetric size v_a

$$v_a = \frac{1-2p}{2(1-p)} \frac{v_M^{2(1-p)} - 1}{v_M^{(1-2p)} - 1}, \qquad \text{for } p \neq \frac{1}{2} \tag{34}$$

which is rearrange to solve for the power-law index p by iteration method from

$$p = \frac{1}{2 \ln v_M} \ln\left(\frac{v_a - q v_M}{v_a - q}\right) + \frac{1}{2}, \qquad \text{with} \quad q = \frac{1-2p}{2(1-p)} \tag{35}$$

and the following conditions are used to check the convergence of the solution

$$v_a = q\frac{v_M^{2(1-p)} - 1}{v_M^{(1-2p)} - 1} \tag{36a}$$

$$v_M = \left(\frac{v_a - q}{v_a - qv_M}\right)^{1/(1-2p)} \tag{36b}$$

Note that the right hand side of (34) has to be positive since v_a is positive. Furthermore, $v_M > 1$ results in

$$\frac{v_M^{2(1-p)} - 1}{v_M^{(1-2p)} - 1} > 0 \quad \Rightarrow \quad \frac{1-2p}{2(1-p)} > 0 \tag{37}$$

which imposes the condition $p \in (0.5, 1)$. The power index p can thus be determined if v_a and v_M are known. For given v_a and v_M, if the solution for p is not possible, a different law for size distribution should be considered.

The total fractional volume f_{sT} of brine inclusions is calculated by integrating over the size distribution

$$f_{sT} = \int_1^{v_M} dv\, f_s(v) = f_{s0}\frac{v_M^{2(1-p)} - 1}{2(1-p)}, \qquad \text{for } p \neq 1 \tag{38}$$

where $v_M = v_{sM}/v_{s0}$ is the volumetric size of the largest inclusions. When the total fractional volume is known from ground-truth data, f_{s0} can be solved by using (38) and the solution for the power-law index p to determine the power-law distribution of sizes.

Now let's examine how the size distribution changes with temperature. When the temperature varies, volumes of individual brine pockets also vary. Assume that the volumes of all brine pockets change at the same rate; i.e., for two different temperatures T_0 and T,

$$\frac{v_s(T_0)}{v_{s0}(T_0)} = \frac{v_s(T)}{v_{s0}(T)} \tag{39}$$

Also assume that new brine pockets do not appear nor existing brine pockets do not disappear when the temperature vary; i.e., the density number of the pockets is conserved. This signifies

$$\frac{f_s(T_0)}{v_s(T_0)} = \frac{f_s(T)}{v_s(T)} \quad \text{and} \quad \frac{f_{s0}(T_0)}{v_{s0}(T_0)} = \frac{f_{s0}(T)}{v_{s0}(T)} \tag{40}$$

Let the size distribution at temperature T_0 be power law with power index $p(T_0)$

$$f_s(T_0) = f_{s0}(T_0)\, v^{1-2p(T_0)} \tag{41}$$

Substituting (41) in (40) renders

$$\frac{f_s(T)}{v_s(T)} = \frac{f_{s0}(T_0)}{v_s(T_0)}\, v^{1-2p(T_0)} \tag{42}$$

From (39), (40), and (42), it is obvious that

$$f_s(T) = f_{s0}(T)\, v^{1-2p(T_0)} \tag{43}$$

Equation (43) indicates that the power index does not change as the temperature varies when the above assumptions are reasonable. Thus, if ground-truth data are not available at all temperatures under consideration, the index obtained at a temperature may be used at a different temperature when there is no severe brine loss and the ice is undeformed. Otherwise, ground truth has to be used to determine the size distribution. For air bubbles, the size distribution is derived in the same manner or, if ground truth is available, the size distribution can be obtained from section images.

b. Shape Distribution

The shapes of brine inclusions have been observed as substantially ellipsoidal [91]. It is also observed from the thin sections [91] of sea ice grown at US Army Cold Regions Research and Engineering Laboratory that only inclusions of small sizes has a more rounded spheroidal form. Thus, a slowly varying logarithmic function is used to describe the shape distribution

$$e_a(v) = (e_{aM} - e_{am})\frac{\ln v}{\ln v_M} + e_{am} \tag{44a}$$

$$e_b(v) = (e_{bM} - e_{bm})\frac{\ln v}{\ln v_M} + e_{bm} \tag{44b}$$

where axial ratio $e_a = a/c$ and $e_b = b/c$. Subscript M and m are for maximum and minimum values, respectively. This shape distribution implies that inclusions are

substantially ellipsoidal at large and medium size and small sizes are more rounded. When the temperature is increasing during a warming cycle, the shape of the inclusions becomes more rounded. The variation on the sea ice structure is described with reshaping factors operating on the maximum axial ratios e_{aM} and e_{bM}. Suppose the maximum axial ratio $e_{bM}(T_0)$ is at temperature T_0 and the highest temperature of the warming cycle is T_h at which the axial ratio is $e_{bM}(T_h)$, then the axial ratio at a temperature T between the low T_0 and the high T_h assumes the form

$$e_{bM}(T) = [e_{bM}(T_0) - e_{bM}(T_h)]\{1 - \exp[P(T - T_h)]\} + e_{bM}(T_h) \tag{45}$$

where P is the reshaping index and the temperatures are in negative Celsius degrees. Index P should not be too small such that the value of $e_{bM}(T)$ is rather preserved at temperature T_0. Similar formulas apply to e_{aM}. This thermal variation describes the smoothing process which makes the brine inclusions approach the more rounded spheroidal form with increasing temperature. For air bubble, the shapes have been considered as rather rounded in form of spheroid or sphere [26,91]. Therefore, the shapes of air bubbles do not change as much as those of brine inclusions and assumed to be unaffected by temperature.

c. Correlation Lengths

When the size distribution is specified, local correlation lengths of a brine inclusion can be calculated from (18). Furthermore, correlation lengths also vary as a function of temperature since the size of an individual inclusion change with temperature. If section images of sea ice are available at the temperatures under consideration, (18) can be applied to find the correlation lengths. If the size measurements are only made at a fix temperature T_0, the correlation lengths a different temperature T may be estimated under the assumptions in subsection 6.4a. From (40)

$$v_s(T) = \frac{f_s(T)}{f_s(T_0)} v_s(T_0) \tag{46}$$

The size distributions at different temperatures in (41) and (42) lead to the relation

$$\frac{f_s(T)}{f_s(T_0)} = \frac{f_{s0}(T)\, v^{1-2p(T_0)}}{f_{s0}(T_0)\, v^{1-2p(T_0)}} = \frac{f_{s0}(T)}{f_{s0}(T_0)} \tag{47}$$

Relation (46) and the ratios in (47) together with the definition of normalized volumetric size (30) give

$$v_s(T) = \frac{v f_{s0}(T)}{f_{s0}(T_0)}\, v_{s0}(T_0) \tag{48}$$

Volume $v_s(T)$ and $v_{s0}(T_0)$ of an ellipsoidal inclusion are calculated from the sizes as

$$v_s(T) = \frac{4\pi}{3} e_a(T) e_b(T) c^3(T) \tag{49a}$$

$$v_{s0}(T_0) = \frac{4\pi}{3} e_{am}(T_0) e_{bm}(T_0) c_m^3(T_0) \tag{49b}$$

where m denotes the minimum. Substituting (49) in (48) and using (18) render the local correlation lengths corresponding to the inclusion

$$\ell_{x'}(T) = \left[\frac{v f_{s0}(T)}{6 f_{s0}(T_0)} \frac{e_{am}(T_0) e_{bm}(T_0)}{e_a(T) e_b(T)}\right]^{\frac{1}{3}} c_m(T_0) \tag{50a}$$

$$\ell_{y'}(T) = e_b(T)\ell_{x'}(T), \qquad \ell_{z'}(T) = e_a(T)\ell_{x'}(T) \tag{50b}$$

which only requires measurements at temperature T_0. Correlation lengths for air bubbles can be obtained in the same manner.

d. Constituent Characteristics

As aforementioned, sea ice contains an ice background, brine inclusions, and air bubbles. While the real part of ice permittivity is not sensitive to temperature, the imaginary part is dispersive and varies with temperature. An empirical formula to calculate the imaginary part of ice permittivity as a function of temperature at microwave frequencies is given in [92]. For brine in sea ice, the permittivity is large compared to that of ice and both real and imaginary parts decrease as frequency increases. Empirical formulas to compute complex dielectric constants of brine in terms of temperatures and microwave frequencies are reported in [93].

The constituent phases in sea ice are related thermodynamically. When temperature of sea ice varies, fractional volume of brine inclusions and air bubbles changes accordingly. Based on phase equilibrium, Cox and Weeks [94] have provided equations for determining fractional volumes of brine inclusions and air bubbles in sea ice in the temperature range of $-2°C$ to $-30°C$. The required input parameters are bulk ice density, salinity, and temperature. The salt $Na_2SO_4 \cdot 10H_2O$ crystalizes at $-8.2°C$, however, the phase change is much stronger at about $-23°C$ which is the eutectic temperature of $NaCl \cdot 2H_2O$ corresponding to the precipitation of the salt (sodium chloride dihydride). This strong phase change causes a kink in the phase curves as a function of temperature. At low temperature, sea ice therefore contains solid salt. The presence of solid salt, however, is negligible even below the $NaCl \cdot 2H_2O$ eutectic temperature [94].

6.5 Results and Discussion

a. Data Comparisons

In this section, the results calculated from the model is compared with experimental data. Relative permittivities of sea ice grown at US Army Cold Regions and Research Engineering Laboratory (CRREL) were measured [91]. The measurements were made with transmission method for wave normally incident of a slab of sea ice; therefore, only permittivity $\epsilon_{eff\rho}$ corresponding to ordinary wave were obtained and the extraordinary components were not considered and would not be studied in this section.

The sea ice slab was taken from an saline ice sheet (Sheet 85-3) to a laboratory environment where the temperature was controllable. The measurements were made at temperature intervals during progressive warming of the ice slab from $-32°C$ to $-2°C$ for wave frequency of 4.8 GHz. The in situ salinity was 0.62% reduced to

0.54% before testing and further reduced to 0.42% after testing due to brine loss during the process. Only final bulk ice density of 0.866 g/cm^3 was reported. For a given set of temperature, salinity, ice density, and wave frequency, fractional volumes and permittivities of the constituents in sea ice are calculated from the empirical formulas as discussed in section 6.4. Typically in this case, the total fractional volumes of brine inclusions and air bubbles are in the order of 10%. The real part of ice relative permittivity is 3.15 and the imaginary parts are in the order of 0.001. The real and imaginary parts of the brine permittivities calculated from [93] are about one order of magnitude higher than the real part of the ice relative permittivity.

For ice structure, the dendritic planes normal to the C axes show marginal tilt of $2-4°$ and can be modeled as vertical. Two photographs of horizontal thin sections before and after thermal modification were presented. It is seen from the photographs that the C axes are randomly oriented in azimuthal directions. Initially at $-30°$C, the minimum, average, and maximum of the minor semi-axes are estimated as 0.05 mm, 0.01 mm, and 0.30 mm, respectively. To calculate the power-law index for brine inclusion, the normalized volumetric sizes are considered as the cubics of the ratios of the above minor semi-axes; this gives the power index of 0.8945 for the size distribution. The initial axial ratio e_{bm} for a brine inclusion of smallest size is 1 for the spheroidal shape. The maximum axial ratio e_{bM} is roughly estimated to be 8 to describe the substantially ellipsoidal shape of the large inclusions. Vertical section images were also available but not large enough to see the structures of the inhomogeneities; therefore, the sizes for major axes of the scatterers have to be chosen and sensitivity analyses will be done to study the corresponding uncertainty. The choice for the initial minimum and maximum major axial ratios are $e_{am} = 2$ and $e_{aM} = 10$ to cover the range of variation of the brine inclusion sizes. After the thermal modification, the axial ratios for brine inclusions are taken to be $e_{bM} = 1.5$ and $e_{aM} = 3$ to account for the effect of rounded shapes. For air bubbles, the

effect on the effective permittivity is not as strong as that due to brine inclusions. Air bubbles are much more rounded than brine inclusions. The shape change in air bubbles is therefore not large and the bubble form is considered as spheroid having circular cross section as observed in the horizontal thin sections. The axial ratios of air bubbles are taken to be uniform with $e_b = 1$ and $e_a = 2$. The initial minor semi-axes of air bubbles is taken to be the same as those of smallest brine inclusions and thus the power index is also 0.8945. While the bubble shape is considered unchanged thermally, the bubble size variation as a function of temperature is taken into account.

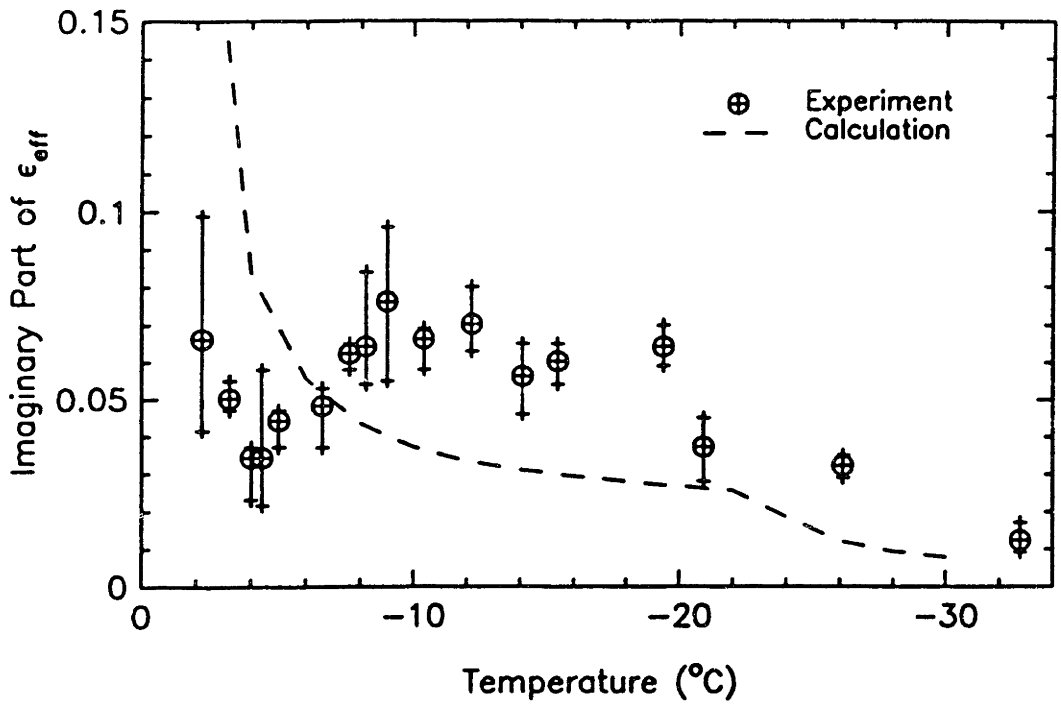

Figure 6.5.1 Imaginary part of effective permittivity: curve from theoretical calculations only accounts for size distributions

To explain the behavior of sea ice permittivity observed in the experiment, the theoretical model is first simplified to identify the responsible physical mechanisms then the complexity is added to the more complete model to arrive at the better description of the medium. For now, the brine loss during the warming process is ignored and the shape of the brine inclusions is considered as uniform with the

average axial ratios $e_b = 3$ and $e_a = 5$ which are kept constant with respect to temperature. The size distributions for both brine inclusions and air bubbles are, however, included. The results from the calculation for the imaginary part of effective permittivity ϵ_{eff_p} is plotted in Figure 6.5.1 together with the measured data obtained from the experiment. In general, the theoretical curve shows an increasing trend as temperature increases. This is due to the increase of scatterer fractional volumes at higher temperature. The kink observed at about $-22°C$ (the calculations are made at intervals of $2°C$ started from $-30°C$) is due to the phase change associated with the precipitation of sodium chloride dihydride. The steep slope on the theoretical curve in the higher temperature range is caused by the fast increase in scatterer fractional volumes. Compared with the experimental data, the theoretical results are too low at low temperatures and too high at high temperatures.

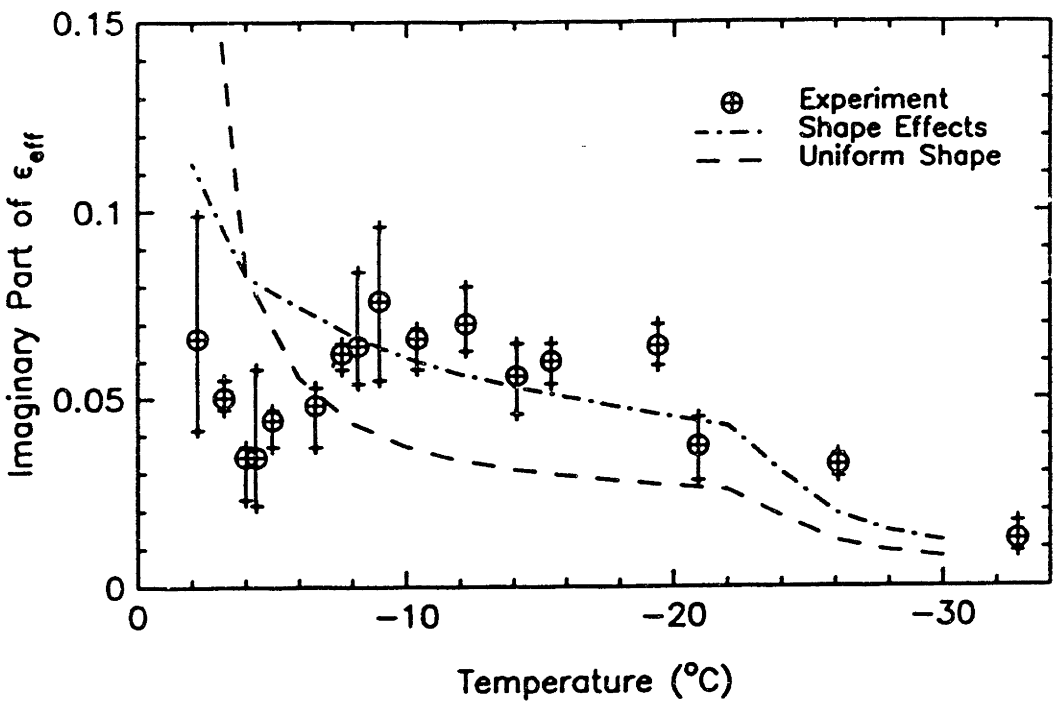

Figure 6.5.2 Imaginary part of effective permittivity: curve from theoretical calculations accounts for size and shape distributions and thermal variation in the shapes of brine inclusions

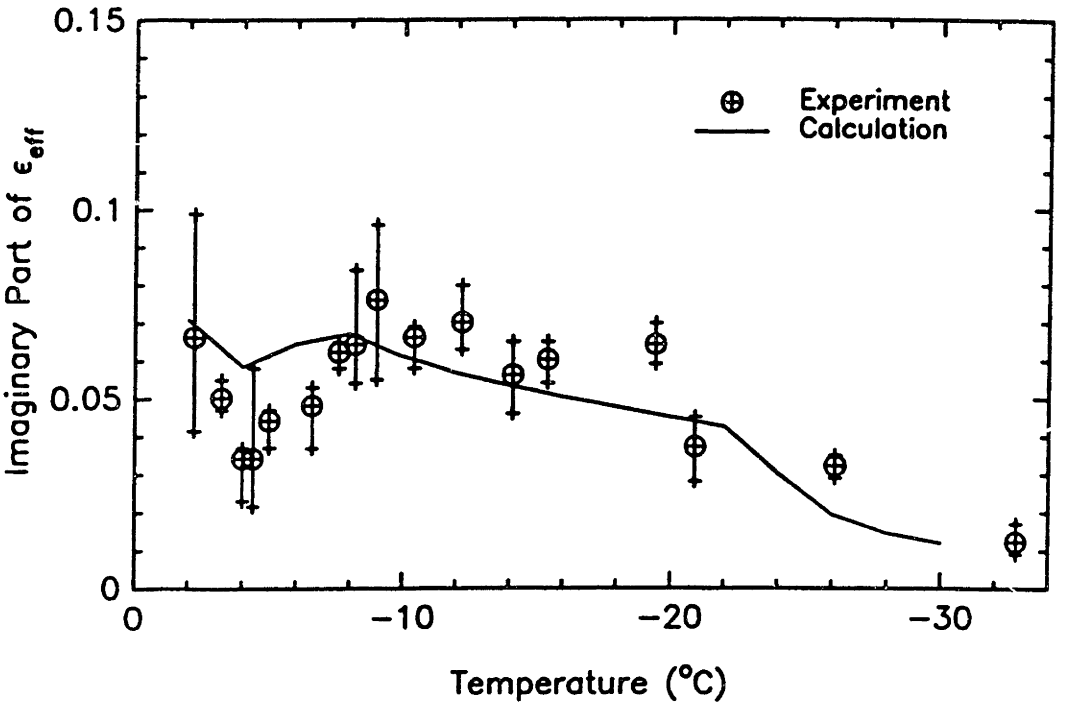

Figure 6.5.3 Imaginary part of effective permittivity: curve is obtained from the complete model including all of the thermal variations

The shape distribution of brine inclusions and their shape variation due to temperature are now considered. The brine inclusions are divided into 20 subspecies; test calculations done with 99 subspecies indicate good convergence for results obtained with 20 subdivisions. The results are shown in Figure 6.5.2. Compared to the old theoretical results, the comparison between the new curve is higher at low temperatures and lower at high temperatures. In the low temperature range, the higher results are due to the existence of more substantially ellipsoidal brine inclusions which have stronger depolarization effect and larger cross sections. At higher temperatures, the effect of rounded inclusions are more prominent in the competition with the increasing effect of higher fractional volumes to render the results to lower values. Regarding the experimental data, the comparison is much better except at temperatures higher than $-8°C$ the calculated results are still larger than the mea-

sured values. This is because the brine loss has not been accounted for. If the brine loss represented by the decrease in salinity from 0.54% to 0.42% is incorporated in the model by an assumed linear decrease in salinity from −8°C to −4°C, the theoretical curve shown in Figure 6.5.3 explains all the trends observed in the experimental data for the imaginary part of the effective permittivity. The real parts of the permittivity are presented in Figure 6.5.4 which indicates that the calculated values are within 10% lower than the measured data. The analysis in this subsection is based as much as possible on available ground-truth data. The lack of ground truth information has necessitated some assumptions. The uncertainty associated with the assumptions can be estimated with a sensitivity analysis in the next subsection.

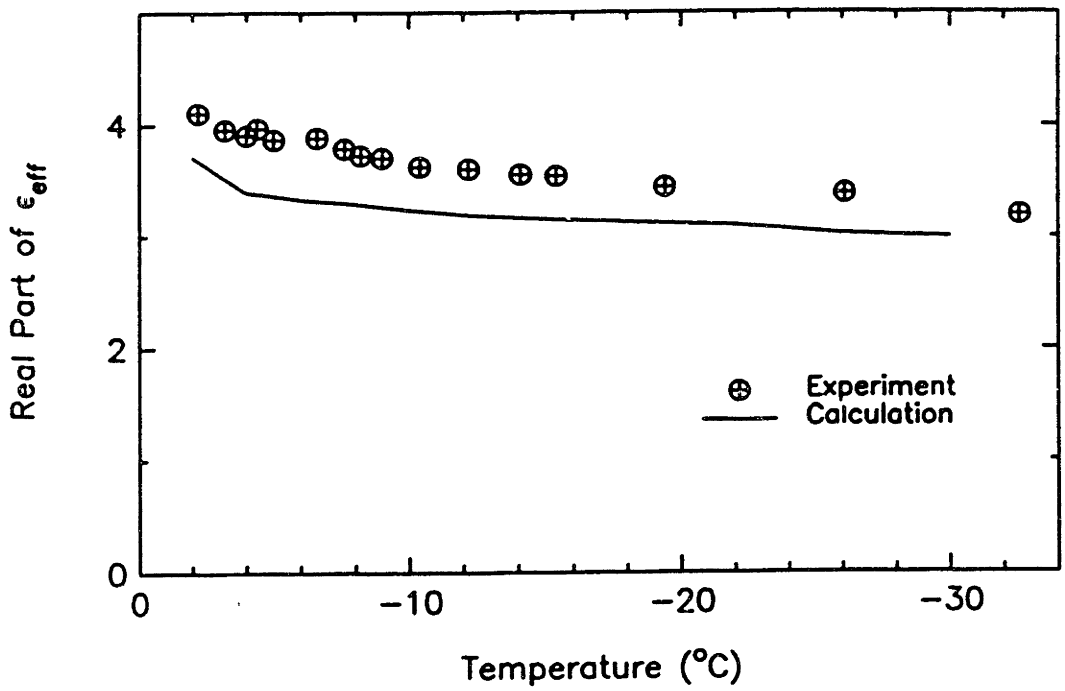

Figure 6.5.4 Real part of effective permittivity: curve is obtained from the complete model including all of the thermal variations

b. Sensitivity Analysis

The sensitivity analysis in this subsection is to estimate the uncertainty due to the

assumptions made in the last subsection. First, as recognized from the model, the shape effect is important. In Figure 6.5.5, the dash-dot curves are computed with values of the axial ratios varied by ±20% from those used in the last theoretical calculation taken as the reference. The results show that the effect of ellipsoidal shapes is most important in the middle range of temperatures. The insensitivity of shape at −2°C is due to the rounded form of the scatterers and at low temperatures due to low fractional volume of brine inclusions.

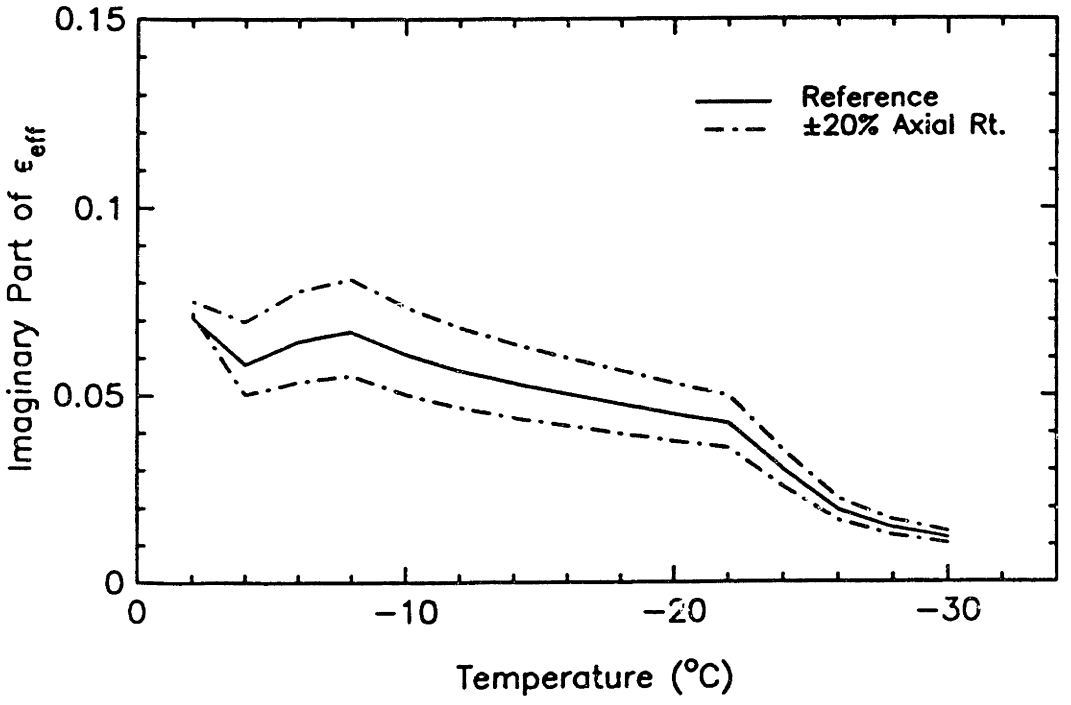

Figure 6.5.5 Imaginary part of effective permittivity: solid curve is for reference and dash-dot curves are obtained by varying the axial ratios by ±20%

Another assumption is that the ice density 0.866 g/cm^3 has been used in all of the previous theoretical calculations. This values should not be constant as the salinity changes due to the brine loss. The sensitivity analysis of the ice density is done by varying the density by ±5% (to keep the variation within the density range of gas-free sea ice) and the results are shown in Figure 6.5.6.

The sensitivity of the size distribution can also be studied by varying the

maximum normalized volumetric size by ±10% for example. This will affect the power-law index and thus the size distribution of the brine inclusions and the air bubbles. The calculations show results close to the reference curve indicating a week sensitivity in this case due to the small size of the scatterers compared to the wavelength. The sensitivity analysis in this subsection indicates that the assumptions are rather reasonable or, at least, do not lead to too large deviation.

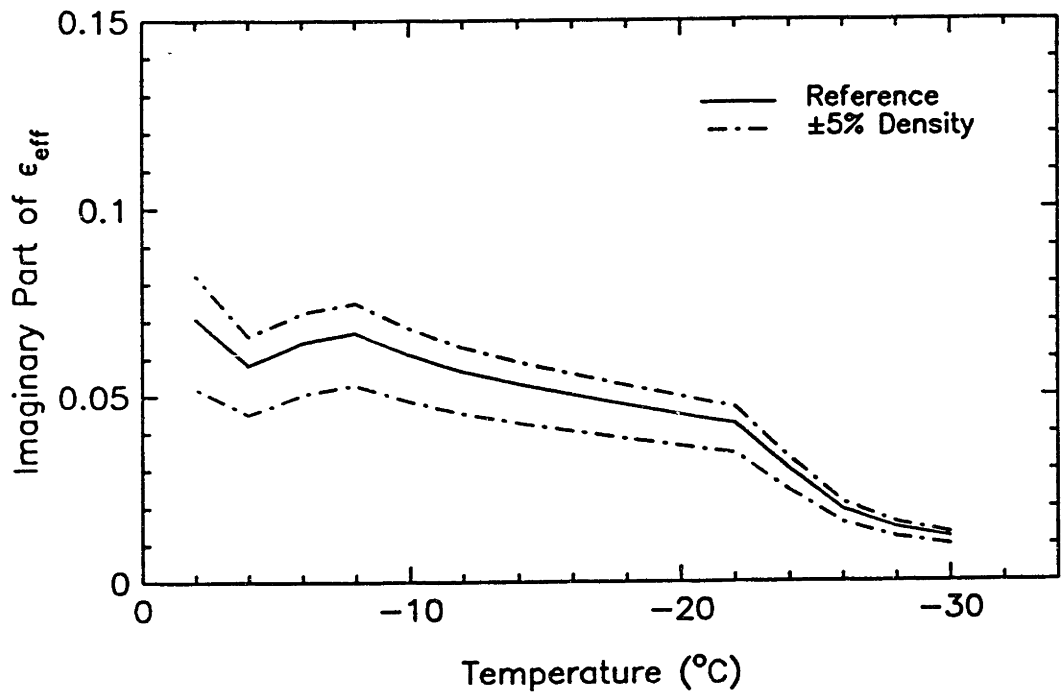

Figure 6.5.6 Imaginary part of effective permittivity: solid curve is for reference and dash-dot curves are obtained by varying the bulk ice density by ±5%

6.6 Summary

This chapter presents an electromagnetic wave model which accounts for the complexity of the multi-phase inhomogeneities with multiple species characterized by orientation, size, and shapes distributions. The size variety of scatterers in a species is described in terms of the number density or the fractional volume as a function of normalized volumetric sizes. The shape variation is take into consideration by sub-

dividing a species into many species based on the similarity in scatterer shapes. The model also describes the effective anisotropy of the medium due to a preferred alignment of scatterers. For the multi-species medium with orientation, size, and shape distributions, the effective permittivity of the inhomogeneous medium is derived with the extended strong fluctuation theory. The polarimetric scattering coefficients are then obtained under the distorted Born approximation. The model is suitable for characterizing sea ice with embedded brine inclusions and air bubbles. The thermodynamics of the constituents in sea ice is also included in the model to incorporate the thermal variations in the ice structure and properties. Comparisons of theoretical results with measured data for sea ice permittivities from CRREL are made and the trends observed from the experimental measurements are explained. Sensitivity of model input parameters are analyzed to estimate the uncertainty in the parameter assumptions or inaccuracies in ground truth measurements. This model provides an analytical tool to study electromagnetic properties of sea ice and other geophysical media under effects of varying environmental conditions.

Chapter 7
Summary

Electromagnetic wave models for polarimetric remote sensing of geophysical media have been presented in this thesis. At the beginning of the thesis, a general review has been done on the analytic wave, the modified radiative transfer, and the traditional radiative transfer theories. The radiative transfer theory can account for more complicated properties of the media but ignores the phase information which is important to polarimetric remote sensing with monostatic radar. The modified radiative transfer theory considers both the phase and the multiple scattering but involves with more mathematical complexity which limits the applicability to simple media. The wave theory includes the coherent effect and all the multiple interaction between medium interface and scatterer, the multiple scattering to some extent, and rather complex medium characteristics. The wave theory is then chosen to develop the theoretical models for applications in polarimetric remote sensing of geophysical media.

Methods describing polarimetric properties of the media such as scattering matrix, covariance matrix, Mueller matrix, Stokes vector, polarization signature, and polarimetric scattering coefficients are then discussed. The complex scattering matrix relates the incident and the scattered fields expressed in two orthogonal polarimetric components. The covariance matrix is defined by the product of the polarimetric feature vector and its transposed complex conjugate. Mueller matrix operating on incident Stokes vector gives the scattered Stokes vector. Both covariance and Mueller

matrices can be expressed in terms of polarimetric scattering coefficients defined based on ensemble averages of scattered fields. Polarization signature is a graphical method of description. These methods are useful in characterizing polarimetric properties of geophysical media.

The theoretical models are developed in the subsequent chapters increasingly in physical complexity along with experimental result comparisons, interpretations, and simulations for various geophysical media including snow, sea ice, and vegetation. In Chapter 2, the fully polarimetric backscattering coefficients have been obtained from the layer model with spheroidal scatterers. The top layer is modelled as an isotropic random medium, the middle layer as an anisotropic random medium, and the underlying layer as a homogeneous medium. The strong fluctuation theory is used to calculated the effective permittivities of the scattering layers and the distorted Born approximation is applied to derive the scattered fields. The dyadic Green's functions are used in the calculations and the backscattering processes are explained. The model results are illustrated for bare and snow covered sea ice. The physical information conveyed in the elements of the covariance matrices are discussed especially for the correlation coefficient ρ. The copolarization signatures for the layer random media are obtained with the Mueller matrices and explained with the scattering coefficients contained in the covariance matrices.

In Chapter 3, the extended strong fluctuation theory is used to calculate effective permittivities of scattering regions containing randomly oriented spheroidal scatterers and the distorted Born approximation is applied to derive the scattered fields from the layered media. The model is applied to explain the backscattering from a soybean canopy. The leaves are considered to have disc-like shape with random orientation. Theoretical results are compared with measured backscattering coefficients σ_{hh}, σ_{vv}, and σ_{hv} of wave frequency 5.3 GHz over the range 0-5(incident angles for 10 different growth stages of the soybean. The copolarized returns

are matched well but the calculated cross-polarized returns are lower than the measurements because multiple scattering are ignored. Polarization signatures are then simulated to study polarimetric properties of the soybean canopy. The model is also used to investigate radar configurations and biophysical conditions for applications in inversion of biomass and soil moisture.

Chapter 4 considers inhomogeneous media with ellipsoidal scatterers. The ellipsoids are aligned vertically and oriented randomly in azimuthal directions. In this model, the cross-polarized return is obtained from the first-order distorted Born approximation. The theoretical results are shown to compare well with the measured data for thick first-year sea ice and the scattering mechanisms are explained. From the polarimetric simulation, it is shown that covariance matrices as well as polarization signatures convey further information regarding the characteristics and structure of the media as compared to the conventional backscattering coefficients. The model, however, only accounts for one type of scatterers in a host medium with two-phase mixing.

In Chapter 5, a layer model with scattering regions containing multiple species of scatterers are presented. The species are allowed to have different size, shape, and permittivity. After the scatterer correlation is analyzed, the effective permittivity of the multi-species medium is derived with the extended strong fluctuation theory. The polarimetric scattering coefficients is then calculated under the distorted Born approximation. The model indicates that non-spherical scatterers with larger cross section give higher permittivity and backscattering. For a mixture of oblate (disc-like) and prolate (needle-like) spheroids, the depolarization effect is stronger when the disc-like portion is increased. The model laid out in this chapter paves the way for an extension to account for more complexity of geophysical media where the multiple species can have size and shape distributions.

A model which accounts for the complexity of the multi-phase inhomogeneities

with multiple species characterized by orientation, size, and shapes distributions is developed in Chapter 6. The size variety of scatterers in a species is described in terms of the number density or the fractional volume as a function of normalized volumetric sizes. The shape variation is take into consideration by subdividing a species into many species based on the similarity in scatterer shapes. The model also describes the effective anisotropy of the medium due to a preferred alignment of scatterers. For the multi-species medium with orientation, size, and shape distributions, the effective permittivity of the inhomogeneous medium is derived with the extended strong fluctuation theory. The polarimetric scattering coefficients are then obtained under the distorted Born approximation. The model is suitable for characterizing sea ice with embedded brine inclusions and air bubbles. The thermodynamics of the constituents in sea ice is also included in the model to incorporate the thermal variations in the ice structure and properties. Comparisons of theoretical results with measured data for sea ice permittivities from CRREL are made and the trends observed from the experimental measurements are explained. Sensitivity of model input parameters are analyzed to estimate the uncertainty in the parameter assumptions or inaccuracies in ground truth measurements.

The models developed in this thesis provides physical insights into wave propagation and scattering in geophysical media for applications in polarimetric remote sensing. The models explain measured data and interpret polarimetric characteristics of geophysical media. It has been shown that fully polarimetric data convey additional information regarding the remotely sensed media and thereby provide more accurate identification and classification of terrain types in radar imagery. The models have been able to describe inhomogeneous media with layer configuration, multi-species of multi-phase, orientation, size, and shape distributions. Mechanisms responsible for physical trends observed in experimental have been identified by the models. In the future, further theoretical developments together with validating ex-

periments are necessary to account for more complex natural media incorporated in a large scale system. The models for remote sensing can thus be used in the planning of measurement campaigns and apply to data interpretation as a part of an operating monitor of geophysical environment.

Appendix A
Transmission and Reflection Coefficients

The transmission and reflection coefficients are obtained by matching the boundary conditions at the interfaces where the tangential components of the electric and magnetic fields are continuous. The boundary conditions for the zeroth-order mean fields can be written explicitly as

$$\left.\begin{aligned} \hat{z}\times\left\langle\overline{F}_0(\overline{r})\right\rangle &= \hat{z}\times\left\langle\overline{F}_1(\overline{r})\right\rangle \\ \hat{z}\times\nabla\times\left\langle\overline{F}_0(\overline{r})\right\rangle &= \hat{z}\times\nabla\times\left\langle\overline{F}_1(\overline{r})\right\rangle \end{aligned}\right\} \text{ at } z=0 \tag{A.1a}$$

$$\left.\begin{aligned} \hat{z}\times\left\langle\overline{F}_1(\overline{r})\right\rangle &= \hat{z}\times\left\langle\overline{F}_2(\overline{r})\right\rangle \\ \hat{z}\times\nabla\times\left\langle\overline{F}_1(\overline{r})\right\rangle &= \hat{z}\times\nabla\times\left\langle\overline{F}_2(\overline{r})\right\rangle \end{aligned}\right\} \text{ at } z=-d_1 \tag{A.1b}$$

$$\left.\begin{aligned} \hat{z}\times\left\langle\overline{F}_2(\overline{r})\right\rangle &= \hat{z}\times\left\langle\overline{F}_3(\overline{r})\right\rangle \\ \hat{z}\times\nabla\times\left\langle\overline{F}_2(\overline{r})\right\rangle &= \hat{z}\times\nabla\times\left\langle\overline{F}_3(\overline{r})\right\rangle \end{aligned}\right\} \text{ at } z=-d_2 \tag{A.1c}$$

The boundary conditions are satisfied by coefficients composed of half-space Fresnel coefficients and phase factors as expressed in (66, Chapter 2). The phase factors in the exponents account for the wave propagation to the boundaries. The Fresnel reflection and transmission coefficients have been derived as shown in [29]. For the coordinate systems defined in Chapter 2, the Fresnel coefficients are given as follows:

(1) At boundary $z=0$ between the isotropic media of region 0 and region 1

$$R_{01hh} = -R_{10hh} = \frac{k_{0z}-k_{1z}}{k_{0z}+k_{1z}} \tag{A.2a}$$

$$R_{01vv} = -R_{10vv} = \frac{k_1^2 k_{0z}-k_0^2 k_{1z}}{k_1^2 k_{0z}+k_0^2 k_{1z}} \tag{A.2b}$$

$$T_{01hh} = \frac{2k_{0z}}{k_{0z} + k_{1z}}, \quad T_{10hh} = \frac{2k_{1z}}{k_{1z} + k_{0z}} \tag{A.2c}$$

$$T_{01vv} = \frac{2k_0 k_1 k_{0z}}{k_1^2 k_{0z} + k_0^2 k_{1z}}, \quad T_{10vv} = \frac{2k_1 k_0 k_{1z}}{k_0^2 k_{1z} + k_1^2 k_{0z}} \tag{A.2d}$$

(2) At boundary $z = -d_1$ between isotropic region 1 and anisotropic region 2

$$R_{12hh} = -1 + \frac{k_2^2 k_x T_{12he}}{k_\rho U_d} \sin\psi + \frac{T_{12ho}}{k_\rho G_d}\left(k_\rho^2 \cos\psi + k_y k_{2z}^o \sin\psi\right) \tag{A.3a}$$

$$R_{12hv} = \frac{k_1 k_x k_{2z}^o T_{12ho}}{k_\rho k_{1z} G_d} \sin\psi + \frac{k_1 T_{12he}}{k_\rho k_{1z} U_d}\left(k_\rho^2 k_{2z}^{ed} \cos\psi - k_y k_{2z}^{o2} \sin\psi\right) \tag{A.3b}$$

$$R_{12vh} = \frac{k_2^2 k_x T_{12ve}}{k_\rho U_d} \sin\psi + \frac{T_{12vo}}{k_\rho G_d}\left(k_\rho^2 \cos\psi + k_y k_{2z}^o \sin\psi\right) \tag{A.3c}$$

$$R_{12vv} = 1 + \frac{k_1 k_x k_{2z}^o T_{12vo}}{k_\rho k_{1z} G_d} \sin\psi + \frac{k_1 T_{12ve}}{k_\rho k_{1z} U_d}\left(k_\rho^2 k_{2z}^{ed} \cos\psi - k_y k_{2z}^{o2} \sin\psi\right) \tag{A.3d}$$

$$R_{21oo} = \frac{G_d E_e (k_{2z}^o - k_{1z})}{G_u D_d (k_{2z}^o + k_{1z})} \tag{A.3e}$$

$$R_{21oe} = \frac{2k_x k_{2z}^o U_d}{G_u D_e}(k_{1z} - k_{2z}^o) \cdot (k_y \sin\psi - k_{1z} \cos\psi)\sin\psi \tag{A.3f}$$

$$R_{21eo} = \frac{k_2^2 k_x G_d}{U_u D_e}\left(k_{2z}^{ed} - k_{2z}^{eu}\right)(k_{1z} - k_{2z}^o) \cdot (k_y \sin\psi + k_{1z} \cos\psi)\sin\psi \tag{A.3g}$$

$$R_{21ee} = -\frac{U_d I_e}{U_u D_e} \tag{A.3h}$$

$$T_{12ho} = \frac{2k_{1z} G_d}{k_\rho D_e (k_{1z} + k_{2z}^o)}\left[k_\rho^2\left(k_2^2 k_{1z} - k_1^2 k_{2z}^{ed}\right)\cos\psi + k_y\left(k_1^2 k_{2z}^{o2} - k_2^2 k_{1z} k_{2z}^{ed}\right)\sin\psi\right] \tag{A.3i}$$

$$T_{12he} = \frac{2k_x k_{1z} U_d}{k_\rho D_e}\left(k_\rho^2 + k_{1z} k_{2z}^o\right)\sin\psi \tag{A.3j}$$

$$T_{12vo} = -\frac{2k_1k_2^2k_xk_{1z}G_d(k_{1z}-k_{2z}^{ed})}{k_\rho D_e(k_{1z}+k_{2z}^{o})}\sin\psi \tag{A.3k}$$

$$T_{12ve} = \frac{2k_1U_d}{k_\rho D_e}\left(k_\rho^2k_{1z}\cos\psi + k_yk_{1z}k_{2z}^{o}\sin\psi\right) \tag{A.3l}$$

$$T_{21oh} = \frac{k_2^2k_xR_{21oe}}{k_\rho U_d}\sin\psi + \frac{1}{k_\rho G_u}\left(k_\rho^2\cos\psi - k_yk_{2z}^{o}\sin\psi\right) + \frac{R_{21oo}}{k_\rho G_d}\left(k_\rho^2\cos\psi + k_yk_{2z}^{o}\sin\psi\right) \tag{A.3m}$$

$$T_{21ov} = \frac{k_1k_xk_{2z}^{o}R_{21oo}}{k_\rho k_{1z}G_d}\sin\psi - \frac{k_1k_xk_{2z}^{o}}{k_\rho k_{1z}G_u}\sin\psi - \frac{k_1R_{21oe}}{k_\rho k_{1z}U_d}\left(k_yk_{2z}^{o2}\sin\psi - k_\rho^2k_{2z}^{ed}\cos\psi\right) \tag{A.3n}$$

$$T_{21eh} = \frac{k_2^2k_x}{k_\rho U_u}\sin\psi + \frac{k_2^2k_xR_{21ee}}{k_\rho U_d}\sin\psi + \frac{R_{21eo}}{k_\rho G_d}\left(k_\rho^2\cos\psi + k_yk_{2z}^{o}\sin\psi\right) \tag{A.3o}$$

$$T_{21ev} = \frac{k_1k_xk_{2z}^{o}R_{21eo}}{k_\rho k_{1z}G_d}\sin\psi - \frac{k_1}{k_\rho k_{1z}U_u}\left(k_yk_{2z}^{o2}\sin\psi - k_\rho^2k_{2z}^{eu}\cos\psi\right) - \frac{k_1R_{21ee}}{k_\rho k_{1z}U_d}\left(k_yk_{2z}^{o2}\sin\psi - k_\rho^2k_{2z}^{ed}\cos\psi\right) \tag{A.3p}$$

(3) At boundary $z = -d_2$ between anisotropic region 2 and isotropic region 3

$$R_{23oo} = \frac{G_uG_e(k_{2z}^{o}-k_{3z})}{G_dF_e(k_{2z}^{o}+k_{3z})} \tag{A.4a}$$

$$R_{23oe} = \frac{2k_xk_{2z}^{o}U_u}{G_dF_e}(k_{2z}^{o}-k_{3z}) \cdot (k_y\sin\psi + k_{3z}\cos\psi)\sin\psi \tag{A.4b}$$

$$R_{23eo} = \frac{k_2^2k_xG_u}{U_dF_e}\left(k_{2z}^{ed}-k_{2z}^{eu}\right)(k_{2z}^{o}-k_{3z}) \cdot (k_y\sin\psi - k_{3z}\cos\psi)\sin\psi \tag{A.4c}$$

$$R_{23ee} = -\frac{U_uH_e}{U_dF_e} \tag{A.4d}$$

$$T_{23oh} = \frac{k_2^2k_xR_{23oe}}{k_\rho U_u}\sin\psi + \frac{1}{k_\rho G_d}\left(k_\rho^2\cos\psi + k_yk_{2z}^{o}\sin\psi\right) + \frac{R_{23oo}}{k_\rho G_u}\left(k_\rho^2\cos\psi - k_yk_{2z}^{o}\sin\psi\right) \tag{A.4e}$$

$$T_{23ov} = \frac{k_3 k_x k_{2z}^{o} R_{23oo}}{k_\rho k_{3z} G_u} \sin\psi - \frac{k_3 k_x k_{2z}^{o}}{k_\rho k_{3z} G_d} \sin\psi + \frac{k_3 R_{23oe}}{k_\rho k_{3z} U_u} \left(k_y k_{2z}^{o2} \sin\psi - k_\rho^2 k_{2z}^{eu} \cos\psi \right) \tag{A.4f}$$

$$T_{23eh} = \frac{k_2^2 k_x R_{23ee}}{k_\rho U_u} \sin\psi + \frac{k_2^2 k_x}{k_\rho U_d} \sin\psi + \frac{R_{23eo}}{k_\rho G_u} \left(k_\rho^2 \cos\psi - k_y k_{2z}^{o} \sin\psi \right) \tag{A.4g}$$

$$T_{23ev} = \frac{k_3 k_x k_{2z}^{o} R_{23eo}}{k_\rho k_{3z} G_u} \sin\psi + \frac{k_3 R_{23ee}}{k_\rho k_{3z} U_u} \left(k_y k_{2z}^{o2} \sin\psi - k_\rho^2 k_{2z}^{eu} \cos\psi \right) + \frac{k_3}{k_\rho k_{3z} U_d} \left(k_y k_{2z}^{o2} \sin\psi - k_\rho^2 k_{2z}^{ed} \cos\psi \right) \tag{A.4h}$$

In the above expressions, the following definitions have been used

$$G_d \equiv \sqrt{k_x^2 + \left(k_y \cos\psi + k_{2z}^{o} \sin\psi \right)^2} \tag{A.5a}$$

$$G_u \equiv \sqrt{k_x^2 + \left(k_y \cos\psi - k_{2z}^{o} \sin\psi \right)^2} \tag{A.5b}$$

$$U_d \equiv \left\{ \frac{\epsilon_{eff2\rho'}}{\epsilon_{eff2\rho'} - \epsilon_{eff2z'}} \left(k_\rho^2 + k_{2z}^{ed2} - k_2^2 \right) \left[k_\rho^2 + k_{2z}^{ed2} - k_2^2 \left(1 + \frac{\epsilon_{eff2z'}}{\epsilon_{eff2\rho'}} \right) \right] \right\}^{\frac{1}{2}} \tag{A.5c}$$

$$U_u \equiv \left\{ \frac{\epsilon_{eff2\rho'}}{\epsilon_{eff2\rho'} - \epsilon_{eff2z'}} \left(k_\rho^2 + k_{2z}^{eu2} - k_2^2 \right) \left[k_\rho^2 + k_{2z}^{eu2} - k_2^2 \left(1 + \frac{\epsilon_{eff2z'}}{\epsilon_{eff2\rho'}} \right) \right] \right\}^{\frac{1}{2}} \tag{A.5d}$$

$$D_e \equiv k_\rho^2 \left(k_2^2 k_{1z} - k_1^2 k_{2z}^{ed} \right) \cos^2\psi + \left[k_2^2 \left(k_{1z} - k_{2z}^{ed} \right) \left(k_x^2 + k_{1z} k_{2z}^{o} \right) + k_y^2 k_{2z}^{o} \left(k_2^2 - k_1^2 \right) \right] \sin^2\psi + k_y \left(k_{1z} + k_{2z}^{o} \right) \left(k_{2z}^{o} - k_{2z}^{ed} \right) \left(k_\rho^2 + k_{1z} k_{2z}^{o} \right) \cos\psi \sin\psi \tag{A.5e}$$

$$E_e \equiv k_\rho^2 \left(k_2^2 k_{1z} - k_1^2 k_{2z}^{ed} \right) \cos^2\psi + \left[k_2^2 \left(k_{1z} - k_{2z}^{ed} \right) \left(k_x^2 - k_{1z} k_{2z}^{o} \right) - k_y^2 k_{2z}^{o} \left(k_2^2 - k_1^2 \right) \right] \sin^2\psi - k_y \left(k_{1z} - k_{2z}^{o} \right) \left(k_{2z}^{o} + k_{2z}^{ed} \right) \left(k_\rho^2 - k_{1z} k_{2z}^{o} \right) \cos\psi \sin\psi \tag{A.5f}$$

$$
\begin{aligned}
I_e \equiv\ & k_\rho^2 \left(k_2^2 k_{1z} - k_1^2 k_{2z}^{eu}\right) \cos^2\psi \\
& + \left[k_2^2 \left(k_{1z} - k_{2z}^{eu}\right)\left(k_x^2 + k_{1z} k_{2z}^{o}\right) + k_y^2 k_{2z}^{o}\left(k_2^2 - k_1^2\right)\right] \sin^2\psi \\
& + k_y \left(k_{1z} + k_{2z}^{o}\right)\left(k_{2z}^{o} - k_{2z}^{eu}\right)\left(k_\rho^2 + k_{1z} k_{2z}^{o}\right) \cos\psi \sin\psi
\end{aligned} \tag{A.5g}
$$

$$
\begin{aligned}
F_e \equiv\ & k_\rho^2 \left(k_2^2 k_{3z} + k_3^2 k_{2z}^{eu}\right) \cos^2\psi \\
& + \left[k_2^2 \left(k_{3z} + k_{2z}^{eu}\right)\left(k_x^2 + k_{3z} k_{2z}^{o}\right) + k_y^2 k_{2z}^{o}\left(k_2^2 - k_3^2\right)\right] \sin^2\psi \\
& - k_y \left(k_{3z} + k_{2z}^{o}\right)\left(k_{2z}^{o} + k_{2z}^{eu}\right)\left(k_\rho^2 + k_{3z} k_{2z}^{o}\right) \cos\psi \sin\psi
\end{aligned} \tag{A.5h}
$$

$$
\begin{aligned}
G_e \equiv\ & k_\rho^2 \left(k_2^2 k_{3z} + k_3^2 k_{2z}^{eu}\right) \cos^2\psi \\
& + \left[k_2^2 \left(k_{3z} + k_{2z}^{eu}\right)\left(k_x^2 - k_{3z} k_{2z}^{o}\right) - k_y^2 k_{2z}^{o}\left(k_2^2 - k_3^2\right)\right] \sin^2\psi \\
& + k_y \left(k_{3z} - k_{2z}^{o}\right)\left(k_{2z}^{o} - k_{2z}^{eu}\right)\left(k_\rho^2 - k_{3z} k_{2z}^{o}\right) \cos\psi \sin\psi
\end{aligned} \tag{A.5i}
$$

$$
\begin{aligned}
H_e \equiv\ & k_\rho^2 \left(k_2^2 k_{3z} + k_3^2 k_{2z}^{ed}\right) \cos^2\psi \\
& + \left[k_2^2 \left(k_{3z} + k_{2z}^{ed}\right)\left(k_x^2 + k_{3z} k_{2z}^{o}\right) + k_y^2 k_{2z}^{o}\left(k_2^2 - k_3^2\right)\right] \sin^2\psi \\
& - k_y \left(k_{3z} + k_{2z}^{o}\right)\left(k_{2z}^{o} + k_{2z}^{ed}\right)\left(k_\rho^2 + k_{3z} k_{2z}^{o}\right) \cos\psi \sin\psi
\end{aligned} \tag{A.5j}
$$

Appendix B
Isotropic Coefficients

Coefficient $\Psi^{ab}_{1\mu\tau}$ in the scattering terms of the isotropic random medium are derived from Chapter 2 with (69a) for the DGF, (72a) for the mean field, and (83) for their components which are combined to form $\Psi^{ab}_{1\mu\tau}$ in the manner determined by the first term in (82) and the definition in (85). All the exponential functions have been incorporated into $\mathcal{I}_1^{abcd}$ and $\Psi^{ab}_{1\mu\tau}$ are thus composed of D's, U's, $\hat{h}$'s, and $\hat{v}$'s. For backscattering, D's and U's are evaluated at $\overline{k}_{\rho i}$ and $\hat{h}$'s and $\hat{v}$'s can be expressed in terms of incident polar angle θ_{0i} and incident azimuthal angle ϕ_{0i} as

$$\hat{h}(k^u_{1z}) = \begin{bmatrix} \sin\phi_{0i} \\ -\cos\phi_{0i} \\ 0 \end{bmatrix}, \quad \hat{v}(k^u_{1z}) = \frac{1}{k_1}\begin{bmatrix} k_{1z}\cos\phi_{0i} \\ k_{1z}\sin\phi_{0i} \\ k_0\sin\theta_{0i} \end{bmatrix} \tag{B.1a}$$

$$\hat{h}(k^d_{1z}) = \begin{bmatrix} \sin\phi_{0i} \\ -\cos\phi_{0i} \\ 0 \end{bmatrix}, \quad \hat{v}(k^d_{1z}) = \frac{1}{k_1}\begin{bmatrix} -k_{1z}\cos\phi_{0i} \\ -k_{1z}\sin\phi_{0i} \\ k_0\sin\theta_{0i} \end{bmatrix} \tag{B.1b}$$

$$\hat{h}(k^u_{1zi}) = \begin{bmatrix} -\sin\phi_{0i} \\ \cos\phi_{0i} \\ 0 \end{bmatrix}, \quad \hat{v}(k^u_{1zi}) = \frac{1}{k_1}\begin{bmatrix} -k_{1z}\cos\phi_{0i} \\ -k_{1z}\sin\phi_{0i} \\ k_0\sin\theta_{0i} \end{bmatrix} \tag{B.1c}$$

$$\hat{h}(k^d_{1zi}) = \begin{bmatrix} -\sin\phi_{0i} \\ \cos\phi_{0i} \\ 0 \end{bmatrix}, \quad \hat{v}(k^d_{1zi}) = \frac{1}{k_1}\begin{bmatrix} k_{1z}\cos\phi_{0i} \\ k_{1z}\sin\phi_{0i} \\ k_0\sin\theta_{0i} \end{bmatrix} \tag{B.1d}$$

The unit vectors of the polarization bases for the upgoing and downgoing waves are shown in Figure B.1 to help ease the derivation and illustrate the backscattering processes. As seen from the figure, a and b respectively describe scattered and

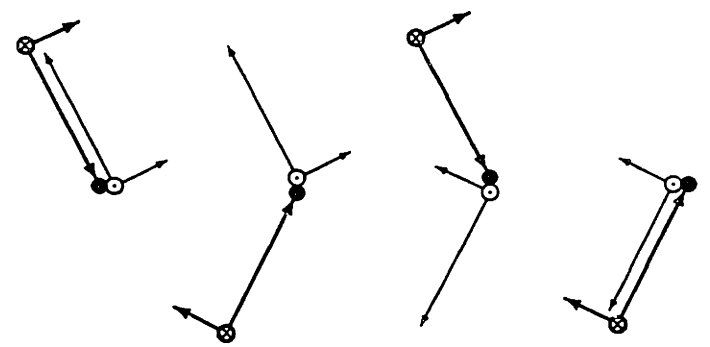

Figure B.1 Polarization bases for incident (thick lines) and scattered (thin lines) waves : $\hat{h}$ = cross or dot circles, $\hat{v}$ = short arrows, $\overline{k}$ = long arrows; black circles are for scatterer

incident wave types which can be upgoing or downgoing wave constituting the four processes depicted in Figure 2.5.1. The algebra is straight forward and the results for $\Psi_{1\mu\tau}^{ab}$ can be written as follows:

(1) For h-polarized return due to h-polarized transmission (hh)

$$\Psi_{1hh}^{-1-1} = -D_{1hh}^2(\overline{k}_{\rho i}) - D_{1hv}^2(\overline{k}_{\rho i}) \tag{B.2a}$$

$$\Psi_{1hh}^{-1+1} = -D_{1hh}(\overline{k}_{\rho i})U_{1hh}(\overline{k}_{\rho i}) - k_1^{-2}\left(k_0^2\sin^2\theta_{0i} - k_{1z}^2\right)D_{1hv}(\overline{k}_{\rho i})U_{1hv}(\overline{k}_{\rho i}) \tag{B.2b}$$

$$\Psi_{1hh}^{+1-1} = -U_{1hh}(\overline{k}_{\rho i})D_{1hh}(\overline{k}_{\rho i}) - k_1^{-2}\left(k_0^2\sin^2\theta_{0i} - k_{1z}^2\right)U_{1hv}(\overline{k}_{\rho i})D_{1hv}(\overline{k}_{\rho i}) \tag{B.2c}$$

$$\Psi_{1hh}^{+1+1} = -U_{1hh}^2(\overline{k}_{\rho i}) - U_{1hv}^2(\overline{k}_{\rho i}) \tag{B.2d}$$

(2) For h-polarized return due to v-polarized transmission (hv)

$$\Psi_{1hv}^{-1-1} = -D_{1hh}(\overline{k}_{\rho i})D_{1vh}(\overline{k}_{\rho i}) - D_{1hv}(\overline{k}_{\rho i})D_{1vv}(\overline{k}_{\rho i}) \tag{B.3a}$$

$$\Psi_{1hv}^{-1+1} = -D_{1hh}(\overline{k}_{\rho i})U_{1vh}(\overline{k}_{\rho i}) - k_1^{-2}\left(k_0^2\sin^2\theta_{0i} - k_{1z}^2\right)D_{1hv}(\overline{k}_{\rho i})U_{1vv}(\overline{k}_{\rho i}) \tag{B.3b}$$

$$\Psi_{1hv}^{+1-1} = -U_{1hh}(\overline{k}_{\rho i})D_{1vh}(\overline{k}_{\rho i}) - k_1^{-2}\left(k_0^2\sin^2\theta_{0i} - k_{1z}^2\right)U_{1hv}(\overline{k}_{\rho i})D_{1vv}(\overline{k}_{\rho i}) \quad \text{(B.3c)}$$

$$\Psi_{1hv}^{+1+1} = -U_{1hh}(\overline{k}_{\rho i})U_{1vh}(\overline{k}_{\rho i}) - U_{1hv}(\overline{k}_{\rho i})U_{1vv}(\overline{k}_{\rho i}) \quad \text{(B.3d)}$$

(3) For v-polarized return due to h-polarized transmission (vh)

$$\Psi_{1vh}^{-1-1} = D_{1vh}(\overline{k}_{\rho i})D_{1hh}(\overline{k}_{\rho i}) + D_{1vv}(\overline{k}_{\rho i})D_{1hv}(\overline{k}_{\rho i}) \quad \text{(B.4a)}$$

$$\Psi_{1vh}^{-1+1} = D_{1vh}(\overline{k}_{\rho i})U_{1hh}(\overline{k}_{\rho i}) + k_1^{-2}\left(k_0^2\sin^2\theta_{0i} - k_{1z}^2\right)D_{1vv}(\overline{k}_{\rho i})U_{1hv}(\overline{k}_{\rho i}) \quad \text{(B.4b)}$$

$$\Psi_{1vh}^{+1-1} = U_{1vh}(\overline{k}_{\rho i})D_{1hh}(\overline{k}_{\rho i}) + k_1^{-2}\left(k_0^2\sin^2\theta_{0i} - k_{1z}^2\right)U_{1vv}(\overline{k}_{\rho i})D_{1hv}(\overline{k}_{\rho i}) \quad \text{(B.4c)}$$

$$\Psi_{1vh}^{+1+1} = U_{1vh}(\overline{k}_{\rho i})U_{1hh}(\overline{k}_{\rho i}) + U_{1vv}(\overline{k}_{\rho i})U_{1hv}(\overline{k}_{\rho i}) \quad \text{(B.4d)}$$

(4) For v-polarized return due to v-polarized transmission (vv)

$$\Psi_{1vv}^{-1-1} = D_{1vh}^2(\overline{k}_{\rho i}) + D_{1vv}^2(\overline{k}_{\rho i}) \quad \text{(B.5a)}$$

$$\Psi_{1vv}^{-1+1} = D_{1vh}(\overline{k}_{\rho i})U_{1vh}(\overline{k}_{\rho i}) + k_1^{-2}\left(k_0^2\sin^2\theta_{0i} - k_{1z}^2\right)D_{1vv}(\overline{k}_{\rho i})U_{1vv}(\overline{k}_{\rho i}) \quad \text{(B.5b)}$$

$$\Psi_{1vv}^{+1-1} = U_{1vh}(\overline{k}_{\rho i})D_{1vh}(\overline{k}_{\rho i}) + k_1^{-2}\left(k_0^2\sin^2\theta_{0i} - k_{1z}^2\right)U_{1vv}(\overline{k}_{\rho i})D_{1vv}(\overline{k}_{\rho i}) \quad \text{(B.5c)}$$

$$\Psi_{1vv}^{+1+1} = U_{1vh}^2(\overline{k}_{\rho i}) + U_{1vv}^2(\overline{k}_{\rho i}) \quad \text{(B.5d)}$$

With $k_1^2 = k_0^2\sin^2\theta_{0i} + k_{1z}^2$ and the definitions of $W^{(+1)} = U$ and $W^{(-1)} = D$, all of the above expressions for Ψ's can be summarized as

$$\Psi_{1\mu\tau}^{ab} = \pm W_{\mu h}^{(a)}(\overline{k}_{\rho i})W_{\tau h}^{(b)}(\overline{k}_{\rho i}) \pm k_1^{-2}\left(k_0^2\sin^2\theta_{0i} + abk_{1z}^2\right)W_{\mu v}^{(a)}(\overline{k}_{\rho i})W_{\tau v}^{(b)}(\overline{k}_{\rho i}) \quad \text{(B.6)}$$

where the minus signs are for $\mu = h$ and the plus signs are for $\mu = v$.

Appendix C
Anisotropic Coefficients

Coefficient $\Psi^{pq}_{2\mu\tau,jk}$ in the scattering terms of the anisotropic random medium are derived from Chapter 2 with (83), (69b), and (72b) for the components of the DGF and the mean field which are combined according to the second term in (82) and the definition in (86) to form $\Psi^{pq}_{2\mu\tau,jk}$. The results for the coefficients can be expressed as follows:

(1) For the h-polarized return due to the h-polarized transmission (hh)

$$\Psi^{ou\,ou}_{2hh,jk} = D_{2ho}(-\overline{k}_\rho)U_{2ho}(\overline{k}_{\rho i})o_j(k^{ou}_{2z})o_k(k^{ou}_{2zi}) \tag{C.1}$$

$$\Psi^{ou\,od}_{2hh,jk} = D_{2ho}(-\overline{k}_\rho)D_{2ho}(\overline{k}_{\rho i})o_j(k^{ou}_{2z})o_k(k^{od}_{2zi}) \tag{C.2}$$

$$\Psi^{ou\,eu}_{2hh,jk} = D_{2ho}(-\overline{k}_\rho)U_{2he}(\overline{k}_{\rho i})o_j(k^{ou}_{2z})e_k(k^{eu}_{2zi}) \tag{C.3}$$

$$\Psi^{ou\,ed}_{2hh,jk} = D_{2ho}(-\overline{k}_\rho)D_{2he}(\overline{k}_{\rho i})o_j(k^{ou}_{2z})e_k(k^{ed}_{2zi}) \tag{C.4}$$

$$\Psi^{od\,ou}_{2hh,jk} = U_{2ho}(-\overline{k}_\rho)U_{2ho}(\overline{k}_{\rho i})o_j(k^{od}_{2z})o_k(k^{ou}_{2zi}) \tag{C.5}$$

$$\Psi^{od\,od}_{2hh,jk} = U_{2ho}(-\overline{k}_\rho)D_{2ho}(\overline{k}_{\rho i})o_j(k^{od}_{2z})o_k(k^{od}_{2zi}) \tag{C.6}$$

$$\Psi^{od\,eu}_{2hh,jk} = U_{2ho}(-\overline{k}_\rho)U_{2he}(\overline{k}_{\rho i})o_j(k^{od}_{2z})e_k(k^{eu}_{2zi}) \tag{C.7}$$

$$\Psi^{od\,ed}_{2hh,jk} = U_{2ho}(-\overline{k}_\rho)D_{2he}(\overline{k}_{\rho i})o_j(k^{od}_{2z})e_k(k^{ed}_{2zi}) \tag{C.8}$$

$$\Psi^{eu\,ou}_{2hh,jk} = -D_{2he}(-\overline{k}_\rho)U_{2ho}(\overline{k}_{\rho i})e_j(k^{eu}_{2z})o_k(k^{ou}_{2zi}) \tag{C.9}$$

$$\Psi^{eu\,od}_{2hh,jk} = -D_{2he}(-\overline{k}_\rho)D_{2ho}(\overline{k}_{\rho i})e_j(k^{eu}_{2z})o_k(k^{od}_{2zi}) \tag{C.10}$$

$$\Psi^{eu\,eu}_{2hh,jk} = -D_{2he}(-\overline{k}_\rho)U_{2he}(\overline{k}_{\rho i})e_j(k^{eu}_{2z})e_k(k^{eu}_{2zi}) \tag{C.11}$$

$$\Psi^{eu\,ed}_{2hh,jk} = -D_{2he}(-\overline{k}_\rho)D_{2he}(\overline{k}_{\rho i})e_j(k^{eu}_{2z})e_k(k^{ed}_{2zi}) \tag{C.12}$$

$$\Psi^{ed\,ou}_{2hh,jk} = -U_{2he}(-\overline{k}_\rho)U_{2ho}(\overline{k}_{\rho i})e_j(k^{ed}_{2z})o_k(k^{ou}_{2zi}) \tag{C.13}$$

$$\Psi^{ed\,od}_{2hh,jk} = -U_{2he}(-\overline{k}_\rho)D_{2ho}(\overline{k}_{\rho i})e_j(k^{ed}_{2z})o_k(k^{od}_{2zi}) \tag{C.14}$$

$$\Psi^{ed\,eu}_{2hh,jk} = -U_{2he}(-\overline{k}_\rho)U_{2he}(\overline{k}_{\rho i})e_j(k^{ed}_{2z})e_k(k^{eu}_{2zi}) \tag{C.15}$$

$$\Psi^{ed\,ed}_{2hh,jk} = -U_{2he}(-\overline{k}_\rho)D_{2he}(\overline{k}_{\rho i})e_j(k^{ed}_{2z})e_k(k^{ed}_{2zi}) \tag{C.16}$$

(2) For the h-polarized return due to the v-polarized transmission (hv)

$$\Psi^{ou\,ou}_{2hv,jk} = D_{2ho}(-\overline{k}_\rho)U_{2vo}(\overline{k}_{\rho i})o_j(k^{ou}_{2z})o_k(k^{ou}_{2zi}) \tag{C.17}$$

$$\Psi^{ou\,od}_{2hv,jk} = D_{2ho}(-\overline{k}_\rho)D_{2vo}(\overline{k}_{\rho i})o_j(k^{ou}_{2z})o_k(k^{od}_{2zi}) \tag{C.18}$$

$$\Psi^{ou\,eu}_{2hv,jk} = D_{2ho}(-\overline{k}_\rho)U_{2ve}(\overline{k}_{\rho i})o_j(k^{ou}_{2z})e_k(k^{eu}_{2zi}) \tag{C.19}$$

$$\Psi^{ou\,ed}_{2hv,jk} = D_{2ho}(-\overline{k}_\rho)D_{2ve}(\overline{k}_{\rho i})o_j(k^{ou}_{2z})e_k(k^{ed}_{2zi}) \tag{C.20}$$

$$\Psi^{od\,ou}_{2hv,jk} = U_{2ho}(-\overline{k}_\rho)U_{2vo}(\overline{k}_{\rho i})o_j(k^{od}_{2z})o_k(k^{ou}_{2zi}) \tag{C.21}$$

$$\Psi^{od\,od}_{2hv,jk} = U_{2ho}(-\overline{k}_\rho)D_{2vo}(\overline{k}_{\rho i})o_j(k^{od}_{2z})o_k(k^{od}_{2zi}) \tag{C.22}$$

$$\Psi^{od\,eu}_{2hv,jk} = U_{2ho}(-\overline{k}_\rho)U_{2ve}(\overline{k}_{\rho i})o_j(k^{od}_{2z})e_k(k^{eu}_{2zi}) \tag{C.23}$$

$$\Psi^{od\,ed}_{2hv,jk} = U_{2ho}(-\overline{k}_\rho)D_{2ve}(\overline{k}_{\rho i})o_j(k^{od}_{2z})e_k(k^{ed}_{2zi}) \tag{C.24}$$

$$\Psi^{eu\,ou}_{2hv,jk} = -D_{2he}(-\overline{k}_\rho)U_{2vo}(\overline{k}_{\rho i})e_j(k^{eu}_{2z})o_k(k^{ou}_{2zi}) \tag{C.25}$$

$$\Psi^{eu\,od}_{2hv,jk} = -D_{2he}(-\overline{k}_\rho)D_{2vo}(\overline{k}_{\rho i})e_j(k^{eu}_{2z})o_k(k^{od}_{2zi}) \tag{C.26}$$

$$\Psi^{eu\,eu}_{2hv,jk} = -D_{2he}(-\overline{k}_\rho)U_{2ve}(\overline{k}_{\rho i})e_j(k^{eu}_{2z})e_k(k^{eu}_{2zi}) \tag{C.27}$$

$$\Psi^{eu\,ed}_{2hv,jk} = -D_{2he}(-\overline{k}_\rho)D_{2ve}(\overline{k}_{\rho i})e_j(k^{eu}_{2z})e_k(k^{ed}_{2zi}) \tag{C.28}$$

$$\Psi^{ed\,ou}_{2hv,jk} = -U_{2he}(-\overline{k}_\rho)U_{2vo}(\overline{k}_{\rho i})e_j(k^{ed}_{2z})o_k(k^{ou}_{2zi}) \tag{C.29}$$

$$\Psi^{ed\,od}_{2hv,jk} = -U_{2he}(-\overline{k}_\rho)D_{2vo}(\overline{k}_{\rho i})e_j(k^{ed}_{2z})o_k(k^{od}_{2zi}) \tag{C.30}$$

$$\Psi^{ed\,eu}_{2hv,jk} = -U_{2he}(-\overline{k}_\rho)U_{2ve}(\overline{k}_{\rho i})e_j(k^{ed}_{2z})e_k(k^{eu}_{2zi}) \tag{C.31}$$

$$\Psi^{ed\,ed}_{2hv,jk} = -U_{2he}(-\overline{k}_\rho)D_{2ve}(\overline{k}_{\rho i})e_j(k^{ed}_{2z})e_k(k^{ed}_{2zi}) \tag{C.32}$$

(3) For the v-polarized return due to the h-polarized transmission (vh)

$$\Psi^{ou\,ou}_{2vh,jk} = -D_{2vo}(-\overline{k}_\rho)U_{2ho}(\overline{k}_{\rho i})o_j(k^{ou}_{2z})o_k(k^{ou}_{2zi}) \tag{C.33}$$

$$\Psi^{ou\,od}_{2vh,jk} = -D_{2vo}(-\overline{k}_\rho)D_{2ho}(\overline{k}_{\rho i})o_j(k^{ou}_{2z})o_k(k^{od}_{2zi}) \tag{C.34}$$

$$\Psi^{ou\,eu}_{2vh,jk} = -D_{2vo}(-\overline{k}_\rho)U_{2he}(\overline{k}_{\rho i})o_j(k^{ou}_{2z})e_k(k^{eu}_{2zi}) \tag{C.35}$$

$$\Psi^{ou\,ed}_{2vh,jk} = -D_{2vo}(-\overline{k}_\rho)D_{2he}(\overline{k}_{\rho i})o_j(k^{ou}_{2z})e_k(k^{ed}_{2zi}) \tag{C.36}$$

$$\Psi^{od\,ou}_{2vh,jk} = -U_{2vo}(-\overline{k}_\rho)U_{2ho}(\overline{k}_{\rho i})o_j(k^{od}_{2z})o_k(k^{ou}_{2zi}) \tag{C.37}$$

$$\Psi^{od\,od}_{2vh,jk} = -U_{2vo}(-\overline{k}_\rho)D_{2ho}(\overline{k}_{\rho i})o_j(k^{od}_{2z})o_k(k^{od}_{2zi}) \tag{C.38}$$

$$\Psi^{od\,eu}_{2vh,jk} = -U_{2vo}(-\overline{k}_\rho)U_{2he}(\overline{k}_{\rho i})o_j(k^{od}_{2z})e_k(k^{eu}_{2zi}) \tag{C.39}$$

$$\Psi^{od\,ed}_{2vh,jk} = -U_{2vo}(-\overline{k}_\rho)D_{2he}(\overline{k}_{\rho i})o_j(k^{od}_{2z})e_k(k^{ed}_{2zi}) \tag{C.40}$$

$$\Psi^{eu\,ou}_{2vh,jk} = D_{2ve}(-\overline{k}_\rho)U_{2ho}(\overline{k}_{\rho i})e_j(k^{eu}_{2z})o_k(k^{ou}_{2zi}) \tag{C.41}$$

$$\Psi^{eu\,od}_{2vh,jk} = D_{2ve}(-\overline{k}_\rho)D_{2ho}(\overline{k}_{\rho i})e_j(k^{eu}_{2z})o_k(k^{od}_{2zi}) \tag{C.42}$$

$$\Psi^{eu\,eu}_{2vh,jk} = D_{2ve}(-\overline{k}_\rho)U_{2he}(\overline{k}_{\rho i})e_j(k^{eu}_{2z})e_k(k^{eu}_{2zi}) \tag{C.43}$$

$$\Psi^{eu\,ed}_{2vh,jk} = D_{2ve}(-\overline{k}_\rho)D_{2he}(\overline{k}_{\rho i})e_j(k^{eu}_{2z})e_k(k^{ed}_{2zi}) \tag{C.44}$$

$$\Psi^{ed\,ou}_{2vh,jk} = U_{2ve}(-\overline{k}_\rho)U_{2ho}(\overline{k}_{\rho i})e_j(k^{ed}_{2z})o_k(k^{ou}_{2zi}) \tag{C.45}$$

$$\Psi^{ed\,od}_{2vh,jk} = U_{2ve}(-\overline{k}_\rho)D_{2ho}(\overline{k}_{\rho i})e_j(k^{ed}_{2z})o_k(k^{od}_{2zi}) \tag{C.46}$$

$$\Psi^{ed\,eu}_{2vh,jk} = U_{2ve}(-\overline{k}_\rho)U_{2he}(\overline{k}_{\rho i})e_j(k^{ed}_{2z})e_k(k^{eu}_{2zi}) \tag{C.47}$$

$$\Psi^{ed\,ed}_{2vh,jk} = U_{2ve}(-\overline{k}_\rho)D_{2he}(\overline{k}_{\rho i})e_j(k^{ed}_{2z})e_k(k^{ed}_{2zi}) \tag{C.48}$$

(4) For the v-polarized return due to the v-polarized transmission (vv)

$$\Psi^{ou\,ou}_{2vv,jk} = -D_{2vo}(-\overline{k}_\rho)U_{2vo}(\overline{k}_{\rho i})o_j(k^{ou}_{2z})o_k(k^{ou}_{2zi}) \tag{C.49}$$

$$\Psi^{ou\,od}_{2vv,jk} = -D_{2vo}(-\overline{k}_\rho)D_{2vo}(\overline{k}_{\rho i})o_j(k^{ou}_{2z})o_k(k^{od}_{2zi}) \tag{C.50}$$

$$\Psi^{ou\,eu}_{2vv,jk} = -D_{2vo}(-\overline{k}_\rho)U_{2ve}(\overline{k}_{\rho i})o_j(k^{ou}_{2z})e_k(k^{eu}_{2zi}) \tag{C.51}$$

$$\Psi^{ou\,ed}_{2vv,jk} = -D_{2vo}(-\overline{k}_\rho)D_{2ve}(\overline{k}_{\rho i})o_j(k^{ou}_{2z})e_k(k^{ed}_{2zi}) \tag{C.52}$$

$$\Psi^{od\,ou}_{2vv,jk} = -U_{2vo}(-\overline{k}_\rho)U_{2vo}(\overline{k}_{\rho i})o_j(k^{od}_{2z})o_k(k^{ou}_{2zi}) \tag{C.53}$$

$$\Psi^{od\,od}_{2vv,jk} = -U_{2vo}(-\overline{k}_\rho)D_{2vo}(\overline{k}_{\rho i})o_j(k^{od}_{2z})o_k(k^{od}_{2zi}) \tag{C.54}$$

$$\Psi^{od\,eu}_{2vv,jk} = -U_{2vo}(-\overline{k}_\rho)U_{2ve}(\overline{k}_{\rho i})o_j(k^{od}_{2z})e_k(k^{eu}_{2zi}) \tag{C.55}$$

$$\Psi^{od\,ed}_{2vv,jk} = -U_{2vo}(-\overline{k}_\rho)D_{2ve}(\overline{k}_{\rho i})o_j(k^{od}_{2z})e_k(k^{ed}_{2zi}) \tag{C.56}$$

$$\Psi^{eu\,ou}_{2vv,jk} = D_{2ve}(-\overline{k}_\rho)U_{2vo}(\overline{k}_{\rho i})e_j(k^{eu}_{2z})o_k(k^{ou}_{2zi}) \tag{C.57}$$

$$\Psi^{eu\,od}_{2vv,jk} = D_{2ve}(-\overline{k}_\rho)D_{2vo}(\overline{k}_{\rho i})e_j(k^{eu}_{2z})o_k(k^{od}_{2zi}) \tag{C.58}$$

$$\Psi^{eu\,eu}_{2vv,jk} = D_{2ve}(-\overline{k}_\rho)U_{2ve}(\overline{k}_{\rho i})e_j(k^{eu}_{2z})e_k(k^{eu}_{2zi}) \tag{C.59}$$

$$\Psi^{eu\,ed}_{2vv,jk} = D_{2ve}(-\overline{k}_\rho)D_{2ve}(\overline{k}_{\rho i})e_j(k^{eu}_{2z})e_k(k^{ed}_{2zi}) \tag{C.60}$$

$$\Psi^{ed\,ou}_{2vv,jk} = U_{2ve}(-\overline{k}_\rho)U_{2vo}(\overline{k}_{\rho i})e_j(k^{ed}_{2z})o_k(k^{ou}_{2zi}) \tag{C.61}$$

$$\Psi^{ed\,od}_{2vv,jk} = U_{2ve}(-\overline{k}_\rho)D_{2vo}(\overline{k}_{\rho i})e_j(k^{ed}_{2z})o_k(k^{od}_{2zi}) \tag{C.62}$$

$$\Psi^{ed\,eu}_{2vv,jk} = U_{2ve}(-\overline{k}_\rho)U_{2ve}(\overline{k}_{\rho i})e_j(k^{ed}_{2z})e_k(k^{eu}_{2zi}) \tag{C.63}$$

$$\Psi^{ed\,ed}_{2vv,jk} = U_{2ve}(-\overline{k}_\rho)D_{2ve}(\overline{k}_{\rho i})e_j(k^{ed}_{2z})e_k(k^{ed}_{2zi}) \tag{C.64}$$

where o_j (or o_k) and e_j (or e_k) are the $j,k = x,y,x$ components of unit vector $\hat{o}$ and $\hat{e}$ defined in section 2.4. For backscattering, $\overline{k}_\rho = -\overline{k}_{\rho i}$ and $o_j(k^{ou}_{2z})$, $o_j(k^{od}_{2z})$, $e_j(k^{eu}_{2z})$, and $e_j(k^{ed}_{2z})$ are evaluated for the backscattered waves similarly to the procedure in Appendix B.

Appendix D
Correlation Integrations

D.1 Integrations for $\mathcal{I}_1^{abcd}$

The integrations over z_1 and z_1^o in (85a) of Chapter 2 are carried out to give

$$\mathcal{I}_1^{abcd} = \int_{-\infty}^{\infty} d\beta_z \Phi_1(2\overline{k}_{\rho i}, \beta_z) \cdot \frac{1 - e^{i(\beta_z - \kappa_{ab})d_1}}{\beta_z - \kappa_{ab}} \cdot \frac{1 - e^{-i(\beta_z - \kappa_{cd})d_1}}{\beta_z - \kappa_{cd}} \tag{D.1}$$

Using (74) and (24b) from Chapter 2 for the isotropic correlation functions in (D.1) yields

$$\mathcal{I}_1^{abcd} = \delta_1 \ell_1^3 \pi^{-2} (\mathcal{A}_1 + \mathcal{B}_1) \tag{D.2}$$

where $\mathcal{A}_1$ and $\mathcal{B}_1$ are integrals over β_z defined as

$$\mathcal{A}_1 = \int_{-\infty}^{\infty} d\beta_z \frac{1 - e^{i(\beta_z - \kappa_{ab})d_1} + e^{i(\kappa_{cd} - \kappa_{ab})d_1}}{(\beta_z^2 \ell_1^2 + 1 + 4k_{\rho i}^2 \ell_1^2)^2 (\beta_z - \kappa_{ab})(\beta_z - \kappa_{cd})} \tag{D.3}$$

$$\mathcal{B}_1 = \int_{-\infty}^{\infty} d\beta_z \frac{-e^{-i(\beta_z - \kappa_{cd})d_1}}{(\beta_z^2 \ell_1^2 + 1 + 4k_{\rho i}^2 \ell_1^2)^2 (\beta_z - \kappa_{ab})(\beta_z - \kappa_{cd})} \tag{D.4}$$

The integrations over β_z in (D.3) and (D.4) are carried out with the contour integration method. For $\mathcal{A}_1$, the imaginary part of β_z has to be positive for the integral to converge. Thus, $\mathcal{A}_1$ can be taken as the integral along the positively oriented contour composed of the real β_z axis and the infinite semi-circle on the upper half of the complex β_z plane and centered at origin $\beta_z = 0$. Note that the integral over the semi-circle vanishes on account of Jordan's lemma. The chosen contour encloses simple poles at $\beta_z = \kappa_{ab}, \kappa_{cd}$ (if the imaginary parts of the simple poles are positive) and a double pole at $\beta_z = \kappa_1 = i\ell^{-1}\sqrt{1 + 4k_{\rho i}^2 \ell_1^2}$. Integral $\mathcal{A}_1$ is

therefore composed of the residue contribution from the enclosed poles. According to the residue theorem, the result for $\mathcal{A}_1$ is

$$\mathcal{A}_1 = 2\pi i \left\{ \frac{e^{i(\kappa_{cd}-\kappa_{ab})d_1}}{(\kappa_{ab}^2\ell_1^2+1+4k_{\rho i}^2\ell_1^2)^2(\kappa_{ab}-\kappa_{cd})} \quad (\text{if } \mathrm{Im}\kappa_{ab}>0) \right.$$
$$+ \frac{1}{(\kappa_{cd}^2\ell_1^2+1+4k_{\rho i}^2\ell_1^2)^2(\kappa_{cd}-\kappa_{ab})} \quad (\text{if } \mathrm{Im}\kappa_{cd}>0)$$
$$- \frac{id_1 e^{i(\kappa_1-\kappa_{ab})d_1}}{\ell_1^4(\kappa_1-\kappa_1^*)^2(\kappa_1-\kappa_{ab})(\kappa_1-\kappa_{cd})}$$
$$- \frac{1-e^{i(\kappa_1-\kappa_{ab})d_1}+e^{i(\kappa_{cd}-\kappa_{ab})d_1}}{\ell_1^4(\kappa_1-\kappa_1^*)^2(\kappa_1-\kappa_{ab})(\kappa_1-\kappa_{cd})}$$
$$\left. \cdot \left[\frac{2}{\kappa_1-\kappa_1^*} + \frac{1}{\kappa_1-\kappa_{ab}} + \frac{1}{\kappa_1-\kappa_{cd}} \right] \right\} \tag{D.5}$$

For $\mathcal{B}_1$, the same contour integration method is used except that the infinite semi-circle is in the lower half of the complex β_z plane for convergence of the integral. The integration contour is now negatively oriented along the real β_z axis and the lower semi-circle enclosing simple poles at $\beta_z = \kappa_{ab}, \kappa_{cd}$ (if the imaginary parts of the simple poles are negative) and a double pole at $\beta_z = \kappa_1^* = -i\ell^{-1}\sqrt{1+4k_{\rho i}^2\ell_1^2}$. The result for $\mathcal{B}_1$ is

$$\mathcal{B}_1 = 2\pi i \left\{ \frac{e^{i(\kappa_{cd}-\kappa_{ab})d_1}}{(\kappa_{ab}^2\ell_1^2+1+4k_{\rho i}^2\ell_1^2)^2(\kappa_{ab}-\kappa_{cd})} \quad (\text{if } \mathrm{Im}\kappa_{ab}<0) \right.$$
$$+ \frac{1}{(\kappa_{cd}^2\ell_1^2+1+4k_{\rho i}^2\ell_1^2)^2(\kappa_{cd}-\kappa_{ab})} \quad (\text{if } \mathrm{Im}\kappa_{cd}<0)$$
$$- \frac{id_1 e^{-i(\kappa_1^*-\kappa_{cd})d_1}}{\ell_1^4(\kappa_1^*-\kappa_1)^2(\kappa_1^*-\kappa_{ab})(\kappa_1^*-\kappa_{cd})}$$
$$- \frac{e^{-i(\kappa_1^*-\kappa_{cd})d_1}}{\ell_1^4(\kappa_1^*-\kappa_1)^2(\kappa_1^*-\kappa_{ab})(\kappa_1^*-\kappa_{cd})}$$
$$\left. \cdot \left[\frac{2}{\kappa_1^*-\kappa_1} + \frac{1}{\kappa_1^*-\kappa_{ab}} + \frac{1}{\kappa_1^*-\kappa_{cd}} \right] \right\} \tag{D.6}$$

Substituting (D.6) and (D.5) in (D.4) yields $\mathcal{I}_1^{abcd}$ which is rearranged to obtain the result in (87) for the isotropic random medium.

D.2 Integrations of $\mathcal{I}^{pqrs}_{2jklm}$

The integrations over z_2 and z_2^o in (86a) are carried out to give

$$\mathcal{I}^{pqrs}_{2jklm} = \int_{-\infty}^{\infty} d\beta_z \Phi_{2jklm}(2\overline{k}_{\rho i}, \beta_z) \cdot \frac{e^{i(\beta_z - \kappa_{pq})d_1} - e^{i(\beta_z - \kappa_{pq})d_2}}{\beta_z - \kappa_{pq}} \cdot \frac{e^{-i(\beta_z - \kappa_{rs})d_1} - e^{-i(\beta_z - \kappa_{rs})d_2}}{\beta_z - \kappa_{rs}} \tag{D.7}$$

Using (80), (79), and (39b) for the anisotropic correlation functions in (D.7) yields

$$\mathcal{I}^{pqrs}_{2jklm} = \delta_{2jklm} \ell^2_{2\rho'} \ell_{2z'} \pi^{-2} (\mathcal{A}_2 + \mathcal{B}_2) \tag{D.8}$$

where integral $\mathcal{A}_2$ and $\mathcal{B}_2$ are defined as

$$\mathcal{A}_2 = \int_{-\infty}^{\infty} d\beta_z \frac{e^{i(\kappa_{rs} - \kappa_{pq})d_1} - e^{i(\kappa_{rs} d_1 - \kappa_{pq} d_2)} e^{i(d_2 - d_1)\beta_z} + e^{i(\kappa_{rs} - \kappa_{pq})d_2}}{D^2(2\overline{k}_{\rho i}, \beta_z)(\beta_z - \kappa_{pq})(\beta_z - \kappa_{rs})} \tag{D.9}$$

$$\mathcal{B}_2 = \int_{-\infty}^{\infty} d\beta_z \frac{-e^{i(\kappa_{rs} d_2 - \kappa_{pq} d_1)} e^{-i(d_2 - d_1)\beta_z}}{D^2(2\overline{k}_{\rho i}, \beta_z)(\beta_z - \kappa_{pq})(\beta_z - \kappa_{rs})} \tag{D.10}$$

In (D.9) and (D.10), $D(2\overline{k}_{\rho i}, \beta_z)$ is a quadratic expression in β_z given by

$$D(2\overline{k}_{\rho i}, \beta_z) = \mathcal{L}_2^2 \beta_z^2 + 2k_{yi}(\ell^2_{2z'} - \ell^2_{2\rho'}) \sin(2\psi) \beta_z + \left[1 + 4k^2_{xi} \ell^2_{2\rho'} + 4k^2_{yi}(\ell^2_{2\rho'} \cos^2\psi + \ell^2_{2z'} \sin^2\psi)\right] \tag{D.11}$$

with $\mathcal{L}_2^2 = \ell^2_{2\rho'} \sin^2\psi + \ell^2_{2z'} \cos^2\psi$. The integrations over β_z in (D.9) and (D.10) are carried out with the contour integration method as in the last section of this appendix. In consideration of the convergence, the contour for $\mathcal{A}_2$ is taken to be positively oriented along the real β_z axis and the upper infinite semi-circle and that for $\mathcal{B}_2$ is negatively oriented along the real β_z axis and the lower infinite semi-circle. Integral $\mathcal{I}^{pqrs}_{2jklm}$ is thus composed of the contribution from the residues of two simple poles at $\beta_z = \kappa_{pq}, \kappa_{rs}$ and two double poles corresponding to the two zeros of quadratic equation $D(2\overline{k}_{\rho i}, \beta_z) = 0$ at $\beta_z = \kappa_2, \kappa_2^*$ for $\kappa_2 = \mathcal{L}_2^{-2}\left[-k_{yi}(\ell^2_{2z'} - \ell^2_{2\rho'}) \sin(2\psi) + i\sqrt{(1+4k^2_{xi}\ell^2_{2\rho'})\mathcal{L}_2^2 + 4k^2_{yi}\ell^2_{2\rho'}\ell^2_{2z'}}\right]$. The residue theorem then gives the result in (107) for the anisotropic random medium. Note that the anisotropic result approaches the isotropic result in the limits of $\ell_{2z'} \to \ell_{2\rho'}$ and $d_1 \to 0$.

Appendix E
Average over Eulerian Angles

This appendix show the average over the random orientation, described by Eulerian angles, of the tensor $\overline{\overline{\xi}}$. The averaging integral is

$$\left\langle \overline{\overline{\xi}}(\bar{r}) \right\rangle = \int_0^{2\pi} d\gamma \int_0^{\pi} d\beta \int_0^{2\pi} d\alpha \; p(\alpha,\beta,\gamma)\, \overline{\overline{T}}^{-1} \cdot \overline{\overline{\xi}} \cdot \overline{\overline{T}} \tag{E.1}$$

where the probability density function of the random orientation is $p(\alpha,\beta,\gamma) = \sin\beta/(8\pi^2)$ and rotation tensor $\overline{\overline{T}}$ given by

$$\overline{\overline{T}} = \begin{bmatrix} \cos\gamma\cos\beta\cos\alpha - \sin\gamma\sin\alpha & -\sin\gamma\cos\beta\cos\alpha - \cos\gamma\sin\alpha & \sin\beta\cos\alpha \\ \cos\gamma\cos\beta\sin\alpha + \sin\gamma\cos\alpha & -\sin\gamma\cos\beta\sin\alpha + \cos\gamma\cos\alpha & \sin\beta\sin\alpha \\ -\cos\gamma\sin\beta & \sin\gamma\sin\beta & \cos\beta \end{bmatrix} \tag{E.2}$$

Tensor $\overline{\overline{\xi}}(\hat{r})$ in the global coordinates (x,y,z) is obtained with the rotation operation

$$\overline{\overline{\xi}}(\hat{r}) = \overline{\overline{T}}^{-1} \cdot \overline{\overline{\xi}}(\hat{r}') \cdot \overline{\overline{T}} = \overline{\overline{T}}^{-1} \cdot \begin{bmatrix} \xi_{x'} & 0 & 0 \\ 0 & \xi_{y'} & 0 \\ 0 & 0 & \xi_{z'} \end{bmatrix} \cdot \overline{\overline{T}} = \begin{bmatrix} \xi_{xx} & \xi_{xy} & \xi_{xz} \\ \xi_{yx} & \xi_{yy} & \xi_{yz} \\ \xi_{zx} & \xi_{zy} & \xi_{zz} \end{bmatrix} \tag{E.3}$$

Explicitly, the elements of $\overline{\overline{\xi}}(\hat{r})$ in the global coordinates are

$$\begin{aligned} \xi_{xx} =& \xi_{x'} \left(\cos^2\gamma\cos^2\beta\cos^2\alpha + \sin^2\gamma\sin^2\alpha - 2\sin\gamma\cos\gamma\cos\beta\sin\alpha\cos\alpha \right) \\ &+ \xi_{y'} \left(\cos^2\gamma\cos^2\beta\sin^2\alpha + \sin^2\gamma\cos^2\alpha + 2\sin\gamma\cos\gamma\cos\beta\sin\alpha\cos\alpha \right) \\ &+ \xi_{z'} \left(\cos^2\gamma\sin^2\beta \right) = \xi_{x'} a_{xxx} + \xi_{y'} a_{yxx} + \xi_{z'} a_{zxx} \end{aligned} \tag{E.4a}$$

$$\begin{aligned}\xi_{xy} = &-\xi_{x'}\left(\sin\gamma\cos\gamma\cos^2\beta\cos^2\alpha + \cos^2\gamma\cos\beta\sin\alpha\cos\alpha\right.\\ &\left.-\sin^2\gamma\cos\beta\sin\alpha\cos\alpha - \sin\gamma\cos\gamma\sin^2\alpha\right)\\ &-\xi_{y'}\left(\sin\gamma\cos\gamma\cos^2\beta\sin^2\alpha - \cos^2\gamma\cos\beta\sin\alpha\cos\alpha\right.\\ &\left.+\sin^2\gamma\cos\beta\sin\alpha\cos\alpha - \sin\gamma\cos\gamma\cos^2\alpha\right)\\ &-\xi_{z'}\left(\sin\gamma\cos\gamma\sin^2\beta\right) = \xi_{x'}a_{xxy} + \xi_{y'}a_{yxy} + \xi_{z'}a_{zxy}\end{aligned} \tag{E.4b}$$

$$\begin{aligned}\xi_{xz} =&\xi_{x'}\left(\cos\gamma\sin\beta\cos\beta\cos^2\alpha - \sin\gamma\sin\beta\sin\alpha\cos\alpha\right)\\ &+\xi_{y'}\left(\cos\gamma\sin\beta\cos\beta\sin^2\alpha + \sin\gamma\sin\beta\sin\alpha\cos\alpha\right)\\ &+\xi_{z'}\left(-\cos\gamma\sin\beta\cos\beta\right) = \xi_{x'}a_{xxz} + \xi_{y'}a_{yxz} + \xi_{z'}a_{zxz}\end{aligned} \tag{E.4c}$$

$$\xi_{yx} =\xi_{x'}a_{xyx} + \xi_{y'}a_{yyx} + \xi_{z'}a_{zyx} = \xi_{x'}a_{xxy} + \xi_{y'}a_{yxy} + \xi_{z'}a_{zxy} \tag{E.4d}$$

$$\begin{aligned}\xi_{yy} =&\xi_{x'}\left(\sin^2\gamma\cos^2\beta\cos^2\alpha + \cos^2\gamma\sin^2\alpha + 2\sin\gamma\cos\gamma\cos\beta\sin\alpha\cos\alpha\right)\\ &+\xi_{y'}\left(\sin^2\gamma\cos^2\beta\sin^2\alpha + \cos^2\gamma\cos^2\alpha - 2\sin\gamma\cos\gamma\cos\beta\sin\alpha\cos\alpha\right)\\ &+\xi_{z'}\left(\sin^2\gamma\sin^2\beta\right) = \xi_{x'}a_{xyy} + \xi_{y'}a_{yyy} + \xi_{z'}a_{zyy}\end{aligned} \tag{E.4e}$$

$$\begin{aligned}\xi_{yz} = &-\xi_{x'}\left(\sin\gamma\sin\beta\cos\beta\cos^2\alpha + \cos\gamma\sin\beta\sin\alpha\cos\alpha\right)\\ &-\xi_{y'}\left(\sin\gamma\sin\beta\cos\beta\sin^2\alpha - \cos\gamma\sin\beta\sin\alpha\cos\alpha\right)\\ &-\xi_{z'}\left(-\sin\gamma\sin\beta\cos\beta\right) = \xi_{x'}a_{xyz} + \xi_{y'}a_{yyz} + \xi_{z'}a_{zyz}\end{aligned} \tag{E.4f}$$

$$\xi_{xz} =\xi_{x'}a_{xzx} + \xi_{y'}a_{yzx} + \xi_{z'}a_{zzx} = \xi_{x'}a_{xxz} + \xi_{y'}a_{yxz} + \xi_{z'}a_{zxz} \tag{E.4g}$$

$$\xi_{xy} =\xi_{x'}a_{xzy} + \xi_{y'}a_{yzy} + \xi_{z'}a_{zzy} = \xi_{x'}a_{xyz} + \xi_{y'}a_{yyz} + \xi_{z'}a_{zyz} \tag{E.4h}$$

$$\begin{aligned}\xi_{zz} =&\xi_{x'}\left(\sin^2\beta\cos^2\alpha\right) + \xi_{y'}\left(\sin^2\beta\sin^2\alpha\right) + \xi_z\cos^2\beta\\ =&\xi_{x'}a_{zzx} + \xi_{y'}a_{yzz} + \xi_{z'}a_{zzz}\end{aligned} \tag{E.4i}$$

Integrating over the above elements yields

$$\left\langle\xi_{xx}\right\rangle = \int_0^{2\pi}d\gamma\int_0^{\pi}d\beta\int_0^{2\pi}d\alpha\; p(\alpha,\beta,\gamma)\;\xi_{xx} = \frac{1}{3}\left(\xi_{x'} + \xi_{y'} + \xi_{z'}\right) \tag{E.5a}$$

$$\left\langle\xi_{yy}\right\rangle = \int_0^{2\pi}d\gamma\int_0^{\pi}d\beta\int_0^{2\pi}d\alpha\; p(\alpha,\beta,\gamma)\;\xi_{yy} = \frac{1}{3}\left(\xi_{x'} + \xi_{y'} + \xi_{z'}\right) \tag{E.5b}$$

$$\langle \xi_{zz} \rangle = \int_0^{2\pi} d\gamma \int_0^{\pi} d\beta \int_0^{2\pi} d\alpha \; p(\alpha,\beta,\gamma)\, \xi_{zz} = \frac{1}{3}(\xi_{x'} + \xi_{y'} + \xi_{z'}) \tag{E.5c}$$

$$\langle \xi_{xy} \rangle = \langle \xi_{yx} \rangle = \int_0^{2\pi} d\gamma \int_0^{\pi} d\beta \int_0^{2\pi} d\alpha \; p(\alpha,\beta,\gamma)\, \xi_{yx} = 0 \tag{E.5d}$$

$$\langle \xi_{xz} \rangle = \langle \xi_{zx} \rangle = \int_0^{2\pi} d\gamma \int_0^{\pi} d\beta \int_0^{2\pi} d\alpha \; p(\alpha,\beta,\gamma)\, \xi_{zx} = 0 \tag{E.5e}$$

$$\langle \xi_{yz} \rangle = \langle \xi_{zy} \rangle = \int_0^{2\pi} d\gamma \int_0^{\pi} d\beta \int_0^{2\pi} d\alpha \; p(\alpha,\beta,\gamma)\, \xi_{zy} = 0 \tag{E.5f}$$

For generality, subscript i for the scatterer species i and b for the background are not included in the notation of ξ_j $(j' = x', y', z')$ which can takes on the value of $\xi_{ij'}$ for scatterer species $i = 1, 2, 3, ..., N$ or $\xi_{ij'}$ for the background. The results above are used to obtain (24, Chapter 5). When ξ is replaced by S, (30, Chapter 5) is obtained.

Appendix F
Coefficients in Variances

Polarimetric scattering coefficients in Chapter 5 involve the term Δ_{tnjklm} which are integrals over the Eulerian angles of the probability density function of the random orientation and the variances in the global coordinates. Δ_{tnjklm} is considered a variance averaged over the orientation and defined by

$$\Delta_{tnjklm} = \sum_{u,v}^{x,y,z} \delta_{tnuv} \int_0^{2\pi} d\gamma \int_0^{\pi} d\beta \int_0^{2\pi} d\alpha \; p(\alpha,\beta,\gamma) \; a_{ujk} a_{vlm}$$

There are six subscripts associated with coefficient a's in the above equation. Each subscript can be x, y, or z; therefore, there are $3^6 = 729$ terms in total. After being integrated, 540 terms becomes zero and the remaining non-zero terms are presented in this appendix. The coefficients a's, given in Appendix E, come from the rotation operation on the tensors. As an example, consider the following integration of the product of the orientation probability and $a_{xxx}a_{xxx}$

$$\int_0^{2\pi} d\gamma \int_0^{\pi} d\beta \int_0^{2\pi} d\alpha \; p(\alpha,\beta,\gamma) \; a_{xxx}a_{xxx} = \int_0^{2\pi} d\gamma \int_0^{\pi} \beta \int_0^{2\pi} d\alpha \; \frac{\sin\beta}{8\pi^2}$$
$$\cdot \left(\cos^2\gamma\cos^2\beta\cos^2\alpha + \sin^2\gamma\sin^2\alpha - 2\sin\gamma\cos\gamma\cos\beta\sin\alpha\cos\alpha\right)^2$$
$$= \int_0^{2\pi} d\gamma \int_0^{\pi} \beta \int_0^{2\pi} d\alpha \; \frac{\sin\beta}{8\pi^2}$$
$$\Big[\cos^4\gamma\cos^4\beta\cos^4\alpha + \sin^4\gamma\sin^4\alpha + 4\sin^4\gamma\cos^2\gamma\cos^2\beta\sin^2\alpha\cos^2\alpha$$
$$+ 2\cos^2\gamma\cos^2\beta\cos^2\alpha\sin^2\gamma\sin^2\alpha - 4\cos^2\gamma\cos^2\beta\cos^2\alpha\sin\gamma\cos\gamma\cos\beta\sin\alpha\cos\alpha$$
$$-4\sin^2\gamma\sin^2\alpha\sin\gamma\cos\gamma\cos\beta\sin\alpha\cos\alpha\Big] = \frac{384}{1920} = \frac{1}{5}$$

Followed are all of the 189 non-zero results for the integrals in Δ_{tnjklm}

For $uv = xx$, the results are

$$\int_0^{2\pi} d\gamma \int_0^{\pi} d\beta \int_0^{2\pi} d\alpha\ p(\alpha,\beta,\gamma)\ a_{xxx}a_{xxx} = 1/5 \tag{F.1a}$$

$$\int_0^{2\pi} d\gamma \int_0^{\pi} d\beta \int_0^{2\pi} d\alpha\ p(\alpha,\beta,\gamma)\ a_{xxx}a_{xyy} = 1/15 \tag{F.1b}$$

$$\int_0^{2\pi} d\gamma \int_0^{\pi} d\beta \int_0^{2\pi} d\alpha\ p(\alpha,\beta,\gamma)\ a_{xxx}a_{xzz} = 1/15 \tag{F.1c}$$

$$\int_0^{2\pi} d\gamma \int_0^{\pi} d\beta \int_0^{2\pi} d\alpha\ p(\alpha,\beta,\gamma)\ a_{xxy}a_{xxy} = 1/15 \tag{F.1d}$$

$$\int_0^{2\pi} d\gamma \int_0^{\pi} d\beta \int_0^{2\pi} d\alpha\ p(\alpha,\beta,\gamma)\ a_{xxy}a_{xyx} = 1/15 \tag{F.1e}$$

$$\int_0^{2\pi} d\gamma \int_0^{\pi} d\beta \int_0^{2\pi} d\alpha\ p(\alpha,\beta,\gamma)\ a_{xxz}a_{xxz} = 1/15 \tag{F.1f}$$

$$\int_0^{2\pi} d\gamma \int_0^{\pi} d\beta \int_0^{2\pi} d\alpha\ p(\alpha,\beta,\gamma)\ a_{xxz}a_{xzx} = 1/15 \tag{F.1g}$$

$$\int_0^{2\pi} d\gamma \int_0^{\pi} d\beta \int_0^{2\pi} d\alpha\ p(\alpha,\beta,\gamma)\ a_{xyx}a_{xxy} = 1/15 \tag{F.1h}$$

$$\int_0^{2\pi} d\gamma \int_0^{\pi} d\beta \int_0^{2\pi} d\alpha\ p(\alpha,\beta,\gamma)\ a_{xyx}a_{xyx} = 1/15 \tag{F.1i}$$

$$\int_0^{2\pi} d\gamma \int_0^{\pi} d\beta \int_0^{2\pi} d\alpha\ p(\alpha,\beta,\gamma)\ a_{xyy}a_{xxx} = 1/15 \tag{F.1j}$$

$$\int_0^{2\pi} d\gamma \int_0^{\pi} d\beta \int_0^{2\pi} d\alpha\ p(\alpha,\beta,\gamma)\ a_{xyy}a_{xyy} = 1/5 \tag{F.1k}$$

$$\int_0^{2\pi} d\gamma \int_0^{\pi} d\beta \int_0^{2\pi} d\alpha\ p(\alpha,\beta,\gamma)\ a_{xyy}a_{xzz} = 1/15 \tag{F.1l}$$

$$\int_0^{2\pi} d\gamma \int_0^{\pi} d\beta \int_0^{2\pi} d\alpha\ p(\alpha,\beta,\gamma)\ a_{xyz}a_{xyz} = 1/15 \tag{F.1m}$$

$$\int_0^{2\pi} d\gamma \int_0^{\pi} d\beta \int_0^{2\pi} d\alpha\ p(\alpha,\beta,\gamma)\ a_{xyz}a_{xzy} = 1/15 \tag{F.1n}$$

$$\int_0^{2\pi} d\gamma \int_0^{\pi} d\beta \int_0^{2\pi} d\alpha\ p(\alpha,\beta,\gamma)\ a_{xzx}a_{xzx} = 1/15 \tag{F.1o}$$

$$\int_0^{2\pi} d\gamma \int_0^{\pi} d\beta \int_0^{2\pi} d\alpha\ p(\alpha,\beta,\gamma)\ a_{xzx}a_{xzx} = 1/15 \tag{F.1p}$$

$$\int_0^{2\pi} d\gamma \int_0^{\pi} d\beta \int_0^{2\pi} d\alpha\ p(\alpha,\beta,\gamma)\ a_{xzy}a_{xyz} = 1/15 \tag{F.1q}$$

$$\int_0^{2\pi} d\gamma \int_0^{\pi} d\beta \int_0^{2\pi} d\alpha\ p(\alpha,\beta,\gamma)\ a_{xzy}a_{xzy} = 1/15 \tag{F.1r}$$

$$\int_0^{2\pi} d\gamma \int_0^{\pi} d\beta \int_0^{2\pi} d\alpha\ p(\alpha,\beta,\gamma)\ a_{xzz}a_{xxx} = 1/15 \tag{F.1s}$$

$$\int_0^{2\pi} d\gamma \int_0^{\pi} d\beta \int_0^{2\pi} d\alpha\ p(\alpha,\beta,\gamma)\ a_{xzz}a_{xyy} = 1/15 \tag{F.1t}$$

$$\int_0^{2\pi} d\gamma \int_0^{\pi} d\beta \int_0^{2\pi} d\alpha\ p(\alpha,\beta,\gamma)\ a_{xzz}a_{xzz} = 1/5 \tag{F.1u}$$

For $uv = xy$, the results are

$$\int_0^{2\pi} d\gamma \int_0^{\pi} d\beta \int_0^{2\pi} d\alpha\ p(\alpha,\beta,\gamma)\ a_{zzz}a_{yzz} = 1/15 \tag{F.2a}$$

$$\int_0^{2\pi} d\gamma \int_0^{\pi} d\beta \int_0^{2\pi} d\alpha\ p(\alpha,\beta,\gamma)\ a_{zzz}a_{yyy} = 2/15 \tag{F.2b}$$

$$\int_0^{2\pi} d\gamma \int_0^{\pi} d\beta \int_0^{2\pi} d\alpha\ p(\alpha,\beta,\gamma)\ a_{zzz}a_{yzz} = 2/15 \tag{F.2c}$$

$$\int_0^{2\pi} d\gamma \int_0^{\pi} d\beta \int_0^{2\pi} d\alpha\ p(\alpha,\beta,\gamma)\ a_{zzy}a_{yzy} = -1/30 \tag{F.2d}$$

$$\int_0^{2\pi} d\gamma \int_0^{\pi} d\beta \int_0^{2\pi} d\alpha\ p(\alpha,\beta,\gamma)\ a_{zzy}a_{yyz} = -1/30 \tag{F.2e}$$

$$\int_0^{2\pi} d\gamma \int_0^{\pi} d\beta \int_0^{2\pi} d\alpha\ p(\alpha,\beta,\gamma)\ a_{zzz}a_{yzz} = -1/30 \tag{F.2f}$$

$$\int_0^{2\pi} d\gamma \int_0^{\pi} d\beta \int_0^{2\pi} d\alpha\ p(\alpha,\beta,\gamma)\ a_{zzz}a_{yzz} = -1/30 \tag{F.2g}$$

$$\int_0^{2\pi} d\gamma \int_0^{\pi} d\beta \int_0^{2\pi} d\alpha\ p(\alpha,\beta,\gamma)\ a_{zyz}a_{yzy} = -1/30 \tag{F.2h}$$

$$\int_0^{2\pi} d\gamma \int_0^{\pi} d\beta \int_0^{2\pi} d\alpha\ p(\alpha,\beta,\gamma)\ a_{zyz}a_{yyz} = -1/30 \tag{F.2i}$$

$$\int_0^{2\pi} d\gamma \int_0^{\pi} d\beta \int_0^{2\pi} d\alpha\ p(\alpha,\beta,\gamma)\ a_{zyy}a_{yzz} = 2/15 \tag{F.2j}$$

$$\int_0^{2\pi} d\gamma \int_0^{\pi} d\beta \int_0^{2\pi} d\alpha\ p(\alpha,\beta,\gamma)\ a_{zyy}a_{yyy} = 1/15 \tag{F.2k}$$

$$\int_0^{2\pi} d\gamma \int_0^{\pi} d\beta \int_0^{2\pi} d\alpha\ p(\alpha,\beta,\gamma)\ a_{zyy}a_{yzz} = 2/15 \tag{F.2l}$$

$$\int_0^{2\pi} d\gamma \int_0^{\pi} d\beta \int_0^{2\pi} d\alpha\ p(\alpha,\beta,\gamma)\ a_{zyz}a_{yyz} = -1/30 \tag{F.2m}$$

$$\int_0^{2\pi} d\gamma \int_0^{\pi} d\beta \int_0^{2\pi} d\alpha\ p(\alpha,\beta,\gamma)\ a_{zyz}a_{yzy} = -1/30 \tag{F.2n}$$

$$\int_0^{2\pi} d\gamma \int_0^{\pi} d\beta \int_0^{2\pi} d\alpha\ p(\alpha,\beta,\gamma)\ a_{zzz}a_{yzz} = -1/30 \tag{F.2o}$$

$$\int_0^{2\pi} d\gamma \int_0^{\pi} d\beta \int_0^{2\pi} d\alpha\ p(\alpha,\beta,\gamma)\ a_{zzz}a_{yzz} = -1/30 \tag{F.2p}$$

$$\int_0^{2\pi} d\gamma \int_0^{\pi} d\beta \int_0^{2\pi} d\alpha\ p(\alpha,\beta,\gamma)\ a_{zzy}a_{yyz} = -1/30 \tag{F.2q}$$

$$\int_0^{2\pi} d\gamma \int_0^{\pi} d\beta \int_0^{2\pi} d\alpha\ p(\alpha,\beta,\gamma)\ a_{zzy}a_{yzy} = -1/30 \tag{F.2r}$$

$$\int_0^{2\pi} d\gamma \int_0^{\pi} d\beta \int_0^{2\pi} d\alpha\ p(\alpha,\beta,\gamma)\ a_{zzz}a_{yzz} = 2/15 \tag{F.2s}$$

$$\int_0^{2\pi} d\gamma \int_0^{\pi} d\beta \int_0^{2\pi} d\alpha\ p(\alpha,\beta,\gamma)\ a_{zzz}a_{yyy} = 2/15 \tag{F.2t}$$

$$\int_0^{2\pi} d\gamma \int_0^{\pi} d\beta \int_0^{2\pi} d\alpha\ p(\alpha,\beta,\gamma)\ a_{zzz}a_{yzz} = 1/15 \tag{F.2u}$$

For $uv = xz$, the results are

$$\int_0^{2\pi} d\gamma \int_0^{\pi} d\beta \int_0^{2\pi} d\alpha\, p(\alpha,\beta,\gamma)\, a_{zzz} a_{zzz} = 1/15 \tag{F.3a}$$

$$\int_0^{2\pi} d\gamma \int_0^{\pi} d\beta \int_0^{2\pi} d\alpha\, p(\alpha,\beta,\gamma)\, a_{zzz} a_{zyy} = 2/15 \tag{F.3b}$$

$$\int_0^{2\pi} d\gamma \int_0^{\pi} d\beta \int_0^{2\pi} d\alpha\, p(\alpha,\beta,\gamma)\, a_{zzz} a_{zzz} = 2/15 \tag{F.3c}$$

$$\int_0^{2\pi} d\gamma \int_0^{\pi} d\beta \int_0^{2\pi} d\alpha\, p(\alpha,\beta,\gamma)\, a_{zzy} a_{zzy} = -1/30 \tag{F.3d}$$

$$\int_0^{2\pi} d\gamma \int_0^{\pi} d\beta \int_0^{2\pi} d\alpha\, p(\alpha,\beta,\gamma)\, a_{zzy} a_{zyz} = -1/30 \tag{F.3e}$$

$$\int_0^{2\pi} d\gamma \int_0^{\pi} d\beta \int_0^{2\pi} d\alpha\, p(\alpha,\beta,\gamma)\, a_{zzz} a_{zzz} = -1/30 \tag{F.3f}$$

$$\int_0^{2\pi} d\gamma \int_0^{\pi} d\beta \int_0^{2\pi} d\alpha\, p(\alpha,\beta,\gamma)\, a_{zzz} a_{zzz} = -1/30 \tag{F.3g}$$

$$\int_0^{2\pi} d\gamma \int_0^{\pi} d\beta \int_0^{2\pi} d\alpha\, p(\alpha,\beta,\gamma)\, a_{zyz} a_{zzy} = -1/30 \tag{F.3h}$$

$$\int_0^{2\pi} d\gamma \int_0^{\pi} d\beta \int_0^{2\pi} d\alpha\, p(\alpha,\beta,\gamma)\, a_{zyz} a_{zyz} = -1/30 \tag{F.3i}$$

$$\int_0^{2\pi} d\gamma \int_0^{\pi} d\beta \int_0^{2\pi} d\alpha\, p(\alpha,\beta,\gamma)\, a_{zyy} a_{zzz} = 2/15 \tag{F.3j}$$

$$\int_0^{2\pi} d\gamma \int_0^{\pi} d\beta \int_0^{2\pi} d\alpha\, p(\alpha,\beta,\gamma)\, a_{zyy} a_{zyy} = 1/15 \tag{F.3k}$$

$$\int_0^{2\pi} d\gamma \int_0^{\pi} d\beta \int_0^{2\pi} d\alpha\, p(\alpha,\beta,\gamma)\, a_{zyy} a_{zzz} = 2/15 \tag{F.3l}$$

$$\int_0^{2\pi} d\gamma \int_0^{\pi} d\beta \int_0^{2\pi} d\alpha\, p(\alpha,\beta,\gamma)\, a_{zyz} a_{zyz} = -1/30 \tag{F.3m}$$

$$\int_0^{2\pi} d\gamma \int_0^{\pi} d\beta \int_0^{2\pi} d\alpha\, p(\alpha,\beta,\gamma)\, a_{zyz} a_{zzy} = -1/30 \tag{F.3n}$$

$$\int_0^{2\pi} d\gamma \int_0^{\pi} d\beta \int_0^{2\pi} d\alpha\, p(\alpha,\beta,\gamma)\, a_{zzz} a_{zzz} = -1/30 \tag{F.3o}$$

$$\int_0^{2\pi} d\gamma \int_0^{\pi} d\beta \int_0^{2\pi} d\alpha\, p(\alpha,\beta,\gamma)\, a_{zzz} a_{zzz} = -1/30 \tag{F.3p}$$

$$\int_0^{2\pi} d\gamma \int_0^{\pi} d\beta \int_0^{2\pi} d\alpha\, p(\alpha,\beta,\gamma)\, a_{zzy} a_{zyz} = -1/30 \tag{F.3q}$$

$$\int_0^{2\pi} d\gamma \int_0^{\pi} d\beta \int_0^{2\pi} d\alpha\, p(\alpha,\beta,\gamma)\, a_{zzy} a_{zzy} = -1/30 \tag{F.3r}$$

$$\int_0^{2\pi} d\gamma \int_0^{\pi} d\beta \int_0^{2\pi} d\alpha\, p(\alpha,\beta,\gamma)\, a_{zzz} a_{zzz} = 2/15 \tag{F.3s}$$

$$\int_0^{2\pi} d\gamma \int_0^{\pi} d\beta \int_0^{2\pi} d\alpha\, p(\alpha,\beta,\gamma)\, a_{zzz} a_{zyy} = 2/15 \tag{F.3t}$$

$$\int_0^{2\pi} d\gamma \int_0^{\pi} d\beta \int_0^{2\pi} d\alpha\, p(\alpha,\beta,\gamma)\, a_{zzz} a_{zzz} = 1/15 \tag{F.3u}$$

For $uv = yx$, the results are

$$\int_0^{2\pi} d\gamma \int_0^{\pi} d\beta \int_0^{2\pi} d\alpha\, p(\alpha,\beta,\gamma)\, a_{yxx} a_{xxx} = 1/15 \tag{F.4a}$$

$$\int_0^{2\pi} d\gamma \int_0^{\pi} d\beta \int_0^{2\pi} d\alpha\, p(\alpha,\beta,\gamma)\, a_{yxx} a_{xyy} = 2/15 \tag{F.4b}$$

$$\int_0^{2\pi} d\gamma \int_0^{\pi} d\beta \int_0^{2\pi} d\alpha\, p(\alpha,\beta,\gamma)\, a_{yxx} a_{xzz} = 2/15 \tag{F.4c}$$

$$\int_0^{2\pi} d\gamma \int_0^{\pi} d\beta \int_0^{2\pi} d\alpha\, p(\alpha,\beta,\gamma)\, a_{yxy} a_{xxy} = -1/30 \tag{F.4d}$$

$$\int_0^{2\pi} d\gamma \int_0^{\pi} d\beta \int_0^{2\pi} d\alpha\, p(\alpha,\beta,\gamma)\, a_{yxy} a_{xyx} = -1/30 \tag{F.4e}$$

$$\int_0^{2\pi} d\gamma \int_0^{\pi} d\beta \int_0^{2\pi} d\alpha\, p(\alpha,\beta,\gamma)\, a_{yxz} a_{xxz} = -1/30 \tag{F.4f}$$

$$\int_0^{2\pi} d\gamma \int_0^{\pi} d\beta \int_0^{2\pi} d\alpha\, p(\alpha,\beta,\gamma)\, a_{yxz} a_{xzx} = -1/30 \tag{F.4g}$$

$$\int_0^{2\pi} d\gamma \int_0^{\pi} d\beta \int_0^{2\pi} d\alpha\, p(\alpha,\beta,\gamma)\, a_{yyx} a_{xxy} = -1/30 \tag{F.4h}$$

$$\int_0^{2\pi} d\gamma \int_0^{\pi} d\beta \int_0^{2\pi} d\alpha\, p(\alpha,\beta,\gamma)\, a_{yyx} a_{xyx} = -1/30 \tag{F.4i}$$

$$\int_0^{2\pi} d\gamma \int_0^{\pi} d\beta \int_0^{2\pi} d\alpha\, p(\alpha,\beta,\gamma)\, a_{yyy} a_{xxx} = 2/15 \tag{F.4j}$$

$$\int_0^{2\pi} d\gamma \int_0^{\pi} d\beta \int_0^{2\pi} d\alpha\, p(\alpha,\beta,\gamma)\, a_{yyy} a_{xyy} = 1/15 \tag{F.4k}$$

$$\int_0^{2\pi} d\gamma \int_0^{\pi} d\beta \int_0^{2\pi} d\alpha\, p(\alpha,\beta,\gamma)\, a_{yyy} a_{xzz} = 2/15 \tag{F.4l}$$

$$\int_0^{2\pi} d\gamma \int_0^{\pi} d\beta \int_0^{2\pi} d\alpha\, p(\alpha,\beta,\gamma)\, a_{yyz} a_{xyz} = -1/30 \tag{F.4m}$$

$$\int_0^{2\pi} d\gamma \int_0^{\pi} d\beta \int_0^{2\pi} d\alpha\, p(\alpha,\beta,\gamma)\, a_{yyz} a_{xzy} = -1/30 \tag{F.4n}$$

$$\int_0^{2\pi} d\gamma \int_0^{\pi} d\beta \int_0^{2\pi} d\alpha\, p(\alpha,\beta,\gamma)\, a_{yzx} a_{xxx} = -1/30 \tag{F.4o}$$

$$\int_0^{2\pi} d\gamma \int_0^{\pi} d\beta \int_0^{2\pi} d\alpha\, p(\alpha,\beta,\gamma)\, a_{yzx} a_{xzx} = -1/30 \tag{F.4p}$$

$$\int_0^{2\pi} d\gamma \int_0^{\pi} d\beta \int_0^{2\pi} d\alpha\, p(\alpha,\beta,\gamma)\, a_{yzy} a_{xyx} = -1/30 \tag{F.4q}$$

$$\int_0^{2\pi} d\gamma \int_0^{\pi} d\beta \int_0^{2\pi} d\alpha\, p(\alpha,\beta,\gamma)\, a_{yzy} a_{xzy} = -1/30 \tag{F.4r}$$

$$\int_0^{2\pi} d\gamma \int_0^{\pi} d\beta \int_0^{2\pi} d\alpha\, p(\alpha,\beta,\gamma)\, a_{yzz} a_{xxx} = 2/15 \tag{F.4s}$$

$$\int_0^{2\pi} d\gamma \int_0^{\pi} d\beta \int_0^{2\pi} d\alpha\, p(\alpha,\beta,\gamma)\, a_{yzz} a_{xyy} = 2/15 \tag{F.4t}$$

$$\int_0^{2\pi} d\gamma \int_0^{\pi} d\beta \int_0^{2\pi} d\alpha\, p(\alpha,\beta,\gamma)\, a_{yzz} a_{xzz} = 1/15 \tag{F.4u}$$

For $uv = yy$, the results are

$$\int_0^{2\pi} d\gamma \int_0^{\pi} d\beta \int_0^{2\pi} d\alpha\ p(\alpha,\beta,\gamma)\ a_{yzz}a_{yzz} = 1/5 \tag{F.5a}$$

$$\int_0^{2\pi} d\gamma \int_0^{\pi} d\beta \int_0^{2\pi} d\alpha\ p(\alpha,\beta,\gamma)\ a_{yzz}a_{yyy} = 1/15 \tag{F.5b}$$

$$\int_0^{2\pi} d\gamma \int_0^{\pi} d\beta \int_0^{2\pi} d\alpha\ p(\alpha,\beta,\gamma)\ a_{yzz}a_{yzz} = 1/15 \tag{F.5c}$$

$$\int_0^{2\pi} d\gamma \int_0^{\pi} d\beta \int_0^{2\pi} d\alpha\ p(\alpha,\beta,\gamma)\ a_{yzy}a_{yzy} = 1/15 \tag{F.5d}$$

$$\int_0^{2\pi} d\gamma \int_0^{\pi} d\beta \int_0^{2\pi} d\alpha\ p(\alpha,\beta,\gamma)\ a_{yzy}a_{yyz} = 1/15 \tag{F.5e}$$

$$\int_0^{2\pi} d\gamma \int_0^{\pi} d\beta \int_0^{2\pi} d\alpha\ p(\alpha,\beta,\gamma)\ a_{yzz}a_{yzz} = 1/15 \tag{F.5f}$$

$$\int_0^{2\pi} d\gamma \int_0^{\pi} d\beta \int_0^{2\pi} d\alpha\ p(\alpha,\beta,\gamma)\ a_{yzz}a_{yzz} = 1/15 \tag{F.5g}$$

$$\int_0^{2\pi} d\gamma \int_0^{\pi} d\beta \int_0^{2\pi} d\alpha\ p(\alpha,\beta,\gamma)\ a_{yyz}a_{yzy} = 1/15 \tag{F.5h}$$

$$\int_0^{2\pi} d\gamma \int_0^{\pi} d\beta \int_0^{2\pi} d\alpha\ p(\alpha,\beta,\gamma)\ a_{yyz}a_{yyz} = 1/15 \tag{F.5i}$$

$$\int_0^{2\pi} d\gamma \int_0^{\pi} d\beta \int_0^{2\pi} d\alpha\ p(\alpha,\beta,\gamma)\ a_{yyy}a_{yzz} = 1/15 \tag{F.5j}$$

$$\int_0^{2\pi} d\gamma \int_0^{\pi} d\beta \int_0^{2\pi} d\alpha\ p(\alpha,\beta,\gamma)\ a_{yyy}a_{yyy} = 1/5 \tag{F.5k}$$

$$\int_0^{2\pi} d\gamma \int_0^{\pi} d\beta \int_0^{2\pi} d\alpha\ p(\alpha,\beta,\gamma)\ a_{yyy}a_{yzz} = 1/15 \tag{F.5l}$$

$$\int_0^{2\pi} d\gamma \int_0^{\pi} d\beta \int_0^{2\pi} d\alpha\ p(\alpha,\beta,\gamma)\ a_{yyz}a_{yyz} = 1/15 \tag{F.5m}$$

$$\int_0^{2\pi} d\gamma \int_0^{\pi} d\beta \int_0^{2\pi} d\alpha\ p(\alpha,\beta,\gamma)\ a_{yyz}a_{yzy} = 1/15 \tag{F.5n}$$

$$\int_0^{2\pi} d\gamma \int_0^{\pi} d\beta \int_0^{2\pi} d\alpha\ p(\alpha,\beta,\gamma)\ a_{yzz}a_{yzz} = 1/15 \tag{F.5o}$$

$$\int_0^{2\pi} d\gamma \int_0^{\pi} d\beta \int_0^{2\pi} d\alpha\ p(\alpha,\beta,\gamma)\ a_{yzz}a_{yzz} = 1/15 \tag{F.5p}$$

$$\int_0^{2\pi} d\gamma \int_0^{\pi} d\beta \int_0^{2\pi} d\alpha\ p(\alpha,\beta,\gamma)\ a_{yzy}a_{yyz} = 1/15 \tag{F.5q}$$

$$\int_0^{2\pi} d\gamma \int_0^{\pi} d\beta \int_0^{2\pi} d\alpha\ p(\alpha,\beta,\gamma)\ a_{yzy}a_{yzy} = 1/15 \tag{F.5r}$$

$$\int_0^{2\pi} d\gamma \int_0^{\pi} d\beta \int_0^{2\pi} d\alpha\ p(\alpha,\beta,\gamma)\ a_{yzz}a_{yzz} = 1/15 \tag{F.5s}$$

$$\int_0^{2\pi} d\gamma \int_0^{\pi} d\beta \int_0^{2\pi} d\alpha\ p(\alpha,\beta,\gamma)\ a_{yzz}a_{yyy} = 1/15 \tag{F.5t}$$

$$\int_0^{2\pi} d\gamma \int_0^{\pi} d\beta \int_0^{2\pi} d\alpha\ p(\alpha,\beta,\gamma)\ a_{yzz}a_{yzz} = 1/5 \tag{F.5u}$$

For $uv = yz$, the results are

$$\int_0^{2\pi} d\gamma \int_0^{\pi} d\beta \int_0^{2\pi} d\alpha\ p(\alpha,\beta,\gamma)\ a_{yxx}a_{zxx} = 1/15 \tag{F.6a}$$

$$\int_0^{2\pi} d\gamma \int_0^{\pi} d\beta \int_0^{2\pi} d\alpha\ p(\alpha,\beta,\gamma)\ a_{yxx}a_{zyy} = 2/15 \tag{F.6b}$$

$$\int_0^{2\pi} d\gamma \int_0^{\pi} d\beta \int_0^{2\pi} d\alpha\ p(\alpha,\beta,\gamma)\ a_{yxx}a_{zzz} = 2/15 \tag{F.6c}$$

$$\int_0^{2\pi} d\gamma \int_0^{\pi} d\beta \int_0^{2\pi} d\alpha\ p(\alpha,\beta,\gamma)\ a_{yxy}a_{zxy} = -1/30 \tag{F.6d}$$

$$\int_0^{2\pi} d\gamma \int_0^{\pi} d\beta \int_0^{2\pi} d\alpha\ p(\alpha,\beta,\gamma)\ a_{yxy}a_{zyx} = -1/30 \tag{F.6e}$$

$$\int_0^{2\pi} d\gamma \int_0^{\pi} d\beta \int_0^{2\pi} d\alpha\ p(\alpha,\beta,\gamma)\ a_{yxz}a_{zxz} = -1/30 \tag{F.6f}$$

$$\int_0^{2\pi} d\gamma \int_0^{\pi} d\beta \int_0^{2\pi} d\alpha\ p(\alpha,\beta,\gamma)\ a_{yxz}a_{zzx} = -1/30 \tag{F.6g}$$

$$\int_0^{2\pi} d\gamma \int_0^{\pi} d\beta \int_0^{2\pi} d\alpha\ p(\alpha,\beta,\gamma)\ a_{yyz}a_{zxy} = -1/30 \tag{F.6h}$$

$$\int_0^{2\pi} d\gamma \int_0^{\pi} d\beta \int_0^{2\pi} d\alpha\ p(\alpha,\beta,\gamma)\ a_{yyz}a_{zyx} = -1/30 \tag{F.6i}$$

$$\int_0^{2\pi} d\gamma \int_0^{\pi} d\beta \int_0^{2\pi} d\alpha\ p(\alpha,\beta,\gamma)\ a_{yyy}a_{zxx} = 2/15 \tag{F.6j}$$

$$\int_0^{2\pi} d\gamma \int_0^{\pi} d\beta \int_0^{2\pi} d\alpha\ p(\alpha,\beta,\gamma)\ a_{yyy}a_{zyy} = 1/15 \tag{F.6k}$$

$$\int_0^{2\pi} d\gamma \int_0^{\pi} d\beta \int_0^{2\pi} d\alpha\ p(\alpha,\beta,\gamma)\ a_{yyy}a_{zzz} = 2/15 \tag{F.6l}$$

$$\int_0^{2\pi} d\gamma \int_0^{\pi} d\beta \int_0^{2\pi} d\alpha\ p(\alpha,\beta,\gamma)\ a_{yyz}a_{zyz} = -1/30 \tag{F.6m}$$

$$\int_0^{2\pi} d\gamma \int_0^{\pi} d\beta \int_0^{2\pi} d\alpha\ p(\alpha,\beta,\gamma)\ a_{yyz}a_{zzy} = -1/30 \tag{F.6n}$$

$$\int_0^{2\pi} d\gamma \int_0^{\pi} d\beta \int_0^{2\pi} d\alpha\ p(\alpha,\beta,\gamma)\ a_{yzx}a_{zxz} = -1/30 \tag{F.6o}$$

$$\int_0^{2\pi} d\gamma \int_0^{\pi} d\beta \int_0^{2\pi} d\alpha\ p(\alpha,\beta,\gamma)\ a_{yzx}a_{zzx} = -1/30 \tag{F.6p}$$

$$\int_0^{2\pi} d\gamma \int_0^{\pi} d\beta \int_0^{2\pi} d\alpha\ p(\alpha,\beta,\gamma)\ a_{yzy}a_{zyz} = -1/30 \tag{F.6q}$$

$$\int_0^{2\pi} d\gamma \int_0^{\pi} d\beta \int_0^{2\pi} d\alpha\ p(\alpha,\beta,\gamma)\ a_{yzy}a_{zzy} = -1/30 \tag{F.6r}$$

$$\int_0^{2\pi} d\gamma \int_0^{\pi} d\beta \int_0^{2\pi} d\alpha\ p(\alpha,\beta,\gamma)\ a_{yzz}a_{zxx} = 2/15 \tag{F.6s}$$

$$\int_0^{2\pi} d\gamma \int_0^{\pi} d\beta \int_0^{2\pi} d\alpha\ p(\alpha,\beta,\gamma)\ a_{yzz}a_{zyy} = 2/15 \tag{F.6t}$$

$$\int_0^{2\pi} d\gamma \int_0^{\pi} d\beta \int_0^{2\pi} d\alpha\ p(\alpha,\beta,\gamma)\ a_{yzz}a_{zzz} = 1/15 \tag{F.6u}$$

For $uv = zx$, the results are

$$\int_0^{2\pi} d\gamma \int_0^{\pi} d\beta \int_0^{2\pi} d\alpha\, p(\alpha,\beta,\gamma)\, a_{zzz} a_{xxx} = 1/15 \tag{F.7a}$$

$$\int_0^{2\pi} d\gamma \int_0^{\pi} d\beta \int_0^{2\pi} d\alpha\, p(\alpha,\beta,\gamma)\, a_{zzz} a_{xyy} = 2/15 \tag{F.7b}$$

$$\int_0^{2\pi} d\gamma \int_0^{\pi} d\beta \int_0^{2\pi} d\alpha\, p(\alpha,\beta,\gamma)\, a_{zzz} a_{xzz} = 2/15 \tag{F.7c}$$

$$\int_0^{2\pi} d\gamma \int_0^{\pi} d\beta \int_0^{2\pi} d\alpha\, p(\alpha,\beta,\gamma)\, a_{zzy} a_{xxy} = -1/30 \tag{F.7d}$$

$$\int_0^{2\pi} d\gamma \int_0^{\pi} d\beta \int_0^{2\pi} d\alpha\, p(\alpha,\beta,\gamma)\, a_{zzy} a_{xyx} = -1/30 \tag{F.7e}$$

$$\int_0^{2\pi} d\gamma \int_0^{\pi} d\beta \int_0^{2\pi} d\alpha\, p(\alpha,\beta,\gamma)\, a_{zzx} a_{xzz} = -1/30 \tag{F.7f}$$

$$\int_0^{2\pi} d\gamma \int_0^{\pi} d\beta \int_0^{2\pi} d\alpha\, p(\alpha,\beta,\gamma)\, a_{zzx} a_{xzx} = -1/30 \tag{F.7g}$$

$$\int_0^{2\pi} d\gamma \int_0^{\pi} d\beta \int_0^{2\pi} d\alpha\, p(\alpha,\beta,\gamma)\, a_{zyz} a_{xzy} = -1/30 \tag{F.7h}$$

$$\int_0^{2\pi} d\gamma \int_0^{\pi} d\beta \int_0^{2\pi} d\alpha\, p(\alpha,\beta,\gamma)\, a_{zyz} a_{xyx} = -1/30 \tag{F.7i}$$

$$\int_0^{2\pi} d\gamma \int_0^{\pi} d\beta \int_0^{2\pi} d\alpha\, p(\alpha,\beta,\gamma)\, a_{zyy} a_{xzx} = 2/15 \tag{F.7j}$$

$$\int_0^{2\pi} d\gamma \int_0^{\pi} d\beta \int_0^{2\pi} d\alpha\, p(\alpha,\beta,\gamma)\, a_{zyy} a_{zyy} = 1/15 \tag{F.7k}$$

$$\int_0^{2\pi} d\gamma \int_0^{\pi} d\beta \int_0^{2\pi} d\alpha\, p(\alpha,\beta,\gamma)\, a_{zyy} a_{zzz} = 2/15 \tag{F.7l}$$

$$\int_0^{2\pi} d\gamma \int_0^{\pi} d\beta \int_0^{2\pi} d\alpha\, p(\alpha,\beta,\gamma)\, a_{zyz} a_{zyz} = -1/30 \tag{F.7m}$$

$$\int_0^{2\pi} d\gamma \int_0^{\pi} d\beta \int_0^{2\pi} d\alpha\, p(\alpha,\beta,\gamma)\, a_{zyz} a_{zxy} = -1/30 \tag{F.7n}$$

$$\int_0^{2\pi} d\gamma \int_0^{\pi} d\beta \int_0^{2\pi} d\alpha\, p(\alpha,\beta,\gamma)\, a_{zzx} a_{zzx} = -1/30 \tag{F.7o}$$

$$\int_0^{2\pi} d\gamma \int_0^{\pi} d\beta \int_0^{2\pi} d\alpha\, p(\alpha,\beta,\gamma)\, a_{zzx} a_{zxx} = -1/30 \tag{F.7p}$$

$$\int_0^{2\pi} d\gamma \int_0^{\pi} d\beta \int_0^{2\pi} d\alpha\, p(\alpha,\beta,\gamma)\, a_{zzy} a_{zyz} = -1/30 \tag{F.7q}$$

$$\int_0^{2\pi} d\gamma \int_0^{\pi} d\beta \int_0^{2\pi} d\alpha\, p(\alpha,\beta,\gamma)\, a_{zzy} a_{zxy} = -1/30 \tag{F.7r}$$

$$\int_0^{2\pi} d\gamma \int_0^{\pi} d\beta \int_0^{2\pi} d\alpha\, p(\alpha,\beta,\gamma)\, a_{zzz} a_{xxx} = 2/15 \tag{F.7s}$$

$$\int_0^{2\pi} d\gamma \int_0^{\pi} d\beta \int_0^{2\pi} d\alpha\, p(\alpha,\beta,\gamma)\, a_{zzz} a_{zyy} = 2/15 \tag{F.7t}$$

$$\int_0^{2\pi} d\gamma \int_0^{\pi} d\beta \int_0^{2\pi} d\alpha\, p(\alpha,\beta,\gamma)\, a_{zzz} a_{zzz} = 1/15 \tag{F.7u}$$

For $uv = zy$, the results are

$$\int_0^{2\pi} d\gamma \int_0^{\pi} d\beta \int_0^{2\pi} d\alpha\ p(\alpha,\beta,\gamma)\ a_{xxx}a_{yxx} = 1/15 \tag{F.8a}$$

$$\int_0^{2\pi} d\gamma \int_0^{\pi} d\beta \int_0^{2\pi} d\alpha\ p(\alpha,\beta,\gamma)\ a_{xxx}a_{yyy} = 2/15 \tag{F.8b}$$

$$\int_0^{2\pi} d\gamma \int_0^{\pi} d\beta \int_0^{2\pi} d\alpha\ p(\alpha,\beta,\gamma)\ a_{xxx}a_{yzz} = 2/15 \tag{F.8c}$$

$$\int_0^{2\pi} d\gamma \int_0^{\pi} d\beta \int_0^{2\pi} d\alpha\ p(\alpha,\beta,\gamma)\ a_{xxy}a_{yxy} = -1/30 \tag{F.8d}$$

$$\int_0^{2\pi} d\gamma \int_0^{\pi} d\beta \int_0^{2\pi} d\alpha\ p(\alpha,\beta,\gamma)\ a_{xxy}a_{yyx} = -1/30 \tag{F.8e}$$

$$\int_0^{2\pi} d\gamma \int_0^{\pi} d\beta \int_0^{2\pi} d\alpha\ p(\alpha,\beta,\gamma)\ a_{xxz}a_{yxz} = -1/30 \tag{F.8f}$$

$$\int_0^{2\pi} d\gamma \int_0^{\pi} d\beta \int_0^{2\pi} d\alpha\ p(\alpha,\beta,\gamma)\ a_{xxz}a_{yzx} = -1/30 \tag{F.8g}$$

$$\int_0^{2\pi} d\gamma \int_0^{\pi} d\beta \int_0^{2\pi} d\alpha\ p(\alpha,\beta,\gamma)\ a_{xyx}a_{yxy} = -1/30 \tag{F.8h}$$

$$\int_0^{2\pi} d\gamma \int_0^{\pi} d\beta \int_0^{2\pi} d\alpha\ p(\alpha,\beta,\gamma)\ a_{xyx}a_{yyx} = -1/30 \tag{F.8i}$$

$$\int_0^{2\pi} d\gamma \int_0^{\pi} d\beta \int_0^{2\pi} d\alpha\ p(\alpha,\beta,\gamma)\ a_{xyy}a_{yxx} = 2/15 \tag{F.8j}$$

$$\int_0^{2\pi} d\gamma \int_0^{\pi} d\beta \int_0^{2\pi} d\alpha\ p(\alpha,\beta,\gamma)\ a_{xyy}a_{yyy} = 1/15 \tag{F.8k}$$

$$\int_0^{2\pi} d\gamma \int_0^{\pi} d\beta \int_0^{2\pi} d\alpha\ p(\alpha,\beta,\gamma)\ a_{xyy}a_{yzz} = 2/15 \tag{F.8l}$$

$$\int_0^{2\pi} d\gamma \int_0^{\pi} d\beta \int_0^{2\pi} d\alpha\ p(\alpha,\beta,\gamma)\ a_{xyz}a_{yyz} = -1/30 \tag{F.8m}$$

$$\int_0^{2\pi} d\gamma \int_0^{\pi} d\beta \int_0^{2\pi} d\alpha\ p(\alpha,\beta,\gamma)\ a_{xyz}a_{yzy} = -1/30 \tag{F.8n}$$

$$\int_0^{2\pi} d\gamma \int_0^{\pi} d\beta \int_0^{2\pi} d\alpha\ p(\alpha,\beta,\gamma)\ a_{xzx}a_{yzz} = -1/30 \tag{F.8o}$$

$$\int_0^{2\pi} d\gamma \int_0^{\pi} d\beta \int_0^{2\pi} d\alpha\ p(\alpha,\beta,\gamma)\ a_{xzx}a_{yzx} = -1/30 \tag{F.8p}$$

$$\int_0^{2\pi} d\gamma \int_0^{\pi} d\beta \int_0^{2\pi} d\alpha\ p(\alpha,\beta,\gamma)\ a_{xzy}a_{yyz} = -1/30 \tag{F.8q}$$

$$\int_0^{2\pi} d\gamma \int_0^{\pi} d\beta \int_0^{2\pi} d\alpha\ p(\alpha,\beta,\gamma)\ a_{xzy}a_{yzy} = -1/30 \tag{F.8r}$$

$$\int_0^{2\pi} d\gamma \int_0^{\pi} d\beta \int_0^{2\pi} d\alpha\ p(\alpha,\beta,\gamma)\ a_{xzz}a_{yxx} = 2/15 \tag{F.8s}$$

$$\int_0^{2\pi} d\gamma \int_0^{\pi} d\beta \int_0^{2\pi} d\alpha\ p(\alpha,\beta,\gamma)\ a_{xzz}a_{yyy} = 2/15 \tag{F.8t}$$

$$\int_0^{2\pi} d\gamma \int_0^{\pi} d\beta \int_0^{2\pi} d\alpha\ p(\alpha,\beta,\gamma)\ a_{xzz}a_{yzz} = 1/15 \tag{F.8u}$$

For $uv = zz$, the results are

$$\int_0^{2\pi} d\gamma \int_0^{\pi} d\beta \int_0^{2\pi} d\alpha\ p(\alpha,\beta,\gamma)\ a_{zzz}a_{zzz} = 1/5 \tag{F.9a}$$

$$\int_0^{2\pi} d\gamma \int_0^{\pi} d\beta \int_0^{2\pi} d\alpha\ p(\alpha,\beta,\gamma)\ a_{zzz}a_{zyy} = 1/15 \tag{F.9b}$$

$$\int_0^{2\pi} d\gamma \int_0^{\pi} d\beta \int_0^{2\pi} d\alpha\ p(\alpha,\beta,\gamma)\ a_{zzz}a_{zzz} = 1/15 \tag{F.9c}$$

$$\int_0^{2\pi} d\gamma \int_0^{\pi} d\beta \int_0^{2\pi} d\alpha\ p(\alpha,\beta,\gamma)\ a_{zzy}a_{zzy} = 1/15 \tag{F.9d}$$

$$\int_0^{2\pi} d\gamma \int_0^{\pi} d\beta \int_0^{2\pi} d\alpha\ p(\alpha,\beta,\gamma)\ a_{zzy}a_{zyz} = 1/15 \tag{F.9e}$$

$$\int_0^{2\pi} d\gamma \int_0^{\pi} d\beta \int_0^{2\pi} d\alpha\ p(\alpha,\beta,\gamma)\ a_{zzz}a_{zzz} = 1/15 \tag{F.9f}$$

$$\int_0^{2\pi} d\gamma \int_0^{\pi} d\beta \int_0^{2\pi} d\alpha\ p(\alpha,\beta,\gamma)\ a_{zzz}a_{zzz} = 1/15 \tag{F.9g}$$

$$\int_0^{2\pi} d\gamma \int_0^{\pi} d\beta \int_0^{2\pi} d\alpha\ p(\alpha,\beta,\gamma)\ a_{zyz}a_{zzy} = 1/15 \tag{F.9h}$$

$$\int_0^{2\pi} d\gamma \int_0^{\pi} d\beta \int_0^{2\pi} d\alpha\ p(\alpha,\beta,\gamma)\ a_{zyz}a_{zyz} = 1/15 \tag{F.9i}$$

$$\int_0^{2\pi} d\gamma \int_0^{\pi} d\beta \int_0^{2\pi} d\alpha\ p(\alpha,\beta,\gamma)\ a_{zyy}a_{zzz} = 1/15 \tag{F.9j}$$

$$\int_0^{2\pi} d\gamma \int_0^{\pi} d\beta \int_0^{2\pi} d\alpha\ p(\alpha,\beta,\gamma)\ a_{zyy}a_{zyy} = 1/5 \tag{F.9k}$$

$$\int_0^{2\pi} d\gamma \int_0^{\pi} d\beta \int_0^{2\pi} d\alpha\ p(\alpha,\beta,\gamma)\ a_{zyy}a_{zzz} = 1/15 \tag{F.9l}$$

$$\int_0^{2\pi} d\gamma \int_0^{\pi} d\beta \int_0^{2\pi} d\alpha\ p(\alpha,\beta,\gamma)\ a_{zyz}a_{zyz} = 1/15 \tag{F.9m}$$

$$\int_0^{2\pi} d\gamma \int_0^{\pi} d\beta \int_0^{2\pi} d\alpha\ p(\alpha,\beta,\gamma)\ a_{zyz}a_{zzy} = 1/15 \tag{F.9n}$$

$$\int_0^{2\pi} d\gamma \int_0^{\pi} d\beta \int_0^{2\pi} d\alpha\ p(\alpha,\beta,\gamma)\ a_{zzz}a_{zzz} = 1/15 \tag{F.9o}$$

$$\int_0^{2\pi} d\gamma \int_0^{\pi} d\beta \int_0^{2\pi} d\alpha\ p(\alpha,\beta,\gamma)\ a_{zzz}a_{zzz} = 1/15 \tag{F.9p}$$

$$\int_0^{2\pi} d\gamma \int_0^{\pi} d\beta \int_0^{2\pi} d\alpha\ p(\alpha,\beta,\gamma)\ a_{zzy}a_{zyz} = 1/15 \tag{F.9q}$$

$$\int_0^{2\pi} d\gamma \int_0^{\pi} d\beta \int_0^{2\pi} d\alpha\ p(\alpha,\beta,\gamma)\ a_{zzy}a_{zzy} = 1/15 \tag{F.9r}$$

$$\int_0^{2\pi} d\gamma \int_0^{\pi} d\beta \int_0^{2\pi} d\alpha\ p(\alpha,\beta,\gamma)\ a_{zzz}a_{zzz} = 1/15 \tag{F.9s}$$

$$\int_0^{2\pi} d\gamma \int_0^{\pi} d\beta \int_0^{2\pi} d\alpha\ p(\alpha,\beta,\gamma)\ a_{zzz}a_{zyy} = 1/15 \tag{F.9t}$$

$$\int_0^{2\pi} d\gamma \int_0^{\pi} d\beta \int_0^{2\pi} d\alpha\ p(\alpha,\beta,\gamma)\ a_{zzz}a_{zzz} = 1/5 \tag{F.9u}$$

The results of the integrations show that many combinations of a's have one of the values: $-1/30$, $1/15$, $2/15$, or $1/5$. Actually, the results can be written in compact forms due to the symmetry in the combinations of the subscripts. By defining the averaging operator L as

$$L = \int_0^{2\pi} d\gamma \int_0^{\pi} d\beta \int_0^{2\pi} d\alpha \; p(\alpha, \beta, \gamma) \tag{F.10}$$

the non-zero terms can simply be expressed as

$$La_{uvv}a_{uvv} = 1/5 \tag{F.10a}$$

$$La_{rvv}a_{svw} = 2/15 \tag{F.10b}$$

$$La_{uvv}a_{uww} = La_{uvw}a_{uvw} = La_{uvw}a_{uwv} = La_{uww}a_{vww} = 1/15 \tag{F.10c}$$

$$La_{rvw}a_{svw} = La_{rvw}a_{swv} = -1/30 \tag{F.10d}$$

where subscript r, s, u, v, or w can be x, y, or z.

References

[1] J. B. Keller, "Accuracy and Validity of the Born and Rytov Approximation," *Journal of the Optical Society of America,* Vol. 59, pp. 1003-1004, August 1969.

[2] M. Zuniga and J. A. Kong, "Active Remote Sensing of Random Media," *Journal of Applied Physics,* Vol. 51, pp. 4-79, 1980.

[3] M. A. Zuniga, T. M. Habashy, and J. A. Kong, "Active Remote Sensing of Layered Random Media," *IEEE Transactions on Geoscience Electronics,* Vol. GE-17, No. 4, pp. 296-302, October 1979.

[4] J. K. Lee and J. A. Kong, "Active Microwave Remote Sensing of an Anisotropic Random Medium Layer," *IEEE Transactions on Geoscience and Remote Sensing,* Vol. GE-23, No. 6, pp. 910 - 923, November 1985.

[5] M. Borgeaud, J. A. Kong, and F. C. Lin, "Microwave Remote Sensing of Snow-covered Sea Ice," *Proceeding of the IGARSS'86 Symposium*, pp. 133-138, Zürich, September 8-11, 1986.

[6] M. Borgeaud, R. T. Shin, and J. A. Kong, "Theoretical Models for Polarimetric Radar Clutter," *Journal of Electromagnetic Waves and Applications*, Vol. 1, No. 1, pp. 73-89, 1987.

[7] M. Borgeaud, S. V. Nghiem, R. T. Shin, and J. A. Kong, "Theoretical Models for Polarimetric Microwave Remote Sensing of Earth Terrain," *Journal of Electromagnetic Waves and Applications*, Vol. 3, No. 1, pp. 61-81, 1989.

[8] M. A. Zuniga, J. A. Kong, and L. Tsang, "Depolarization Effects in the Active Remote Sensing of Random Media," *Journal of Applied Physics,* Vol. 51, No. 5, pp. 2315-2325, May 1980.

[9] D. A. de Wolf, "Electromagnetic Reflection from an Extended Turbulent Medium: Cumulative Forward-Scatter Single Backscatter Approximation," *IEEE Transactions on Antennas and Propagation,* Vol. AP-19, No. 2, pp. 254-262, March 1971.

[10] S. Rosenbaum and L. W. Bowles, "Clutter Return from Vegetated Areas," *IEEE Transactions on Antennas and Propagation,* Vol. AP-22, No. 2, pp. 227-236, March 1974.

[11] R. H. Lang, "Electromagnetic Backscattering from a Sparse Distribution of Lossy Dielectric Scatterers," *Radio Science,* Vol. 16, No 1, pp. 15-30, 1981.

[12] R. H. Lang and J. S. Sidhu, "Electromagnetic Backscattering from a Layer of Vegetation: A Discrete Approach," *IEEE Transactions on Geoscience and Remote Sensing,* Vol. GE-21, No. 1, pp. 62-71, January 1983.

[13] A. K. Fung and H. S. Fung, "Application of First-Order Renormalization Method to Scattering from a Vegetation-like Half-space," *IEEE Transactions on Geoscience Electronics,* Vol. GE-15, No. 4, pp. 189-195, October 1977.

[14] H. S. Tan, A. K. Fung, and H. Eom, "A Second-order Renormalization Theory for Cross-polarized Backscatter from a Half Space Random Medium," *Radio Science,* Vol. 15, No. 6, pp. 1059-1065, November-December 1980.

[15] H. T. Chuah and H. S. Tan, "A High Order Renormalization Method for Radar Backscatter from a Random Medium," *IEEE Transactions on Geoscience and Remote Sensing,* Vol. 27, No. 1, pp. 79-85, January 1989.

[16] J. K. Lee and J. A. Kong, "Electromagnetic Wave Scattering in a Two-layer Anisotropic Random Medium," *Journal of the Optical Society of America,* Vol. 2, pp. 2171 -2186, December 1985.

[17] L. Tsang and J. A. Kong, "Scattering of Electromagnetic Waves from Random Media with Strong Permittivity Fluctuations," *Radio Science,* Vol. 16, No. 3, pp. 303-320, May-June 1981.

[18] A. Stogryn, "The Bilocal Approximation for the Effective Dielectric Constant of an Isotropic Random Medium," *IEEE Transactions on Antennas and Propagation,* Vol. AP-32, No. 5, pp. 517-520, May 1984.

[19] L. Tsang, J. A. Kong, and R. W. Newton, "Application of Strong Fluctuation Random Medium Theory to Scattering of Electromagnetic Waves from a Half-space of Dielectric Mixture," *IEEE Transactions on Antennas and Propagation,* Vol. AP-30, No. 2, pp. 292-302, March 1982.

[20] L. Tsang and J. A. Kong, "Application of Strong Fluctuation Random Medium Theory to Scattering from Vegetation-Like Half Space," *IEEE Transactions on Geoscience and Remote Sensing,* Vol. GE-19, No. 1, pp. 62-69, January 1981.

[21] F. C. Lin, J. A. Kong, and R. T. Shin, "Theoretical Models for Active and Passive Microwave Remote Sensing of Snow-covered Sea Ice," *IGARSS'87,* University of Michigan, Ann Arbor, Michigan, May 18-21, 1987.

[22] Y. Q. Jin and J. A. Kong, "Strong Fluctuation Theory for Scattering, Attenuation, and Transmission of Microwave Through Snowfall," *IEEE Transactions on Geoscience and Remote Sensing,* Vol. GE-23, No. 5, pp. 754-760, September 1985.

[23] S. V. Nghiem, F. C. Lin, J. A. Kong, R. T. Shin, and H. A. Yueh, "Three-layer Random Medium Model for Fully Polarimetric Remote Sensing of Geophysical Media," *Digest of the Progress in Electromagnetics Research Symposium,* p. 267, Boston, Massachusetts, July 1989.

[24] F. Vallese and J. A. Kong, "Correlation Function Studies for Snow and Ice," *Journal of Applied Physics,* Vol. 52, No. 8, pp. 4921-4925, August 1981.

[25] A. Stogryn, "Correlation Functions for Random Granular Media in Strong Fluctuation Theory," *IEEE Transactions on Geoscience and Remote Sensing,* Vol. GE-22, pp. 150-154, 1984.

[26] D. K. Perovich and A. J. Gow, "A Statistical Description of Microstructure of Young Ice," *North American Sea Ice Workshop*, University of Massachusetts, Amherst, Massachusetts, June 26-28, 1989.

[27] L. Tsang, E. Njoku, and J. A. Kong, "Microwave Thermal Emission from a Stratified Medium with Nonuniform Temperature Distribution," *Journal of Applied Physics,* Vol. 46, No. 12, pp. 5127-5133, December 1975.

[28] M. A. Zuniga and J. A. Kong, "Mean Dyadic Green's Function for a Two-layer Random Medium," *Radio Science,* Vol. 16, No. 6, pp. 1255-1270, November-December 1981.

[29] J. K. Lee and J. A. Kong, "Dyadic Green's Functions for Layered Anisotropic Medium," *Electromagnetics,* Vol. 3, pp. 111-130, 1983.

[30] S. Chandrasekhar, *Radiative Transfer*, Dover, New York, 1960.

[31] A. Ishimaru, *Wave Propagation and Scattering in Random Media. Vol I: Single Scattering and Transport Theory.* Academic Press, New-York, 1978.

[32] L. Tsang, J. A. Kong, and R. T. Shin, *Theory of Microwave Remote Sensing*, John Wiley & Sons, New-York, 1985.

[33] R. L. Fante, "Relation between Radiative Transport Theory and Maxwell's Equations in Dielectric Media," *Journal of the Optical Society of America,* No. 71, pp. 460-468, 1981.

[34] V. I. Tatarskii, *The Effects of Turbulent Atmosphere on Wave Propagation*, National Tech. Information Service, Springfield, Virginia, 1971.

[35] L. Tsang and J. A. Kong, "Microwave Remote Sensing of a Two-layer Random Medium," *IEEE Transactions on Antennas and Propagation,* Vol. AP-24, pp. 283-287, 1976.

[36] L. Tsang and J. A. Kong, "Wave Theory for Microwave Remote Sensing of a Half-space Random Medium with Three-dimensional Variation," *Radio Science,* Vol. 14, pp. 359-369, 1979.

[37] M. A. Zuniga and J. A. Kong, "Modified Radiative Transfer Theory for a Two-layer Random Medium," *Journal of Applied Physics,* Vol. 51, No. 10, pp. 5228-5244, October 1980.

[38] J. K. Lee and J. A. Kong, "Modified Radiative Transfer Theory for a Two-layer Anisotropic Random Medium," *Journal of Electromagnetic Wave and Applications*, Vol. 2, No. 3/4, pp. 391-424, 1988.

[39] Y. Kuga and A. Ishimaru, "Retroreflectance from a Dense Distribution of Spherical Particles," *Journal of the Optical Society of America A: Optics and Image Science,* Series 2, Vol. 1, No. 8, pp. 831-835, August 1984.

[40] F. T. Ulaby, R. K. Moore, and A. K. Fung, *Microwave Remote Sensing Active and Passive, Vol. III, From Theory to Applications,* Artech House, Dedham, Massachusetts, 1986.

[41] A. K. Fung and H. J. Eom, "A Theory of Wave Scattering from an Inhomogeneous Layer with an Irregular Interface," *IEEE Transactions on Antennas and Propagation,* Vol. ap-29, pp. 899-910, 1989.

[42] R. T. Shin and J. A. Kong, "Theory for Thermal Microwave Emission from a Homogenous Layer with Rough Surfaces Containing Spherical Scatterers," *Journal of Geophysical Research,* Vol. 87, No. B7, pp. 5566-5576, July 1982.

[43] M. A. Karam and A. K. Fung, "Propagation and Scattering in Multi0layered Random Media with Rough Interfaces," *Electromagnetics,* Vol. 2, pp. 239-256, 1982.

[44] M. A. Karam and A. K. Fung, "Electromagnetic Scattering from a Layer of Finite Length, Randomly Oriented, Dielectric Circular Cylinders over a Rough Interface with Application to Vegetation," *International Journal of Remote Sensing,* Vol. 9, No. 6, pp. 1109-1134, 1988.

[45] R. T. Shin and J. A. Kong, "Radiative Transfer Theory for Active Remote Sensing of Two-layer Random Medium," in *Progress in Electromagnetics Research,* Vol. 1, Ed. by J.A. Kong, Elsevier, 1988.

[46] L. Tsang and J. A. Kong, "Theory for Thermal Microwave Emission from a Bounded Medium Containing Spherical Scatterers," *Journal of Applied Physics,* Vol. 48, pp. 3593-3599, August 1977.

[47] L. Tsang and J. A. Kong, "Thermal Microwave Emission from a Random Homogeneous Layer over a Homogeneous Medium Using the Method Invariant Imbedding," *Radio Science,* Vol. 12, pp. 185-195, 1977.

[48] J. A. Kong, R. Shin, J. C. Shiue, and L. Tsang, "Theory and Experiment for Passive Microwave Remote Sensing of Snowpacks," *Journal of Geophysical Research,* Vol. 84, No. B10, pp. 5669-5673, September 1979.

[49] R. T. Shin and J. A. Kong, "Radiative Transfer Theory for Active Remote Sensing of a Homogenous Layer Containing spherical Scatterers," *Journal of Applied Physics,* Vol. 52, No. 6, pp. 4221-4230, June 1981.

[50] L. Tsang and J. A. Kong, "Thermal Microwave Emission from a Three-layer Random Medium with Three-dimensional Variations," *IEEE Transactions on Geoscience and Remote Sensing,* Vol. GE-18, No. 2, pp. 212-216, April 1980.

[51] L. Tsang, J. A. Kong, and R. T. Shin "Radiative Transfer Theory for Active Sensing of a Layer of Nonspherical Particles," *Radio Science,* Vol. 19, No. 2, pp. 629-642, March-April 1984.

[52] S. L. Chuang, J. A. Kong, and L. Tsang, "Radiative Transfer Theory for Passive Microwave Remote Sensing of a Two-layer Random Medium with Cylindrical Structures," *Journal of Applied Physics,* Vol. 51, No. 11, pp. 5588-5593, November 1980.

[53] A. Ishimaru, D. Lesselier, and C. Yeh, "Multiple Scattering Calculations for Nonspherical Particles Based on the Vector Radiative Transfer Theory," *Radio Science,* Vol. 19, No. 5, pp. 1356-1366, October 1984.

[54] M. A. Karam and A. K. Fung, "Scattering from Randomly Oriented Circular Discs with Application to Vegetation," *Radio Science,* Vol. 18, No. 4, pp. 557-565, July-August 1983.

[55] L. Tsang, M. C. Kubacsi, and J. A. Kong, "Radiative Transfer Theory for Active Sensing of a Layer of Small Ellipsoidal Scatters," *Radio Science,* Vol. 16, No. 3, pp. 321-329, May-June 1981.

[56] M. A. Karam and A. K. Fung, "Leaf-shape Effects in Electromagnetic Wave Scattering from Vegetation," *IEEE Transactions on Geoscience and Remote Sensing,* Vol. GE-27, No. 6, pp. 687-697, November 1989.

[57] L. Tsang and A. Ishimaru, "Radiative Wave Equations for Vector Electromagnetic Propagation in Dense Nontenuous Media," *Journal of Electromagnetic Waves and Applications*, Vol. 1, No. 1, pp. 52-72, 1987.

[58] H. A. Yueh, R. T. Shin, and J. A. Kong, "Scattering from Randomly Oriented Scatterers with Strong Permittivity Fluctuations," *Journal of Electromagnetic Waves and Applications*, Vol. 4, No. 10, pp. 983-1004, 1990.

[59] G. Stokes, "On the Composition and Resolution of Streams of Polarized Light from Different Sources," *Proceedings of the Cambridge Philosophical Society*, Vol. 1, pp. 140-147, 1852.

[60] Lord Rayleigh, *Scientific Papers by Lord Rayleigh*, Vol. III, Dover Publications, New York, 1964.

[61] H. Poincaré, *Théorie Mathématique de la Lumière*, Vol. 2, Paris, 1892.

[62] H. Mueller, "The Foundation of Optics," *Journal of the Optical Society of America,* Vol. 38, pp. 661, 1948.

[63] R. C. Jones, "A New Calculus for the Treatment of Optical systems–Part I. Description and Discussion of the Calculus," *Journal of the Optical society of America,* Vol. 31, pp. 488-493, 1941.

[64] H. C. van de Hulst, *Light Scattering by Small Particles*, Dover Publications, New York, 1981.

[65] A. Ishimaru, *Wave Propagation in Random Media,* Vol. 1-2, Academic Press, New York, 1978.

[66] J. A. Kong, A. A. Swartz, H. A. Yueh, L. M. Novak, and R. T. Shin, "Identification of Terrain cover Using the Optimum Polarimetric Classifier," *Journal of Electromagnetic Waves and Applications,* Vol. 2, pp. 171-194, 1987.

[67] M. Born and E. Wolf, *Principle of Optics*, Pergamon Press, New York, 1980.

[68] S. Chandrasekhar, *Radiative Transfer*, Dover Publications, New York, 1960.

[69] D. Deirmendjian, *Electromagnetic Scattering on Spherical Polydispersions*, American Elsevier, New York, 1969.

[70] E. M. Kennaugh, "Effects of the Type of Polarization on Echo Characteristics," Report 389-9, Antenna Lab., Ohio State University, 1951.

[71] V. H. Rumsey, "Part I–Transmission between Elliptically Polarized Antennas," *Proc. I.R.E.,* Vol. 39, pp. 535-540, 1951.

[72] G. A. Deschamps, "Part II–Geometrical Representation of the Polarization of a Plane Electromagnetic Wave," *Proc. I.R.E.,* Vol. 39, pp. 540-544, 1951.

[73] M. J. Walker, "Matrix Calculus and the Stokes Parameters of Polarized Radiation," *American Journal of Physics,* Vol. 22, pp. 170-174, 1954.

[74] G. A. Deschamps and P. E. Mast, "Poincaré Sphere Representation of Partially Polarized Fields," *IEEE Trans. Antennas Propagat.,* Vol. AP-21, 1973.

[75] J. R. Huynen, "Phenomenological Theory of Radar Targets," in *Electromagnetic Scattering,* edited by P. L. E. Uslenghi, Academic Press, New York, 1978.

[76] P. S. Hauge, "Mueller Matric Ellipsometry with Imperfect Compensator," *Journal of the Optical Society of America,* Vol. 68, pp. 1519-1528, 1978.

[77] G. A. Ioannidis and D. E. Hammers, "Optimum Antenna Polarizations for Target Discrimination in Clutter," *IEEE Trans. Antennas Propagat.,* Vol. AP-27, pp. 357-363, 1979.

[78] A. B. Kostinski and W.-M. Boerner, "On Foundations of Radar Polarimetry," *IEEE Trans. Antennas Propagat,,* Vol. AP-34, 1986.

[79] K. Kim, L. Mandel, and E. Wolf, "Relationship between Jones and Mueller Matrices for Random Media," *Journal of the Optical Society of America A,* Vol. 4, pp. 433-437, 1987.

[80] J. J. van Zyl, H. A. Zebker, and C. Elachi, "Imaging Radar Polarization Signatures: Theory and Observation," *Radio Science,* Vol. 22, pp. 529-543, 1987.

[81] J. A. Kong, *Electromagnetic Wave Theory,* Wiley-Interscience, New York, 1986.

[82] A. Stogryn, "A Note on the Singular Part of the Dyadic Green's Function in Strong Fluctuation Theory," *Radio Science*, Vol. 18, pp. 1283-1286, 1983.

[83] M. Borgeaud, J. A. Kong, R. T. Shin, and S. V. Nghiem, "Theoretical Models for Polarimetric Microwave Remote Sensing of Earth Terrain," *Proceedings of the 1988 NATO Advanced Research Workshop*, Nuremberg, F. R. Germany, September, 1988.

[84] F. T. Ulaby and M. A. El-Rayes, "Microwave Dielectric Spectrum of Vegetation – Part II: Dual-Dispersion Model," *IEEE Transactions on Geoscience and Remote Sensing,* vol. GE-25, No. 5, pp. 550-557, 1987.

[85] M. T. Hallikainen, F. T. Ulaby, M. C. Dobson, M. A. El-Rayes, and L.-K. Wu, "Microwave Dielectric Behavior of Wet Soil – Part I: Empirical Models and Ex-

perimental Observations," *IEEE Transactions on Geoscience and Remote Sensing,* vol GE-23, No. 1, pp. 25-34, 1985.

[86] Y. S. Kim, R. K. Moore, and R. G. Onstott, "Theoretical and Experimental Study of Radar Back Scatter from Sea Ice," *RSL Tech. Rep. 331-37,* University of Kansas Center for Research, Inc. Lawrence, Kansas, 1984.

[87] F. C. Lin, "Theoretical Models for Microwave Remote Sensing of Snow-covered Sea Ice," *Ph.D. Thesis,* Department of Electrical Engineering and Computer Science, Massachusetts Institute of Technology, 1988.

[88] H. H. Lim, S. H. Yueh, R. T. Shin, and J. A. Kong, "Correlation Function for a Random Collection of Discrete Scatterers," *10th International Geoscience & Remote Sensing Symposium (IGARSS'90),* College Park, Maryland, May 20-24, 1990.

[89] E. Kreyszig, *Advanced Engineering Mathematics,* Fourth Edition, John Wiley & Sons, Inc., New York, 1979.

[90] D. K. Perovich and A. J. Gow, "A Statistical Description of Microstructure of Young Ice," *North American Sea Ice Workshop,* University of Massachusetts, Amherst, Massachusetts, June 26-28, 1989.

[91] A. J. Gow, S. A. Arcone, and S. G. McGrew, "Microwave and Structure Properties of Saline Ice," *CRREL Report 87-20,* US Army Cold Regions Research & Engineering Laboratory, October 1987.

[92] M. E. Tiuri, A. H. Sihvola, E. G. Nyfors, and M. T. Hallikainen, "The Complex Dielectric Constant of Snow at Microwave Frequencies," *IEEE Journal of Ocean Engineering,* Vol. OE-9, No. 5, pp. 377-382, December 1984.

[93] A. Stogryn and G. J. Desargant, "The Dielectric Properties of Brine in Sea Ice at Microwave Frequencies," *IEEE Transactions on Antennas and Propagation,* Vol. AP-33, No. 5, pp. 523-532, May 1985.

[94] G. F. N. Cox and W. F. Weeks, "Equations for Determining the Gas and Brine Volumes in Sea-ice Samples," *Journal of Glaciology,* Vol. 29, No. 012, pp. 306-316, 1983.

Biography

Son V. Nghiem received his B.S. degree (1985) in Electrical Engineering with Summa Cum Laude Honor from Texas A & M University, his S.M. degree (1988), and his E.E. degree (1991) in Electrical Engineering from Massachusetts Institute of Technology where he is completing the Ph. D. degree. His research interest encompasses electromagnetic wave theory, polarimetric remote sensing, and atmospheric and ionospheric effects on wave propagation. He is a member of the IEEE and the Honor Society of Phi Kappa Phi.